The Morphology and Dynamics of Galaxies from LCDM Models

PARRY, OWEN,HUW

The Morphology and Dynamics of Galaxies

from ΛCDM Models

Owen Huw Parry

Ph.D. Thesis, September 2011

Abstract

The formation and evolution of galaxies is studied using two alternative modelling techniques within the context of the ΛCDM cosmogony. In particular, we consider the capacity of the models to reproduce the fundamental components and internal structure of galaxies.

We begin by outlining the theoretical basis for the study, describing the standard paradigm for structure formation and the details of the modelling techniques we employ. The extent of our current understanding of the processes responsible for morphological transformation is explored and we discuss what the structure of the Milky Way and its satellites can reveal about the wider pictures of galaxy formation and cosmology.

Using data from two semi-analytical models, we investigate the origin of the disks and spheroids that represent the coarse-grain detail of galactic structure. Major galaxy mergers, which have long been regarded as the main mechanism by which elliptical galaxies and spiral bulges are generated, are found to play only a minor role in spheroid formation for all but the most massive systems. The models make similar predictions in many respects but disagree on the importance of gravitationally unstable disks in forming spheroids, serving to illustrate the uncertainty that remains in modelling morphology even at this basic level.

We go on to introduce a smoothed particle hydrodynamics code which includes models for radiative gas heating and cooling, the structure of the interstellar medium, star formation and evolution, chemical enrichment and feedback from supernovae. We present a set of simulations that focus on a single Milky Way-mass galaxy and its local environment and summarise its bulk properties and formation history. We also show results from a code comparison project, which aims to quantify the effects of different physical mechanisms and modelling approaches on the formation of a galaxy disk.

Our simulations also resolve the formation of a population of satellite galaxies which have a luminosity function similar to those found around the Milky Way. Through comparison with a dissipationless version of the same simulation, we determine that the baryonic component in each satellite has little effect on the structure of its dark matter halo. We also find a statistically significant discrepancy between the central mass densities of the simulated and observed satellites.

Finally, we consider the formation of the haloes of hot gas and stars which surround the main galaxy disk. We find qualitative agreement with several observed properties of the Milky Way's stellar halo and with recent theoretical studies of the two components in the literature.

The Morphology and Dynamics of Galaxies from ΛCDM Models

Owen Huw Parry

A thesis submitted to the University of Durham
in accordance with the regulations for
admittance to the Degree of Doctor of Philosophy.

Institute for Computational Cosmology
Department of Physics
University of Durham
September 2011

Contents

List of Figures

List of Tables

Declaration

The work described in this thesis was undertaken between 2007 and 2011 while the author was a research student under the supervision of Prof. Carlos S. Frenk and Dr. Vincent R. Eke at the Institute for Computational Cosmology (ICC) in the Department of Physics at the University of Durham. This work has not been submitted for any other degree at the University of Durham or any other university.

Parts of the work contained in Chapter 2 have been published in the paper

- Parry, O. H.; Eke, V. R.; Frenk, C. S., 2009, MNRAS, 396, 1972.

Parts of the work contained in Chapter 4 have been submitted in the form of a paper:

- Parry, O. H.; Eke, V. R.; Frenk, C. S., Okamoto, T., 2011, submitted to MNRAS

Parts of the work contained in Chapter 3 are being prepared for publication in the form of a paper:

- Scannapieco, C.; Wadepuhl M.; Parry, O. H.; Navarro, J. F. et al., in preparation, The Aquila Project: The Effects of Feedback and Numerical Methods on Simulations of Galaxy Formation

All figures and tables were produced by the author, except for the following:

- Fig. 1.1: Originally from Larson et al. (2011), NASA/WMAP public domain image.
- Fig. 1.2: NASA/STScI public domain image
- Table 3.2 and Figs. 3.22, 3.23, 3.27, 3.28, 3.29 and 3.31: Produced for the Aquila project by Cecilia Scannapieco (AIP, Potsdam)
- Figs. 3.21, 3.25 and 3.30: Produced for the Aquila project by Markus Wadepuhl (MPA, Munich)

All simulations for which results are presented were run and analysed by the author, except for the following:

- *Aq-C-4*, *Aq-C-5* and *Aq-C-6*: Run by Takashi Okamoto (CCS, University of Tsukuba).

- *G3, G3-BH,G3-CR* and *Arepo*: Run by Markus Wadepuhl.
- *G3-CS*: Run by Cecilia Scannapieco.
- *G3-GIMIC (level 5)*: Run by Rob Crain (CAS, Swinburne University of Technology).
- *G3-MM*: Run by Giuseppe Murante and Pierluigi Monaco (INAF, Trieste).
- *G3-CK*: Run by Chiaki Kobayashi (Mount Stromblo Observatory, Canberra).
- *GAS*: Run by Greg Stinson (JHI, University of Central Lancashire).
- *R, R-LSFE* and *R-AGN*: Run by Romain Teyssier (ITP, Zurich).

Parts of the discussion in Section 3.7 were written in collaboration with Cecilia Scannapieco and Markus Wadepuhl.
The simulation code described in Chapter 3 was written by Takashi Okamoto and based on the N-body+SPH code GADGET-3, written by Volker Springel (HITS, Heidelberg).
The software used to compute X-ray luminosities in Chapter 5 was written by Rob Crain.

Acknowledgements

This thesis could not have been completed without the substantial guidance and advice provided by my supervisors, Vince Eke and Carlos Frenk. I would like to thank Vince for keeping me on the scientific straight-and-narrow whenever it looked like I might have been about to veer into the undergrowth and for regularly asking one of the most important questions of all - "What is point?". I am grateful to Carlos, for his truly remarkable ability to motivate, to enthuse and to see the big picture (and for having at least three anecdotes for every occasion).

My thanks to the incomparable Lydia Heck, for keeping COSMA functioning despite the best efforts of those pesky "users" and for always being a friendly face around the department. I am indebted to Takashi Okamoto, John Helly and Rob Crain for providing numerous pieces of computer code and helpful advice and to my collaborators Cecilia Scannapieco, Markus Wadepuhl and Julio Navarro for all their considerable efforts in the Aquila project.

Thanks to officemates and other friends from Durham past and present, from whom I've learnt an enormous amount and who've made the last four years a great experience, including: Rich Bielby, Andrew Cooper, Daniel John, Mark Lovell, Ben Lowing, Matt Middleton, Tim Rawle and Dave Wake. My thanks in particular to Mike Hill for convincing me that climbing mountains in the rain can be enjoyable. Sometimes.

To my family - my heartfelt gratitude for offering help and support at every stage and for reminding me what is really important in life. But most of all, to Cherie. For more love, support, kindness, patience and tolerance than anybody deserves. This thesis is for her.

Poets say science takes away from the beauty of the stars - mere globs of gas atoms. I too can see the stars on a desert night, and feel them. But do I see less or more? The vastness of the heavens stretches my imagination - stuck on this carousel my little eye can catch one-million-year-old light... far more marvelous is the truth than any artists of the past imagined it.

— Richard P. Feynman

Chapter 1 | *Introduction*

In this thesis, we use computational modelling techniques to investigate the formation of galaxies, within the standard cosmological paradigm for structure formation. In particular, we examine the capacity of current models to explain the origins of galaxy morphology and structure. This introductory chapter outlines the concepts and modelling techniques that frame our investigation. We describe two widely used computational methods for following the evolution of galaxies, which take complementary approaches to the problem; semi-analytical models and hydrodynamical simulations. We go on to discuss the extent of current observational and theoretical knowledge with regard to galaxy morphology and the physical mechanisms thought to influence it. Finally, we present a brief overview of the morphologically distinct components in our own Milky Way galaxy and consider what they can reveal about its evolution and about cosmology. First though, we lay out the theoretical framework around which all modern galaxy formation models are constructed, which describes the growth of structure in the Universe over cosmic time. We also recall the key discoveries that led to its widespread acceptance.

1.1 The Standard Paradigm for Structure Formation

1.1.1 The Expansion of the Universe

Einstein's general theory of relativity (Einstein, 1916) describes the equivalence of matter and energy and their effect on the geometry of the Universe. In this formalism, gravity emerges as a natural consequence of the way in which mass and energy shape space-time. In 1922, Alexander Friedman demonstrated a solution to Einstein's field equations for the case of an isotropic, homogeneous universe[1] to obtain a pair of equations (Fried-

[1]These two assumptions constitute the well known *Cosmological Principle*. They were introduced by Einstein in order to simplify the problem, but may be justified if *inflation* accurately describes the behaviour of the early Universe (see section 1.1.2)

man, 1922) that describe an expanding universe:

$$H(a)^2 \equiv \left(\frac{\dot{a}}{a}\right)^2 = \frac{8\pi G}{3}\rho + \frac{\Lambda}{3} - \frac{kc^2}{a^2} \tag{1.1}$$

$$\frac{\ddot{a}}{a} = \frac{-4\pi G}{3}(\rho + \frac{3P}{c^2}) + \frac{\Lambda}{3} \tag{1.2}$$

The equations specify the evolution of the expansion factor, $a(t)$, which is defined as the ratio between the physical size of a scale at time t, relative to its size today. $H(a)$ is called the Hubble parameter, G is Newton's gravitational constant and c the speed of light, while ρ and P are the density and pressure of the matter-radiation fluid assumed to make up the Universe. The constant k describes the Universe's geometry. The cases $k < 0$, $k = 0$ and $k > 0$ correspond to hyperbolic, flat (Euclidean) and spherical geometries respectively. Λ is the *cosmological constant*, which makes a contribution to the expansion over and above that of matter and radiation and can be interpreted as the intrinsic energy of the vacuum. We shall see later that observations support a non-zero value for Λ, though its physical origin is as yet undetermined. The contribution of each component to the total energy density depends on their equation of state, $P = w\rho c^2$, where w is a constant which is zero for non-relativistic, collisionless matter ("dust"); $1/3$ for radiation and relativistic matter; and -1 for a cosmological constant (inducing a negative pressure from a positive energy density).

Setting $k = 0$ and incorporating the Λ term into the total density (i.e. writing $\Lambda = 8\pi G\rho_\Lambda$ and $\rho' = \rho + \rho_\Lambda$) one can calculate the density required to make the universe flat, the *critical density*:

$$\rho_{\rm crit} = \frac{3H(a)^2}{8\pi G} \tag{1.3}$$

It is convenient (and conventional) to express the total density, or contributions from particular components, as fractions of the critical density. For example for baryonic matter:

$$\Omega_b = \frac{\rho_b}{\rho_{\rm crit}} \tag{1.4}$$

The expansion of the Universe modifies the wavelength of photons travelling through it. If a photon with wavelength λ_e is emitted when the expansion factor has a value a, the same photon will be observed to have a longer wavelength $\lambda_o = \lambda_{\rm e}/a$ today. This is typically referred to in terms of *redshift*, the ratio between the change in wavelength and

the emitted wavelength:

$$z = \frac{\lambda_{\rm o} - \lambda_{\rm e}}{\lambda_{\rm e}} \equiv a^{-1} - 1 \tag{1.5}$$

In 1929, some years after Friedman proposed his solutions, Hubble made the discovery that nearby galaxies are receding from us with velocities proportional to their distances (Hubble, 1929), revolutionising modern astronomy and lending credibility for the first time to the idea of a universal expansion. Nonetheless, many remained uncomfortable with the concept, not least because it implies that the entire Universe was once confined to a single point in space-time - the "Big Bang" singularity. The theory received a huge boost in 1965, with the discovery of the cosmic microwave background (CMB) radiation (Penzias & Wilson, 1965; Dicke et al., 1965), which had been predicted as a signature of the initial hot and dense state of the universe (Gamow, 1948a,b; Alpher & Herman, 1948). There are, however, several well known problems with the standard Big Bang cosmogony.

- The Horizon Problem: Precise measurements of the CMB temperature show relative deviations from uniformity of less than one part in 10^5 across the sky (Smoot et al., 1992). It can be demonstrated that if $a(t)$ grows more slowly than t in the early universe, as it does for both the matter-dominated ($a(t) \propto t^{2/3}$) and radiation-dominated ($a(t) \propto t^{1/2}$) cases, then particle horizons exist. If regions of the early universe were not in causal contact at the epoch of recombination, it is difficult to explain why the CMB is so smooth (Dicke, 1961).

- The Flatness Problem: The current density of the universe appears to be close to the critical value; $\Omega = 1$. The Friedman equations, however, imply that initial values of Ω that deviate even slightly from unity rapidly evolve away from it (Dicke, 1961), corresponding to either a 'Big Crunch' in which gravity quickly reverses the expansion and collapses the Universe back to a singularity, or a 'Big Rip' in which the Universe expands so quickly that no structures form. At the earliest time at which current physics can be applied (The Planck time, $t \sim 10^{-35}s$), the value of Ω must have been equal to unity to better than one part in 10^{52} in order to explain its value today (Peacock, 1999). The Standard Big Bang Cosmogony provides no reason why this should be the case.

- The Monopoles Problem: In the very high energy regime of the early universe, the

strong weak and electromagnetic forces are expected to be unified. Under such conditions 'Grand Unified Theories' predict the production of a number of stable, high mass particles, including the magnetic monopole, in vast quantities, such that they should in fact dominate the mass-energy density of the universe today (e.g. Zeldovich & Khlopov, 1978), though none has ever been detected.

Perhaps more important than any of these, the standard Big Bang Theory offers no explanation for the formation of structure in the Universe. In the next section we explore an extension to the theory that may offer a solution to the problems discussed above and a natural mechanism to initiate structure formation.

1.1.2 Inflation

In 1981, Guth (1981) proposed that the Horizon and Flatness problems could be eliminated if the very early Universe (perhaps $10^{-35}s < t < 10^{-32}s$) underwent a phase of exponential growth, that is, $a(t) \propto e^{Ht}$. The mechanism for the expansion is a scalar field with a potential that quickly decays [2]. An exponential expansion means that causal contact is maintained during the inflationary period and thermal equilibrium can be achieved before recombination. Inflation also drives Ω rapidly towards unity, irrespective of its initial value (e.g. Peacock, 1999). The abundance of monopoles is no longer an issue, since inflation occurs after the temperature of the Universe has dropped below that necessary for their production and hence dilutes their spatial concentration to a level at which we would not expect to observe them. Inflation also provides a neat explanation for structure formation. Quantum fluctuations existing before inflation are amplified during the exponential expansion, seeding density perturbations that can then grow via gravitational instability. The perturbations are expected to be well represented by a nearly scale-invariant Gaussian random field (Hawking, 1982; Starobinsky, 1982; Bardeen et al., 1983), that is, fluctuations have an amplitude that is roughly independent of their scale. The *power spectrum* of fluctuations (effectively prevalence as a function of scale) can be computed by taking the Fourier transform of the two point correlation

[2] Guth's original model in fact proved to be flawed, in that it would result in a strongly inhomogeneous Universe inconsistent with observations (Guth & Weinberg, 1983), though subsequent developments removed this characteristic.

function, which is defined as

$$\xi_2(\Delta) = \langle \rho(\mathbf{r})\rho(\mathbf{r}+\Delta)\rangle. \tag{1.6}$$

The power spectrum of a Gaussian random field can be written as

$$P(k) = Ak^n, \tag{1.7}$$

where k is the wavenumber. Measurements of the primordial power spectrum from CMB data (e.g. Komatsu et al., 2011) and the clustering of galaxies in large surveys (e.g. Reid et al., 2010) are consistent with n just slightly less than one. Hence, although there is no clear motivation for the inflation and its associated field within the standard model of particle physics, the theory appears to provide a good description of the observations and constitutes an integral part of modern cosmogony.

1.1.3 Cold Dark Matter

Circumstantial evidence for an unseen mass component of the Universe has existed for some time. For example, Zwicky (1933) showed that there is insufficient luminous mass in the Coma cluster to gravitationally bind its galaxies. Many early studies of the rotation curves of spiral galaxies, particularly M31, found that they remain flat out to large radii (Babcock, 1939; van de Hulst et al., 1957; Rubin & Ford, 1970) rather than decaying like $1/r^{1/2}$ as expected if the visible matter represented the true extent of the mass distribution. In a similar vein, but from a theoretical perspective, Ostriker & Peebles (1973) showed that galaxy disks tend to be gravitationally unstable without the influence of a substantial (and unobserved) halo of material. The by-then numerous confirmations of high galaxy velocities in clusters were reinforced by gravitational lensing measurements that strengthened the case for missing mass (Walsh et al., 1979).

It was against this background that some of the first detailed theories for the identity of the dark matter were developed. Many baryonic candidates had been proposed, from faint stars, to diffuse cold gas, to black holes, but none appeared to make a sufficiently large contribution. Purely baryonic dark matter was eventually ruled out by observations of the CMB, because it implies much larger temperature fluctuations than are observed (Smoot et al., 1992).

Two classes of particle emerged as candidates for the non-baryonic dark matter, termed *hot* and *cold*, depending on whether they have relativistic or non-relativistic ve-

locities at recombination respectively. The neutrino was proposed as a hot dark matter (HDM) candidate (Cowsik & McClelland, 1973; Zeldovich et al., 1982) after experiments suggested it had a mass of a few tens of eV, but was quickly ruled out by simulations that demonstrated the structures formed in such models are entirely unlike those observed in galaxy surveys (White et al., 1983). The relativistic velocities of HDM particles allow them to *free stream* out of small scale density perturbations, such that the first structures to form are of supercluster masses ($> 10^{15}\ \mathrm{M}_{\odot}$).

Cold dark matter (CDM) models proposed a much heavier particle to account for the missing mass, with postulated supersymmetric particles (sparticles) like the neutralino (e.g. Edsjö & Gondolo, 1997) framed as favoured candidates. The first detailed calculations of the linear evolution of the CDM power spectrum were made by Peebles (1982, 1984a) and the consequences of the model for structure formation were laid out in full by Blumenthal et al. (1984). A convincing validation of CDM followed a short time later, when Davis et al. (1985) showed that structures forming in CDM simulations had very similar clustering properties to those in the CfA galaxy redshift survey (Huchra et al., 1983). Nonetheless, their best-fit model assumed a flat Universe and it was becoming increasingly clear that observations did not support $\Omega_m = 1$. This point was made neatly by White et al. (1993), who used the predictions made by Big Bang nucleosynthesis to place an upper limit on the dark matter density of the Universe. The observed abundances of Hydrogen, Helium, Helium-3, Lithium and Deuterium constrain Ω_b to be around 0.04 (assuming $\mathrm{H}_0 \sim 70 \mathrm{kms}^{-1}\mathrm{Mpc}^{-1}$). By measuring the baryon fraction in the Coma cluster and assuming it should be close to the mean value for the Universe as a whole, White et al. (1993) showed that $\Omega_{\mathrm{DM}} \leq 0.3$, in apparent conflict with the predicted outcome of inflation in the early Universe. Either the nucleosynthesis calculations were severely flawed, the inflationary paradigm was incorrect, or a significant proportion of the energy density of the Universe must be in some other entirely unfamiliar form.

1.1.4 Dark Energy

Several models had been proposed in the 80s and 90s that revived Einstein's cosmological constant (Λ) as a means to explain the additional energy density required by inflation (Peebles, 1984b; Lahav et al., 1991; Carroll et al., 1992). It was even claimed to be necessary to explain galaxy clustering (Efstathiou et al., 1990; Saunders et al., 1991) and faint

number counts (Fukugita et al., 1990), but there was no observational evidence to support a non-zero value. This changed in dramatic fashion in 1998, when it was shown by two independent groups that the expansion of the universe is accelerating (Riess et al., 1998; Goldhaber & Perlmutter, 1998). By assuming type Ia supernovae (SNe) are *standard candles*, they were able to estimate distances and hence an expansion rate. Incredibly, the data were consistent with $\Omega_\Lambda \sim 0.7$ and hence $\Omega \sim 1$, exactly as required by inflation. While observational data are consistent with the simplest form of dark energy, with a constant equation of state parameter $w = -1$, in principle numerous forms are possible. In *quintessence* models (Caldwell et al., 1998), w need not be constant in time, or even spatially homogeneous. Distinguishing between the different possibilities is extremely challenging, requiring incredibly precise measurements. Nonetheless, there is now a considerable amount of research activity devoted to trying to constrain dark energy models with various methods, including baryon acoustic oscillations (Schlegel et al., 2011), redshift space distortions (Blake et al., 2011) and more detailed type Ia SNe measurements (Sánchez & the Des collaboration, 2010).

1.1.5 Successes and Future Challenges

ΛCDM is now widely accepted as the standard cosmogony, despite the fact that both of its central components remain unidentified. In the case of the dark energy, as described above, this situation looks unlikely to change in the near future. With regard to the dark matter, however, there are more grounds for optimism. It may be possible to create the particle directly in high energy collider experiments, such as those at the LHC (e.g. Kane & Watson, 2008) or to detect the recoil of atomic nuclei as dark matter scatters off them (e.g. Goodman & Witten, 1985). Many of the best candidates are also Majorana particles (their own anti-particles), such that a self-annihilation signal may be detectable in gamma rays (Jungman et al., 1996), perhaps from the centre of the Galaxy (Aharonian et al., 2004; Springel et al., 2008a).

Aside from these fundamental challenges to the theory, two sets of observational data are often cited as being inconsistent with the predictions of ΛCDM . The first is the abundance of satellite galaxies in the Local Group, which is much lower than the abundance of low mass structures in dark matter simulations (Moore et al., 1999; Klypin et al., 1999). The second is the inferred mass distribution in dwarf galaxies, which has

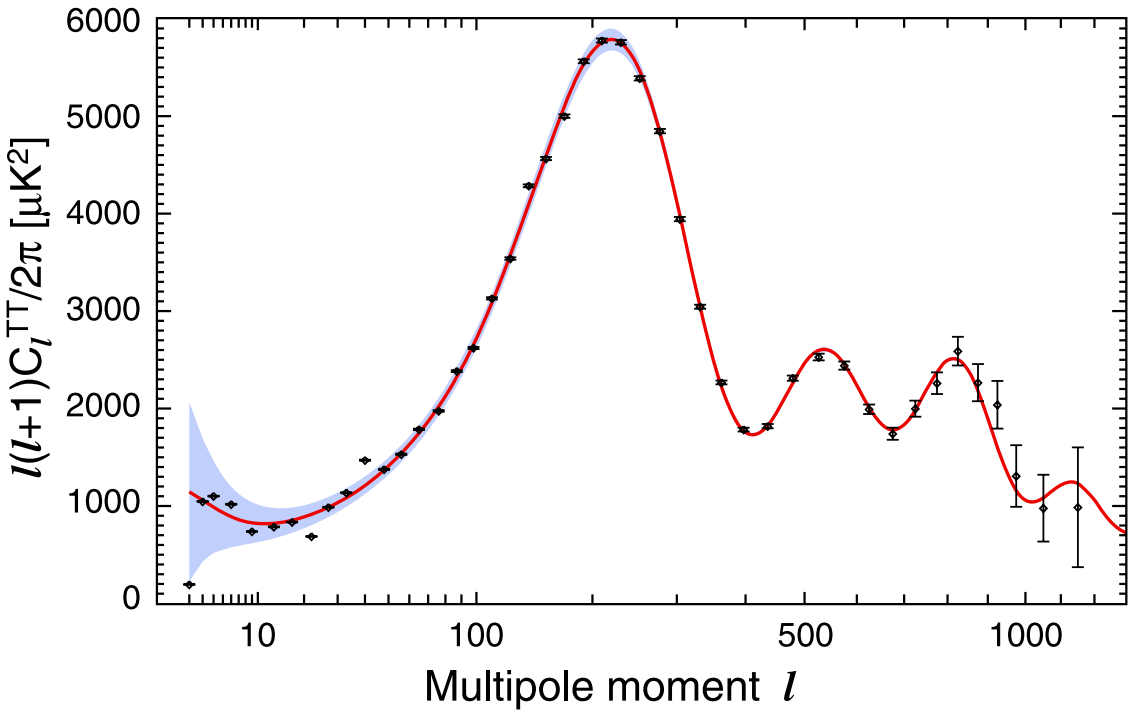

Figure 1.1 The power spectrum of the Cosmic Microwave Background measured by the WMAP satellite (black points with error bars) and the best fit ΛCDM model (red curve) from Larson et al. (2011). Shaded regions represent the effects of cosmic variance.

been claimed to be at odds with the strongly peaked density profiles of ΛCDM dark matter haloes (e.g. Goerdt et al., 2006). Both of these issues are considered in this thesis; we defer a more detailed discussion to Chapter 4.

Although undeniably incomplete, ΛCDM provides an accurate description of a wide range of observational datasets, including galaxy clustering and large scale structure (Percival et al., 2007; Ferramacho et al., 2009; Sánchez et al., 2009), the statistical properties of the Lyman-α forest (Cen et al., 1994; Hernquist et al., 1996), the mass function of galaxy clusters (Vikhlinin et al., 2009) and distortions in the large scale mass field due to weak gravitational lensing (Van Waerbeke et al., 2005). Perhaps the most outstanding achievement of ΛCDM , however, is its capacity to explain the power spectrum of the CMB (e.g. Komatsu et al., 2011). *Acoustic peaks* are generated by oscillations in the photon-baryon fluid before recombination, which imprint well-defined scales in the distribution of temperature fluctuations. The peaks are exactly of the form predicted by ΛCDM . Figure 1.1 illustrates the level of agreement, with the model (red curve) falling

Table 1.1 Current estimates for the cosmological parameters of the ΛCDM model from Komatsu et al. (2011).

Ω_Λ	0.725 ± 0.016
$\Omega_{\rm DM}$	0.229 ± 0.015
Ω_b	0.0458 ± 0.0016
H_0	$70.2 \pm 1.4 {\rm kms}^{-1}{\rm Mpc}^{-1}$
n_s	$0.968^{\pm}0.012$
σ_8	0.816 ± 0.024

almost exclusively within the very small statistical uncertainties. These data, combined with distance estimates derived from baryon acoustic oscillations (BAO, Percival et al., 2010) and recent measurements of H_0 (Riess et al., 2009) now constrain the parameters of the standard model to an accuracy of a few percent (see table 1.1).

With this well-defined and highly successful cosmological model in place, much of the theoretical focus has now turned to developing models to examine its implications for the formation of galaxies. The non-linear nature of the gravitational collapse and the complexity of the baryonic processes involved, make efficient computational methods essential to make progress. Two classes of computer model are in widespread use today, hydrodynamical simulations and semi-analytical models, both of which are employed in this thesis. In the next section we describe a numerical method that increasingly underpins both techniques.

1.2 The N-body Method

The proposed properties of the dark matter mean that it can be modelled as a collisionless, self-gravitating fluid. The time-dependent gravitational potential can be obtained from the density field by solving Poisson's Equation:

$$\nabla^2 \Phi(\mathbf{r}, t) = 4\pi G \rho(\mathbf{r}, t) \tag{1.8}$$

where $\Phi(\mathbf{r}, t)$ is the gravitational potential, G is Newton's gravitational constant and $\rho(\mathbf{r}, t)$ is the density field. Numerical solutions can be found by discretising the mass field into particles and computing their dynamics under Newton's equations of motion;

this is the essence of the N-body method. To prevent the discretisation itself from causing unphysical effects (two-body large-angle scattering events, or the creation of bound pairs of particles), forces must be "softened" to sub-Newtonian values at small separations. This effectively spreads the mass of each particle out over a softening kernel which, for the simulation code we introduce later, takes the form of a cubic spline function (Monaghan & Lattanzio, 1985).

The N-body problem essentially reduces to finding an algorithm with which to compute the gravitational acceleration on each particle that is as efficient and as accurate as possible. The most accurate and least efficient is the *direct summation*, or particle-particle method, whereby the exact Newtonian force on each particle due to every other particle is computed. The number of calculations then scales as N^2, making the method impractical for all but the smallest systems. A better alternative is the particle-mesh (PM) technique (e.g. Klypin & Shandarin, 1983). Particle masses are mapped to a mesh or grid and Poisson's equation is solved to obtain the potential at each grid point. The gradient of the potential at the location of each particle is then obtained by a finite differencing method. There are a number of ways in which mass can be associated with a grid point, but a common choice is the cloud in cell (CIC) technique. Each particle's mass contributes to several grid points, weighted by the inverse separation. Given this gridded density field $\rho(\mathbf{r})$, Eqn. 1.8 can be efficiently solved in k-space by using a Fast Fourier Transform (FFT) algorithm (Cooley & Tukey, 1965). The potential can be written as a convolution of the density field with the Green's Function ($\mathcal{G}$) that describes the form of the interaction:

$$\Phi(\mathbf{r}) = [\mathcal{G}(\mathbf{r}) * \rho(\mathbf{r})] \tag{1.9}$$

Taking the Fourier transform (denoted by a circumflex) and using the convolution theorem gives:

$$\Phi\hat{(}\mathbf{k}) = \mathcal{G}\hat{(}\mathbf{r})\rho\hat{(}\mathbf{r}) \tag{1.10}$$

Hence the procedure is to Fourier transform the density field, multiply by the Fourier transform of the appropriate Green's function and transform the result back to obtain the potential at every grid point.

While the PM method is fast, with the number of operations scaling as $N\log_{10}\mathrm{N}$, obtaining a reasonable resolution typically requires a large number of grid points, which can make the FFT calculation very memory-intensive. An efficient strategy is to use a

fairly coarse grid to evaluate forces over large distances and an alternative technique for the short range force. One can use direct summation - the particle-particle, particle-mesh ($\mathrm{P^3M}$) method (Hockney & Eastwood, 1981; Efstathiou & Eastwood, 1981), but a more efficient choice for strongly clustered particle distributions is a "tree" algorithm. The principle is to subdivide the simulation volume hierarchically into "nodes", with the first level of the hierarchy (the whole volume) representing the root of the tree and the highest level representing the leaves. Many ways of dividing the volume are possible, but for simulations in Cartesian coordinates, a conceptually simple approach is the octree (Barnes & Hut, 1986), in which a cubic volume is split in half along each dimension, giving eight subvolumes. The tree is constructed by recursively dividing nodes until the leaves each contain at most N_{max} particles, where N_{max} is typically chosen to be one. At each level, nodes are linked to their parent node in the level above.

With the tree thus constructed, the force on a particular particle can be computed by "walking" the tree. The algorithm starts at the root node and tests the criterion $r > \frac{l}{\theta}$, where r is the distance to the node, l is the physical size of the node and θ is a numerical parameter called the opening angle. If the inequality is satisfied, the force from that node is added to the total force on the particle. If not, the node is "opened" and the criterion is re-evaluated for each of the child nodes. The process is repeated until all the mass in the simulation volume has contributed to the force. In the simplest case, each node is treated as a point mass at the position of its centre of mass (a monopole method). Better accuracy can be achieved at fixed tree depth by computing higher order moments of each node's mass distribution (e.g. Hernquist, 1987; Wadsley et al., 2004), but similar overall accuracy and speed can be obtained simply by ascending further into the tree. The Tree-PM method is an efficient algorithm for cosmological simulations, where the range of relevant length scales is large. It forms the basis of the gravity calculation for all of the simulations studied in this thesis.

1.2.1 Evolution and Time Stepping

Given the force calculation described above, there are many ways in principle in which a system of particles can be evolved forward in time. The following focuses primarily on the scheme employed in the GADGET-3 simulation code, which is used throughout this work.

Several well known numerical integration techniques (e.g. Runge-Kutta) are found to result in poor energy conservation and lead to unstable long-term behaviour when applied to N-body simulations. Such behaviour can be avoided if a *symplectic* scheme is used, that is, one that preserves the form of the Hamiltonian and in which each integration step is a series of *canonical transformations*. Two examples of canonical transformations are the 'drift' operator, which changes the position of each particle, keeping the momentum constant and the 'kick' operator, which evolves the momentum at a fixed position. The widely used class of *Leapfrog* integrators use a combination of these operators to evolve the system, employing either a drift-kick-drift (DKD) or kick-drift-kick (KDK) technique. In each case, one coordinate (position or momentum) is evolved to the middle of the time step. That value is then used to evolve the second coordinate for a full step, before the first coordinate is evolved for the remaining half step. In GADGET-3, the Tree-PM algorithm computes the short-range and long-range forces separately. The potential is separated in a similar way, with short range kicks and intermediate drift steps performed on smaller time steps than the long range force kick, while the symplectic nature of the integration scheme is preserved.

In cosmological simulations, the large dynamic range involved makes the use of individual particle time steps essential in order to keep the total runtime low. Particle paths in high density regions, where the local potential varies most rapidly, can then be integrated accurately, while similar error levels can be achieved in less dense regions using a much smaller number of calculations. In practice, the time step is chosen according to the acceleration on each particle. An important consequence of using individual time steps is that it breaks the symplectic nature of the integration scheme, although the impact is fairly small if a KDK leapfrog integrator is used, as is the case in GADGET-3.

1.2.2 Initial Conditions

The last key element required to run an N-body simulation is the initial distribution of particles. In the cosmological ab initio simulations explored in this work, the mass distribution depends only on the form of the density perturbations generated by inflation.

The first step in creating cosmological initial conditions is to generate a smooth density field onto which the perturbations can be imposed. This is typically achieved either by arranging particles in a uniform grid, or by creating a 'glass-like' configuration by

evolving a Poissonian distribution with the sign of gravity reversed until the residual forces on all particles are negligible (White, 1996). The perturbation field can be created in the following way. First, a linear theory power spectrum, $P(k)$, is computed that is consistent with the best estimates of the cosmological parameters, as listed in Table 1.1. A random realisation of this model is then constructed in Fourier space by sampling modes up to the Nyquist frequency of the particle distribution and choosing their amplitudes at random from a Rayleigh distribution with second moment $P(k)$. This realisation may then be Fourier transformed to obtain the displacement field. Finally, the displacement field is interpolated to the particle positions and the particles are moved accordingly. Initial velocities can be assigned using the Zel'dovich approximation (Zel'Dovich, 1970), which is valid at sufficiently high redshifts (the simulations in this work begin at $z = 127$).

The N-body technique is used to compute gravitational interactions in both of the theoretical approaches described in this work. In the next section, we discuss the first of the two methods that we employ to model the baryonic physics.

1.3 Semi-Analytical Models

Many of the concepts behind modern semi-analytical models and indeed galaxy formation theory in general, can be traced to two important papers. White & Rees (1978) were the first to propose that galaxy formation takes place as a result of the cooling of gas in dark matter haloes and found that a constant mass-to-light ratio for all haloes leads to many more faint galaxies than are observed. Building on this work, White & Frenk (1991) developed a model that included prescriptions for gas cooling, star formation, feedback and chemical enrichment, from which all modern semi-analytical models are derived. The fundamental philosophy of their model and those that followed it, is to develop physically or empirically motivated, parameterised prescriptions to describe astrophysical processes which are poorly understood. Parameters can then be tuned so as to reproduce particular observational datasets. The luminosity and gas content of the Milky Way (e.g. Kauffmann et al., 1993), the galaxy luminosity function in the B and K bands (e.g. Cole et al., 2000) and the mass function of supermassive black holes (e.g. Bower et al., 2006) have all been used as constraints. Increasingly sophisticated techniques for

searching the substantial parameter space now allow models to match a whole host of observational data simultaneously (Benson & Bower, 2010b) and make predictions for galaxy properties not used in the calibration.

In the following subsections we discuss how some of the most influential physical processes are implemented in semi-analytical models, focussing in particular on those affecting one of the main focuses of this thesis, galaxy morphology. These descriptions also serve to outline the basic concepts behind modern galaxy formation theory.

1.3.1 Dark Matter Haloes and Merger Trees

In order to construct a galaxy population, semi-analytical models require information about the hierarchical growth of dark matter haloes and the details of their structure. The former is defined by the evolution of the initial density perturbations through gravitational instability, which is purely a function of the cosmology. This process is encapsulated by dark matter "merger trees", which specify the complete formation history of a given halo at $z = 0$. Merger trees can be constructed analytically; a common technique is to use the Extended Press Schecter (EPS) formalism to predict the conditional mass function of haloes, which gives the probability that a halo had progenitors of particular masses at some earlier epoch. More commonly, modern semi-analytical models tend to extract merger trees from N-body simulations. This can be achieved by identifying gravitationally bound structures at different output times (e.g. Springel et al., 2001a; Knollmann & Knebe, 2009) and then linking structures between consecutive outputs by tracing particles from progenitor to descendant (e.g. Helly et al., 2003).

1.3.2 Radiative Cooling

The amount of gas initially available to cool is a fixed fraction of the mass of the dark matter halo (the cosmic baryon fraction, $\Omega_{\rm b}/\Omega_{\rm m}$) although reionisation decreases this fraction in haloes with virial temperatures $< 10^4 K$, where the pressure of the IGM suppresses gas infall (Efstathiou, 1992). Accreting gas shock-heats as it falls into the halo's potential well and is typically assumed to attain the virial temperature (although see Benson & Bower, 2010a). Gas can then cool through several mechanisms,the relative importances of which depend on its density, temperature and chemical composition. They are i) inverse Compton scattering of CMB photons by free electrons, ii) line emis-

sion from collisionally excited atoms, iii) the deceleration of free electrons in the ionised gas (Bremsstrahlung) and iv) molecular Hydrogen cooling due to transitions between rotational or vibrational states. The rate of radiative losses is further modified by reionisation, which removes bound electrons that would otherwise have contributed to atomic line cooling. One way to model this is simply to prevent cooling in haloes below a certain mass after reionisation (Benson et al., 2002). Cooling can also be restricted in more massive haloes by injecting energy from SNe (e.g. Bower et al., 2001) or active galactic nuclei (AGN, e.g. Croton et al., 2006; Bower et al., 2006) or through thermal conductivity, which transports energy in from the outer halo (Benson et al., 2003). The final piece of information necessary to obtain the cooling time is the gas density, which follows from assuming some radial distribution for the hot gas, for instance a cored, NFW or isothermal profile. As it cools and collapses, the angular momentum that the gas acquired during the expansion and turnaround of the halo causes it to naturally settle into a disk. For low mass haloes, cooling is very rapid and the supply of cold gas is limited purely by the rate at which gas can free-fall onto the disk. For high mass haloes, a *quasi-static* hot atmosphere forms, from which new gas can be accreted as it cools.

1.3.3 Star Formation

In the absence of a clear picture of how interstellar gas clouds collapse to form stars, semi-analytical models typically parameterise the star formation rate as being proportional to $M_{\rm cold}/\tau$, where $M_{\rm cold}$ is the total cold gas mass and τ is a characteristic star formation timescale. The empirical relation found between the cold gas surface density and star formation rate density (Schmidt, 1959; Kennicutt, 1998) in disk galaxies suggests $\tau \propto t_{\rm dyn}$, where $t_{\rm dyn}$ is the dynamical time of the galaxy. The efficiency of star formation is modified by any process that affects $M_{\rm cold}$, in particular feedback that can re-heat gas in the disk and prevent cooling from the hot halo. The interplay between cooling, star formation, stellar evolution and feedback processes can be described by the movement of mass between 'reservoirs' of cold gas, hot gas and stars. Each process then contributes one or several terms to a set of differential equations that govern how mass moves between the reservoirs.

1.3.4 Feedback

The necessity of feedback processes to reconcile the dark matter halo mass function with the galaxy luminosity function has been known for some time (White & Rees, 1978). The faint end slope can be significantly modified by stellar feedback, since SNe driven winds can escape the shallower potentials far more easily (Larson, 1974; Dekel & Silk, 1986). SNe feedback is usually modelled by moving some fraction of the cold reservoir of gas available for star formation back to the hot gas reservoir (re-heating), or by removing it from the halo entirely (ejection). Alternatively, feedback can modify the entropy profile of the hot gas, affecting its ability to cool in the first place. The rate at which gas is re-heated or ejected is typically taken to be proportional to $\dot{M}_* V_c^{\alpha}$, where $\dot{M}_*$ is the star formation rate, V_c is the halo circular velocity and α is a free parameter. $\alpha = 2$ is found to give a reasonable match to the faint-end slope of the luminosity function. At the bright-end, it has been shown that the observed exponential break can be reproduced if the energy output from AGN reduces the efficiency of star formation in massive haloes (Croton et al., 2006; Bower et al., 2006). This requires a model for the growth of supermassive black holes (SMBHs); we describe the technique used for two particular semi-analytical models in Chapter 2. In brief, SMBHs are assumed to accrete mass as a result of gas inflows driven by mergers and the buckling of gravitationally unstable disks, as well as from the flow of material cooling out of the hot halo. AGN energy output increases during episodes of rapid accretion, which reduces or prevents cooling and gives rise to a self-regulating system.

1.3.5 Chemical Enrichment and Stellar Population Synthesis

As stellar populations evolve, they return mass to the ISM, enriched with the heavy elements that are synthesised in stars. More massive stars are responsible for more significant stellar winds and hence the rate of enrichment depends on the stellar initial mass function (IMF). Models typically track the abundances of a selection of elements in the hot and cold gas reservoirs, updating them as gas cools, new stars form and gas is added to the system through mergers. Enrichment of the hot gas leads to shorter cooling times due to the additional channels for line cooling. Chemical composition is also important for the observable properties of the galaxy, since it affects both the spectral properties

of the stars and the optical depth of gas, which is modified by dust extinction. Stellar colours and luminosities can be computed using population synthesis models (e.g. Bruzual & Charlot, 2003) which describe the spectral energy distributions of stars as a function of age and metallicity, which are stored by the model for stars forming at each timestep. Given the metallicity, the sizes of the bulge and disk components and a randomly assigned inclination angle, the dust attenuation can be computed as a function of wavelength and the luminosities of galaxies in various bands computed. The contribution to the infrared luminosity resulting from the heating of dust can also be calculated (e.g. Guiderdoni et al., 1998).

1.3.6 Mergers and Disk Instabilities

Two mechanisms are known that can transform rotationally supported disks into dispersion supported spheroids. The first, galaxy mergers, are an inevitable consequence of hierarchical structure formation. Galaxies and their dark matter haloes can survive the initial accretion into a more massive halo and orbit as a satellite until the process of dynamical friction (Chandrasekhar, 1943) extracts all of their orbital energy. The timescale on which this occurs depends on parameters of the orbit, the mass of the satellite and the dynamical time of the host halo. Even in N-body simulations, where orbits can be tracked directly, dark matter substructures often fall below the resolution limit of the simulation before sinking to the centre, so a timescale must be calculated to track the merger of the baryonic component. In this case orbital parameters can be obtained from the substructure itself, or from a distribution previously derived from N-body simulations (e.g. Benson, 2005). The consequences of the merger typically depend on parameters such as the central-satellite mass ratio, the gas fraction and the bulge-to-total ratio of the central galaxy. Specific models choose different outcomes depending on their own set of parameters, but typically mergers with low mass ratios are assumed to destroy disks and produce spheroidal descendants and gas-rich, low bulge-to-total ratio mergers are assumed to induce gas inflows that result in a starburst. We discuss the choice of these parameters for two particular semi-analytical models in Chapter 2. A second channel for spheroid formation included in some models is the collapse of gravitationally unstable galaxy disks. Strongly self-gravitating disks are thought to form bars when gravitationally perturbed (Efstathiou et al., 1982), which may then evolve into “peanut-

shaped" spheroids through resonant processes (Combes et al., 1990). A measure of the extent to which a disk is self-gravitating is the ratio between the disk and halo contributions to the circular velocity in the vicinity of the disk. This mechanism is also discussed further in the context of the semi-analytical models analysed in Chapter 2.

1.3.7 Bulge and Disk Sizes

The size of the bulge and disk in each galaxy is dictated by the angular momentum of the gas, and the gravitational interaction between the bulge, disk and halo. A distribution of the angular momenta of dark matter haloes (usually phrased in terms of the dimensionless spin parameter, λ) can be derived from N-body simulations (e.g. Bett et al., 2007). Typically it is assumed that the gas retains the same specific angular momentum as the halo as it collapses. The size of the disk can be calculated using the formalism of Mo et al. (1998). This takes into account the angular momentum of the gas, the self-gravity from the disk and bulge and the gravity of the halo, modified by adiabatic contraction due to the presence of the galaxy. The size of bulges formed through mergers can be calculated by conserving the energy of the progenitors and of the orbit and assuming virial equilibrium. Similarly, the sizes of bulges formed through disk instabilities follow from conserving the initial energy of the bulge-disk system (Cole et al., 2000).

The general techniques described above form the framework for modern semi-analytical models for galaxy formation, although naturally, the specifics of the implementations vary from model to model and additional physical processes are often included. In Chapter 2, we investigate the origins of galaxy morphology in two particular models and contrast details of their implementations.

1.4 Hydrodynamical Simulations

An alternative to semi-analytical modelling is to explicitly follow the dissipative collapse of gas in dark matter haloes by modelling hydrodynamical interactions, in addition to the gravitational forces included in N-body simulations. A typical approach is to treat the baryonic component as an ideal gas that obeys the continuity equation,

$$\frac{\partial \rho}{\partial t} + \nabla.(\rho \mathbf{v}) = 0, \tag{1.11}$$

the Euler equation,

$$\frac{\partial(\rho\mathbf{v})}{\partial t} + \nabla.(\rho\mathbf{v}^2) + \nabla P = -\rho\nabla\Phi, \tag{1.12}$$

and the energy equation

$$\frac{\partial\rho u}{\partial t} + \nabla.[(\rho u + P)\mathbf{v}] = \rho\mathbf{v}.(\nabla\Phi), \tag{1.13}$$

where ρ,$\mathbf{v}$,P, are the gas mass density, velocity and pressure respectively, Φ is the gravitational potential and u is the total specific energy. Two popular techniques for solving these key equations in an astrophysical context have emerged over the past few decades; Smoothed Particle Hydrodynamics (SPH) and Adaptive Mesh Refinement (AMR) [3]. SPH simulations are used extensively in this thesis; we describe the basic principles of the technique below.

1.4.1 Smoothed Particle Hydrodynamics

SPH simulation codes employ a 'Lagrangian' approach to the calculation of hydrodynamic forces. The fluid is discretised by mass and hydrodynamic quantities and their derivatives are computed in a frame moving with the fluid elements (particles). The fundamental tenet of SPH is that the value of a hydrodynamic quantity at a particular point in the fluid, $Q(\mathbf{r})$, can be computed through a weighted average over neighbouring particles. In terms of continuous quantities:

$$Q(\mathbf{r}) = \int Q(\mathbf{r}')W(\mathbf{r}-\mathbf{r}', h)d\mathbf{r}' \tag{1.14}$$

The weighting function $W(\mathbf{r}, h)$ is known as the smoothing kernel and h is the smoothing length. The kernel is normalised to unity,

$$\int W(\mathbf{r}-\mathbf{r}', h)d\mathbf{r} = 1 \tag{1.15}$$

and tends to a delta function in the limit of an infinite number of particles, or equivalently, a vanishingly small smoothing length.

$$\lim_{\mathrm{h}\to 0} W(\mathbf{r}-\mathbf{r}', h) = \delta(\mathbf{r}-\mathbf{r}') \tag{1.16}$$

A number of different forms for the smoothing kernel are described in the literature (e.g. Thomas & Couchman, 1992; Fulk & Quinn, 1996; Cabezón et al., 2008; Read et al., 2010),

[3] Although hybrid schemes also exist, see for example Springel (2010)

but a common choice is a spline function (Monaghan & Lattanzio, 1985),

$$W(r,h) = \frac{8}{\pi h^3} \begin{cases} 1 - 6(\frac{r}{h})^2 + 6(\frac{r}{h})^3, & 0 \leq \frac{r}{h} \leq \frac{1}{2}, \\ 2(1 - \frac{r}{h})^3, & \frac{1}{2} < \frac{r}{h} < 1, \\ 0, & \frac{r}{h} > 1. \end{cases} \tag{1.17}$$

where the specific form above is that used by Springel et al. (2001b), which evaluates to zero for $r > h$. It has continuous first and second derivatives and implies an error term that falls off approximately as h^2. The smoothing length is constantly updated by the SPH algorithm, such that the kernel contains a fixed number, $N_{\rm ngb}$, of particles.

For all practical purposes, the exact solution in equation 1.14 is approximated by a summation over particles:

$$Q(\mathbf{r}) = \sum_{\rm i=1}^{N} Q_{\rm i} \frac{m_i}{\rho_i} W(\mathbf{r} - \mathbf{r_i}, h). \tag{1.18}$$

Although the sum is technically over all particles in the fluid, the form of kernel in equation 1.17 ensures that only neighbouring particles within a distance h contribute. It follows then, that a particle's density is simply calculated by summing the weighted masses of its neighbours. Spatial derivatives can be obtained by differentiating the expression for the chosen quantity:

$$\nabla Q(\mathbf{r}) = \sum_{\rm i=1}^{N_{\rm ngb}} Q_{\rm i} \frac{m_i}{\rho_i} \nabla W(\mathbf{r} - \mathbf{r_i}, h). \tag{1.19}$$

Using the approximations described by equations 1.18 and 1.19 one can cast the fluid equations, 1.12 and 1.13, purely in terms of the hydrodynamic properties of neighbouring particles and the smoothing kernel. There is some freedom in precisely how these equations are formulated, with the choices affecting which quantities are conserved by the method, as well as the ease with which the algorithms can be implemented. The SPH code used most extensively in this thesis is based on an entropy-conserving formulation due to Springel & Hernquist (2002). The equation of motion, through which the momenta of particles can be evolved forward in time is:

$$\frac{d\mathbf{v}_i}{dt} = -\sum_{j=1}^{N_{ngb}} m_j \left[f_i \frac{P_i}{\rho_i^2} \nabla_i W_{ij}(h_i) + f_j \frac{P_j}{\rho_j^2} \nabla_i W_{ij}(h_j) \right] - \Pi_{ij} \nabla_i W_{ij}, \tag{1.20}$$

where f_i and f_j are so called grad-h terms introduced to account for the effects of varying the smoothing lengths of SPH particles:

$$f_i = \left(1 + \frac{h_i}{3\rho_i}\frac{\partial \rho_i}{\partial h_i}\right) \tag{1.21}$$

and $W_{\rm ij} = W(|\mathbf{r}_i - \mathbf{r}_j|, h)$ is a symmetric form of the kernel that ensures momentum is implicitly conserved.

The term $\Pi_{\rm ij}$ introduces an artificial viscosity between particles, which is necessary for SPH to be able to resolve shocks. It was first introduced by Monaghan & Gingold (1983) and modified by Balsara (1995) to ensure that viscous forces vanish in pure shear flows ($\nabla \times \mathbf{v} \neq 0, \nabla.\mathbf{v} = 0$), where no shock should form. Without this modification, angular momentum tends to be spuriously transferred out of the inner regions of disks as they form, particularly in low resolution simulations (Steinmetz, 1996). In contrast to many SPH codes, the Springel & Hernquist (2002) formulation evolves a function of the specific entropy (s), rather than the internal energy. The entropic function is defined as

$$A(s) = \frac{P}{\rho^\gamma}, \tag{1.22}$$

where γ is the adiabatic index. $A(s)$ is evolved for each particle according to

$$\frac{dAi}{dt} = -\frac{\gamma - 1}{\rho_i^\gamma}\mathcal{L}(\rho_i, u_i) + \frac{1}{2}\frac{\gamma - 1}{\rho_i^{\gamma-1}}\sum_{\rm j=1}^{N_{\rm ngb}} m_j \Pi_{\rm ij} v_{\rm ij}.\nabla_{\rm i}\overline{W_{\rm ij}}, \tag{1.23}$$

where $\mathcal{L}$ is the emissivity per unit volume, which encompasses all sinks and sources of energy due to radiative cooling and heating. Equations 1.20 and 1.23 are sufficient to describe complex hydrodynamical interactions and form the basis for this formulation of the SPH method.

Hydrodynamical simulations use the techniques outlined above to track the interactions of gas as it falls into dark matter haloes and initiates the process of galaxy formation. However, as with semi-analytical models, our lack of understanding of many of the physical processes involved mean these processes must, for the moment, be modelled as parameterised prescriptions that couple to the more detailed treatment of the hydrodynamics. The particular modelling techniques used in our SPH galaxy formation code, including the treatment of radiative cooling, star formation, chemical enrichment and feedback processes are described in detail in Chapter 3 In the next section we describe the state of current observational and theoretical knowledge with respect to one of the main focuses of this thesis, the origins of galaxy morphology.

1.5 The Origins of Galaxy Morphology

The morphological type of a galaxy describes more than merely its physical appearance; it reveals the key processes that have shaped it and continue to affect its evolution. Hubble's well established classification scheme for galaxies (Hubble, 1926, 1936) has survived with only modest modification (de Vaucouleurs, 1959; Van den Bergh, 1960; Sandage, 1961), precisely because the disks and spheroids that it describes are fundamental products of the formation process. Understanding the origins of such structures is therefore of central importance if we are to build up a coherent picture of galaxy formation and evolution.

1.5.1 Observational Insights

Modern observational facilities like the Hubble Space Telescope (HST) have made it possible to probe progressively higher redshifts and together with large imaging surveys like the Sloan Digital Sky Survey (SDSS), have helped to reveal how galaxy morphology changes with time. A significant trend in the low redshift universe is the 'morphology-density' relation (Davis & Geller, 1976; Dressler, 1980; Postman & Geller, 1984; Dressler et al., 1997), which shows that denser regions contain proportionally more early-type galaxies. This relation holds at least back to $z \sim 1$ (Postman et al., 2005). At higher redshifts, between $z \sim 0.5$ and 2, there appears to be a rapid breakdown of the Hubble classification system (Van den Bergh, 2002; Papovich et al., 2005) with the proportion of galaxies classed as irregulars or peculiars rising steadily, particularly at faint magnitudes (e.g., Brinchmann & Ellis, 2000). Nonetheless, a substantial fraction of giant spirals are observed at moderate redshifts (e.g., Ravindranath et al., 2004). Some authors have claimed that this population shows very little evolution up to the present, implying that at least some Hubble sequence galaxies were in place at $z \sim 1$ (Marleau & Simard, 1998; Ravindranath et al., 2004), whilst it has also been argued that many of the higher redshift sample would have become bulge dominated in the intervening time, so they are not directly comparable to their $z = 0$ counterparts (Bell, 2008). Before $z = 2$, the majority of galaxies appear to be either highly irregular or centrally compact (Giavalisco et al., 1996; Dickinson, 2000; Daddi, 2004). In the nearby Universe, there are many examples of galaxies with complex and disturbed morphology but the majority are well described

by the classical Hubble Sequence. A dramatic example of a spiral galaxy with a central stellar spheroid and rotating disk of stars, gas and dust is seen in Fig. 1.2.

Figure 1.2 M81: A spectacular, example of a nearby spiral galaxy consisting of a stellar bulge and a thin disk of rotating gas, stars and dust.

Discussion of galaxy morphology is complicated by the fact that it can be i) poorly defined, ii) subjective and iii) wavelength-dependent. i) and ii) are most obviously associated with the 'by-eye' morphologies that have historically been assigned to galaxies by consensus among astronomers. This ambiguity is removed by considering quantitative measures (many of which correlate reasonably well with Hubble-type) including bulge-to-total ratio, concentration, asymmetry, clumpiness and Sersic index. iii) is less easy to bypass and makes multi-wavelength studies essential to understand whether apparent trends with redshift represent genuine structural change. However, the most fundamental challenge to building up a coherent picture of morphological evolution is the difficulty in linking populations seen at different epochs. The timescales associated with morphological transformation are such that we will only ever see a snapshot in the development of each galaxy. This is, of course, a challenge in studying many aspects of

galaxy evolution, but it serves to emphasise that the most important insights will come from theoretical models that are informed and constrained by what we observe.

1.5.2 The Role of Mergers

Hydrodynamical simulations with sufficient resolution to investigate morphological evolution remain highly computationally taxing to perform for large samples of galaxies (although significant progress is being made in this respect; see for example Croft et al., 2008; Crain et al., 2009; Hahn et al., 2010; Schaye et al., 2010; Feldmann et al., 2011). They have therefore tended to concentrate instead on very high resolution studies of individual galaxies, embedded in cosmological environments (e.g. Thacker & Couchman, 2001; Abadi et al., 2003; Governato et al., 2007; Scannapieco et al., 2009; Okamoto et al., 2010; Wadepuhl & Springel, 2010; Guedes et al., 2011). Semi-analytical techniques provide a complementary approach, aiming to capture the most important characteristics of the hydro simulations, whilst also providing sufficient numbers of galaxies to make statistical comparisons with observational data.

Our current understanding of galaxy formation tells us a little about how morphology develops. It is well known, for instance, that angular momentum acquired by a proto-galactic gas cloud through tidal torques operating during its expansion and collapse will naturally cause it to settle into a disk (Hoyle, 1949; Peebles, 1969; White, 1984). However, the combination of mechanisms required to explain morphological change beyond this phase are poorly understood. Toomre (1977) was the first to put forward the idea that mergers could be responsible for the formation of elliptical galaxies. Indeed, the importance of mergers in the hierarchical cold dark matter (CDM) model makes them a natural candidate for such a role (e.g. Frenk et al., 1985). Early CDM galaxy formation models stressed the possibility that, through a combination of mergers and gas accretion, a single galaxy could be identified with several morphological types on the Hubble sequence at various stages in its lifetime (White & Frenk, 1991), a view supported by hydrodynamical simulations (Steinmetz & Navarro, 2002). Numerous simulations have confirmed at least that major mergers, or very strong gravitational encounters, can lead to the complete destruction of a disk and the formation of a spheroid with properties similar to elliptical galaxies (e.g., White, 1978; Negroponte & White, 1983; Barnes, 1992; Barnes & Hernquist, 1996; Bekki & Shioya, 1997; Naab et al., 1999; Springel & Hernquist,

2005; Naab & Burkert, 2003; Cox et al., 2006). In virialised clusters, the relative velocities of galaxies make strong gravitational interactions of any kind infrequent, but mergers could still have been important for generating ellipticals in the progenitor groups which came together to form them. On the other hand, the end product of a merger is not necessarily a dispersion-dominated spheroid. Several simulations have shown that even mergers between disks of roughly equal mass can produce stellar remnants dominated by rotation, providing a large fraction of the gas survives the initial starburst. The outcome is largely determined by the initial gas content of the progenitors (Barnes & Hernquist, 1996; Bournaud et al., 2005; Springel & Hernquist, 2005; Naab et al., 2006; Hopkins et al., 2008b; Governato et al., 2009) and the merger geometry (Hernquist & Mihos, 1995; Bournaud et al., 2005).

1.5.3 Further Mechanisms for Morphological Transformation

The idea that the Hubble sequence is a simple product of mergers and disk growth through gas accretion is attractive as a theoretical model, but unquestionably an oversimplification. A number of other phenomena have been identified that are likely to have a bearing on morphology, either directly, by changing the stellar dynamics, or indirectly through their effects on the gas content and star formation. For instance, *strangulation* or *suffocation* occurs when a galaxy with a gaseous atmosphere falls into a larger structure, causing further gas cooling to be heavily suppressed (Larson et al., 1980; White & Frenk, 1991). In combination with efficient feedback from supernovae, this can efficiently shut off star formation, leading to the reddening of a satellite's stellar population on a relatively short timescale. In cluster environments, the process of *harassment* (Moore et al., 1996) may play a role in morphological transformation. It involves a series of intense, high speed gravitational encounters that can cause bursts of star formation and even lead to disk disruption. A similar mechanism, more relevant to galaxy environments is *tidal stirring*, in which repeated tidal shocking of (satellite) stellar disks at pericentre can induce spheroid formation on the timescale of a few Gyr (Mayer et al., 2001a,b; Klimentowski et al., 2007, 2009; Łokas et al., 2010). Although most often associated with clusters, *ram pressure stripping* (Gunn & Gott, 1972; Abadi et al., 1999) can potentially affect the morphology of satellite galaxies in any halo with a virial temperature high enough to form a quasi-hydrostatic hot gaseous halo. Besides these well known mechanisms,

any feedback processes that regulate star formation, by reheating gas, or by preventing it from cooling in the first place can influence galaxy morphology by preventing or inhibiting the growth (or regrowth) of stellar disks. The role played by several of these mechanisms is considered in Chapter 2, where we use semi-analytical modelling to obtain a statistical picture of the build up of disks and spheroids. In Chapters 3 to 5 we take a different, but complementary approach, using numerical simulations to focus on the morphology and structure of a single Milky Way-like galaxy. The next section outlines what we can learn about galaxy formation and cosmology from efforts to observe and model our local environment.

1.6 The Structure and Dynamics of the Milky Way and its Satellites

Our own galaxy and its satellites provide us with an unparalleled opportunity to study many environments and processes relevant to galaxy formation at close quarters, from the structure of the multiphase interstellar medium (ISM), to stellar evolution and SNe explosions. We can also use the dynamical and chemical properties of resolved gas clouds and stars in so-called 'near-field cosmology', probing the mass distribution, star formation and assembly history of a (hopefully typical) spiral galaxy, with a level of detail unattainable through observations of external systems. Several visible components of the Milky Way have been identified, initially through star counts but increasingly through spectroscopy which has been used to obtain chemical and dynamical information. Whether these components are truly distinct in terms of their physical origin is still debatable, but in any case, the labels are useful to discuss the Milky Way's structure.

1.6.1 The Thin Disk

The Milky Way is a spiral galaxy with a thin, rotationally supported disk of gas and stars. The stellar component is well fit by an exponential disk with a scale height of ~ 300 pc (e.g. Gilmore & Reid, 1983; Jurić et al., 2008) and a scale length of ~ 2.6 kpc (Jurić et al., 2008). The stars of the thin disk contain the bulk of the Milky Way's heavy elements; with metallicities in the range $-0.65 < [\mathrm{Fe/H}] < 0.15$ (e.g. Schönrich & Binney, 2009); their ages are typically 8-12 Gyr. The (HI) gas disk is more extended than the stellar

component and can be detected in 21 cm emission out to 35 kpc (Kalberla & Dedes, 2008). It is also well described by an exponential radial profile, but is more extended, with a scale length of 3.75 kpc (Kalberla & Dedes, 2008) and a scale height of 3.9 kpc at the position of the sun.

As discussed in the previous section, the formation of a thin disk component follows naturally from the standard cosmological picture - gas is torqued during the expansion and turnaround of halo material, thermalises its infall energy through shocks and then cools, retaining a sufficiently large fraction of its angular that it naturally settles into a rotationally supported structure. From the point of view of informing our understanding of galaxy formation and cosmology, the fact that it forms is perhaps less remarkable than the fact that it survives to the present day. Purcell et al. (2009) point out that in ΛCDM models, most galaxy systems with mass $\sim 10^{12}$ $\mathrm{M}_{\odot}$ are expected to interact with at least one $\sim$ 10^{11} $\mathrm{M}_{\odot}$ satellite since $z = 1$. Their simulations suggest that such an interaction would heat the stellar disk significantly, increasing the scale height to > 2 kpc, although the effect might be weakened by dissipative effects, which are ignored in their simulations.

1.6.2 The Thick Disk

The MW thick disk was only identified relatively recently (Gilmore & Reid, 1983). Like the thin disk, it has an approximately exponential surface brightness profile, with scale length ~ 3.6 kpc (Jurić et al., 2008). Estimates of its scale height range between 0.5 and 1.4 kpc (Gilmore & Reid, 1983; Jurić et al., 2008; Carollo et al., 2010). It rotates in the same sense as the thin disk, but with an apparent velocity lag of $\sim 20 - 50$ kms^{-1} (Chiba & Beers, 2000; Soubiran et al., 2003). Thick disk stars are typically older than those of the thin disk, with ages of $10 - 12$ Gyr (Gilmore et al., 1995). It also has a lower metal content than the thin disk, with values in the range $-1.5 < [\mathrm{Fe/H}] < 0$ (Reddy et al., 2003, 2006; Bensby et al., 2003, 2007; Schönrich & Binney, 2009) and a peak at around -0.5 to -0.6 (Jurić et al., 2008; Carollo et al., 2010). At fixed metallicity, $[\alpha/Fe]$ ratios are higher than in the thin disk (Reddy et al., 2003, 2006; Bensby et al., 2003, 2007), suggesting a shorter star formation timescale (Gilmore & Wyse, 1998). Most of the measured mean abundance ratios in the thick disk are in fact much closer to that of the bulge and stellar halo (Meléndez et al., 2008) and a number of authors have argued that chemical, rather

than spatial or dynamical properties, should be used to distinguish it from the thin disk (e.g. Navarro et al., 2010).

Several plausible formation mechanisms for the thick disk have been put forward:

- Heating of the thin disk by mergers and subhalo interactions (Kazantzidis et al., 2008; Villalobos & Helmi, 2009).
- Direct accretion of disrupted satellites (Abadi et al., 2003).
- Formation in gas rich, rotationally supported clumps (Bournaud et al., 2009) or gas rich mergers (Brook et al., 2004) at high redshift.
- Radial migration of stars from the inner thin disk via resonant mechanisms (Haywood, 2008; Schönrich & Binney, 2009).

The current data do not appear to discriminate strongly between these scenarios, but some clues are apparent. The star-to-star scatter in abundance ratios is small (Reddy et al., 2003, 2006; Bensby et al., 2003, 2007), which implies that the gas from which thick disk stars originally formed was well mixed. This is also consistent with the short star formation timescales implied by the $[\alpha/Fe]$ ratios. The disk heating scenario can only be viable in the absence of any evidence for recent ($z < 2$) merger or interaction, since late heating would tend to blur the clearly distinct chemical properties of the thin and thick disks. Another possible discriminant is the distribution of orbital eccentricities. In contrast to the other scenarios, formation through direct accretion of disrupted satellites would generate a very flat distribution of eccentricities, due to the broad range of typical orbital parameters for infalling satellites in ΛCDM simulations (Sales et al., 2009). One of the primary arguments in favour of the radial migration scenario is that it explains the correlation between V and $[\mathrm{Fe/H}]$ noted by Haywood (2008).

1.6.3 The Bulge-Bar System

We discuss the bulge and bar components of the Galaxy together here, since it is far from clear whether they can, or should be considered as separate structures. References to 'the bulge' should be taken as shorthand for 'the bulge-bar system'.

The bulge of the Milky Way appears to be fairly typical of bulges in late type spirals (Frogel, 1990). It has a stellar mass of $\sim 1.6 \times 10^{10}\ \mathrm{M}_{\odot}$ (Minniti & Zoccali, 2008) and is

approximately triaxial in shape, with axes ratios 10:0.35:0.26 (Rattenbury et al., 2007) and a length of $3.1 - 3.5$ kpc (Gerhard, 2002). It is dispersion dominated, although much less so than many spheroids observed external to the MW, with $V_c/\sigma \sim 0.67$ (Minniti, 1996). Its peak rotational velocity is about 75 kms^{-1} (Minniti et al., 1992; Ibata & Gilmore, 1995; Rich et al., 2007) and its co-rotation radius is $\sim 3 - 4$ kpc (Englmaier & Gerhard, 1999). The bulk of metal rich bulge stars are clearly old, 10 ± 2.5 Gyr (Ortolani et al., 1995; Zoccali et al., 2003), but there is also evidence for younger stellar populations < 2 Gyr (Genzel et al., 1994; Frogel, 1999; van Loon et al., 2003). Stars with a wide range of metallicities are present, but the typical value $[\mathrm{Fe/H}] \sim -0.25$ is closer to that of old disk stars than to the stellar halo (McWilliam & Rich, 1994). [O/Fe] and [Mg/Fe] ratios are significantly higher than the thin disk and also higher than the thick disk, suggesting a very short star formation timescale of ~ 1 Gyr (Zoccali et al., 2007; Lecureur et al., 2007)

1.6.4 The Stellar Halo

A diffuse halo of stars surrounds the Milky Way disk, extending to at least 100 kpc (e.g. Sesar et al., 2010). It contains $\sim 0.1 - 1\%$ of the MW's total stellar mass (Morrison, 1993) and has the lowest mean metallicity of all of the Galaxy's component parts, $< [\mathrm{Fe/H}] > \sim -1.5$ (Laird et al., 1988; Carollo et al., 2010). The most metal-poor stars known (down to $[\mathrm{Fe/H}] \sim -5.4$) are found in the halo (Christlieb et al., 2002; Frebel et al., 2005; Norris et al., 2007) and age estimates suggest they may have formed just a few hundred million years after the Big Bang (e.g. Frebel et al., 2007).

The stellar halo contains a significant amount of substructure (e.g. Ibata et al., 1994; Helmi & White, 1999; Ibata et al., 2001; Vivas et al., 2001; Newberg et al., 2002; Yanny et al., 2003; Belokurov et al., 2007b; Grillmair, 2009; Watkins et al., 2009), but a smooth component is also discernible (Chen et al., 2001; Yanny et al., 2003; Newberg & Yanny, 2006; Sesar et al., 2010, 2011; Deason et al., 2011). The inner halo ($r < 15$ kpc) is particularly devoid of structure (Lemon et al., 2004), as expected from theoretical predictions for the mixing time at those radii (Helmi & White, 1999). The radial density profile of this smooth component is well fit by a broken power law, with a slope of -2.6 out to 27 kpc and -4.6 to at larger radii (Deason et al., 2011). A great deal can be learnt about cosmology and galaxy formation by studying the halo. The properties of its substructures potentially encode details of the Milk Way's merger history, while the dynamics of halo

stars can also be used to constrain the mass profile (e.g. Eyre & Binney, 2009; Gnedin et al., 2010) and shape (e.g. Helmi, 2004; Johnston et al., 2005; Law et al., 2005) of the MW's dark matter halo.

Numerous simulations have demonstrated that the disruption of satellites in ΛCDM models leads naturally to the buildup of a stellar halo (Johnston et al., 1996; Helmi & White, 1999; Bullock et al., 2001; Harding et al., 2001; Abadi et al., 2006; Cooper et al., 2010). Some observed properties have proven difficult to reproduce with pure accretion models though, including the change in slope of the density profile described by Deason et al. (2011), the presence of a high $[\alpha/\mathrm{Fe}]$, high $[\mathrm{Fe/H}]$ population of halo stars in the solar neighbourhood (e.g. Wheeler et al., 1989; Nissen & Schuster, 2010) and the flattened shape of the inner halo (Jurić et al., 2008; Deason et al., 2011). These observations may be explained by a second contribution to the halo from 'in-situ' star formation, that is, stars formed within the Milky Way's main progenitor. For example in simulations by Zolotov et al. (2009), halo stars formed at high redshift ($z \sim 3$), close to the centre of the main progenitor ($1-2$ kpc), from cold accreted gas and were later scattered into the halo by mergers. Font et al. (2011a), on the other hand, found that in-situ star formation took place at larger radii and lower redshift ($z \sim 1-1.5$), with a large fraction occurring in gas cooling directly out of the hot halo.

1.6.5 The Satellites

With the addition of the examples discovered in SDSS data (e.g., Zucker et al., 2004; Martin et al., 2006; Belokurov et al., 2007a; McConnachie et al., 2008), around thirty satellite galaxies are now known to exist around the MW. They are not distributed isotropically, but in a flattened, pancake-like configuration that may reflect preferred infall directions, dictated by nearby large scale structure (Libeskind et al., 2005; Zentner et al., 2005; Kang, 2005; Libeskind et al., 2011; Lovell et al., 2011b). They range in stellar mass from a few times $10^2\ \mathrm{M}_\odot$ to around $2 \times 10^9\ \mathrm{M}_\odot$ (Kim et al., 1998; Belokurov et al., 2010).

At larger galacto-centric distances (relative to the MW or M1), satellites tend to have more gas (Einasto et al., 1974) and are more likely to be of late-type or irregular morphology. Relative to the stellar halo, the dSphs tend to have lower $[\alpha/\mathrm{Fe}]$ at fixed [Fe/H], indicative of a longer star formation timescale. This is consistent with the range of stellar ages, which indicates that several of the dSphs, particularly the largest examples, were

characterised by extended periods of star formation (e.g. Mighell, 1990; Buonanno et al., 1999; Lee et al., 2009). Inhomogeneities in their chemical abundance patterns suggests it was likely also bursty in nature (e.g. Kirby et al., 2011). The classical (bright) and newly discovered faint satellites follow a continuous and relatively tight correlation between luminosity and metallicity (Skillman et al., 1989; Simon & Geha, 2007) which may reflect the ability of higher mass satellites to hold on to enriched gas ejected by supernovae.

Stellar kinematical data suggest that many of the Milky Way's satellites are strongly dark matter dominated. In particular, the ultra-faint dwarfs discovered in SDSS data have mass-to-light ratios of > 1000. Despite the huge range in luminosities, the satellites appear to have very similar central densities (Mateo, 1998; Gilmore et al., 2007; Strigari et al., 2008). This has been interpreted as evidence for a common scale in galaxy formation, although it remains possible that satellites with lower central densities have been missed simply because they would tend to have a lower surface brightness (Bullock et al., 2010).

The potential of the satellite populations of the Milky Way and M31 to constrain aspects of cosmology and galaxy formation has been recognised for some time (e.g. Klypin et al., 1999; Moore et al., 1999). They can be used, for example, as tracers of the gravitational potential of the Milky Way's halo (Watkins et al., 2009), to place constraints on the nature of supernovae feedback (e.g. Dekel & Silk, 1986; Okamoto et al., 2010) and reionisation (e.g. Busha et al., 2010; Font et al., 2011a) and as sensitive probes of the nature of the dark matter (Colín et al., 2000; Macciò & Fontanot, 2010; Polisensky & Ricotti, 2011). We explore these last two applications in detail in Chapter 4.

1.7 Thesis Outline

In the remainder of this thesis, we will use the theoretical framework and computational techniques outlined above to study the morphology and dynamics of galaxies from several different perspectives. In Chapter 2 we investigate the evolution of galaxy morphology in two semi-analytical models, comparing the importance of various physical mechanisms in the buildup of stellar mass in spheroids and disks. In Chapter 3 we introduce a set of SPH galaxy formation simulations of a Milky Way-mass galaxy and show how its morphology and other properties are shaped by its evolution. We also introduce

the *Aquila* project which aims to identify the physics and modelling techniques that determine the bulk properties of the galaxy at $z = 0$, in particular the prevalence of the disk component. In chapters 4 and 5 we use the same set of simulations to determine whether the mass profiles of the galaxy's satellites are compatible with observations of the stellar kinematics in Local Group dwarf galaxies and investigate the properties of the stellar and hot gas haloes found around the main galaxy disk at $z = 0$. Finally, in Chapter 6 we summarise the main results from each of these studies and consider possible directions for future work.

Chapter 2

Galaxy Morphology from Semi-Analytical Models

2.1 Introduction

In this chapter, we investigate the theoretical predictions of two semi-analytical models for galaxy formation, implemented on the ΛCDM Millennium Simulation, the first by De Lucia & Blaizot (2007) (hereafter the MPA model) and the second by Bower et al. (2006) (hereafter the Durham model). We look at the morphological content of each model as a function of redshift and track the evolution of the luminosity function of each type. We go on to determine how a galaxy's formation epoch, and that of its host dark matter halo, affect its final morphology and investigate the role played by major mergers, minor mergers and disk instabilities. Our main goal is to investigate galaxies of all morphological types and to compare and contrast the predictions of the two models, but we also make limited comparisons to observations. The chapter is laid out as follows. In Section 2.2, we describe the N-body simulation and semi-analytical models that form the basis of this analysis. Section 2.3 discusses the methods we use to select and retrieve the data and compares some basic properties of morphology in the models with SDSS data. Our main results are presented in Section 2.5 and we summarise our findings in Section 2.6.

2.2 The N-Body Simulation and Semi-Analytical Models

2.2.1 The Millennium simulation

Both galaxy formation models investigated in this chapter are based on the Millennium Simulation (MS) of the evolution of cold dark matter in a representative cosmological

volume. Completed by the Virgo Consortium in 2004, the MS was for several years the largest published N-body cosmological simulation and still today represents a valuable theoretical dataset with which to describe the evolution of structure in a variety of different environments (see Springel et al., 2005, for a detailed description). It uses 2160^3 ($\sim 10^{10}$) particles to model a cubic region of space,$500h^{-1}$ Mpc on a side,[1] and tracks the evolution of structure between $z = 127$ and the present day. The initial configuration of the particles was constructed using a ΛCDM power spectrum consistent with cosmological parameters from 2dFGRS (Colless et al., 2001) and first year WMAP (Spergel et al., 2003) data. The parameters used were Ω_m = 0.25, Ω_b = 0.045, $h = 0.73$, Ω_Λ = 0.75, $n = 1$ and σ_8 = 0.9[2] at $z = 0$. Particle positions and velocities were recorded in 64 output snapshots.

A friends-of-friends (FOF) algorithm (Davis et al., 1985) was used 'on the fly' to identify groups, linking adjacent particles separated by less than 0.2 times the mean interparticle separation. Groups with 20 or more particles (corresponding to a minimum halo mass of $1.7 \times 10^{10}\ h^{-1}\mathrm{M}_\odot$) were retained for further analysis. The FOF groups were further processed using a version of the SUBFIND algorithm (Springel et al., 2001a) that identifies gravitationally bound locally overdense regions, which we refer here as subhaloes. In the MPA model, a halo, by definition, includes all subhaloes within a FOF group. In the Durham model, on the other hand, a FOF group may be split into more than one halo if: i) a subhalo is outside twice the half-mass radius of the original halo, or ii) a subhalo was identified in a previous snapshot as part of a different halo and has retained 75% or more of its mass (Harker et al., 2006). Both of these conditions are designed to prevent two haloes that are temporarily joined by a tenuous particle bridge being linked together. The latter condition is applied on the basis that a subhalo loses significant mass from its outer layers when falling into a more massive counterpart, but substantially less if it is merely a close encounter. In both models, the descendant of a subhalo is identified by following its most tightly bound particles and the descendant of a halo is that which contains the largest fraction of its most massive subhalo. With the merger trees of these bound structures thus defined, the two models employ

[1]Where h is defined by $H_0 = h \times 100\mathrm{kms}^{-1}\mathrm{Mpc}^{-1}$.

[2]Here, Ω_m, Ω_b and Ω_Λ are the densities of all matter, baryons and dark energy respectively, in units of the critical density ($\rho_{\mathrm{crit}} = 3H^2/8\pi G$), n is the initial power spectrum slope and σ_8 is the rms overdensity predicted today by linear theory for a sphere of radius $8h^{-1}$ Mpc.

different techniques to populate them with galaxies. Many of the principles and basic techniques involved in semi-analytical modelling were outlined in Section 1.3. In the following subsections, we highlight some important differences between the Durham and MPA implementations which could affect their predictions for morphological evolution. Detailed descriptions of the two models can be found in the papers where they were originally presented (Bower et al., 2006; De Lucia & Blaizot, 2007) and references therein, particularly Croton et al. (2006) and Cole et al. (2000).

2.2.2 Gas Cooling, Star Formation and Supernova Feedback

An important difference between the two models is in how they calculate the instantaneous rate of gas cooling. Bower et al. (2006) allow gas to accrete onto the cold disk if it lies within a 'cooling radius', that at which the local cooling time is equal to the 'age' of the halo. They define the halo's age as the time since it last doubled in mass (Cole et al., 2000). De Lucia & Blaizot (2007), on the other hand, define an alternative cooling radius that encompasses all gas with a cooling time less than the halo dynamical time, $t_{\rm dyn} = (G\rho_{\rm vir})^{-1/2}$, where $\rho_{\rm vir}$ is the mean density of the virialised region. The Durham prescription typically results in higher cold gas masses than the MPA prescription by a factor of ~ 2 at $z \lesssim 5$ in central galaxies, rising to a factor of ~ 3.5 by $z \sim 0$.

Stars are assumed to form from the cold disk gas, with Kennicutt (Kennicutt, 1983) and Chabrier (Chabrier, 2003) initial mass functions in the Durham and MPA cases respectively. In both models, the stellar population synthesis model of Bruzual & Charlot (2003) is used to obtain stellar population properties. As described in Section 1.3.4, star formation in the disk affects its development significantly. Stellar winds and supernovae increase the metallicity of the disk material from which further stars form and inject substantial amounts of energy into their surroundings. This can drive gas and metals out of the disk, changing the composition of the surrounding hot gas and altering its cooling time.

In both models, this description is modified somewhat for satellite galaxies, which (instantaneously) lose their hot gas atmospheres on falling into a more massive halo. Satellites are hence unable to replenish their cold gas supplies after being accreted, which mimics the process of *strangulation* described in Section 1.5. Two further effects described in Section 1.5, *ram pressure stripping* and *harassment*, are not included in these models,

although we note that they are expected to be efficient only in cluster environments, which contain a relatively small fraction of the total galaxy population.

2.2.3 Mergers and Disk Instabilities

Two mechanisms incorporated into the Durham and MPA models are responsible for disrupting the stellar disks that would otherwise form as described above – galaxy mergers and disk instabilities. Galaxy mergers occur as a direct consequence of, but are distinct from, the mergers of the haloes that host them. As described in Section 2.2.1, a halo that falls into a more massive system may survive for some time thereafter, as a gravitationally bound subhalo. Hence, the less massive (satellite) galaxy can be followed explicitly until tidal effects disrupt its subhalo sufficiently for it to drop below the 20 particle resolution limit. From this point onwards, in the MPA model, the galaxy is associated with the most bound particle of the subhalo just before it became unresolved. The satellite's orbit is assumed to decay through dynamical friction against the halo material until it merges with the more massive (central or primary) galaxy. Merger timescales are determined differently in the Durham model, with the satellite's orbit chosen at random from the cosmological distribution derived by Benson (2005), as soon as the halo merger has taken place and a dynamical friction timescale calculated accordingly.

In the Durham model, the result of a merger is dictated by the relative masses of the merging galaxies and the gas content of the primary. 'Major' mergers ($M_{\rm sat}/M_{\rm pri} \geq 0.3$), completely disrupt any existing disk, producing a spheroidal remnant that contains all the stars from its progenitor galaxies. Any gas present forms stars in a burst, which are also added to the new spheroid, with some fraction of gas being returned to the hot halo through supernovae feedback. Minor mergers ($M_{\rm sat}/M_{\rm pri}$ <0.3) leave the structure of the primary intact, simply adding the stars from the satellite to the bulge of the primary and its gas to the disk, but may also initiate a burst if $M_{\rm sat}/M_{\rm pri}$ ≥0.1 and the primary has sufficient gas in its disk ($M_{\rm gas}/M_{\rm disk}$ >0.1). The fraction of the available gas that is turned into stars is dictated by star formation and feedback rules, applied over the timescale of the burst.

The MPA model assumes starbursts to occur in all mergers. The mass fraction of gas available to take part is a power-law function of the satellite-central mass ratio ($m_{\rm sat}/m_{\rm central}$). Other than this, the mechanics of mergers are largely similar to the

Durham model. Major mergers are defined in the same fashion and also result in the formation of a spheroid; minor mergers add stars to the primary's bulge and gas to its disk.

In galaxies with strongly self-gravitating disks, that is, where the mass of the disk itself dominates the gravitational potential, the system is unstable to perturbations from nearby satellites or dark matter clumps (Efstathiou et al., 1982; Mo et al., 1998). Both models regard a disk to have become unstable when

$$V_{\rm max}/(GM_{\rm disk}/r_{\rm disk})^{1/2} \leq 1, \tag{2.1}$$

where $M_{\rm disk}$ and $r_{\rm disk}$ are the disk's total mass and radius. In the original formulation by Efstathiou et al. (1982), $V_{\rm max}$ was the maximum of the rotation curve, but this is approximated by the halo virial velocity in the MPA model and the disk's velocity at its half-mass radius in the Durham model. Although the prescriptions will typically agree on whether a particular disk is unstable or not, they deal with the situation somewhat differently. In the MPA model, there is effectively a partial collapse, intended to model the formation of a bar. Mass is moved from the disk into the spheroid until the stability of the system, defined by Eqn. 2.1 is re-established. In the Durham model, instabilities result in the complete collapse of the disk into a spheroid, the size of which is dictated by the rotational energy of the disk just prior to collapse. As with a major merger, a starburst is induced, such that the resulting spheroid contains the original disk's stars, plus those formed in the burst. This more catastrophic outcome is assumed to result from orbital resonances and stellar scattering in the barred system causing it to collapse entirely.

2.2.4 Black Holes and AGN Feedback

Prescriptions for supermassive black hole (BH) growth and feedback from active galactic nuclei (AGN) are relatively recent additions to both models, motivated by the growing body of evidence linking properties of a galaxy's bulge to the mass of its central BH (e.g., Magorrian et al., 1998; Ferrarese & Merritt, 2000; Kormendy & Gebhardt, 2001; Marconi & Hunt, 2003; Häring-Neumayer et al., 2006). Energy produced through accretion of material onto the BH is assumed to restrict gas cooling, particularly in higher mass haloes, impacting on galaxy luminosity, colour and morphology. Different implementations of

AGN feedback could, for instance, dictate whether or not an elliptical galaxy is able to regrow a stellar disk after a major merger.

The prescription used in the Durham model for AGN feedback and BH growth is described in full in Malbon et al. (2007). In the Durham model, BH growth is assumed to take place through four main channels.

- *Major merger-driven accretion* - Tidal forces act to drive disk gas into central regions, fuelling the BH. A constant fraction of the accreted gas, $f_{\rm BH}$, (tuned to match the amplitude of the $M_{\rm BH} - M_{\rm Bulge}$ relation) is added to the BH.

- *Instability-driven accretion* - A fraction, $f_{\rm BH}$, of the gas in the collapsing disk is added to the BH.

- *BH-BH mergers* - When two galaxies merge, their BHs are assumed to merge. Mass loss due to the radiation of gravitational waves is neglected and the mass of the new BH is the sum of the progenitor masses plus any gas accreted.

- *Accretion from cooling flows* - In sufficiently massive haloes, where *quasi-hydrostatic cooling* is taking place, the BH can accrete mass from the cooling flow.

The last mechanism is closely associated with the implementation of AGN feedback in the model. In haloes where a quasi-static hot halo has formed, the energy generated through accretion is assumed to couple efficiently with the hot halo gas. If the energy output of the BH (some constant fraction of its Eddington luminosity) exceeds the rate at which the gas can radiate away energy, then no further gas is allowed to cool. Hence, as soon as a large cooling flow builds up, the feedback becomes sufficient to cut it off. This behaviour plays a key role in reproducing the observed K and B-band luminosity functions out to $z \sim 5$.

The MPA implementation also assumes that gas inflows associated with mergers lead to increased BH accretion rates. Consistent with their starburst model, such inflows are presumed to occur in all mergers, with the accreted fraction of the total gas dependent on the satellite-central mass ratio. A simple phenomenological model is used to describe accretion from quasi-hydrostatic cooling flows; the mass accretion rate ($\dot{m}$) depends on the mass of the black hole, the hot gas fraction and the virial velocity of the halo. The luminosity of the BH at any given time is simply $\eta \dot{m} c^2$, where $\eta \simeq 0.1$ is the efficiency

of mass-energy conversion typically expected close to the event-horizon. Based on this energy output, an adjusted cooling rate is calculated, such that it declines smoothly as the amount of mass accreted rises. As in the Durham model, BH-BH mergers occur and are modelled in a similar fashion. However, no additional accretion is considered during a disk collapse.

2.3 The Data

2.3.1 The Millennium Run Database

All of the data analysed here comes from the online Millennium Run database[3], developed by the German Astrophysical Virtual Observatory (GAVO), which can be accessed through the use of structured query language (SQL) (Lemson & The Virgo Consortium, 2006) and contains galaxy and halo data from the Durham and MPA models. Various properties are associated with each halo, for instance, mass, redshift, position, velocity, number of subhaloes, etc. Galaxies additionally carry many directly and indirectly observable properties, such as observer and rest frame magnitudes in several passbands, stellar mass and radial extent of morphological components. The database has been constructed to make the retrieval of an object's merger tree as efficient as possible (see Lemson & Springel (2006) for a detailed description). This has been achieved by assigning unique IDs in a 'depth-first' manner, such that the progenitors of a given object have IDs lying between that of the object itself and an index it carries called the *lastprogenitorid*. Additional indices identify each object's immediate descendant and largest progenitor. An additional index in the Durham tables identifies every galaxy's main branch.

2.3.2 Definition of Morphology and Construction of Galaxy Samples

To describe a galaxy's morphology we use the bulge-total (B-T) ratio of rest frame K-band luminosity ($R = L_{\mathrm{K,bulge}}/L_{\mathrm{K,total}}$). Although most photometric measurements are made in the B-band, the K-band is preferred here because it reflects the stellar mass quite closely, even at moderate redshifts (e.g. Kauffmann & Charlot, 1998; Lacey et al., 2008). This choice has the further advantage that the predictions are then relatively insensitive

[3]Hosted at http://www.g-vo.org/MyMillennium, with a mirror site at http://galaxy-catalogue.dur.ac.uk:8080/MyMillennium (Both require registration for full access).

to uncertain details of the current star formation and reddening corrections in the model. Galaxies are divided into three broad morphological types: “spirals" ($R < 0.4$), “S0s” ($0.4 \leq R \leq 0.6$) and “ellipticals" ($R > 0.6$). This classification is, to some extent, arbitrary, but at least in the B-band Tran et al. (2001) found that galaxies classified as late Hubble types in the NASA Extragalactic Database are well by a rest-frame B-band B-T ratio of less than 0.4, consistent with our definition of spirals.

In addition, we split our two $z = 0$ galaxy populations by luminosity, with the division at $M_{\rm K} - 5{\rm log}h = -22.17$, i.e. one magnitude fainter than the characteristic luminosity in the K-band (e.g. Cole et al., 2001; Smith et al., 2008). Throughout this work, we refer to these as the *bright* and *faint* populations. Where the r-band is also shown, we divide the populations at $M_{\rm r} - 5{\rm log}h = -19.83$ (Blanton et al., 2001) and define morphological classes according to the same B-T ratios as in the K-band. De Lucia & Blaizot (2007) note that, in order to assign a morphology to a galaxy with confidence, its merger history must be well resolved. They determine that this condition imposes a lower limit of $4 \times 10^9\ h^{-1}{\rm M}_\odot$ in stellar mass, which we apply consistently to the bright and faint populations in both models. This cut has virtually no impact on the bright population but it reduces the numbers in the faint population by $\sim 92 - 94\%$, leaving us with 1,298,118 bright and 1,889,131 faint galaxies in the MPA model and 1,280,154 bright, 1,598,908 faint galaxies in the Durham model.

2.4 Overview of Morphological Characteristics

2.4.1 Evolution of the Morphological Mix

With our galaxy samples defined, we now consider some basic properties of the two models. Firstly, we examine their morphological content, that is, the relative fractions of each morphology at a given redshift. Fig. 2.1 tracks the fraction of the total bright galaxy populations in the K-band (left panel) and r-band (right panel) that are spirals, S0s and ellipticals in each model. The r-band is included here in order to compare with the observational data of Benson et al. (2007).

Clearly, in both bands, the two models differ considerably, particularly at high redshifts. The Durham model predicts a substantial population of ellipticals at early times, with steady evolution to a disk-dominated phase after $z \sim 3 - 4$. In contrast, the MPA

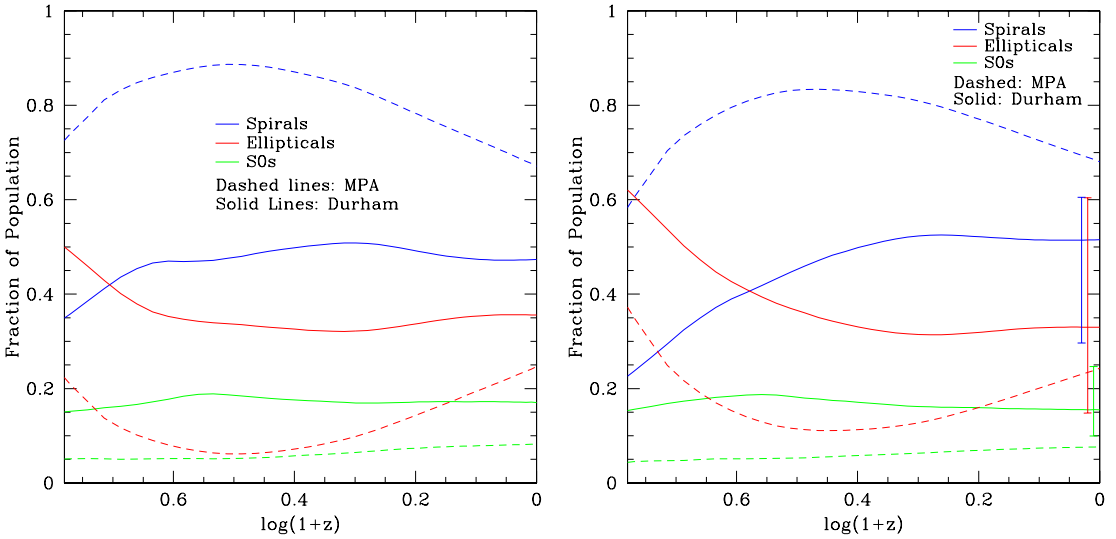

Figure 2.1 The fraction of bright galaxies classified as spirals (blue), S0s (green) and ellipticals (red) in the Durham (solid lines) and MPA (dashed lines) models as a function of redshift. In the left panel, morphology is defined using rest-frame K-band light and in the right panel using rest-frame r-band light. The bars on the right of the r-band panel represent the possible range in each fraction at $z = 0$, calculated using the data of Benson et al. (2007). We explain the origin of these observed ranges in our discussion of Fig. 2.2. Disks are the dominant structures in the MPA model at all times, whereas the Durham model produces a transition from a bulge-dominated phase before $z \sim 3 - 4$ to a disk-dominated phase therefafter. This strikingly different behaviour appears to arise from the contrasting treatment of disk instabilities in the two models. Despite the differences, the two prescriptions arrive at fairly similar fractions at $z = 0$.

Table 2.1 Percentage contribution of each morphology to the bright ($(M_{\rm K} - 5{\rm logh} < -22.17)$) and faint ($(M_{\rm K} - 5{\rm logh} > -22.17)$) present day populations of the MPA and Durham models.

	Durham		MPA	
	Bright	Faint	Bright	Faint
Spirals	51	62	67	72
S0	15	12	8	11
Elliptical	34	26	25	17

model shows more modest evolution, with spirals remaining the most prevalent structures throughout. Even so, the two prescriptions result in fairly similar present day morphological compositions (see Table 2.1 for K-band fractions). Fractions in the Durham model are consistent with the ranges defined by the observational data, but the MPA model seems to produce too many spirals and not enough S0s. We will explain the origin of these ranges in our discussion of Fig. 2.2. The difference between bands for both models is a small offset toward higher B/T values in the r-band, which is a consequence of an increased sensitivity to dust obscuration compared to the K-band, which acts to dim disk light.

Considering instead the faint galaxy population ($M_{\rm K} - 5{\rm logh} > -22.17$, not shown here), we find a very similar result. The plot looks almost identical for MPA galaxies and similar for Durham galaxies, though there is an offset of about $10 - 15\%$ in favour of more spirals at the expense of S0s and ellipticals.

The disagreement at high redshift evident in Fig. 2.1 may be explained by the contrasting treatment of disk instabilities in the two models. As outlined in Section 2.2.3, instabilities trigger a total collapse of the galactic disk in the Durham model, but only a partial “buckling" in the MPA model. As some of the results in Section 2.5 demonstrate, this distinction appears to be the root cause of several differences in galaxy morphology in the two models.

Several attempts have been made to quantify morphology through bulge-total measurements at low redshift (e.g. Tasca & White, 2005; Benson et al., 2007; Driver et al., 2007; Gadotti, 2008). In particular, Benson et al. (2007) showed that the Durham model

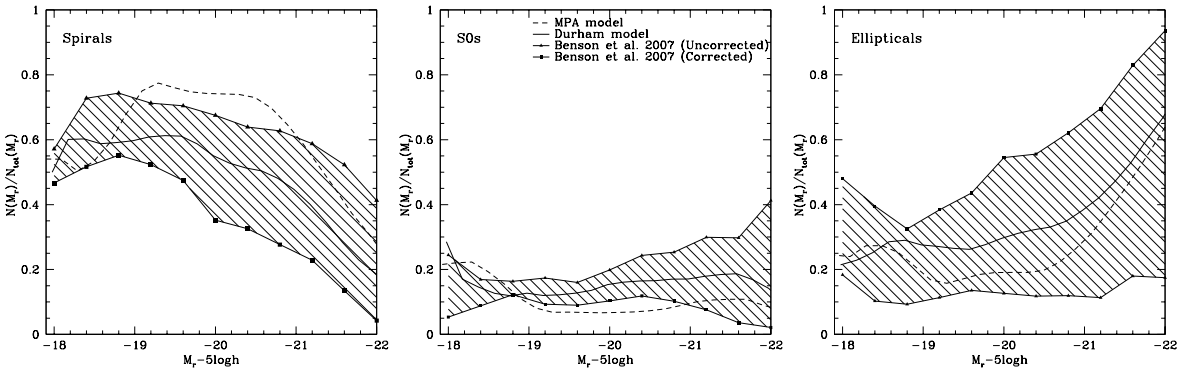

(a) **(b)** **(c)**

Figure 2.2 The fraction of galaxies at $z = 0$ that are spirals **(a)**, S0s **(b)** and ellipticals **(c)**, as a function of rest-frame r-band magnitude in the MPA model (thick dashed line), Durham model (thick solid line) and in the SDSS data (Benson et al., 2007)(connected points). The two sets of points represent the data before (triangles) and after (squares) a correction for biases introduced in the fitting process. This correction is explained in the text. The upper and lower magnitude limits of the plot are dictated by the data. Both models reproduce the general trend and typically lie between the uncorrected and corrected data, although the MPA model appears to have too many spirals and not enough S0s over a range of magnitudes.

(Bower et al., 2006) reproduces the luminosity function of disks and spheroids[4] remarkably accurately. Fig. 2.2 uses their SDSS data to compare the fraction of spirals, S0s and ellipticals in the local universe ($z < 0.12$) as a function of (AB, rest-frame) r-band magnitude, with fractions from the two models at $z = 0$. For this plot, morphologies in the models are defined using rest-frame r-band light for consistency with the data.

Benson et al. determined B/T ratios for their sample of ~ 9000 SDSS galaxies by fitting two component light profiles (bulge + disk) to each image. Analysis of their initial dataset showed that the distribution of disk inclination angles appeared to be biased, leading them to conclude that their code was fitting face-on disks where the bulge varied significantly from the anticipated De Vaucouleurs profile. They applied a statistical correction which attempted to make the distribution of inclination angles uniform, set-

[4]Spheroids were taken to include both the bulges of spirals and elliptical galaxies.

ting B/T to 1 for those galaxies left over after the correction. As Benson et al. point out, this correction will likely overestimate the prevalence of ellipticals and underestimate the number of spirals, but the magnitude of the uncertainty is very difficult to quantify. We have therefore chosen to show the data before and after the applied correction to illustrate the range of uncertainty for each fraction. The ranges at $z = 0$ in Fig. 2.1 are obtained by integrating the corrected and uncorrected fractions for each type, multiplied by the r-band luminosity function (Blanton et al., 2001).

With this in mind, we see in Fig. 2.2 that both models reproduce the general trend in the data - ellipticals are more prevalent at brighter magnitudes, and typically fall between the corrected and uncorrected datasets. The fraction of spirals in the MPA model exceeds the uncorrected data at intermediate magnitudes and the fraction of S0s falls below the corrected data over the same range, but by an amount less than size of the Poisson errors on each datasets (not shown). Consequently, neither model is obviously discrepant with the data, although clearly smaller uncertainties would be desirable in order to place tighter constraints.

2.4.2 The Morphology-Dependent Luminosity Function

The luminosity function provides an important census of any galaxy population. Fig. 2.3 shows the rest-frame B and K-band luminosity functions for each morphological type at $z = 0$, the solid lines representing the Durham model and the dashed lines the MPA model. A galaxy's K-band luminosity can be used as a reasonable proxy for its stellar mass (Kauffmann & Charlot, 1998; Brinchmann & Ellis, 2000; Bell & de Jong, 2001), whilst the B-band is biased toward younger stellar populations and hence is indicative of recent star formation. On both plots, the black vertical dashed line marks the magnitude faintward of which the imposed mass cut at $4 \times 10^9\ h^{-1}\mathrm{M}_\odot$ depletes galaxy densities by $> 5\%$.

Both models produce luminosity functions which, qualitatively at least, share some features with comparable observational data. For instance, the most massive (brightest K-band) galaxies are ellipticals and spirals have a somewhat fainter characteristic magnitude (Nakamura et al., 2003). We also note that spiral galaxies in the MPA model are typically brighter in the B-band than those in the Durham model, suggesting that they have significantly more ongoing star formation or less dust obscuration. In both models,

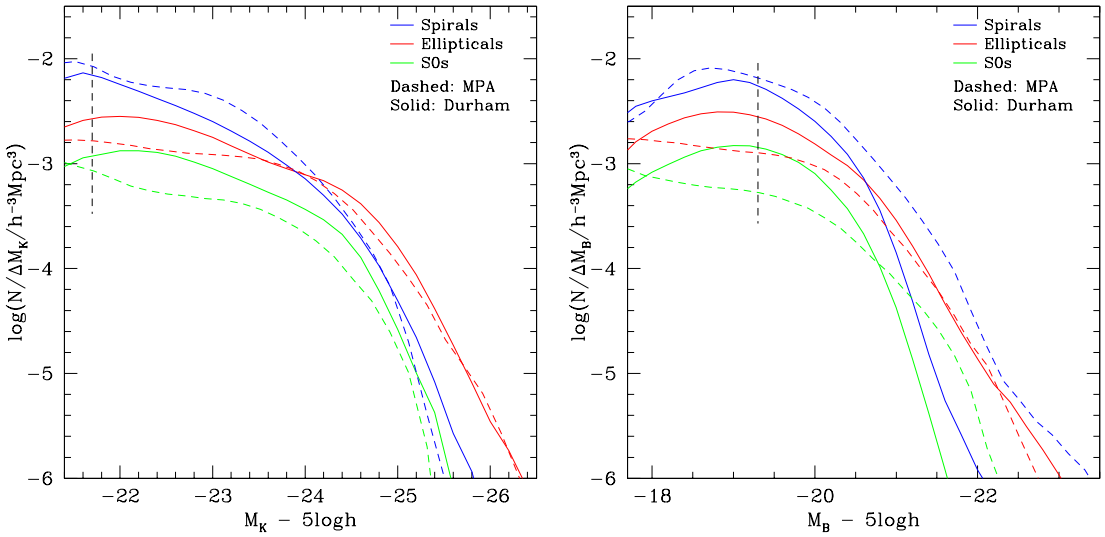

Figure 2.3 The $z = 0$ rest-frame luminosity functions in the K-band (left panel) and B-band (right panel) for each morphology. The solid lines show the Durham model and the dashed lines the MPA model. The black dashed lines indicate the magnitude faintwards of which the imposed mass cut reduces galaxy number densities by $> 5\%$.

ellipticals are the most common morphology at high ($M < M_*$) K-band luminosities, but at the bright end of the B-band LF, the MPA model has at least an order of magnitude more more spirals than the Durham model.

Fig. 2.4 shows the redshift evolution of the K and B-band luminosity functions for each morphology as ratios to the $z = 0$ functions in Fig. 2.3. The reader should note that the bright-end extent of these curves is limited by that of the $z = 0$ data and the faint-end is cut off where the imposed mass cut reduces number densities by $> 5\%$. In the K-band, there is very little evolution in the Durham model between $z \simeq 2$ and $z \simeq 0.5$ for all spirals and S0s and for all but the brightest ellipticals, suggesting that a substantial proportion of their mass was already in place at that time. At the bright end, there is already a sizeable population of ellipticals at $z = 5$ in both models. The early dominance of ellipticals in the Durham model seen in Fig. 2.1 comes mostly from galaxies excluded from this plot by the faint-end cut off. The number density of bright ellipticals in the Durham model declines slightly from $z \simeq 2$ to $z \simeq 0.5$, a result both of mergers between ellipticals and their transformation into S0s or spirals for those able to

grow a disk. The trend is in the opposite sense for the MPA model, indicating that the extra spirals already in place at $z = 5$ compared to the Durham model make merging a process that typically increases elliptical number density. Evolution of the faint-end K-band is more significant in the MPA model, particularly for ellipticals. This may reflect weaker supernovae feedback, that allows more star formation in satellite galaxies.

The Durham B-band functions are consistent with a peak in star formation somewhere around $z = 2$, for spirals and S0s, and somewhat earlier for ellipticals. In the MPA model, there is a steady decline in B-band light for all types since $z \simeq 5$, suggestive of consistently earlier star formation than in the Durham model. The history of star formation in the different types is examined more closely in the next section.

2.5 Results and Discussion

In the previous section, we saw that there is some disagreement between the Durham and MPA galaxy formation models in their predictions for the evolution of the relative abundances of galaxies of different morphological type. In this section, we explore the reasons for these differences by investigating the formation paths of galaxies in the two models. Firstly, we track the build up of a galaxy's dark halo and its stars with the goal of identifying how its final morphology is determined. We then examine in more detail how spheroids form in each model and the roles played by mergers and disk instabilities.

2.5.1 Halo Formation

As described in Section 2.2.3, galaxy mergers follow the mergers of their host haloes after a time delay due to the gradual decay of the satellite's orbit through dynamical friction. One might expect, then, that the manner of a halo's formation might play a significant role in determing the merger history of its galaxy and hence its final morphology.

We define the formation redshift of a halo, $z_{\rm hform}$, as that at which half of its final mass was contained in a single progenitor. Haloes in the database are linked, through their unique IDs, to the galaxies that they host, making it straightforward to relate the time of formation of a halo to the morphology of its galaxies. We consider only 'FOF haloes' since they can be associated with galaxies in both models, as opposed to the modified Durham haloes which cannot always be linked to MPA galaxies. This allows

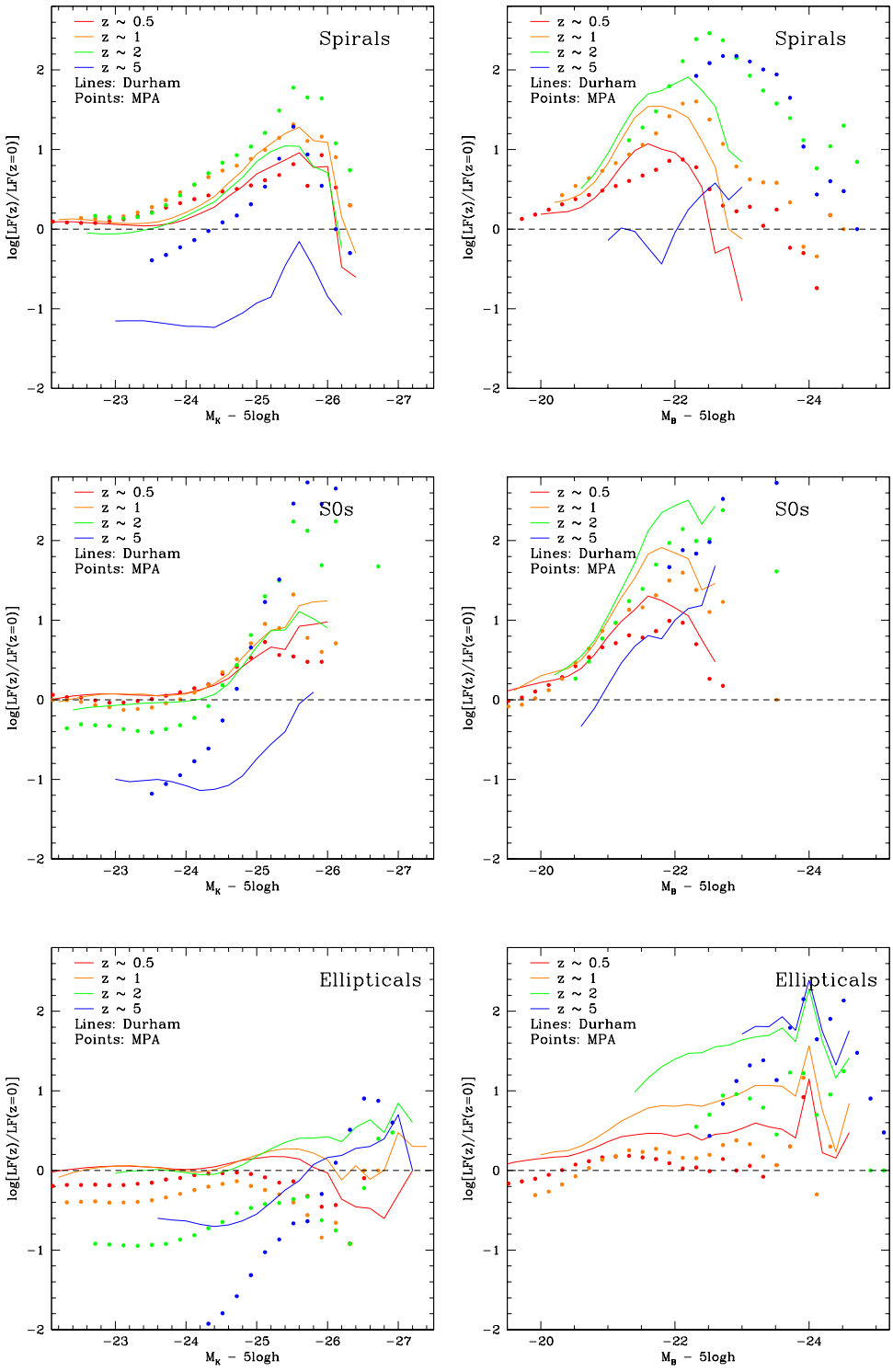

Figure 2.4 The evolution of the K-band (left column) and B-band (right column) rest-frame luminosity functions for spirals (top row), S0s (middle row) and ellipticals (bottom row), plotted as ratios to the $z = 0$ luminosity functions in Fig. 2.3. Curves are cut off at a magnitude faintward of which the mass cut at $4 \times 10^9\ h^{-1}\mathrm{M}_\odot$ reduces number densities by $> 5\%$. At the bright end, they are cut off at the limit of the equivalent $z = 0$ function.

us to compare the morphologies of galaxies in the two models for a common halo population. We consider only central galaxies and limit our sample to haloes in the mass range $0.5 - 2 \times 10^{12}\ h^{-1}\mathrm{M}_{\odot}$, a factor of two either side of the mass of a 'Milky Way type' halo.

Fig. 2.5 shows the distribution of z_{hform} for bright spirals, S0s and ellipticals in the Durham (solid line) and MPA (dashed line) models. Relatively few galaxies in the faint sample exist in haloes within this mass range, making the equivalent plot extremely noisy.

Given that major galaxy mergers disrupt disk structures, one might naïvely have expected later forming haloes, which merged more recently, preferentially to host ellipticals. In the Durham model, this effect is marginal, but can be seen in the median formation redshifts for haloes hosting each type. Haloes with elliptical central galaxies have a median formation redshift of 1.17, compared to 1.28 for those with spiral or S0 centrals. In the MPA model, haloes hosting ellipticals have a median formation redshift of 1.28, in comparison to 1.38 for those hosting S0s and 1.17 for those hosting spirals.

The spike in haloes forming near $z = 0$, seen in both models, appears to arise from the difficulty in tracking objects between snapshots. When a halo passes through a more massive counterpart, it may appear to have merged with it, but, if it emerges on the other side, it is labelled as a newly formed object. In this way, some merger tree branches are broken. If the break occurs after the real formation time and on the main branch, the final time halo will appear to have formed at that epoch. In most cases, the less massive halo falls back into its counterpart and merges before the last snapshot; thus it is no longer considered a main branch progenitor. Hence, the spike at $z = 0$ is a boundary effect - it identifies those cases where insufficient time has passed for a subsequent merger to erase evidence of a fly-through.

The above explanation is supported by the fact that the late-forming haloes are invariably found close to the virial radii of larger haloes. Furthermore, we find that the low redshift spike disappears if we consider instead the formation of the Durham haloes, for which considerable effort has been made to repair broken merger trees and eliminate such 'false mergers' (Helly et al., 2003).

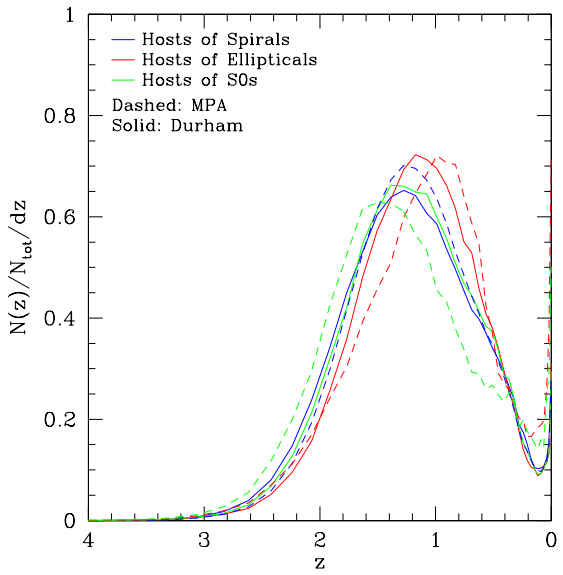

Figure 2.5 The distribution of formation redshifts for haloes hosting galaxies of each morphological type in the Durham (solid) and MPA (dashed) models. Only haloes in a 'Milky Way type' mass range ($0.5 - 2 \times 10^{12}\ h^{-1}\mathrm{M}_{\odot}$) are considered here for the reasons outlined in the text. The median formation redshifts for spiral, S0 and elliptical hosts are 1.17, 1.38 and 1.28 respectively in the MPA model, and 1.28, 1.28 and 1.17 in the Durham Model. All curves are normalised such that they integrate to unity.

2.5.2 Galaxy Assembly and Formation

Having established the extent to which galaxy morphology depends on the epoch of halo formation, we now consider the formation of galaxies directly. We define two different 'formation epochs': i) the stellar assembly redshift, z_{a}, when half of the stars in a present-day galaxy were first assembled in a single progenitor, and ii) the stellar formation redshift, z_{f}, when half of the stars in a present-day galaxy had formed in any of its progenitors. The three panels in Fig. 2.6 compare the distributions of these two redshifts for spirals, S0s and ellipticals.

The two models show the same general trend for both formation and assembly to occur earliest in elliptical galaxies and latest in spirals, with S0s intermediate between the two. Given that early-type galaxies are typically observed to have older stellar populations, it is reassuring that both models predict that they form most of their stars first. Less

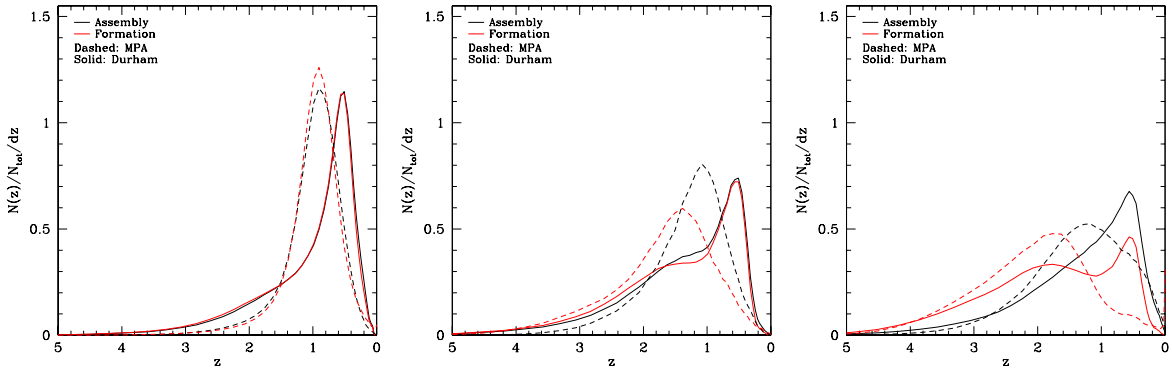

Figure 2.6 The distributions of the stellar assembly and stellar formation redshifts for bright ($M_{\rm K} - 5{\rm logh} < -22.17$) spirals **(a)**, S0s **(b)** and ellipticals **(c)** in the MPA (dashed line) and Durham (solid line) models. All curves are normalised such that they integrate to unity.

intuitive, perhaps, is the fact that ellipticals also assemble their stellar mass before either S0s or spirals. Late assembly, however, does not imply late merging. Steady, in-place star formation in a disk naturally results in a relatively narrow distribution of assembly times, which are typically later than for elliptical and S0 galaxies where mergers play a more important role. The fact that the formation and assembly epochs of spirals (and also S0s in the Durham model) are generally coincident suggests that this is indeed the case: when the formation threshold is reached, the stars are already in one object. In the Durham model, disks typically form at $z \sim 0.55$, although a significant fraction form at $z > 1$. In the MPA model the typical formation redshift of disks is $z \sim 0.9$.

In both models, we effectively see two characteristic formation times for ellipticals and S0s, a primary peak at $z \sim 1.5 - 2$ and a secondary peak at $z \sim 0.55$. The latter coincides with the typical epoch of spiral galaxy formation and is more pronouced in the Durham model. This secondary peak is the result of disk instability: these ellipticals and S0s are, in effect, failed spirals, having had very similar star formation histories up to $z \sim 0.55$, before becoming unstable and collapsing into a spheroid with the attendant conversion of residual gas into stars. Some of these spheroids may partially regrow a stellar disk and end up as S0s or perhaps even as spirals, but others remain as ellipticals

up to the present day, either because the instability occurred very late on, or because their gas cooling rate was restricted by feedback or lack of gas. Since disk instabilities have a much gentler effect in the MPA model, their influence on the distribution of stellar formation times of ellipticals and S0s is minor.

Minor and major mergers play an important role in building up most of the ellipticals in the MPA model and those whose stars form in the higher redshift peak in the Durham model, as evidenced by the fact the stellar formation times are earlier than the stellar assembly times. This asynchronism between stellar formation and assembly in CDM-based models of elliptical galaxies was first highlighted by Kauffmann (1996) and has recently been investigated in the MPA model by De Lucia et al. (2006). Our results for MPA ellipticals are in agreement with theirs. The distributions of $z_{\rm a}$ and $z_{\rm f}$ for faint galaxies ($M_{\rm K}-5{\rm log}h < -22.17$) in both models are similar to those for bright galaxies but shifted slightly to higher redshift and with a more significant high redshift tail. Also, the lower redshift peak in the Durham model, corresponding to galaxies forming through disk instabilities, is much less pronounced for faint objects.

2.5.3 Major Mergers, Minor Mergers and Disk Instabilities

The differences between the Durham and MPA models uncovered so far appear to stem from the roles played by the main spheroid-forming mechanisms. In this section, we compare the relative contributions of three processes that contribute to the build-up of spheroids: major mergers, minor mergers and disk instabilities. We remind the reader that in both models the distinction between major and minor mergers is made on the basis of the relative baryonic masses of the satellite and primary, with the boundary corresponding to $M_{\rm sat}/M_{\rm pri} = 0.3$. In both models, major mergers are assumed to disrupt completely any pre-existing galactic disks.

The incidence of major mergers and the redshift when the main branch progenitor of a present-day galaxy was last involved in a major merger, $z_{\rm mm}$, can be readily obtained by tracing back the galaxy's merger tree. The analysis below includes galaxies above our resolution limits of $1.7 \times 10^{10}\ h^{-1}{\rm M}_{\odot}$ for the dark matter mass of the halo and $4 \times 10^{9}\ h^{-1}{\rm M}_{\odot}$ for the stellar mass of the galaxy. The statistics of major mergers are surprising and revealing. Of the total bright $M_{\rm K} - 5{\rm log}h < -22.17$) population, only 49% of ellipticals, 2% of S0s and 2% of spirals in the MPA model, or 41%, 2.5% and 1.5% respec-

tively in the Durham model, undergo a main branch major merger in their entire formation history. In both models, this fraction is largely independent of total stellar mass for spirals and S0s, but not so for ellipticals. Combining the bright and faint populations together, in the Durham model, 100% of the highest mass ($1 - 4 \times 10^{12}\ h^{-1}\mathrm{M}_{\odot}$) ellipticals have major mergers, but this fraction falls to $< 3\%$ around the lower mass limit of $4 \times 10^{9}\ h^{-1}\mathrm{M}_{\odot}$. In the MPA model, only $\sim 15\%$ of ellipticals with mass $1.6 \times 10^{10}\ h^{-1}\mathrm{M}_{\odot}$ have a major merger, but the proportion rises sharply either side of this mass, to around $\sim 80\%$ at the low mass end, and close to 100% for masses $> 2.5 \times 10^{11}\ h^{-1}\mathrm{M}_{\odot}$. In both models, more than half of the total elliptical population do not undergo a main branch major merger at any point. These results are consistent with the conclusions reached by De Lucia et al. (2006) for MPA ellipticals.

The distribution of z_{mm} for each morphological type in the bright population is displayed in Fig. 2.7. There is reasonable agreement between the two models for spirals and ellipticals, but not for the S0s, which appear to trace the elliptical distribution in the MPA case, but the spiral distribution in the Durham case. As one might expect, ellipticals typically have had the most recent major mergers, but nonetheless, of the small fraction of spirals and S0s that have undergone major mergers at all, some experience them at very late times ($z < 0.1$) and yet still manage to recover a stellar disk. The faint population shows similar behaviour to that illustrated in Fig. 2.7. Given that major mergers are this infrequent, the alternative mechanisms of minor mergers and disk instabilities must be important in spheroid formation. Applying a similar analysis to instabilities reveals that virtually all ellipticals have experienced such an event at some point in their formation history. However, the fraction of the total galaxy population that is unstable at a particular redshift differs substantially between the two models. In any one snapshot, approximately 1% of MPA galaxies are unstable but, in the Durham model, the figure is much higher: $\sim 16\%$ at $z = 6$, falling to $\sim 2\%$ at $z = 2$. This difference accounts for the higher proportion of ellipticals seen at early times in the Durham model, as illustrated in Fig. 2.1. Early forming disks in the Durham model are inherently less stable than those in the MPA model, largely as a consequence of their higher cold gas content.

To quantify the relative impact of instabilities, major mergers and minor mergers on galaxy morphology, we determine the fraction of stellar mass in present-day spheroids that was incorporated into the spheroid by each process. The complexity of the SQL

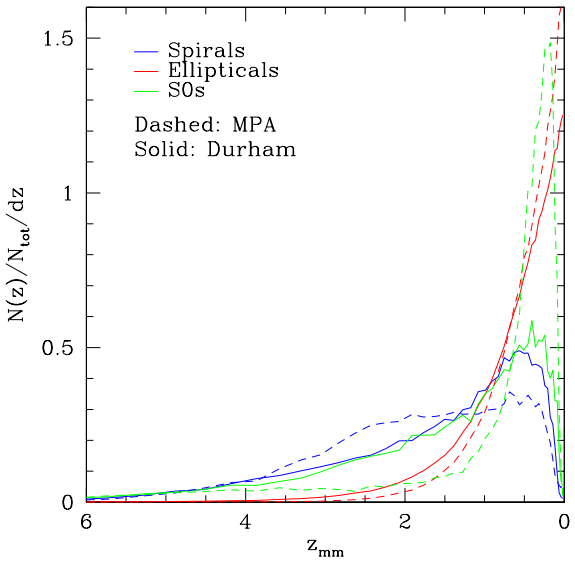

Figure 2.7 The distribution of the last (main branch) major merger experienced by spirals (blue), S0s (green) and ellipticals (red) in the Durham (solid line) and MPA (dashed line) bright ($M_{\rm K} - 5{\rm log}h < -22.17$) galaxy populations. Each curve is normalised such that they integrate to unity. The median values of $z_{\rm mm}$ are 2.62, 0.83, and 0.41 for spirals, S0s and ellipticals respectively in the MPA model, and 2.07, 1.63 and 0.51 in the Durham model.

query needed for this calculation made it necessary to use the 'milli-millennium' datasets, which were generated using the same two semi-analytical models on halo merger trees constructed from a smaller version of the Millennium simulation (1/512 of the volume). Even though the milli-millennium simulation has somewhat less structure on the largest scales, its cosmological parameters and other attributes are identical, so our statistical results will be similar in both simulations.

Fig. 2.8 shows the average fraction of stellar mass in the bulge component of a galaxy that is present due to each of the three spheroid-forming mechanisms, as a function of the total stellar mass of the galaxy. These fractions include stars that may have formed in the bulge as a result of a starburst induced by any of the three processes. As expected from our previous results, instabilities contribute considerably more to bulges in the Durham model, dominating in all but the most massive galaxies, where most stars are brought in by, or formed in, major mergers. In the MPA model, it is minor mergers that

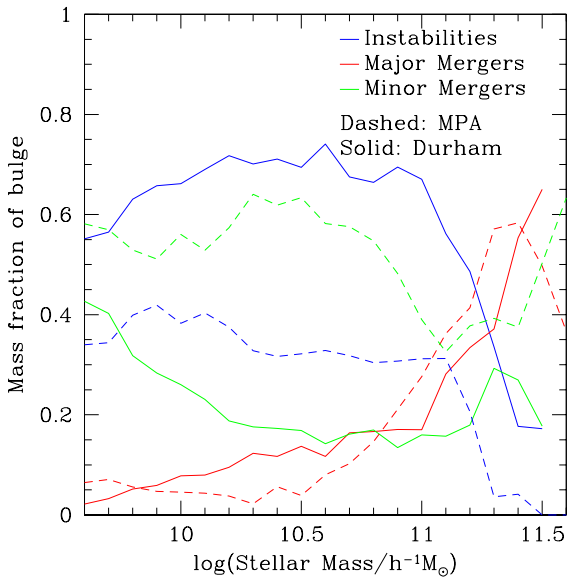

Figure 2.8 The fractional contributions of instabilities (blue), minor mergers (green) and major mergers (red) to the stellar content of spheroids, as a function of total galaxy mass, in the Durham (solid lines) and MPA (dashed lines) models.

are responsible for the bulk of stellar mass in spheroids, but, again, major mergers are dominant at the highest masses.

Other galaxy formation models have used slightly different values for and definitions of the mass ratio that identifies a major merger. For example Somerville et al. (2008) use a value of 0.25 and include all dark matter within a radius of twice the NFW scale-length of the halo. We have tested the sensitivity of the above result to the baryonic mass ratio used to define a major merger in the Durham model. Values between 0.25 and 0.35 modify the fractions in Fig. 2.8 by only a few percent and a value of < 0.01 is required in order to make major mergers the dominant channel for bulge growth above a stellar mass of $\sim 5 \times 10^{10}\ h^{-1}\mathrm{M}_{\odot}$. Considering instead a version of the Durham model which employs a more realistic prescription for gas stripping in satellites (Font et al., 2008), we find that major mergers occur more frequently. This appears to be mainly the result of a higher satellite mass (in cold baryons) at the point of merger, which reduces the mass ratio. Also, since the total baryonic satellite mass is larger, the merger timescale is shorter, which in turn means that the central galaxy has less time to increase the mass ratio by

cooling more gas before the merger occurs. Nonetheless, in this model, major mergers still account for $< 20\%$ of bulge stars in galaxies less massive than $\sim 5 \times 10^{11}\ h^{-1}\mathrm{M}_{\odot}$ and at higher masses they contribute almost identical fractions to those seen in the Bower et al. model.

Several authors have considered the role of mergers in spheroid formation, although none to our knowledge has included disk instabilities alongside mergers as a channel for bulge growth. Kang et al. (2007) used a semi-analytical model similar in structure to the Durham and MPA models and were able to match the observed fraction of boxy early-type galaxies as a function of luminosity and halo mass by assuming that gas poor major mergers result in boxy remnants. Khochfar & Silk (2006) used another semi-analytical model, though without AGN feedback or N-body dark matter merger trees, to examine the contribution of 'quiescent'and 'merger' processes - stars formed in progenitor disks and in merger-induced starbursts respectively. They found that bulges and elliptical galaxies are dominated by quiescently formed stars. The aspects of spheroid formation investigated by Khochfar & Silk (2006) and Kang et al. (2007) and their methods of analysis differ considerably from those presented here, making it difficult to determine whether their results are consistent or not with spheroid formation in the Durham and MPA models. Hopkins et al. (2008a) used a 'semi-empirical' model, based on an observationally constrained halo occupation distribution, combined with theoretical estimates for merger timescales to track galaxy mergers. They found that gas rich major mergers can account for the observed mass-density of all red, early types at $z = 0$ and the dichotomy in the kinematic properties of ellipticals. These results appear, qualitatively at least, to be inconsistent with the Durham and MPA models, suggesting that major mergers alone are sufficient to explain the formation of spheroids. The frequency of major mergers implied by their results certainly seems to exceed that in either the Durham or MPA semi-analytical prescriptions, though we note that they do not attempt to follow the processes of cooling, star formation and feedback that influence the major merger rates in these two models.

As the above results have demonstrated, not only are major mergers a relatively infrequent occurrence in both the Durham and MPA models, but their overall fractional contribution to building spheroids is typically small compared to the other two mechanisms in all but the largest galaxies. The importance of disk instabilities, particularly in

the Durham model, suggests a possible observational test of this, perhaps unexpected, conclusion, because the rotation properties of spheroids should differ depending on whether they formed predominantly through mergers or instabilities.

The relative importance of rotational and random motions in spheroidal systems is measured by the ratio of rotational speed to velocity dispersion, V/σ, which is often plotted against the galaxy's ellipticity to determine whether its shape is supported by rotation or by velocity anisotropy (Illingworth, 1977; Binney, 1978; Kormendy, 1993; Kormendy & Kennicutt, 2004a; Kormendy & Fisher, 2008). During major mergers, tidal forces transfer angular momentum from the baryonic component to the dark halo (e.g. Frenk et al., 1985; Zavala et al., 2008) so the resulting merger remnants tend to have low V/σ and a shape that is supported by velocity anisotropy. Spheroids forming through disk instabilities on the other hand are expected to retain a significant proportion of the angular momentum of the progenitor disk, ending up close to the 'isotropic rotator' line in the V/σ *vs* flattening diagram. Our findings are qualitatively consistent with observations: low luminosity ellipticals (Davies et al., 1983) and most 'classical' spiral bulges (Illingworth & Schechter, 1982; Kormendy & Illingworth, 1982) are found to be nearly isotropic, oblate rotators, whereas most giant ellipticals have insignificant rotation (Bertola & Capaccioli, 1975; Illingworth, 1977). A detailed analysis of fast and slow rotators using integral field spectroscopy (Emsellem et al., 2007) leads to similar conclusions, with massive ellipticals exhibiting negligible rotation and the fastest rotators tending to be of lower luminosity.

An important caveat to the test described above is that major mergers can also produce spheroids that are disky and rapidly rotating. Several simulations of mergers between equal mass, gas rich disks have shown that, despite a large burst taking place, enough gas may survive to form a new, rotationally supported stellar disk within the remnant (Barnes & Hernquist, 1996; Bournaud et al., 2005; Springel & Hernquist, 2005; Naab et al., 2006; Hopkins et al., 2008b). Merger geometry is also likely to influence remnant structure (Hernquist & Mihos, 1995; Bournaud et al., 2005). These considerations may make our proposed test of the models less clear cut.

The differences in the fractions of spheroid stars added by instabilities in the two models are unsurprising given the contrasting prescriptions for instability already discussed, but it is not simply the dominance of this mechanism that decreases the fractional

contribution from minor mergers in the Durham case. The average mass added by minor mergers is typically somewhat larger in the MPA model for any given galaxy. This difference appears to stem from two aspects of the models. The Durham model has a longer characteristic star formation timescale and also stronger supernovae feedback, which inhibits star formation in lower mass galaxies and efficiently depletes the cold gas available to form stars in satellites. Hence, there is less mass on average in each Durham satellite. At the high mass end, however, supernova feedback is less effective, and so the mass brought in by major mergers is more similar in the two models. As Fig. 2.8 shows, the two models, in fact, agree rather well on the fractional contribution of major mergers to spheroid formation.

2.6 Summary

In this chapter we have investigated the origin and evolution of galaxy morphology in the ΛCDM cosmology using publicly available data from two semi-analytical galaxy formation models, the Durham and MPA models (Bower et al., 2006; De Lucia & Blaizot, 2007), both of which are based on the Millennium dark matter simulation. Morphology was defined for each galaxy by means of the bulge-to-total ratio in K-band luminosity; we distinguished between the behaviour of bright ($M_{\rm K} - 5{\rm logh} < -22.17$) and faint ($M_{\rm K} - 5{\rm logh} > -22.17$) galaxies.

There are many similarities, but also fundamental disagreements in the predictions of the two models. One of the largest differences involves the redshift evolution of the morphological fractions: spirals are the most common systems at all times in the MPA model, while ellipticals dominate in the Durham model at redshifts $z > 4$. The main cause of this and other differences highlighted below is the different treatment of disk instabilities in the two models. In the Durham model, instabilities are not only more common at early times, but also have more catastrophic consquences: the sudden conversion of the entire disk, first into a bar and then into a spheroid. Nevertheless, the two models predict a fairly comparable morphological mix at the present day.

In comparison with data from Benson et al. (2007), the substantial systematic uncertainties involved in the process of fitting bulge and disk light profiles mean that only weak constraints can be placed on the fraction of each morphological type as a function

of absolute r-band magnitude. Neither model is obviously inconsistent with the data, but clearly smaller systematic uncertainties would be desirable. The bright galaxy populations consist of 51%, 15% and 34% of spirals, S0s and ellipticals respectively in the Durham model, and 67%, 8% and 25% respectively in the MPA model.

For typical Milky-Way type haloes, we find that the formation time of the halo has, at most, only a small effect on the morphology of the central galaxy. In both models, haloes hosting ellipticals form slightly later than haloes hosting spirals or S0s, although this effect is only marginal in the Durham model.

Our analysis confirms previous studies (Kauffmann, 1996; De Lucia et al., 2006) that show that ellipticals galaxies form most of their stars before the bulk of the galaxy is assembled. In fact, the ellipticals form and assemble their stars earlier than galaxies of other present-day morphological types, although the late 'assembly' times of spirals are a consequence of in-situ star formation, rather than mergers. In general, the MPA model predicts slightly earlier star formation for galaxies of all types. In the Durham model, there is a significant population of S0s and ellipticals that formed at relatively low redshift from the recent collapse of unstable disks, yielding spheroids that never regrow a sizeable stellar disk. The differences in the stellar formation histories predicted by the two models are, in principle, accessible to observational tests.

Perhaps the most surprising conclusion of this study is that, with the exception of the brightest ellipticals (stellar mass $M_* \gtrsim 2.5 \times 10^{11}\ h^{-1}\mathrm{M}_\odot$), major mergers are *not* the primary mechanism by which most spheroids (ellipticals and spiral bulges) assemble their mass. Elliptical galaxies are more likely than spirals or S0s to have undergone a recent major merger, but nonetheless more than half of them do not experience one throughout their whole formation history (involving galaxies above the resolution limits of our calculations). Major mergers are even rarer for spirals, affecting $< 4\%$ of galaxies; their bulges are almost universally formed by minor mergers or disk instabilities. These conclusions would appear to be quite robust for galaxy formation in a ΛCDM universe since they are common to both the MPA and Durham models, in spite of the substantial differences in the detailed modelling of key physical processes.

An important difference between the two models concerns the channel through which less massive ellipticals and bulges acquire their mass. In the Durham model, disk instabilities are responsible for the bulk of the stellar mass in spheroids at $z = 0$, whereas

in the MPA model, minor mergers contribute the most. In the Durham model at least, these results appear to be relatively insensitive to the mass ratio at which a merger is defined as 'major'. Varying the value between 0.25 and 0.35 typically alters the fractions in Fig. 2.8 by less than a few percent for any given stellar mass; in order for major mergers to become the dominant channel for bulge growth in galaxies larger than $\sim 5 \times 10^{10}\ h^{-1}\mathrm{M}_{\odot}$, the ratio would need to be lowered to < 0.01. Adding a more realistic prescription for gas stripping of satellites (Font et al., 2008) increases the importance of major mergers, but they still contribute $< 20\%$ of spheroid mass in galaxies smaller than $\sim 5 \times 10^{11}\ h^{-1}\mathrm{M}_{\odot}$. Mergers as a whole contribute less mass to spheroids in the Durham model because strong supernova feedback suppresses star formation especially strongly in low mass satellite galaxies.

The dominant role of disk instabilities in the production of spheroids, particularly in the Durham model, offers a possible observational test, since spheroids formed this way will tend to rotate faster than spheroids formed through mergers. However, this test would be complicated by the fact that gas rich major mergers can also produce high V/σ remnants. What is clear is that a more precise comparison between theory and observations will require more detailed modelling of disk instabilities than we have attempted here.

More generally, semi-analytical techniques offer, at present, only a somewhat crude way to model the processes that establish galaxy morphology. It is therefore remarkable that such a simplified approach can lead to some important conclusions that appear to be robust to the modelling details. This approach also serves to identify specific processes that deserve further study, for example, through direct hydrodynamical simulations. In the next chapter, we introduce one such simulation and describe how it can inform our understanding of many of the processes that shape the morphological evolution of galaxies.

Chapter 3

Hydrodynamical Simulations of a Milky Way Sized Galaxy

3.1 Introduction

Hydrodynamical simulations of galaxy formation are often seen as a complementary approach to semi-analytical models in two respects. Firstly, out of necessity, they have tended to focus on providing a more detailed description of the evolution of a far smaller number of galaxies and have typically explored only a very limited volume of parameter space. Secondly they supply spatial and kinematical information not available from the parameterised prescriptions of semi-analytical models, by modelling hydrodynamic interactions self-consistently. In recent years, advances in computing power and the use of parallel programming techniques have made the first of these distinctions less significant. Simulations are now able to resolve the formation of galaxies in relatively large cosmological volumes (Crain et al., 2009) and systematic parameter studies have even been carried out (Schaye et al., 2010). The second, more fundamental, distinction is magnified at the opposite end of the spectrum - so-called *zoomed* simulations, wherein an individual galaxy or small volume is extracted from a full cosmological simulation and re-simulated at much higher resolution. A natural choice of subject for the zoom technique is the galaxy for which we can assemble the most detailed observational picture, the Milky Way (MW). In this chapter we introduce a simulation that tracks the formation of a MW-mass galaxy, resolved with $\sim 5 \times 10^6$ dark matter and gas particles within the virial radius at $z = 0$. We use two lower resolution simulations to determine the convergence properties of our model and present a detailed analysis of the formation and

$z = 0$ properties of the high resolution galaxy. The same simulation will be used later in this thesis to examine components of the galaxy not discussed here, namely the satellite population (Chapter 4) and the stellar and hot gas haloes (Chapter 5).

In the final section of this chapter we present results from an ambitious code comparison project, *Aquila*, in which eight other hydrodynamics codes were run on the same initial conditions used for our intermediate and low resolution simulations. The main aims of the project were i) to investigate the extent to which hydrodynamical technique and the inclusion of different physics can change the properties of the final galaxy and ii) to highlight the physical mechanisms that promote the formation of a realistic galaxy disk. First though, we introduce our SPH galaxy formation code and explain the details of the initial conditions.

3.2 The Simulation Code

The simulation code employed in this chapter, as well as chapters 4 and 5, is based on an early version of the parallel N-body-SPH code GADGET-3, an update to the publicly available GADGET-2 code. GADGET-3 computes the gravitational interaction between particles using a particle-mesh (PM) method over long distances and an oct-tree method over short distances. Gas particles are additionally subject to hydrodynamic forces calculated using the energy and entropy-conserving formulation of SPH due to Springel & Hernquist (2002) and described briefly in chapter 1. The SPH smoothing lengths of gas particles adapt to changes in density such that the number of neighbours is kept approximately constant. The dynamics are computed by integrating the equations of motion with a leap-frog scheme and using individual particle timesteps, which also adapt to the particle's environment. Efficient algorithms are incorporated to ensure that memory and workload are optimally balanced across processors and that communication between processors is minimized.

In addition to the fundamental interactions followed by GADGET-3, our code includes algorithms to model several baryonic processes known to be important in galaxy formation, which we outline in the following subsections. Complete descriptions of the algorithms can be found in the papers Okamoto et al. (2005), Okamoto et al. (2008b) and Okamoto et al. (2010).

3.2.1 Radiative Processes and the Equation of State

Radiative processes in our model are implemented as described in Wiersma et al. (2009a) and include inverse Compton scattering of CMB photons, thermal Bremsstrahlung, atomic line cooling and photoionisation heating from Hydrogen and Helium. All gas in the simulation volume is ionised and heated by a spatially uniform, time evolving UV background, as calculated by Haardt & Madau (2001). During the reionisation of H and He I ($z = 9$) and He II ($z = 3.5$), an extra two eV per atom of thermal energy is added to the gas, smoothed over Gaussian distributions with widths $\Delta z = 0.0001$ and 0.5 respectively, in order to approximately account for non-equilibrium and radiative-transfer effects (Abel & Haehnelt, 1999). The contributions to heating and cooling from eleven elements (H, He, C, N, O, Ne, Mg, Si, S, Ca and Fe) are interpolated from tables output by CLOUDY (Ferland et al., 1998), using elemental abundances smoothed over the SPH kernel, to approximate the mixing of metals in the interstellar medium (ISM). This avoids unphysical small scale fluctuations in the cooling time that arise if the abundances associated with individual particles are used (Wiersma et al., 2009b).

Failure to resolve the Jeans mass ($M_{\rm J}$) or Jeans length ($\lambda_{\rm J}$) is known to lead to spurious fragmentation through gravitational instability (Bate & Burkert, 1997; Truelove et al., 1997). Techniques employed to avoid this problem typically involve some form of energy injection to maintain an effective pressure that guarantees that the available resolution is sufficient (e.g., Machacek et al., 2001; Robertson & Kravtsov, 2008; Springel & Hernquist, 2003; Ceverino et al., 2010; Schaye et al., 2010). This pressure support has been identified with, for example, a hot phase maintained through energy input by SNe (Springel & Hernquist, 2003) and turbulence induced by the disk's self gravity and rotation (Wada & Norman, 2007). We include a minimum pressure explicitly by adopting a polytropic equation of state (EoS) with $P_{\rm min} \propto \rho^{\gamma_{\rm eff}}$ for gas above the density threshold for star formation and adopt $\gamma_{\rm eff} = 1.4$. For $\gamma_{\rm eff} > 4/3$, the Jeans mass increases with density (e.g., Schaye & Dalla Vecchia, 2008), such that, if it is resolved at the threshold density, it is resolved everywhere. Schaye et al. (2010) showed that, in models where star formation is strongly regulated by stellar feedback, as it is in ours, the choice of $\gamma_{\rm eff}$ has very little impact on the global star formation rate. The density threshold above which gas is allowed to form stars is $n_{\rm H} > 0.1{\rm cm}^{-3}$, where $n_{\rm H}$ is the number density of Hydrogen atoms.

3.2.2 The Multiphase ISM and Star Formation

At sufficiently high pressures, the ISM is known to exist in distinct phases. We follow Springel & Hernquist (2003) by modelling gas above the threshold density using hybrid SPH particles, which are assumed to consist of a series of cold clouds in pressure equilibrium with a surrounding hot phase, that is:

$$\rho_{\rm c} u_{\rm c} = \rho_{\rm h} u_{\rm h}. \tag{3.1}$$

The subscripts *h* and *c* are used throughout this section to indicate properties of the hot and cold phases, in this case density (ρ) and specific energy (u). The cold clouds have an empirically determined mass spectrum of the form

$$\Phi(m) = \frac{dN_{\rm c}}{dm} \propto m^{-\alpha}. \tag{3.2}$$

We adopt $\alpha = 1.7$, guided by observations that suggest a plausible range of $1.5 - 1.9$ (Solomon & Rivolo, 1989; Fukui et al., 2001; Heyer et al., 2001). We follow Samland & Gerhard (2003) in assuming clouds to be spherical, with size at a fixed mass determined solely by the ambient pressure (Elmegreen, 1989):

$$\left(\frac{m}{\rm M_\odot}\right)\left(\frac{r(m)}{\rm pc}\right)^{-2} = 190 P_4^{1/2}, \tag{3.3}$$

where $P_4 = \frac{P/k}{10^4 {\rm kcm}^{-3}}$ and k is the Boltzmann constant. Cold clouds form and grow in our model through thermal instability. The rate of mass increase in the cold phase is equal to the total cooling luminosity divided by the change in specific energy necessary to mode between phases:

$$-\frac{dM_{\rm h}}{dt}|_{\rm TI} = \frac{dM_{\rm c}}{dt}|_{\rm TI} = \frac{\Lambda(\rho_{\rm h}, u_{\rm h}, Z)}{(u_{\rm h} - u_{\rm c})}\frac{M_{\rm h}}{\rho_{\rm h}} \tag{3.4}$$

where $M_{\rm h}$ and $M_{\rm c}$ are the masses in the hot and cold phases, and $\Lambda(\rho_{\rm h}, u_{\rm h}, Z)$ is the cooling function, which is a function of density, temperature (or specific energy) and chemical composition (Z). The temperature of the cold clouds ($T_{\rm c}$) is assumed to be 100K, although we note that results are insensitive to the exact value providing $T_{\rm c} \ll 10^4$ K. Mass can also move from the cold phase to the hot phase due to cloud evaporation. Our code follows the model of Cowie & McKee (1977) in which the rate of evaporation scales linearly with the cloud radius (r):

$$\frac{dM_{\rm h}}{dt}|_{\rm evp} = -\frac{dM_{\rm c}}{dt}|_{\rm evp} = \eta_{\rm evp}\frac{16\pi\mu\kappa r}{25 k_{\rm B}}, \tag{3.5}$$

where $\eta_{\rm evp}$ is an efficiency parameter, μ is the mean molecular weight and κ is the conductivity as specified by Spitzer (1962). The total evaporation rate for the particle is then computed by integrating over the cloud mass function (Eqn. 3.2). The new mass in the hot phase ($M'_{\rm h}$) after a timestep Δt can then be calculated by iteratively solving the equation

$$M'_{\rm h} = M_{\rm h} + M_{\rm evp} - \frac{\Lambda(\rho'_{\rm h}, u_{\rm h}, Z)}{(u_{\rm h} - u_{\rm c})} \frac{M'_{\rm h}}{\rho'_{\rm h}} \Delta t, \tag{3.6}$$

with the constraints that the total volume and mass of the particle remain constant over the timestep. The change in specific energy of the hot phase (over and above that due to adiabatic cooling and shock heating) is then also recalculated, taking into account any energy input from SNe ($\Delta Q_{\rm Sn}$) and the energy involved in cloud evaporation:

$$u'_{\rm h} = u_{\rm h} + \frac{\Delta Q_{\rm Sn} + (u'_{\rm h} - u_{\rm c})\Delta M_{\rm evp}}{M'_{\rm h}}. \tag{3.7}$$

Since $T_{\rm c}$ (and hence $u_{\rm c}$) is constant, the pressure in the cold phase changes only due to the extra mass added by thermal instability cooling and subtracted by star formation; $\rho_{\rm c}$ is then recalculated using the mass-radius radius relation for clouds in Eqn. 3.3. Particles with a non-zero cold cloud mass (i.e. $\rho > \rho_{\rm th}$), are eligible to form stars. Star formation takes place in each cloud on a timescale related to the dynamical time, which can be calculated directly from Eqn. 3.3:

$$t_{\rm dyn} = \left[\frac{3\pi}{32 G \rho(m)}\right]^{1/2} \simeq 0.32 P_4^{-3/8} \left(\frac{m}{M_\odot}\right)^{1/4} {\rm Myr}, \tag{3.8}$$

The star formation rate (SFR) is then

$$\dot{m}_* = c_* \frac{m}{t_{\rm dyn}}, \tag{3.9}$$

where c_* is the star formation efficiency, which is set to reproduce the normalisation of the Kennicutt-Schmidt law (Kennicutt, 1998). $c_* = 0.005$ is used for all the simulations presented in this chapter. The total SFR for each SPH particle is obtained by integrating Eqn. 3.9 over all clouds deemed capable of supporting star formation (which we assume to be in the mass range $10^4 - 10^6$ M$_\odot$).

SPH particles spawn new collisionless star particles in a stochastic fashion, with a probability that depends on their star formation timescale and the mass in cold clouds:

$$p = \frac{M_{\rm c}}{m_{\rm p,*}} \left[1 - exp\left(\frac{-\Delta t}{t_*}\right)\right] \tag{3.10}$$

Each star particle represents a single stellar population with a Chabrier (2003) initial mass function (IMF) and inherits the chemical properties of the gas that it formed from.

3.2.3 Recycling, Enrichment and Feedback Energy

As the stellar populations associated with each star particle evolve, they return mass, energy and newly synthesised heavy elements to the ISM, due to mass loss (particularly from AGB stars), type Ia and type II SNe explosions.

Each time mass and energy from a star particle are distributed, its nearest gas neighbours have to be identified (using the oct-tree employed for the gravity calculation). Running a neighbour search for each star particle at every dynamical timestep is highly computationally expensive and would dominate the run-time of the code at low redshift, so we instead choose coarser steps for the feedback. Initially, each feedback step has length $t_{8M_\odot}/50$, where $t_{8M_\odot}$is the lifetime of an $8\ \mathrm{M}_\odot$star [1]. When the age of the stellar population passes $t_{8M_\odot}$, the feedback steps lengthen to $100\ \mathrm{Myr}$, still short enough to model the release of mass and energy from type Ia SNe and AGB stars. In practice, feedback products are distributed at probabilistically selected dynamical timesteps, such that the average interval between them is the feedback step. For type II SNe, for instance, the probability of a feedback event is:

$$p_{\mathrm{II}} = \frac{\int_{\mathrm{t}}^{t+\Delta t} \mathrm{r_{II}(t')dt'}}{\int_{\mathrm{t}}^{t_0+\Delta t_{\mathrm{II}}} \mathrm{r_{II}(t')dt'}} \tag{3.11}$$

where, Δt is the dynamical step, Δt_{II} is the type II step, t_0 is the time of the last feedback event and $r_{\mathrm{II}}(t)$ is the SNe type II rate at time t. When p_{II} exceeds a randomly generated number between zero and one, the mass, metal and energy output expected over the interval Δt_{II} are shared equally among neighbouring gas particles and p_{II} is set to zero for the remainder of the feedback step. Δt is almost always much shorter than Δt_{II}, but is explicitly limited to a maximum of $\Delta t_{\mathrm{II}}/2$ to ensure the validity of Eqn. 3.11. We assume an energy per SN (type II or Ia) of 10^{51} erg s^{-1}. Lifetimes and yields from Portinari et al. (1998) are used to compute $r_{\mathrm{II}}(t)$ as well as the quantities of mass, metals and energies returned in each feedback event. Yields due to mass loss from low and intermediate mass stars are taken from Marigo (2001).

3.2.4 Supernovae Winds

The perennial problem with the distribution of stellar feedback energy in cosmological hydrodynamical simulations has been that the star-forming gas that receives the energy

[1] $t_{8M_\odot} \sim 40$ Myr at solar metallicity

is dense enough to radiate it away before it can have any dynamical effect (Katz et al., 1996a). This is likely to be a consequence of the inability to resolve the detailed structure of the ISM (e.g., Dalla Vecchia & Schaye, 2008; Ceverino & Klypin, 2009). We employ a commonly used technique to circumvent this limitation, which consists of imparting kinetic energy to gas particles directly (e.g., Navarro & White, 1993; Mihos & Hernquist, 1994; Springel & Hernquist, 2003). The velocity we choose to give gas particles that receive SNe energy is motivated by observations that suggest that large scale outflows have velocities that scale with the circular velocity of their host galaxies (Martin, 2005). As a proxy for the host halo's circular velocity, which is computationally expensive to calculate for each particle on-the-fly, we use the local one-dimensional velocity dispersion, determined from neighbouring dark matter particles. This quantity is strongly correlated with the maximum circular velocity, $v_{\rm max}$, in a way that does not evolve with redshift (Okamoto et al., 2010). The mass loading (mass per unit star formation rate) of the wind follows from energy conservation:

$$\eta = \left(\frac{\sigma}{\sigma_0} \right)^{-2} \tag{3.12}$$

where $\sigma_0 = 217 \ \mathrm{kms}^{-1}$ for our choice of IMF and assuming that *all* of the available feedback energy drives winds. This prescription results in a wind speed that increases as the halo grows and hence in a mass loading that is highest at early times. This scaling has been shown to give a much better match to the luminosity function of the Milky Way satellites than models that use a constant wind velocity (Okamoto et al., 2010).

One further addition to the model is needed to ensure that SNe driven winds act as intended. Dalla Vecchia & Schaye (2008) showed that standard kinetic feedback is more effective in low mass galaxies, where wind particles tend to drag neighbouring gas out with them. In high mass galaxies on the other hand, the pressure of the ISM can be sufficient to prevent much of the mass in the wind from escaping. Since we wish to be able to prescribe the mass loading and wind velocity directly, we choose to decouple wind particles from the hydrodynamic calculation for a short time in order to allow them to escape the high density star forming regions. When the density has fallen to $n_{\rm H} = 0.01 cm^{-3}$, the particles feel the usual hydrodynamic force again. A second condition exists to recouple wind particles after a time $10\mathrm{kpc}/\mathrm{v}_{\rm wind}$, though we note that the former criteria is usually satisfied first.

When a gas particle receives SNe energy from a neighbouring star particle, the wind speed ($v_{\rm w}$) is obtained from the local velocity dispersion and then the particle is assigned a probability to be added to the wind:

$$p_{\rm w} = \frac{\Delta Q}{\frac{1}{2} m_{\rm sph} v_{\rm w}^2}, \tag{3.13}$$

where ΔQ is the total feedback energy received by the gas particle and $m_{\rm sph}$ is the current mass of the SPH particle. Note that an SPH particle's mass may increase if it receives mass from SNe or AGB stars in neighbouring star particles, or decrease if it spawns a new star particle, which has a mass of half the original gas particle mass. If $p_{\rm w}$ exceeds unity, that is, if there is energy available in excess of that needed to add the particle to the wind, then the extra energy is distributed to the gas particle's neighbours as an increase in internal energy. This procedure is then repeated as necessary until $\Delta Q \leq \frac{1}{2} m_{\rm sph} v_{\rm w}^2$ for all gas particles and the probabilities recomputed with the new values of ΔQ. The direction in which wind particles are propelled is chosen at random to be parallel or anti-parallel to the vector $(\mathbf{v_0} - \overline{\mathbf{v}}) \times \mathbf{a}_{\rm grav}$ where $\mathbf{v_0}$ is the velocity of the gas particle before it receives feedback energy, $\mathbf{a}_{\rm grav}$ is the gravitational acceleration vector, pointing approximately to the local potential minimum (halo centre) and $\overline{\mathbf{v}}$ is the bulk velocity of the halo, which we approximate on-the-fly by computing the mean velocity of the gas particle's dark matter neighbours. The result of this treatment is a wind launched preferentially along an object's rotation axis (Springel & Hernquist, 2003).

In combination with the modelling of the hydrodynamic and gravitational interactions in GADGET-3, the treatment of the key baryonic processes described above allow our code to track the formation of galaxies, from the early universe to the present day, in realistic cosmological environments. In the next section we describe the initial conditions chosen to (re-)simulate the formation of MW-mass galaxy in a cosmological environment.

3.3 Halo Selection and Initial Conditions

The halo we choose to simulate is one of the six selected for the Aquarius project described in Springel et al. (2008b), halo 'Aq-C' in their labelling system. These haloes were extracted from a cosmological simulation in a cube of comoving volume $(100h^{-1}{\rm Mpc})^3$ and were chosen to have masses close to that of the Milky Way ($\sim 10^{12}$ M$_\odot$) and avoid

Table 3.1 Numerical parameters and characteristics of the three different resolution simulations: dark matter and gas particle masses, the gravitational softening parameter(ϵ) at $z = 0$ and the number of DM and gas particles within the virial radius at $z = 0$.

	$\mathrm{M_{DM}[M_\odot]}$	$\mathrm{M_{gas}[M_\odot]}$	$\epsilon_{\mathrm{phys}}[\mathrm{pc}]$	$N_{\mathrm{DM}}(r < r_{\mathrm{vir}})$	$N_{\mathrm{gas}}(r < r_{\mathrm{vir}})$
Aq-C-4	2.6×10^5	5.8×10^4	257	5,221,824	673,341
Aq-C-5	2.1×10^6	4.7×10^5	514	658,557	106,192
Aq-C-6	1.7×10^7	3.7×10^6	1028	82,062	15,154

dense environments [no neighbour exceeding half its mass within $1h^{-1}$ Mpc][](Navarro et al., 2010). Of the Aquarius haloes, Aq-C was selected for Aquila based on preliminary low resolution simulations that suggested it was the most likely to host a low bulge-to-total galaxy at $z = 0$. It also has the least late-time merger activity and forms half its mass by $z = 3$, 1σ earlier than the median for MW-mass galaxies in the cosmological Millennium II simulation (Boylan-Kolchin et al., 2010).

As in Aquarius, we employ a zoomed resimulation technique, with higher mass boundary particles used to model the large scale potential and lower mass particles in a $\sim 5h^{-1}$Mpc region surrounding the target halo. Extra power is added to the initial particle distribution on small scales in the high resolution region, as described by Frenk et al. (1996). We assume a ΛCDM cosmology, with parameters $\Omega_{\mathrm{m}} = 0.25$, $\Omega_\Lambda = 0.75$, $\Omega_{\mathrm{b}} = 0.045$, $\sigma_8 = 0.9$, $n_{\mathrm{s}} = 1$ and $H_0 = 100h\mathrm{kms}^{-1}\mathrm{Mpc}^{-1} = 73\mathrm{kms}^{-1}\mathrm{Mpc}^{-1}$.

The highest resolution realisation of halo C in Aquarius had a dark matter particle mass of 1.4×10^4 $\mathrm{M_\odot}$. However, the extra computational time associated with hydrodynamic simulations makes such a resolution impractical; our highest resolution instead corresponds to a dark matter particle mass of $\sim 2.6 \times 10^5$ $\mathrm{M_\odot}$ and an initial gas particle mass of 5.8×10^4 $\mathrm{M_\odot}$. In order to conduct convergence studies, we also simulate the halo at two lower resolutions, with particle masses ~ 8 and ~ 64 times larger. We adopt the same naming convention as Springel et al. (2008b), labelling the three runs (in order of decreasing resolution) Aq-C-4, Aq-C-5 and Aq-C-6. Table 3.1 lists the numerical parameters of each simulation. Note that the softening parameter, ϵ, is a physical value, used after $z = 3$; before that epoch ϵ is held fixed in comoving coordinates. In the next section we consider the first results from these three simulations, focussing in particular on the effects of varying the resolution.

3.4 First Results

Initial results from the level four, five and six simulations revealed that several important bulk properties of the main galaxy were sensitive to numerical resolution. In this section we briefly describe the resolution dependence and discuss which aspects of our implementation may be responsible for it. We refer to these initial set of simulations with a subscript *i* (Aq-C-$4_{\rm i}$ etc.), in order to distinguish them from similar runs introduced later in this chapter. The initial conditions are identical to those described in the previous section and the parameters employed are those listed in Table 3.1. Note that throughout this and subsequent chapters we use $r_{\rm vir}$ to refer to the galacto-centric radius enclosing a sphere of mean density $200\rho_{\rm crit}$, which we treat as the extent of the halo and $r_{\rm gal}$ =$0.1r_{\rm vir}$ which we treat as the extent of the central baryonic galaxy disk and bulge.

3.4.1 Resolution Dependent Properties

The most obvious manifestation of resolution dependent behaviour in the code is the difference in the $z = 0$ (stellar) morphology in Aq-C-$4_{\rm i}$, Aq-C-$5_{\rm i}$ and Aq-C-$6_{\rm i}$, illustrated by Fig. 3.1. While a clear disk component exists at level six, the level five galaxy is more bulge dominated and the level four galaxy is close to a pure spheroid, with only a small disk visible in the edge-on projection. We can roughly quantify these differences by measuring the bulge-to-total-ratio (B/T) of the main stellar object. First, we compute the distribution of orbital circularities (ϵ) for stars, with the definition used by Scannapieco et al. (2009): orbits

$$\epsilon = j_z/j_{\rm circ}(r), \tag{3.14}$$

where j_z is the angular momentum of a particle in the z direction (defined by the net angular momentum of all baryons within $0.1r_{\rm vir}$) and $j_{\rm circ}(r)$ is the angular momentum of a circular orbit at the same radius.

B/T can be estimated by assuming the bulge has no net angular momentum, such that the distribution of its orbital circularities is symmetric about zero. In this case the bulge mass is equal to twice the counter-rotating mass, which yields $\rm B/T$ =0.85,0.61 and 0.42 for Aq-C-$4_{\rm i}$, Aq-C-$5_{\rm i}$ and Aq-C-$6_{\rm i}$ respectively. The bulge mass in the lowest resolution is also approximately equal to the total mass in the highest resolution, suggesting

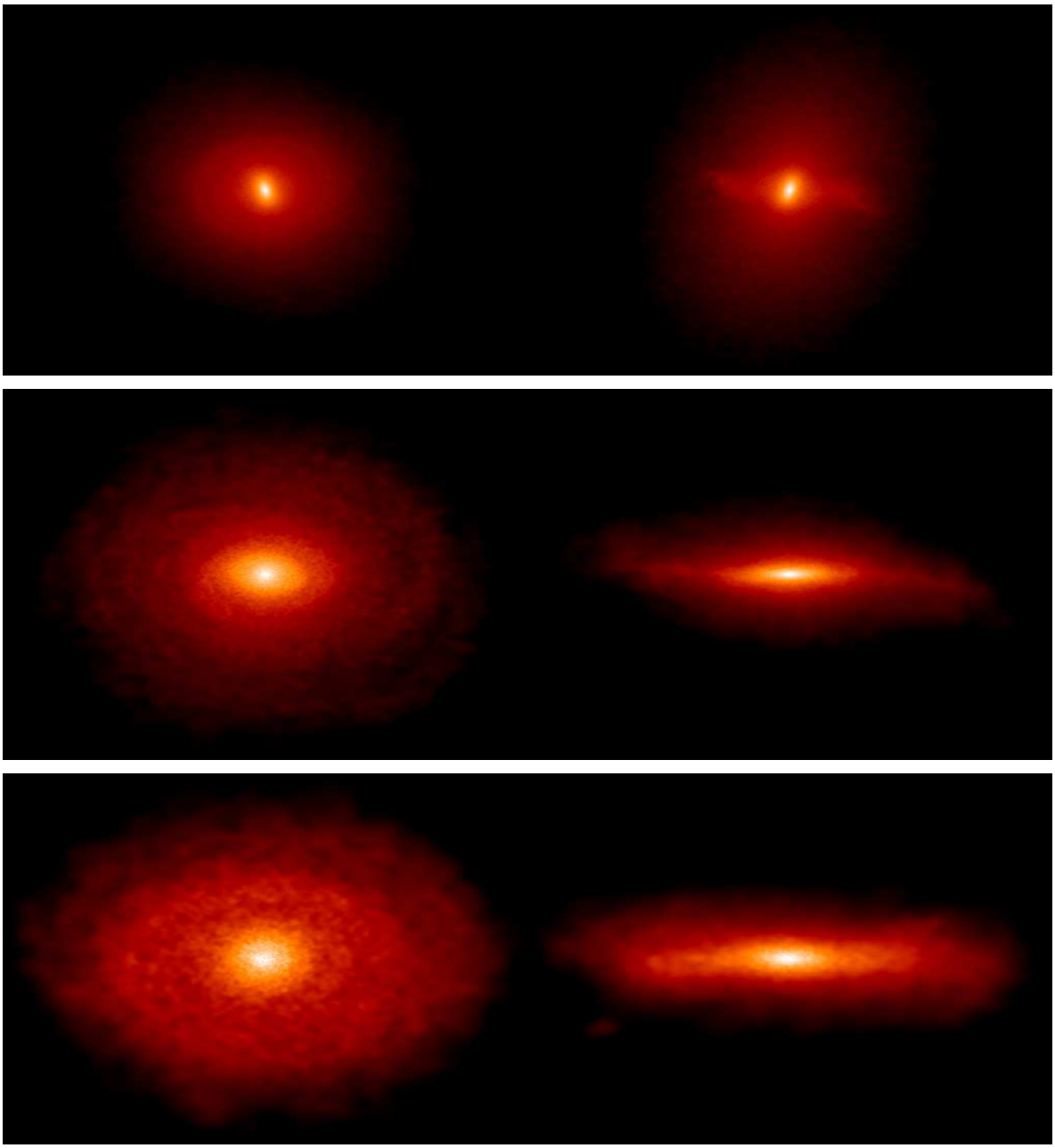

Figure 3.1 Maps of the stellar mass density of the central galaxy in Aq-C-4_i (top row), Aq-C-5_i (centre row) and Aq-C-6_i (bottom row), in face on (left column) and edge-on (right column) projections. Each image is projected through a cube of 40 kpc on a side.

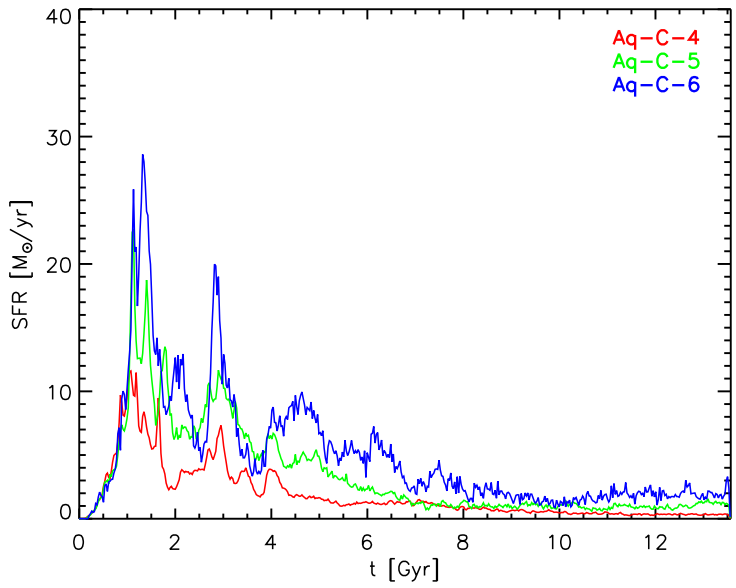

Figure 3.2 A histogram of the stellar ages of stars within $0.1r_{\rm vir}$ at $z = 0$ in the Aq-C-$4_{\rm i}$ (red), Aq-C-$5_{\rm i}$ (green) and Aq-C-$6_{\rm i}$ (blue) simulations, interpreted as a star formation rate. Note that since all stars found in the main galaxy at $z = 0$ are included, satellites that are yet to merge with the main progenitor contribute to the star formation rate at high redshift.

that it may be only disk formation that is inhibited as the resolution is increased. The difference in total stellar mass, approximately a factor of two between different resolutions, is reflected in the star formation histories (SFHs), shown in Fig. 3.2. In fact, we plot a histogram of the stellar ages of stars within $0.1r_{\rm vir}$ at $z = 0$, meaning that star formation that took place in non-main-branch progenitors before they merged is also included.

At higher resolution, the early bursts of star formation, which are associated with a number of low-mass-ratio mergers, are of smaller magnitude and tend to have shorter duration. Even in episodes of more quiescent star formation, the "equilibrium" rate is consistently lower over the entire formation history of the galaxy. In particular, after $\sim z = 1.7$, (t $= 4$Gyr), the mean SFR in the Aq-C-$4_{\rm i}$ is reduced by around a factor of two and four with respect to Aq-C-$5_{\rm i}$ and Aq-C-$6_{\rm i}$, consistent with the lack of disk growth evident in Fig. 3.1. The reason for this lower star formation efficiency is made clear in Fig. 3.3, where we plot the baryon fraction $(f_{\rm b})$ within $r_{\rm vir}$. Following the first major burst of star formation, $f_{\rm b}$ declines much more steeply at higher resolution, generating

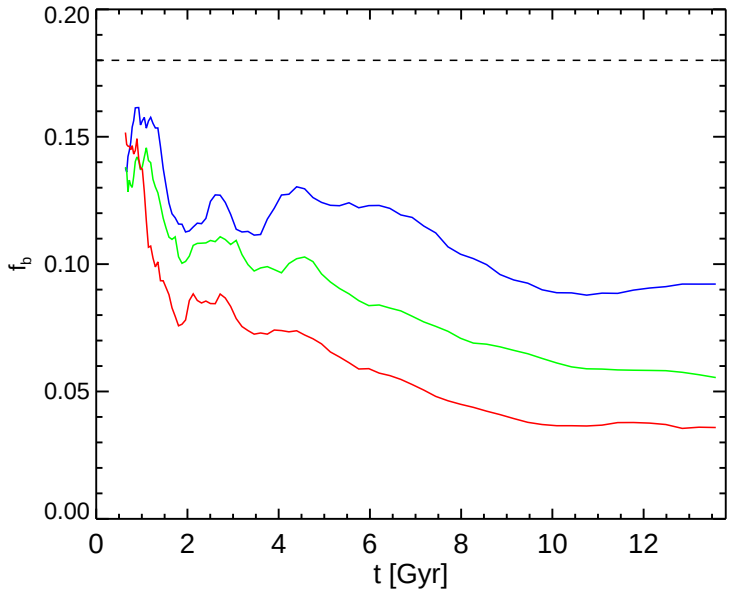

Figure 3.3 The evolution of the baryon fraction within $r_{\rm vir}$ at $z = 0$ in Aq-C-$4_{\rm i}$ (red), Aq-C-$5_{\rm i}$ (green) and Aq-C-$6_{\rm i}$ (blue). The cosmic baryon fraction, $\Omega_{\rm b}/\Omega_{\rm m}$, is indicated by a horizontal dashed line.

large deviations between the three realisations from an early epoch. The only mechanism in the model that can reduce $f_{\rm bar}$ in this way (at least in haloes with a virial temperature $\gtrsim 10^4$ K) is the removal of gas by SNe feedback. Since, less stellar mass forms in Aq-C-$4_{\rm i}$, SNe winds must be significantly more efficient than at lower resolution in order to displace a larger baryonic mass.

There are a number of reasons why more gas might escape the halo as the resolution is increased. It could be that the distribution of initial velocities given to gas particles changes, such that a greater fraction have ($v > v_{\rm esc}$), or that more mass is put into the wind. However, neither of these possibilities is supported by Fig. 3.4, in which we plot the distribution of mass as a function of initial wind velocity for all particles added to the wind over a $\sim 50{\rm Myr}$ interval, beginning at $z \sim 5$. This epoch is chosen to be close to the peak of the first starburst event. There is a small offset in the velocity distribution as the resolution changes, but in the opposite sense necessary to explain the discrepancy. In fact, the lower mean $v_{\rm wind}$ (and hence $\sigma_{\rm DM}$) in Aq-C-$4_{\rm i}$ may simply reflect the additional mass lost from the halo already by this epoch with respect to the lower resolutions. The integral under the curves also reveals the total mass added to the wind over this interval,

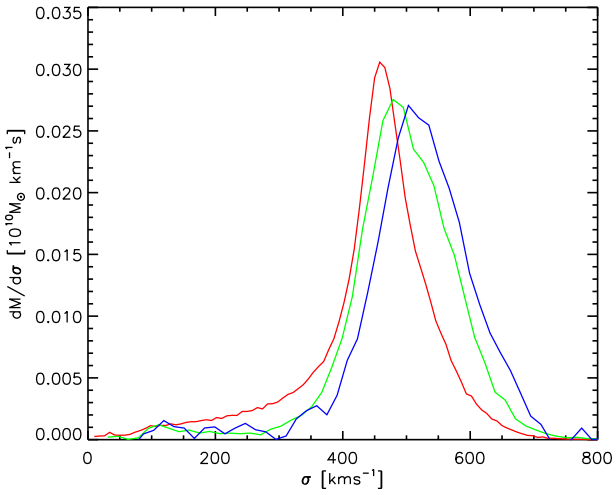

Figure 3.4 The distribution of mass put into the wind as a function of wind velocity over a ~ 50 Myr interval, beginning at $z \sim 5$. Red, green and blue curves show the distributions for Aq-C-$4_{\rm i}$, Aq-C-$5_{\rm i}$ and Aq-C-$6_{\rm i}$ respectively. Note that the integral under each curve gives the total mass added to the wind over this interval.

which is clearly very similar at each resolution. We have checked that this scenario also applies at other redshifts.

A more subtle explanation could be that there is a difference in the *effective* mass loading with resolution. After wind particles are re-coupled hydrodynamically, they interact with gas immediately outside the main galaxy, such that its properties could affect the ability of the wind to escape, or change how much material is dragged out of the halo along with the wind particle itself. In the next section we implement a modification to the code designed to minimise any effects of this nature.

Although the *initial* properties of the wind to appear agree relatively well, it is clear from the differences in the baryon fractions that the net outflow rate increases with the resolution. In fact, we find that having re-coupled, wind particles tend to escape to much larger radii at higher resolution, making re-accretion of ejected gas is less likely. This is demonstrated in Fig. 3.5, where we select all particles put into the wind at $z = 5$ and plot their radial distribution at $z = 3, 1, 0.5$ and 0. The values of $f_{\rm esc}$, labelled in each plot show the fraction of the tracked wind particles that are found outside $r_{\rm vir}$ at each epoch. At progressively later times, the differences between the distributions becoming more pronounced; more than half of the particles have escaped to $> 3r_{\rm vir}$ in Aq-C-$4_{\rm i}$ by

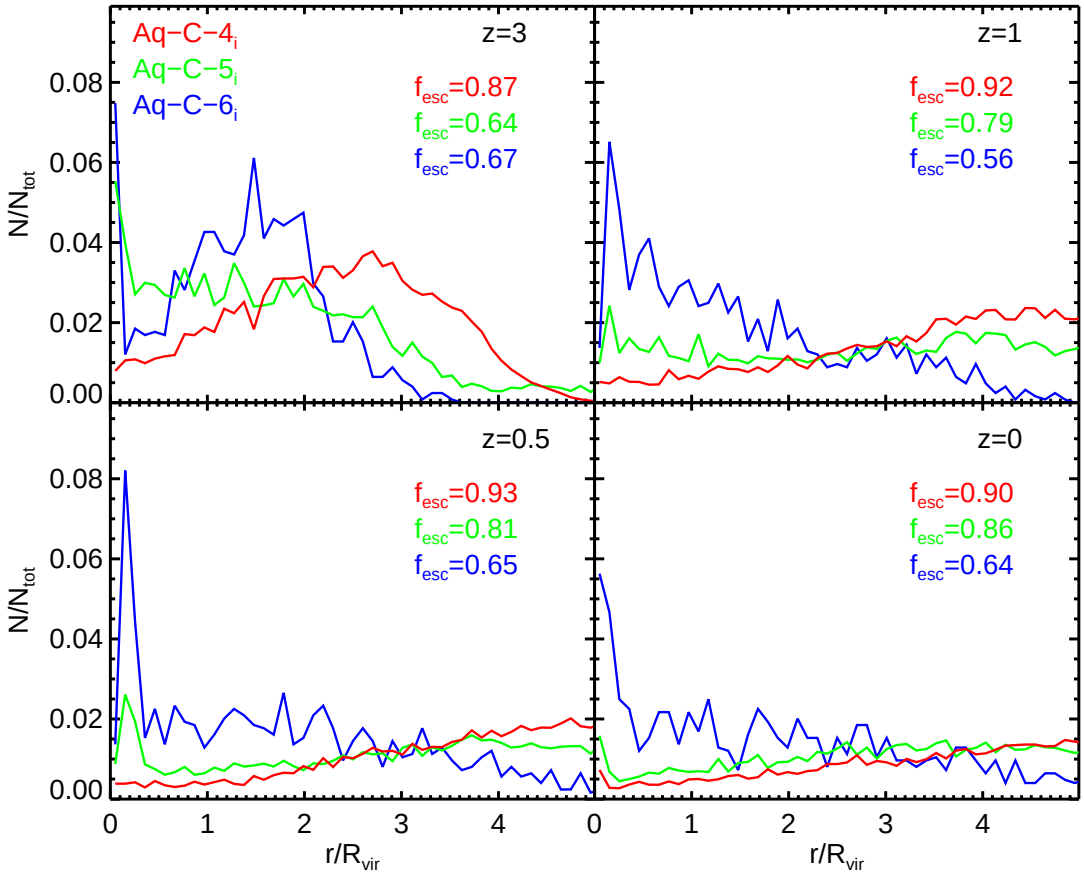

Figure 3.5 The radial distribution of wind particles ejected around $z = 5$, identified at $z = 3$ (top left panel), 1 (top right), 0.5 (bottom left) and 0 (bottom right). The Aq-C-$4_{\rm i}$, Aq-C-$5_{\rm i}$ and Aq-C-$6_{\rm i}$ runs are represented by red, green and blue curves respectively. Labels indicate the fraction of the sample outside the virial radius ($f_{\rm esc}$) at that epoch

$z = 1$, compared to ten to twenty percent in Aq-C-$6_{\rm i}$. In Aq-C-$6_{\rm i}$ and to some extent Aq-C-$5_{\rm i}$, wind particles fall back into the inner parts of the halo between $z = 1$ and $z = 0$, contributing to the formation of the disk, but this re-accretion is almost entirely absent in Aq-C-$4_{\rm i}$. We find a similar situation for several different choices of initial epoch.

We return to these issues in the next section, where several modifications to the code are described that substantially improve its convergence properties. First though, we consider one further aspect of resolution dependence, which may itself explain why the ability of the wind to escape the halo depends on resolution.

3.4.2 Cold Cloud Formation

The $z = 0$ half-mass radius of stars in the halo ($r < r_{\rm vir}$) is found to be much larger than observed for the MW at all three resolutions and also increase substantially with resolution, from 8.5 kpc in Aq-C-$5_{\rm i}$ to 10.5 kpc in Aq-C-$4_{\rm i}$. This increase is caused by a population of stars that form in cold clouds of gas, outside the main gas disk, which increase in abundance dramatically as the resolution increases. Note that these structures should not be confused with the cold clouds that form part of our star formation prescription, which are assumed to exist on much smaller, unresolved, scales. References to *cold clouds* throughout this section should be taken to mean resolved gas structures in the outer part of the halo, typically consisting of a few hundred gas particles in Aq-C-$4_{\rm i}$ ($M \sim 10^6 - 10^7$ M$_\odot$). While it is possible that these clouds represent a real physical phenomenon, associated with scales only just resolved in the level 4 simulation, there is no evidence for any such structure in real galaxies. They are more massive than the majority of observed molecular cloud complexes ($M \sim 10^5 - 10^6$ M$_\odot$) and certainly too numerous at those masses to be identified with the high velocity clouds seen outside the plane of the Galaxy (e.g. Wakker & van Woerden, 1997). In addition, their existence leads to an unrealistically large amount of star formation at large Galacto-centric radii, dwarfing the total mass contributed by the MW's stellar halo. We conclude that the cold clouds are a numerical artifact, generated by some aspect of the modelling process. In this subsection, we describe their defining characteristics and investigate how they form.

The development of the clouds is tracked in Fig. 3.6, which shows the projected gas density in Aq-C-$4_{\rm i}$ at z=8,7,6 and 5.5. Gas ejected by supernovae feedback can be seen flowing out of the main galaxy; note that winds are approximately isotropic at these

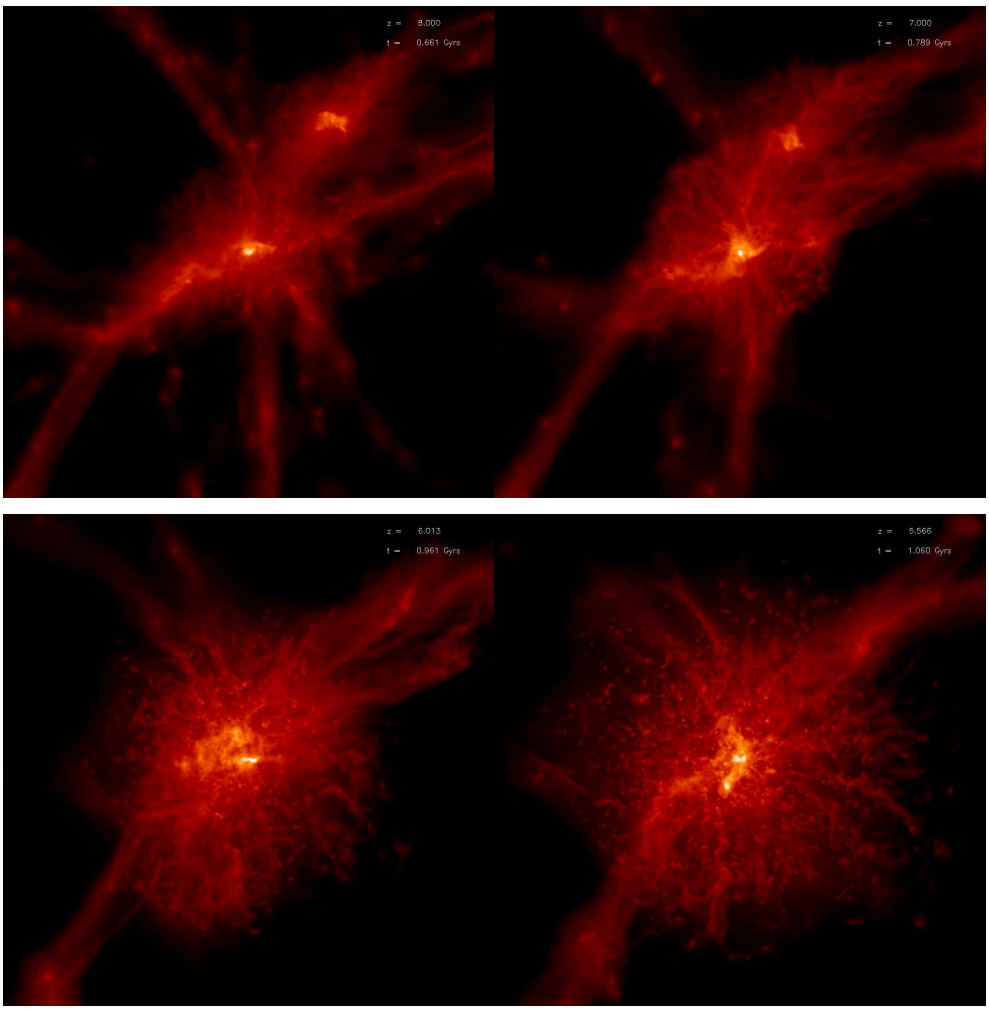

Figure 3.6 Four images of the projected gas density in Aq-C-4_i , at z=8 (top left),7 (top right), 6 (bottom left) and 5.5 (bottom right) tracking the formation of cold clouds. The images are projected through a cube of 50 kpc on a side. Brighter colours correspond to higher gas surface densities.

early times since the disk is not well defined. The axis of rotation of the main object runs roughly from the top left to bottom right of each panel, but at such high redshift the disk is not well defined and hence the axial direction chosen preferentially for winds is not easily identified in these images. The filamentary structure which can be seen clearly at $z = 7$ is a precursor to the clouds and begins to form immediately after the first significant star formation in the central galaxy.

The much clumpier distribution of halo gas at high resolution may explain why wind particles find it easier to escape the halo. The clouds have a relatively small filling factor and contain a large fraction of the gas surrounding the main galaxy, such that the remaining halo gas is lower density than the average in Aq-C-$5_{\rm i}$ and Aq-C-$6_{\rm i}$. Hence outflows encounter less resistance and are able to reach much larger radii, reducing the fraction of wind particles that re-accrete and form a disk at late times.

The clouds are not associated with any dark matter substructure. We can hence estimate the fraction of the total stellar mass forming in clouds by measuring the local dark matter overdensity around newly formed star particles ($\delta_{\rm DM}$). The local density is computed as the SPH kernel weighted sum over the nearest 40 dark matter neighbours and the overdensity is quoted relative to the global dark matter density. In Fig. 3.7 we plot a histogram of $\delta_{\rm DM}$ for stars forming inside $r_{\rm vir}$ over a ~ 100 Myr interval beginning at $z = 5$. Note that the plot is not normalised by the particle mass in each case, it is simply the number of wind particles created. In all three cases, the majority of stars form in regions of high $\delta_{\rm DM}$, corresponding to subhaloes and the central regions of the main galaxy. As the resolution increases, a low $\delta_{\rm DM}$ population, corresponding to star formation in cold clouds, becomes more prevalent. If we assume that an overdensity of ten can be used to divide the two modes of star formation, we find that clouds account for around four percent of the total star formation in Aq-C-$5_{\rm i}$ and ~ 15 percent in Aq-C-$4_{\rm i}$.

An additional consequence of star formation in clouds is that feedback energy is imparted at larger radii, on average, as the resolution is increased. Winds launched from further out in the halo, where the escape velocity is lower, are more likely to be ejected entirely. This effect may exacerbate the resolution dependence of the bulk galaxy properties seen in our first results, by removing more material from the halo at higher resolution. However, we find this effect is less important than those discussed in the previous subsection.

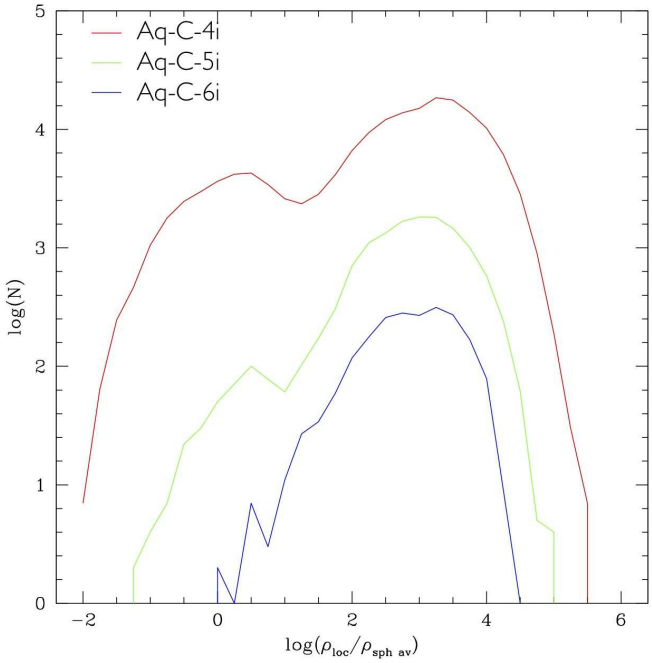

Figure 3.7 Histograms of the dark matter overdensity ($\delta_{\rm DM}$) associated with stars forming in Aq-C-$4_{\rm i}$ (red), Aq-C-$5_{\rm i}$ (green) and Aq-C-$6_{\rm i}$ (blue) over a 100 Myr interval beginning at $z = 5$. Note that the number of particles in each bin are shown, rather than total mass. Local dark matter densities are computed using the masses of the nearest 40 dark matter neighbours weighted by the SPH kernel and the overdensity is quoted relative to the mean cosmic dark matter density.

The images in Fig. 3.4, as well as the timing of the emergence of the first clouds (shortly after the earliest significant star formation) hint at their formation mechanism. We find that cloud formation is in fact triggered by winds particles - gas that receives kinetic energy as part of our SNe feedback prescription. The first phase of the process is the generation of filaments and shell-like structures around the main galaxy, which are associated with the outflows. Having been ejected from the central few kpc and on reaching a sufficiently low density, wind particles are hydrodynamically recoupled and begin to drag neighbouring gas with them towards the outer parts of the halo. While many of the wind particles associated with the first star formation escape the halo, a fraction fall back in, impeding the progress of wind particles following them. With still more gas joining the outflow further in, the material is compressed, forming the filaments and shells. These structures are locally Jeans unstable and begin to fragment and collapse into clouds, although at lower resolution the fragmentation appears to be suppressed to varying degrees by the gravitational softening (recall that $\epsilon \sim 0.5$ and ~ 1.0 kpc at level five and level six respectively). The SPH smoothing length is also larger, reducing the density contrast associated with the shell structures and further suppressing cloud formation at lower resolution.

The elements necessary to facilitate cloud formation appear to be i) a (kinetic) wind model that involves a (short) period of decoupling and ii) a large amount of gas surrounding the main galaxy. At early times, the role of ii) is filled by re-accreting wind particles, but later on a quasi-static hot halo forms, which slows the escape of recoupled wind particles. Rerunning the simulations with either i) or ii) missing suppresses cloud formation. For instance, turning off decoupling altogether, so that most wind particles do not escape the high density regions in the first place, leads to a far smaller number of clouds forming. Decoupling wind particles for a much longer period, such that they do not interact with gas in the outer parts of the halo at all prevents virtually all cloud formation.

While the fragmentation of the shells and filaments is a genuine physical effect, we argue that their formation in the first place is a numerical artifact. Although shells of material and even associated star formation are observed around SNe remnants, the structures in the simulation are on much larger scales. Furthermore, they may be artificially stabilised by weaknesses in the basic SPH method. The underestimation of

mixing due to the suppression of contact instabilities is a well known problem in SPH (e.g. Agertz et al., 2007; Mitchell et al., 2009) and could result in structure in the outflows being preserved over unrealistically long timescales, allowing them to fragment into clouds. Several methods to improve the treatment of contact instabilities in SPH have been proposed in the literature, one of which we implement in the next section in order to model the mixing of ejected wind particles with surrounding halo material more realistically.

3.5 Code Modifications to Improve Convergence

In this section we describe a number of modifications to the model described in section 3.2. The aims of theses changes are twofold; firstly to address the resolution dependence of the mass of baryons ejected from the halo in winds and secondly to prevent the formation of the spurious cold clouds and their associated star formation, which as we have shown, may well be related issues.

3.5.1 Wind Particle Selection

Although our wind model is designed to "kick" a constant mass of neighbouring gas particles with the available SNe energy, regardless of resolution, we find that it breaks down when star forming regions are poorly resolved. Only EoS particles are eligible to be added to the wind, which can have the effect of reducing the mass loading in lower resolution simulations, where more of the energy is imparted thermally to non-EoS neighbours. To avoid this, we allow all gas receiving energy from Type II SNe to be added to the wind. This unfortunately also increases the runtime of the code, since many additional neighbour searches have to be run to determine the dark matter velocity dispersion and hence wind velocity for each gas particle, but the measure is necessary to ensure a resolution independent mass loading. A second, related change is that type Ia feedback energy is always imparted as thermal energy in the new implementation.

3.5.2 Timestep Limiter

Another possible origin for resolution dependent behaviour is a variation in the *effective* mass loading of the wind. This includes gas that the wind particle drags out of the

halo with it that have not received SNe energy directly. The effective mass loading may be underestimated if gas particles with which the wind interacts are on much longer timesteps (as is frequently the case, due to their relative velocities) and do not have the opportunity to react hydrodynamically to its presence. Since the time step hierarchy in GADGET-3 must vary with resolution, it is possible that the effective mass loading will too. To ensure that wind particles interact properly with the gas they encounter, we implement a particle timestep limiter similar to that proposed by Saitoh & Makino (2010). When an SPH particle finds neighbours with timesteps $\geq$4 times its own, they are moved to shorter timesteps where possible. Moving more particles onto shorter timesteps also increases code runtime, but may be necessary to to model kinetic SNe feedback correctly.

3.5.3 Artificial Conductivity

As discussed in the previous section, the formation of the shells and filaments that eventually fragment to form spurious cold clouds may be promoted by the suppression of mixing between outflows and halo material (which can be a hot halo, or previous generations of wind particles). Price (2008) argue that SPH underestimates mixing due to a mismatch between density, which is continuous across fluid interfaces and entropy, which is not. This leads to "pressure blips" that act to keep fluids of different entropy separated and suppress the formation of Kelvin-Helmholtz and Rayleigh-Taylor instabilities. To improve the modelling of mixing in the code, we implement an *artificial conductivity* similar to that suggested by Price (2008), which adds a thermal diffusion term to the SPH equations, smoothing out the entropy across boundaries. In principle, this should allow the structures associated with outflows to break down naturally, suppressing the formation of clouds.

3.5.4 A Resolution Dependent Star Formation Threshold

The final change to the model concerns our choice of star formation density threshold. Motivated by the desire to suppress spurious star formation associated with the clouds, we opt to scale the star formation density threshold with resolution. For irradiated primordial gas, with an approximately isothermal density profile, halving the gravitational softening increases the maximum density that can be resolved by a factor of four. Based

on this consideration, we increase the threshold in the level five and level four runs from $\mathrm{n_H} = 0.1\ \mathrm{cm}{-}3$ to 0.4 and $1.6\ \mathrm{cm}^{-3}$ respectively. Note that the density at which wind particles recouple $n_{\mathrm{H,rec}} = 0.01\ \mathrm{cm}^{-3}$ does *not* change with resolution; allowing it to do so significantly affects the efficiency of the winds.

Using a version of the code in which all four of the above modifications were implemented, we re-ran the level four, five and six simulations of Aq-C. In the next section we analyse the new level four simulation in detail and assess the extent to which the modifications improve convergence.

3.6 The Formation of a Milky Way-Mass Galaxy

Aq-C-4 represents one of the highest resolution *ab-initio* hydodynamical simulations of a MW-mass galaxy ever completed. In this section we study its formation history and properties at $z = 0$, with the aim of giving a general overview in preparation for the more detailed analyses presented in Chapters 4 and 5. For those properties found to show poor convergence in our initial runs, we compare to similar intermediate and low resolution simulations (Aq-C-5 and Aq-C-6), which were also run with the code modifications described in the previous section. In the following, we will focus purely on the model's theoretical predictions rather than comparing to observational data, which we defer until Section 3.7.

3.6.1 Galaxy Morphology

We begin by considering the morphology of the galaxies formed at each resolution, which was seen to vary substantially in the initial simulations runs. In Fig. 3.8, we show face-on and edge-on images of the stars (left column) and gas (right column) in the Aq-C-4 , Aq-C-5 and Aq-C-6 simulations (top to bottom). The stellar component varies much less with resolution than in the initial runs and a clear disk component is apparent in all three cases. Using the procedure described in Section 3.4.1 to obtain B/T, we find values of 0.44,0.52 and 0.46 for Aq-C-4 , Aq-C-5 and Aq-C-6 respectively. Note that the thickness of the disk is limited by both the gravitational softening and the Jeans length of star-forming gas, which decreases with resolution thanks to the higher star formation thresholds. Even in Aq-C-4 these effects lead to a disk that is dynamically hotter than

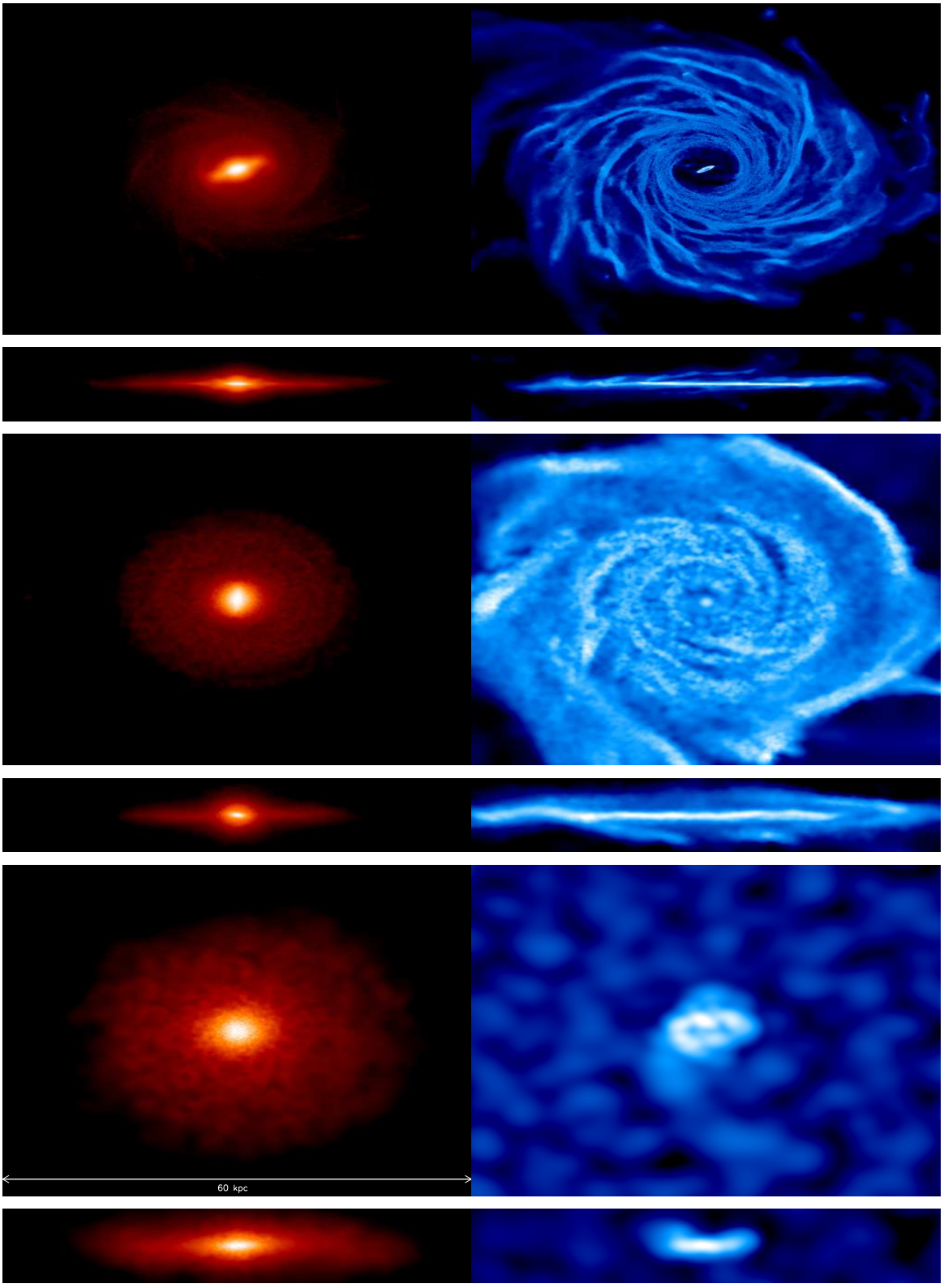

Figure 3.8 Face-on and edge-on maps of the projected stellar mass density (left column) and projected gas mass density (right column) of the central galaxy in Aq-C-4 (top row), Aq-C-5 (centre row) and Aq-C-6 (bottom row). Face-on images have physical size 60 kpc $\times$ 60 kpc, edge on images are 60 kpc $\times$ 13 kpc.

those observed in typical spirals by some margin. This is inevitably true in any hydrodynamical simulation employing a sub-grid model for star formation, since the dynamics of star-forming gas (at $\sim 10^4$ K or greater in our case, due to the enforced equation of state) are not representative of gas cooling in molecular clouds. Spiral structure is resolved in Aq-C-4 , along with a bar, which is also visible to some extent in Aq-C-5 . The gas disks of Aq-C-4 and Aq-C-5 are of similar size, although much more detail of the spiral structure is resolved in the higher resolution case. The gas density is also much lower in the inner few kpc, in the vicinity of the bar. Bars are expected to channel gas into the central regions of galaxies (Shlosman et al., 1989), where it can accrete onto the central black hole (not included in our models) or form stars in a burst. In Aq-C-6 however the gas distribution is very different. There is still a flattened disk, but of ~ 6 times smaller radius and significantly lower mass.

3.6.2 Star Formation and Mass Evolution

The star formation histories of the galaxies, shown in Fig. 3.9, also show good agreement over the three resolution levels, with starbursts of very similar duration and magnitude. Fig. 3.9 in fact shows histograms of the ages of stars within $0.1r_{\rm vir}$ at $z = 0$, hence at high redshift it includes star formation in progenitors that are yet to merge. The second and third bursts at around 3 Gyr and 6 Gyr are associated with accretion events while the first and most significant is driven by a number of gas-rich mergers at $z > 4$. Disk stars are mostly formed in the quiescent period after $\mathrm{t} = 4$ Gyr, $z \sim 1.6$.

The baryon fraction retained by the halo, plotted in Fig. 3.10, also shows much better convergence. Although at $z = 0$ it remains the case that the high resolution simulation has lost the greatest baryonic mass, the discrepancy is greatly reduced relative to our initial simulations and the trend is not maintained at higher redshift. In fact the behaviour after $t \sim 9$ Gyr is qualitatively different in Aq-C-4 , where $f_{\rm bar}$ continues to decline, as opposed to the small increases seen in Aq-C-5 and Aq-C-6 . Our wind prescription results in the halo having just less than a third of the global baryon fraction at $z = 0$.

In Fig. 3.11 we decompose the mass evolution of the halo ($\mathrm{r} < r_{\rm vir}$, left panel) and galaxy ($\mathrm{r} < 0.1r_{\rm vir}$, right panel) into the contributions from dark matter (black curve), stars (cyan), cold gas (blue) and hot gas (red). The halo mass in cold gas is remarkably stable all the way back to $z = 5$, implying that newly cooled gas roughly balances that

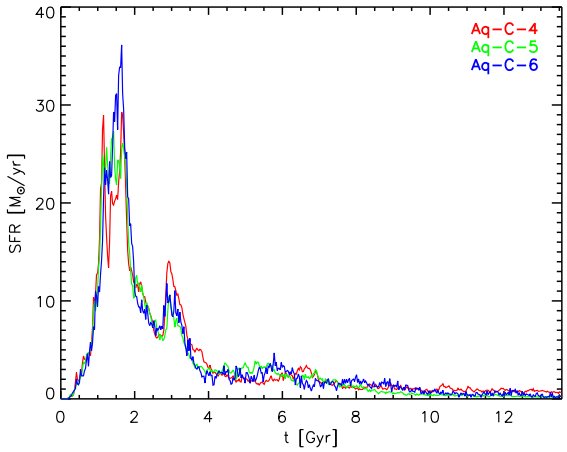

Figure 3.9 A histogram of the stellar ages of stars within $0.1r_{\rm vir}$ at $z = 0$ in Aq-C-4 (red), Aq-C-5 (green) and Aq-C-6 (blue), interpreted as a star formation rate. Since the histogram includes all stars found in the main galaxy at $z = 0$, the rate at high redshift can include a contribution from satellites that are yet to merge with the main progenitor.

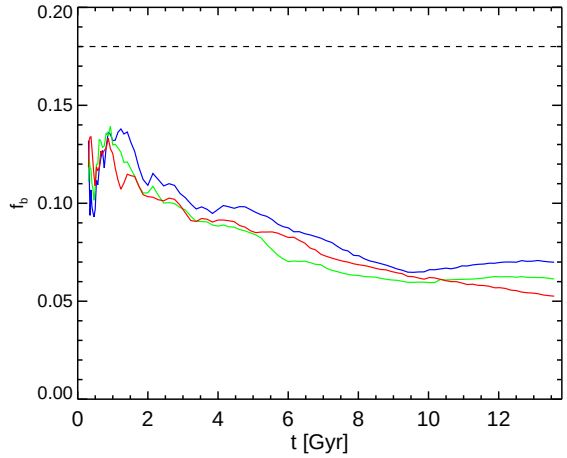

Figure 3.10 The evolution of the baryon fraction within $0.1r_{\rm vir}$ at $z = 0$ in Aq-C-4 (red), Aq-C-5 (green) and Aq-C-6 (blue). The cosmic baryon fraction, $\Omega_{\rm b}/\Omega_{\rm m}$, is indicated by a horizontal dashed line.

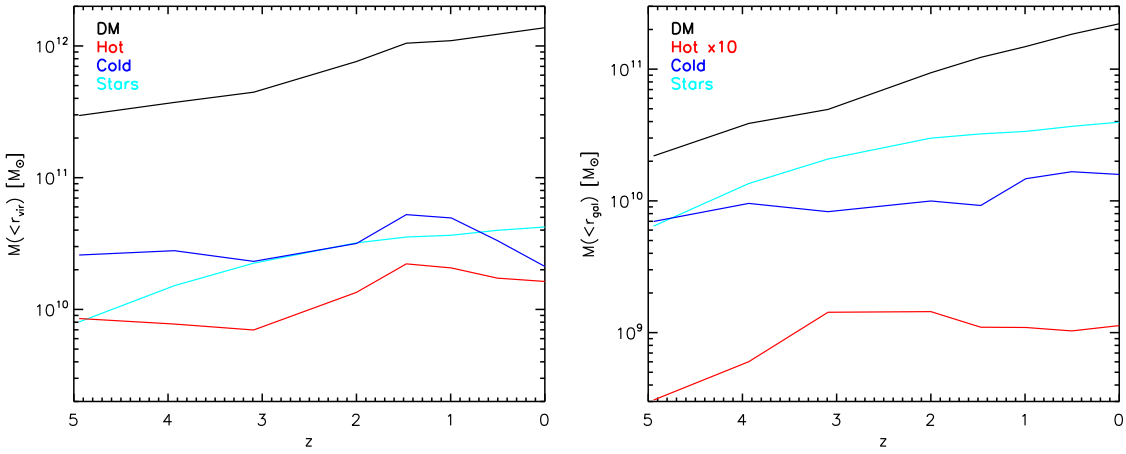

Figure 3.11 The evolution of the mass in dark matter (black), hot gas (red), cold gas (blue) and stars (cyan) within $r_{\rm gal}$= $0.1r_{\rm vir}$ (left panel) and $r_{\rm vir}$ (right panel). Note that the hot gas mass in the right panel is multiplied by a factor of ten in order to reduce the plot range.

used up in star formation and ejected by SNe. The hot gas content also does not change significantly, increasing by a factor of two or so since $z = 3$. As we will show in Chapter 5, this increase tracks the formation of a quasi-static hot halo around the galaxy which provides the bulk of the fuel for star formation at low redshift. Cold baryons however dominate at all epochs, accounting for $\sim$ 80 percent of all baryons at $z = 5$ and $>$ 90 percent at $z = 0$. Within $r_{\rm gal}$, dark matter remains the dominant component of the mass and the baryon fraction falls from $\sim$ 40 percent at $z = 5$ to around 25 percent at $z = 0$. The galaxy's baryonic component becomes progressively more dominated by stars at low redshift, but an appreciable fraction of cold gas ($\sim$ 30 percent) remains at the final time. We note that the total stellar mass at $z = 0$ is 4.2×10^{10} $\rm M_{\odot}$, somewhat lower than the value of $6.4 \pm 0.6 \times 10^{10}$ $\rm M_{\odot}$ estimated for the MW (McMillan, 2011). Hot gas represents only a tiny fraction of the total mass within the galactic radius at all epochs (note that the mass is scaled up by factor of ten in Fig. 3.11). Given the short cooling time at these radii, it may be that this small amount is maintained by outflowing wind particles thermalising their kinetic energy immediately outside the disk.

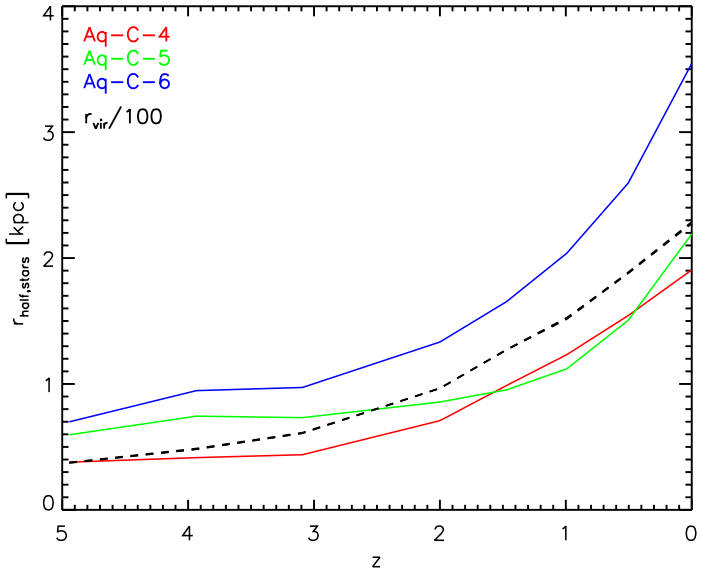

Figure 3.12 The evolution of the half stellar mass radius in Aq-C-4 (red), Aq-C-5 (green) and Aq-C-6 (blue) since $z = 5$. Also plotted for reference is the virial radius scaled down by a factor of 100.

3.6.3 Size Evolution

In our initial set of simulations, the stellar half-mass radius ($r_{\rm h,stars}$) was seen to vary significantly and systematically with resolution, as a result of star formation associated with cold clouds of gas outside the main galaxy disk at higher resolution. In Fig. 3.12 we plot $r_{\rm h,stars}$ for each resolution level. Though a difference with resolution remains, it is in the opposite sense to that seen in out initial runs and is likely explained by size of the gravitational softening in each case. In level six, forces are fully Newtonian on a scale of 3 kpc at $z = 0$ (2.8 times the softening parameter, ϵ), so the magnitude of $r_{\rm h,stars}$ is almost certainly affected. The level four and five values agree to within twenty percent at the final time, suggesting that level five is just sufficient to resolve $r_{\rm h,stars}$. We note that all three values are significantly lower than those found in the initial runs, which is expected given that cold cloud formation is now suppressed. Also plotted in Fig. 3.12 is $r_{\rm vir}$, scaled down by a factor of a hundred. We find that the growth of $r_{\rm h,stars}$ approximately tracks that of $r_{\rm vir}$, particularly after $z = 2$.

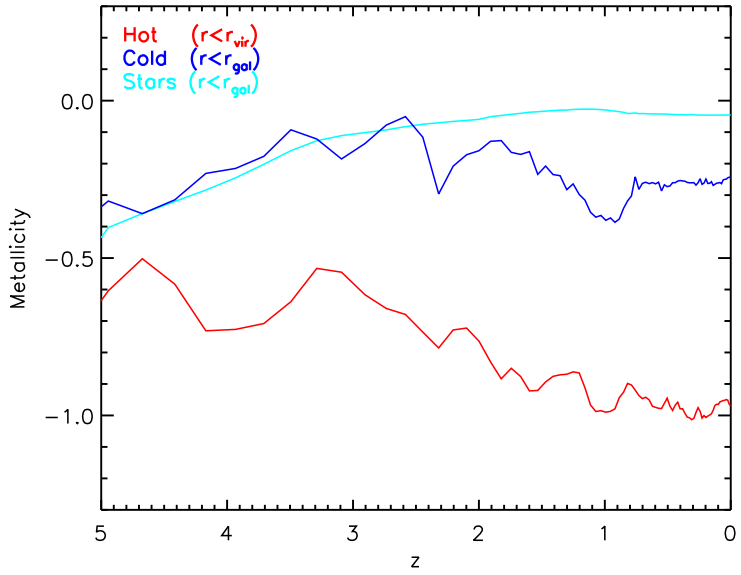

Figure 3.13 The evolution in the mean metallicities of hot gas within $r_{\rm vir}$ (red) and of cold gas (blue) and stars (cyan) within $r_{\rm gal}$= $0.1r_{\rm vir}$ in Aq-C-4 .

3.6.4 Chemical Evolution

As described in Section 3.2, our code tracks the stellar synthesis and distribution by SNe of several individual elements. In Fig. 3.13 however, we simply plot the mean metallicity of baryons in the Aq-C-4 halo, to give an overview of how chemical enrichment proceeds. Metallicity is defined in the conventional way, taking the logarithm of the mass fraction in elements heavier than Hydrogen normalised to the solar value, which we assume to be 0.02. Note that the plot includes cold gas and stars within $r_{\rm gal}$, but hot gas within $r_{\rm vir}$. The mean stellar metallicity rises rapidly during the first burst of star formation, which ends around $z = 3$. It then rises more gradually before eventually declining slightly after $z = 1$ when the bulk of disk stars are forming. The existing stellar population of approximately solar metallicity appears to be diluted by stars forming from less enriched cold gas. The cold gas tracks the stellar metallicity up to $z \sim 2.5$ before declining in two relatively rapid episodes. This could be the result of more metal-rich gas being ejected preferentially by SNe, or an influx of primordial gas cooling onto the galaxy, but it is not clear why either mechanism would only become important after $z = 3$.

3.6.5 Density Profiles

As we argued at the beginning of this chapter, a key advantage of numerical simulations and zoomed re-simulations in particular is that they provide detailed spatial and kinematic information about the galaxy formation process. In the following subsections, we show how the radial distribution of mass builds up over time and how the chemical and dynamical properties of the halo change.

In Fig. 3.14 we show the spherically averaged density profiles of dark matter, hot gas, cold gas and stars at six different epochs, indicated by the labels in each panel. The dashed lines in each panel indicate the profiles at $z = 0$. The inner dark matter profile evolves very little, with halo growth proceeding inside-out, as seen previously in N-body simulations (Helmi et al., 2003; Wang et al., 2011). There is, however, a discernible flattening of the inner few kpc since $z = 3$, which is likely caused by the expulsion of gas from the central SNe. The inner ~ 2 kpc at $z = 0$ are stellar dominated and there is a clear "hole" in the cold gas distribution (also clearly visible in the upper right panel of Fig. 3.8), which may be caused by the stellar bar channelling gas into the centre after $z = 1$. The slight increase in the stellar density in the central ~ 1.5 kpc after $z = 1$ is consistent with this scenario. Most of the hot gas found near the centre of the halo at high redshift has cooled by $z = 1$, but it is the dominant component beyond 100 (60) kpc at $z = 2$ ($z = 0$). The inner stellar distribution has a power law slope of -3.5 to -4 at early times, which becomes shallower at low redshift with the formation of the disk. From $z = 0.5$ onwards, the transition between the disk and the stellar halo is visible as a change in slope from ~ -3 to ~ -4. We consider the density profile and formation of the stellar halo in detail in Chapter 5.

3.6.6 Metallicity Profiles

In Fig. 3.15 we plot spherically averaged metallicity profiles for cold gas and stars within $r_{\rm gal}$ and hot gas within $r_{\rm vir}$. The metallicity of each shell is computed as the logarithm of the total mass fraction of metals in that shell normalised to the solar value, rather than the average of the individual metallicities of all particles in the shell. The enrichment of gas by star formation in the central galaxy leads to negative gradients in all three components at all epochs, with the exception of the hot gas at $z = 5$ and $z = 3$.

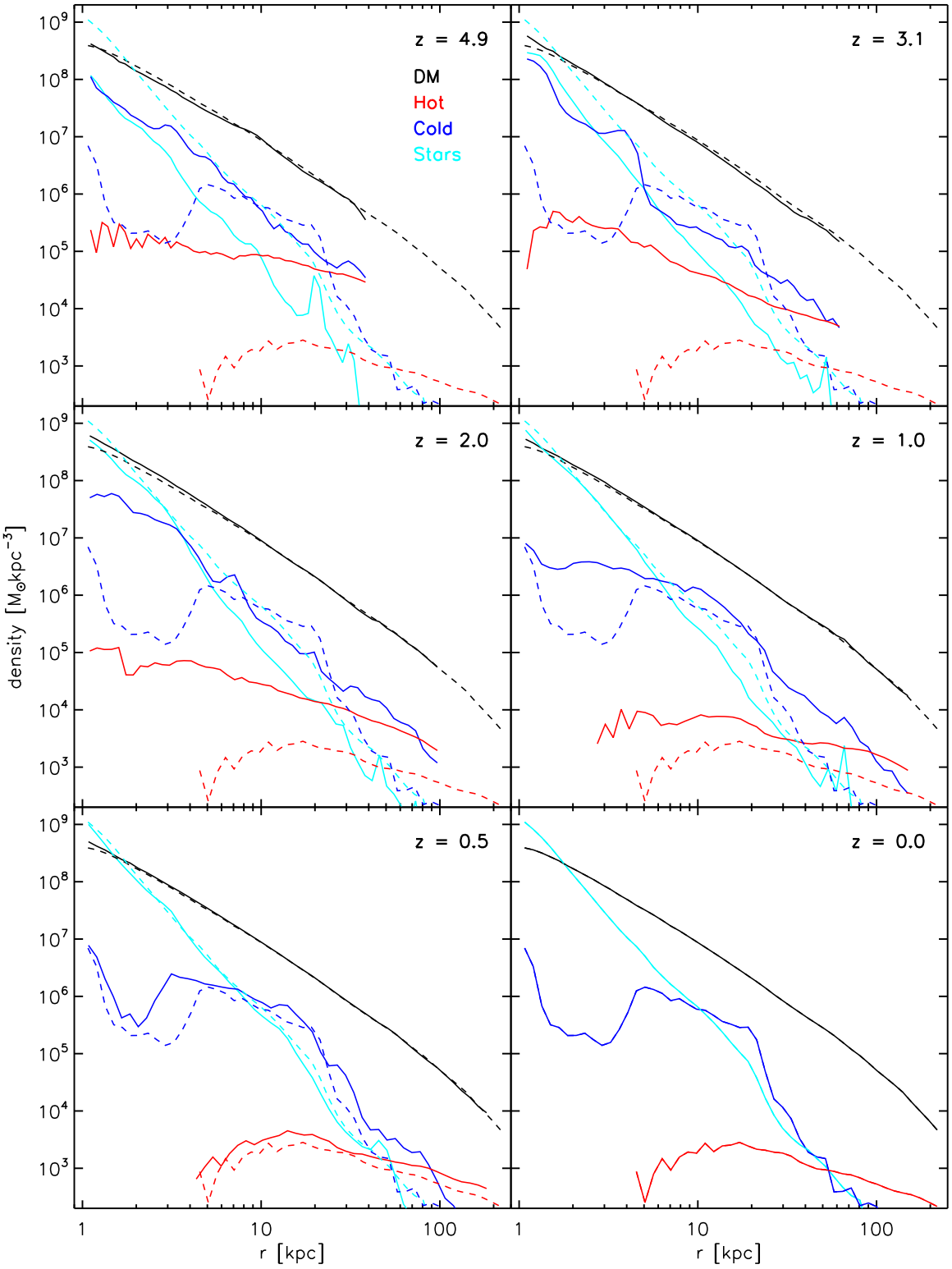

Figure 3.14 Spherically averaged density profiles of dark matter (black), hot gas (red), cold gas (blue) and stars (cyan) in Aq-C-4 at six different redshifts, as indicated by the label in each panel. Profiles extend to the virial radius at each redshift. In each panel, dashed lines show the $z = 0$ profiles for the individual components.

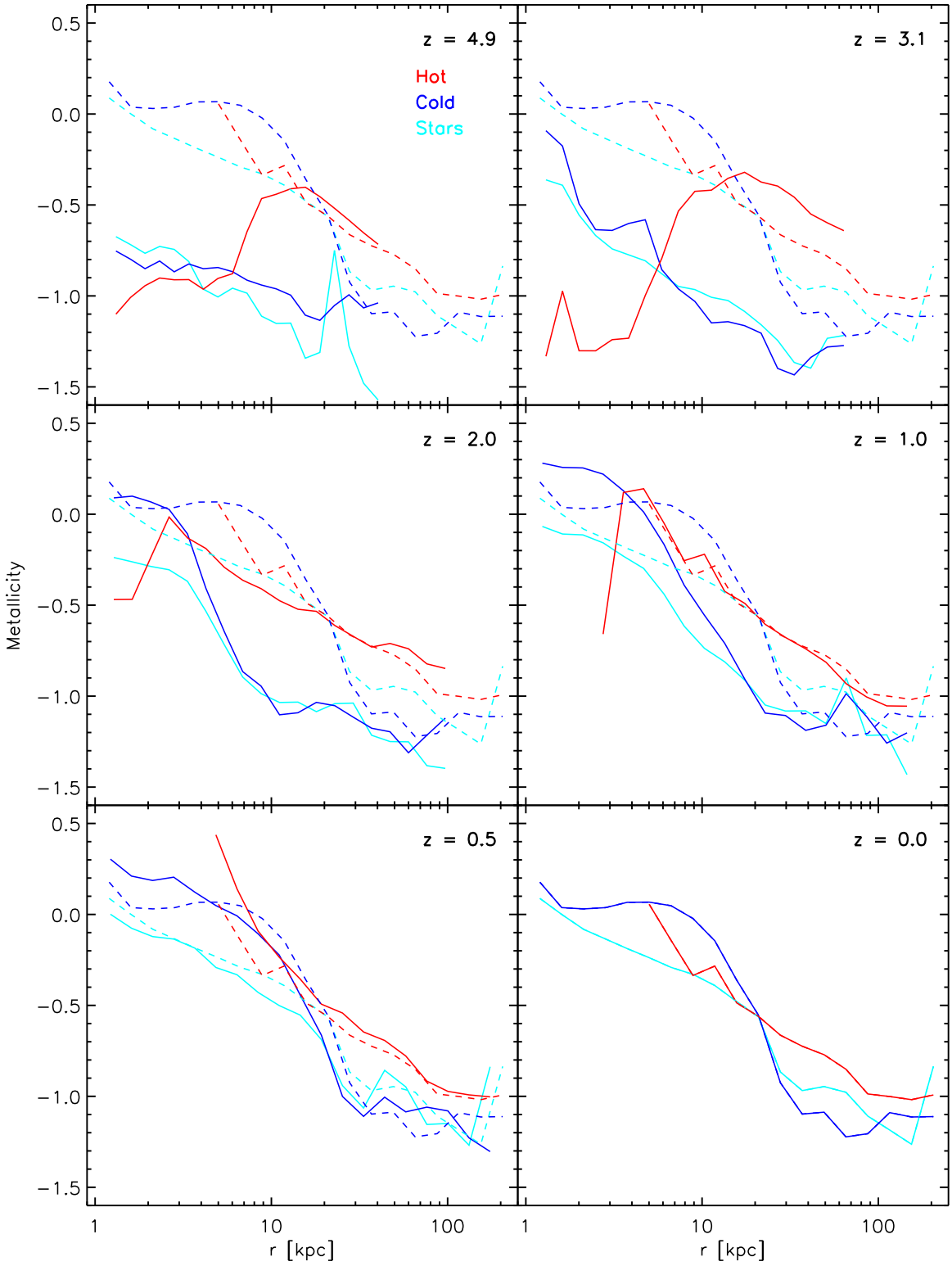

Figure 3.15 Spherically averaged metallicity profiles for hot gas (red), cold gas (blue) and stars (cyan) in Aq-C-4 at six different redshifts, as indicated by the label in each panel. Profiles extend to the virial radius at each redshift. In each panel, dashed lines show the $z = 0$ profiles for the various components.

In Fig. 3.14, the stellar mass assembly of the inner few kpc ("bulge") was shown to be more or less complete by $z = 1$, which is consistent with the lack of late-time evolution in the central metallicity seen here. The formation of disk stars and their enrichment of the cold gas takes mostly takes place after $z = 1$. At first sight, the metallicity profiles of cold gas and stars seem inconsistent with the mean metallicities within the galactic radius, plotted in Fig. 3.13 (-0.05 and -0.25 at $z = 0$ respectively). However, this simply reflects the density profiles, which weight the mean heavily towards the value in the central two or three kpc in the case of the stars and towards the outer parts of the galactic radius in the case of cold gas, due to the "hole" associated with the bar.

3.6.7 Circular Velocity and Velocity Dispersion

In the past, hydrodynamical simulations have struggled to produce realistic rotation curves for disk galaxies, typically finding much more strongly peaked and steeply declining profiles corresponding to strongly centrally concentrated mass distributions. This is a manifestation of the well-known "angular momentum problem". The clumps that merge at high redshift to form present day galaxies have to dissipate their orbital angular momentum through dynamical friction with the dark matter halo. If a large proportion of the baryons are allowed to cool and collapse at the centre of these clumps before they merge, the remnant is left with low angular momentum, and a centrally concentrated distribution (Navarro & Benz, 1991). This suggests that the condensation of baryons in the progenitor clumps must be suppressed by, for example, stellar feedback. Stellar feedback also helps the situation by preferentially removing low angular momentum gas (Governato et al., 2010). Allowing baryons to dissipate all their energy and form dense knots of material also has the effect of dragging more dark matter into the central regions - so called adiabatic contraction (Blumenthal et al., 1986; Gnedin et al., 2004).

Recent simulations have demonstrated that realistic rotation curves can be obtained, either by using very low star formation efficiencies (Agertz et al., 2011), or through highly localised and energetic feedback (Guedes et al., 2011), which requires that the inhomogeneous structure of the ISM is resolved (at least to some extent). Our model falls into the second category, though our spatial resolution is poorer by a factor of two than the simulations of Guedes et al. (2011). Fig. 3.16 shows that the $z = 0$ rotation curve (blue) peaks at ~ 2 kpc and declines fairly gradually out to 20 kpc. In the next section, we

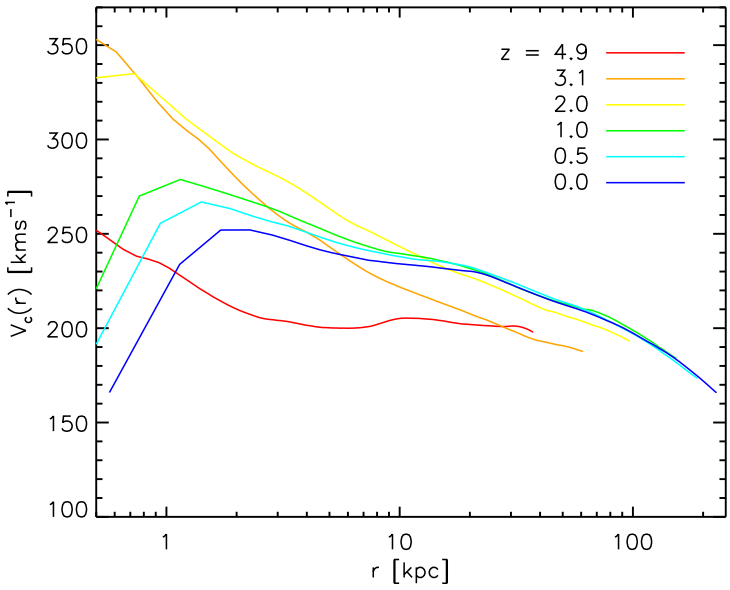

Figure 3.16 Circular velocity profiles for Aq-C-4 at six different redshifts, as indicated by the labels. Profiles extend to the virial radius at each redshift.

compare with observational data directly and demonstrate that Aq-C-5 provides a fairly good match to the rotation curve of the MW. At higher redshift, particularly at $z = 3$, after the most significant merger activity has finished, $V_{\rm c}(r)$ is much more strongly peaked, with a higher maximum value at a smaller radius, though the peak would be even more exaggerated without the influence of SNe at higher redshift. Subsequent feedback acts exactly as described above, removing much of the low angular momentum gas and preventing it being locked up in stars. The maximum circular velocity is hence reduced and the radius at which it occurs moves outwards.

In Fig. 3.17 we show the (3D) velocity dispersion profile, computed in spherical shells around the centre of the main galaxy for dark matter (black) and stars (red). As before a label in each panel indicates the redshift and the $z = 0$ profiles are shown as dashed lines. A negative gradient is apparent in both components at all epochs, although there is considerable noise in the stellar component caused by satellites and their associated streams. The early assembly of Aq-C is evident again in this figure, with the velocity dispersion of the dark matter reaching (and exceeding) its final value by $z = 2$. The central dispersion then declines slightly in the central few kpc, reflecting the "carving out" of the the baryonic core of the halo by feedback. The stellar bulge is very clearly

separated from the disk in this plot after $z = 1$. The bulge dominates within ~ 2 kpc at $z = 0$, with a dispersion of $140\ \mathrm{kms}^{-1}$. At ~ 4 kpc there is a transition to the disk component, which has a dispersion of around $75\ \mathrm{kms}^{-1}$. Outside the disk, the dispersion rises sharply again, where most stars belong to the stellar halo. We will discuss the dynamics of halo stars in more detail in Chapter 5. At most epochs there are several peaks in the profile corresponding to stars in satellites. Note that although satellites and streams represent "cold" spots locally, averaging over spherical annuli can often give a higher dispersion, due to their bulk velocity relative to the rest of the shell.

3.6.8 Angular Momentum Evolution

The evolution of the angular momenta of dark matter, stars and gas determine many important galaxy properties, including morphology, the form of the rotation curve and the size of the disk(s). In the left panel of Fig. 3.18 we track how the specific angular momenta of dark matter and hot gas within the virial radius ($|\mathbf{J}_{\mathrm{DM}}|$,$|\mathbf{J}_{\mathrm{hot}}|$) and cold gas and stars within the galactic radius ($|\mathbf{J}_{\mathrm{cold}}|$, $|\mathbf{J}_{\mathrm{stars}}|$) change over the formation history of the main galaxy. We note that $|\mathbf{J}_{\mathrm{DM}}|$ and $|\mathbf{J}_{\mathrm{hot}}|$ remain relatively constant after $z = 2$, reflecting the fact that the halo is more or less assemembled by that time. $|\mathbf{J}_{\mathrm{cold}}|$ and $|\mathbf{J}_{\mathrm{stars}}|$ continue to grow, both due to the cooling of higher angular momentum hot gas and the ejection of low angular momentum cold gas. Interestingly we find that the specific angular momentum of hot gas exceeds that of the dark matter at all epochs after $z = 4$. The difference is generated by the accretion of two gas-rich satellites. Their hot gas is ram pressure stripped and added to the main halo rapidly, but the dark matter takes longer to succumb to tidal forces, such that the the increase in $|\mathbf{J}_{\mathrm{DM}}|$ lags behind. The eventual increase is less in the case of the dark matter, possibly because some of the lower angular momentum gas is able to cool and form stars.

In the right panel of Fig. 3.18 we show how the orientations of $\mathbf{J}_{\mathrm{hot}}$, $\mathbf{J}_{\mathrm{cold}}$ and $\mathbf{J}_{\mathrm{DM}}$ evolve with redshift relative to $\mathbf{J}_{\mathrm{stars}}$. In this context, it is easy to see how disk formation could be inhibited in this halo. The stellar and cold gas disks are approximately co-planar after $z = 3$, but are nonetheless misalligned with the angular momentum of the halo for much of the time. At several points during the galaxy's evolution the existing disk becomes tilted with respect to the halo, such that it is misalligned with newly accreting gas. This is the origin of the behaviour seen at $z = 4$ to $z = 3$; a new gas disk,

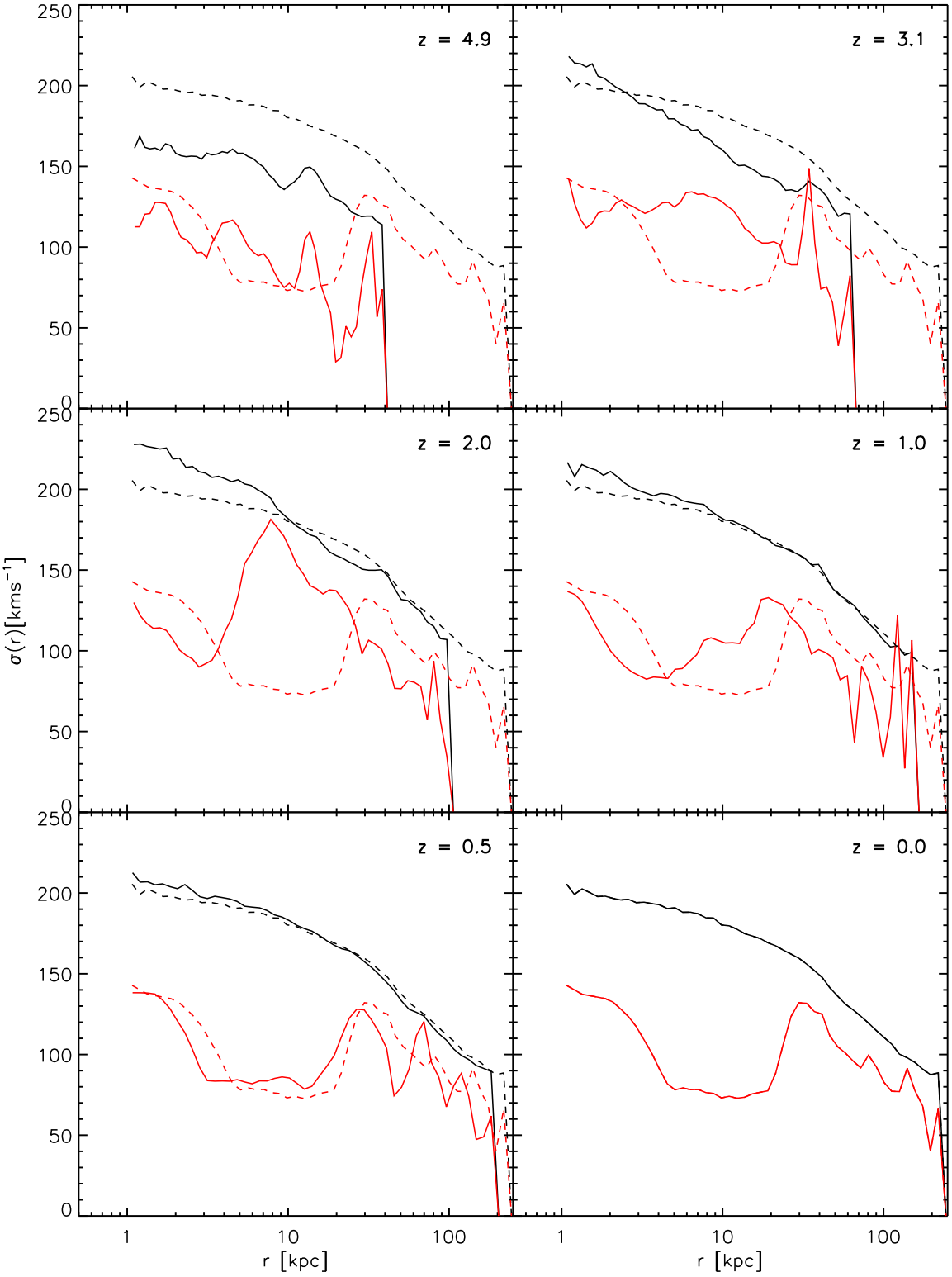

Figure 3.17 Spherically averaged 3D velocity dispersion profiles for Aq-C-4 at six different redshifts, as indicated by the label in each panel. Profiles extend to the virial radius at each redshift. In each panel, dashed lines show the $z = 0$ profile.

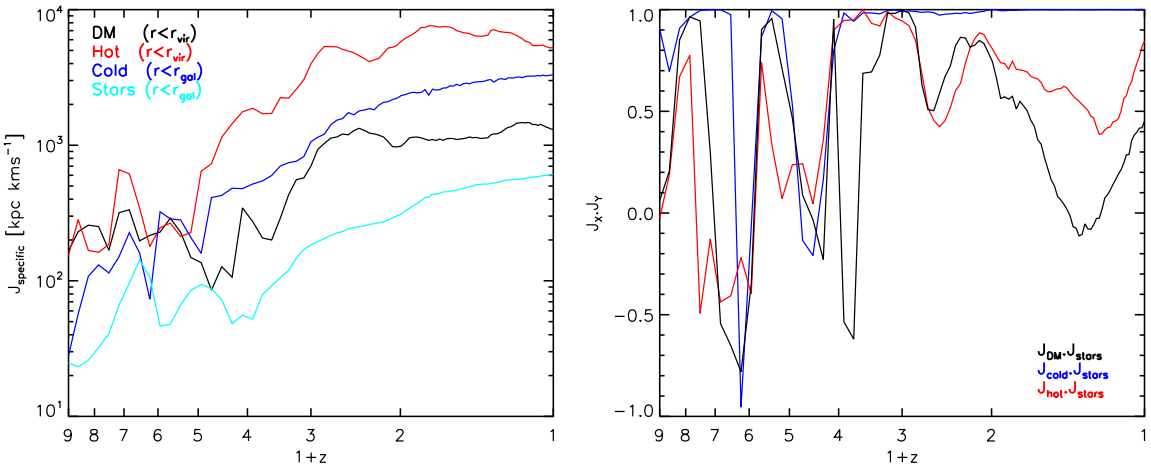

Figure 3.18 *Left Panel*: Evolution of the specific angular momenta of stars and cold gas within $r_{\rm gal}$= $0.1r_{\rm vir}$, hot gas and dark matter within $r_{\rm vir}$. *Right Panel*: The angles between the angular momentum vectors defined by stars within $r_{\rm gal}$, gas within $r_{\rm gal}$ and dark matter within $r_{\rm vir}$.

with a different orientation begins to form at $z > 4$, which eventually comes to dominate the central potential, causing the original disk to buckle and collapse. The two disks are clearly visible in images of the projected stellar and gas mass density at $z \sim 3.5$ shown in Fig. 3.19. In this instance, the initial misallignment appears to be caused by the disk being dragged towards the orbital plane of a merging satellite. The buckled disk accounts for a large fraction of the final bulge mass. After $z = 2$, a somewhat less dramatic tilt is induced by torques due to several large satellites, leading to the formation of a second, slightly misalligned, disk. The tilt is seen as an increasing misallignment between the angular momentum of the halo (accreting gas) and that of the baryonic component in Fig. 3.18. However, because the stellar mass fraction of the (sub-dominant) new disk is similar to that of the main disk, $\mathbf{J}_{\rm gas}$ and $\mathbf{J}_{\rm stars}$ change together smoothly, resulting in no detectable misallignment between them.

3.6.9 Halo Shape

Finally, we consider the evolution in the shape of the dark matter halo of Aq-C-4 and examine whether it has been altered by dissipative behaviour of the baryonic component, relative to the Aquarius dark-matter-only realisation of Aq-C. A rough estimate of the

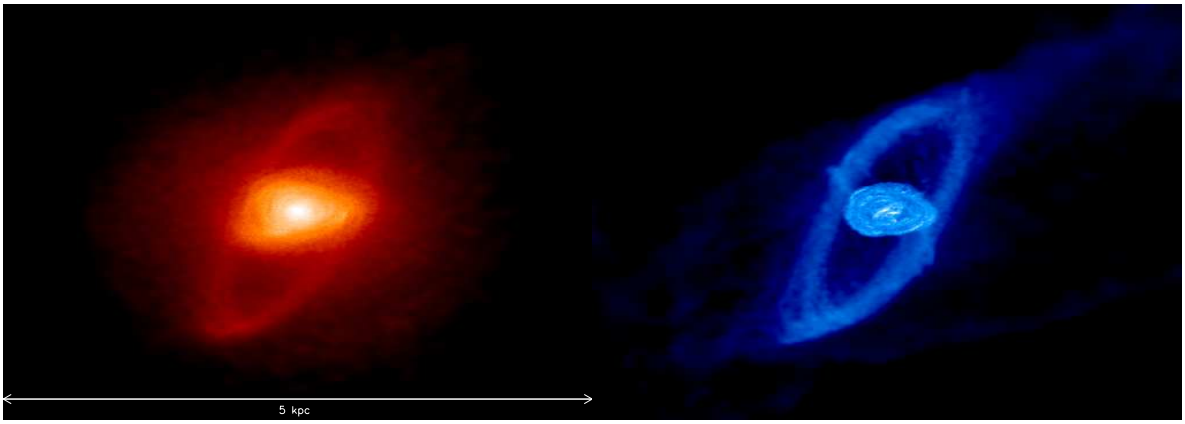

Figure 3.19 Maps of the projected stellar mass density (left panel) and gas mass density (right panel) of the central galaxy in Aq-C-4 at $z \sim 3.5$. Each image is projected through a cube 5 kpc on a side. The original (inner) disk is misalligned with respect to the angular momentum of accreting gas, such that a new disk forms with a different orientation and begins forming stars. The configuration eventually becomes gravitationally unstable, causing the central disk to buckle and collapse.

shape can be obtained by computing the moment of inertia tensor for all dark matter within $r_{\rm vir}$ and diagonalising it to obtain the principal axes. The inertia tensor is defined as

$$I_{\alpha\beta} \equiv \sum_{\rm n=1}^{N_p} m_p(\mathbf{r}_{\rm n}^2 \delta_{\alpha\beta} - r_{\rm n,\alpha} r_{\rm n,\beta}), \tag{3.15}$$

where the sum is over all $N_{\rm p}$ particles, $\mathbf{r}_{\rm n}$ is the position vector of the nth particle, α and β are the tensor indices, running from 1 to 3 and $\delta_{\alpha\beta}$ is the Kronecker delta. Assuming the halo is approximately ellipsoidal, its axis ratios are then the square root of the ratio of eigenvalues. Fig. 3.20 shows the evolution of the axis ratios since $z = 5$, where we adopt the standard notation of *a*,*b* and *c* for the major, intermediate and minor axes. At $z = 5$ the halo is fairly oblate, but it becomes steadily more spherical over time and is only mildly triaxial at $z = 0$. Both axis ratios are significantly larger than those in a dark-matter-only realisation of this halo. Vera-Ciro et al. (2011) found that $\frac{b}{a}$ ($\frac{c}{a}$) evolved from 0.35 (0.45) at $z = 3$ to 0.55 (0.7) at $z = 0$. This result is consistent with findings from N-body simulations that show galaxy disks have a circularising influence on the central potentials of dark matter haloes (Kazantzidis et al., 2010). We note, however that Vera-Ciro et al. (2011) use the reduced moment of inertia tensor to compute axis ratios,

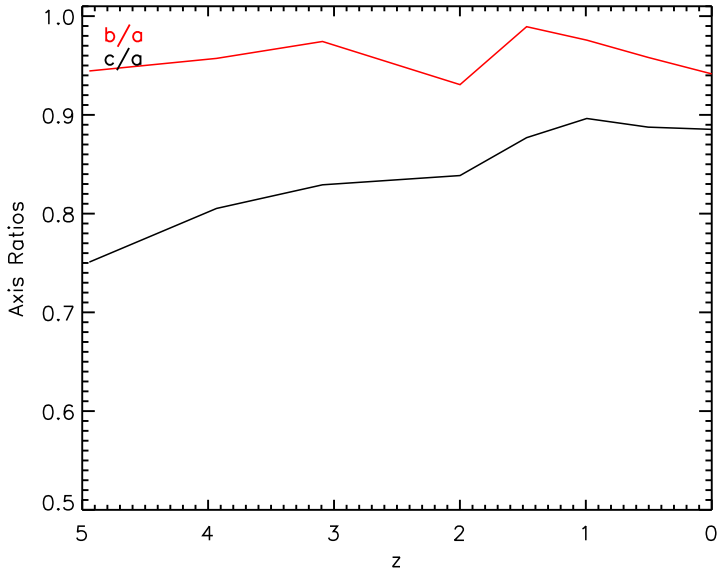

Figure 3.20 The major and minor axis ratios of the dark matter halo in Aq-C-4 , derived from the moment of inertia tensor of all dark matter within $r_{\rm vir}$.

which places less weight on the outer parts of the halo, where the distribution of matter tends to be more spherical or oblate (e.g. Frenk et al., 1988).

Having given an overview of some of the key properties of the main galaxy in Aq-C-4 , in the next section we examine the extent to which they depend on the physical processes that are modelled and the details of the numerical implementation, by considering results from several other hydrodynamics codes. We also assess how well the models are able to reproduce the observational data.

3.7 The Aquila Project

Our Aq-C-5 and Aq-C-6 simulations form part of the Aquila project, which compares results from thirteen different numerical models that use different hydrodynamical technique and prescriptions for various key physical processes. Crucially, all the simulations start from identical initial conditions (those described in Section 3.3), allowing us to directly compare the evolution of the central galaxy between codes in a common cosmological environment. Our analysis focuses in particular on the physics and modelling that promote the formation of a realistic disk; a central unresolved problem in numer-

ical simulations of galaxy formation. Details of the other codes involved in Aquila are discussed in the next subsection. Note that the majority of the results discussed here relate to level five simulations, though we also discuss level six in order to establish how resolution affects the behaviour of each code.

3.7.1 Simulation Codes

Nine simulation codes, using three different methods of hydrodynamical modelling, are involved in Aquila. Table 3.2 lists all of the codes, including the name they are commonly known by in the literature and relevant references and also provides a summary of the numerical techniques and the physics implemented in each model. There is one AMR code (**R**), a Lagrangian moving mesh code, **Arepo** and seven SPH codes. Of these, six (including our own code, **G3-TO**) are based on GADGET-3 (**G3**, **G3-CK**, **G3-CS**, **G3-GIMIC**, **G3-MM**) and one was developed independently (**GAS**). In addition to these nine *fiducial models*, there are four *additional models*, which add or vary a physical prescription relative to the corresponding reference model. These are identified by suffixes describing the variation; **G3-CR** includes stellar feedback due to cosmic ray pressure, **G3-BH** and **R-AGN** include AGN feedback and **R-LSFE** employs a lower star formation efficiency. All of the models include, in some form, treatments of a UV background, (primordial) radiative cooling and star formation.

Where available, we also include data from the semi-analytical model used by Cooper et al. (2010), which used merger trees from the Aquarius level four realisation of Aq-C. The model is almost identical to the "Durham" model (Bower et al., 2006) used in Chapter 2, but with a lower circular velocity threshold ($30\ \mathrm{kms}^{-1}$) to identify haloes in which cooling is suppressed by reionisation. Note that although several incarnations of the Durham semi-analytical model exist, we will refer to these results as the predictions of the GALFORM model.

3.7.2 Definitions and Conventions

To enable a consistent comparison between codes, we define a set of agreed definitions and conventions to be used in the analysis. The centre of the main galaxy is defined to be the potential minimum around which the most massive gravitationally bound structure exists at $z = 0$. The *virial radius* (r_{vir}) and *galactic radius* (r_{gal}) retain the definitions used

Table 3.2. Summary of the characteristics and implemented physics of codes used in the Aquila project. The first column gives the popular name for each code used in the literature, or "-" if none is used.

Code Name	Abbreviation	Reference	Type	UV background		Cooling	Feedback
			$z_{\rm UV}$	spectrum			
Gadget-3	G3	[1]	SPH	6	[10]	primordial [12]	SN (thermal)
Gadget-3	G3-BH	[1]	SPH	6	[10]	primordial [12]	SN (thermal), BH
Gadget-3	G3-CR	[1]	SPH	6	[10]	primordial [12]	SN (thermal), BH,CR
-	G3-CS	[2]	SPH	6	[10]	metal-dependent [13]	SN (thermal)
-	G3-TO	[3]	SPH	9	[11]	metal-dependent [14]	SN (thermal+kinetic)
GIMIC/OWLS	G3-GIMIC	[4]	SPH	9	[11]	metal-dependent [14]	SN (kinetic)
-	G3-MM	[5]	SPH	6	[10]	primordial [12]	SN (thermal)
-	G3-CK	[6]	SPH	6	[10]	metal-dependent [13]	SN (thermal)
GASOLINE	GAS	[7]	SPH	10	[11]	metal-dependent [15]	SN (thermal)
RAMSES	R	[8]	AMR	12	[10]	metal-dependent [16]	SN (thermal)
RAMSES	R-LSFE	[8]	AMR	12	[10]	metal-dependent [16]	SN (thermal)
RAMSES	R-AGN	[8]	AMR	12	[10]	metal-dependent [16]	SN (thermal),BH
Arepo	Arepo	[9]	Moving Mesh	6	[10]	primordial [12]	SN (thermal)

Note. — [1] Springel et al. (2008c); [2] Scannapieco et al. (2005); Scannapieco et al. (2006); [3] Okamoto et al. (2010); [4] Crain et al. (2009); [5] Murante et al. (2010); [6] Kobayashi et al. (2007); [7] Stinson et al. (2006); [8] Teyssier (2002); Rasera & Teyssier (2006); Dubois & Teyssier (2008); [9] Springel (2010); [10] Haardt & Madau (1996); [11] Haardt & Madau (2001); [12] Katz et al. (1996b); [13] Sutherland & Dopita (1993); [14] Wiersma et al. (2009a); [15] Shen et al. (2010); [16] Teyssier et al. (2011)

so far in this chapter. *The halo* will be used to refer to all mass within $r_{\rm vir}$ and *the galaxy* to all baryonic mass within a radius $r_{\rm gal}$.

Where a distinction is drawn between *hot* and *cold* gas, we adopt a temperature threshold of 10^5 K to separate the two phases. For those simulation codes which employ an effective equation of state (e.g. G3, G3-BH,G3-CR, G3-GIMIC G3-TO, Arepo), fluid elements can have an associated temperature in excess of 10^5 K, but still be star forming. To avoid counting this gas in the hot phase, we additionally specify that fluid elements with any current star formation are counted as *cold*. For analysis in which the orientation of the galactic disk is relevant, we rotate to a new coordinate system where the net angular momentum vector of galaxy stars is in the "z" direction.

3.7.3 Morphologies

We begin by considering the morphologies of the main stellar object that forms in each simulation. Fig. 3.21 shows face-on and edge-on images of the projected stellar mass density at $z = 0$ for the fiducial model of each code, with the total galactic stellar mass indicated at the bottom of image. Maps for the additional models are shown in Fig. 3.23. While all of the codes produce galaxies with clear disk and bulge components, their relative dominance varies significantly. Several of the galaxies are barred, most obviously G3-CK, G3-CS and G3-MM. There are also a large range of final stellar masses, from 4×10^{10} $\rm M_{\odot}$ (G3-TO) to 3×10^{11} $\rm M_{\odot}$ (AREPO).

To quantify the relative importance of the disk and bulge, we compute the orbital circularities of stars in each galaxy, defined relative to the net angular momentum of all stars within $r_{\rm gal}$, using the definition in Eqn. 3.14. We note that a purely rotationally supported disk would have $\epsilon = 1$, while a dispersion supported spheroidal component, with no net rotation, will form a symmetric distributions around $\epsilon = 0$. In Fig. 3.22 we plot the distribution of circularities for the fiducial models of each code, with distributions for the additional models shown in Fig. 3.23. The level five and level six simulations are represented by thick and thin lines respectively.

The circularity distributions of the level five simulations confirm the diversity of morphologies seen in Figs. 3.21 and 3.23, with several models forming dominant disks (G3-GIMIC, GAS, R, R-LSFE) and others almost pure spheroids (G3, G3-MM, G3-BH). In some case (AREPO,G3-CR, R-AGN) there are also ambiguous features around $\epsilon = 0.5$,

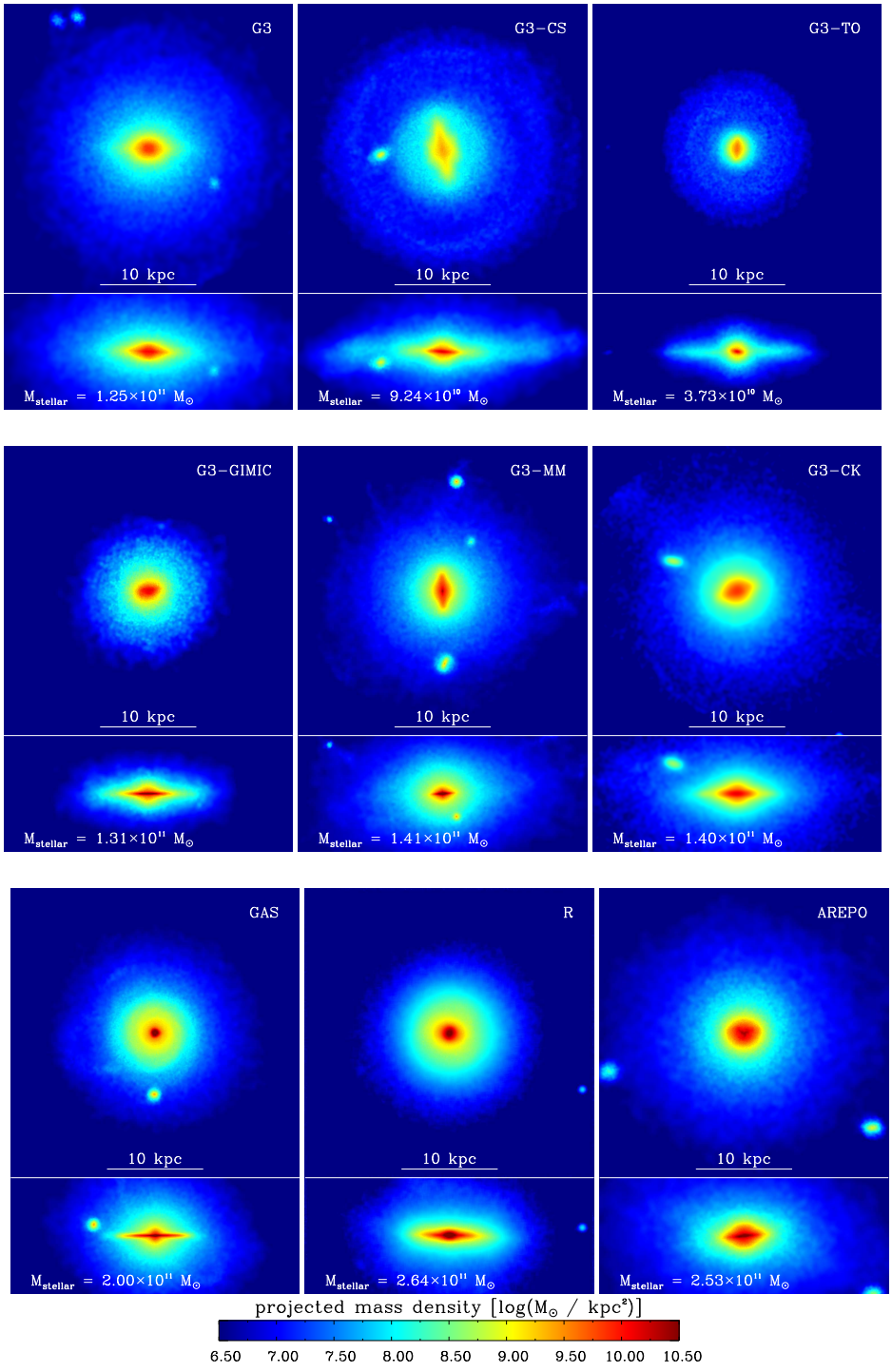

Figure 3.21 Face-on and edge-on maps of the projected stellar mass density for the nine fiducial Aquila models. The face-on images are projected along the net angular momentum vector of stars within $r_{\rm gal}$= $0.1r_{\rm vir}$ and have physical dimensions of 30×30 kpc. The edge-on images are projected in a direction orthogonal to the rotation axis and have dimensions of 30×12 kpc. Each pixel is 58.6 pc on a side and colours show the stellar mass surface density, as indicated by the bar. At the bottom of each panel we include the total stellar mass of each galaxy within ($r_{\rm gal}$).

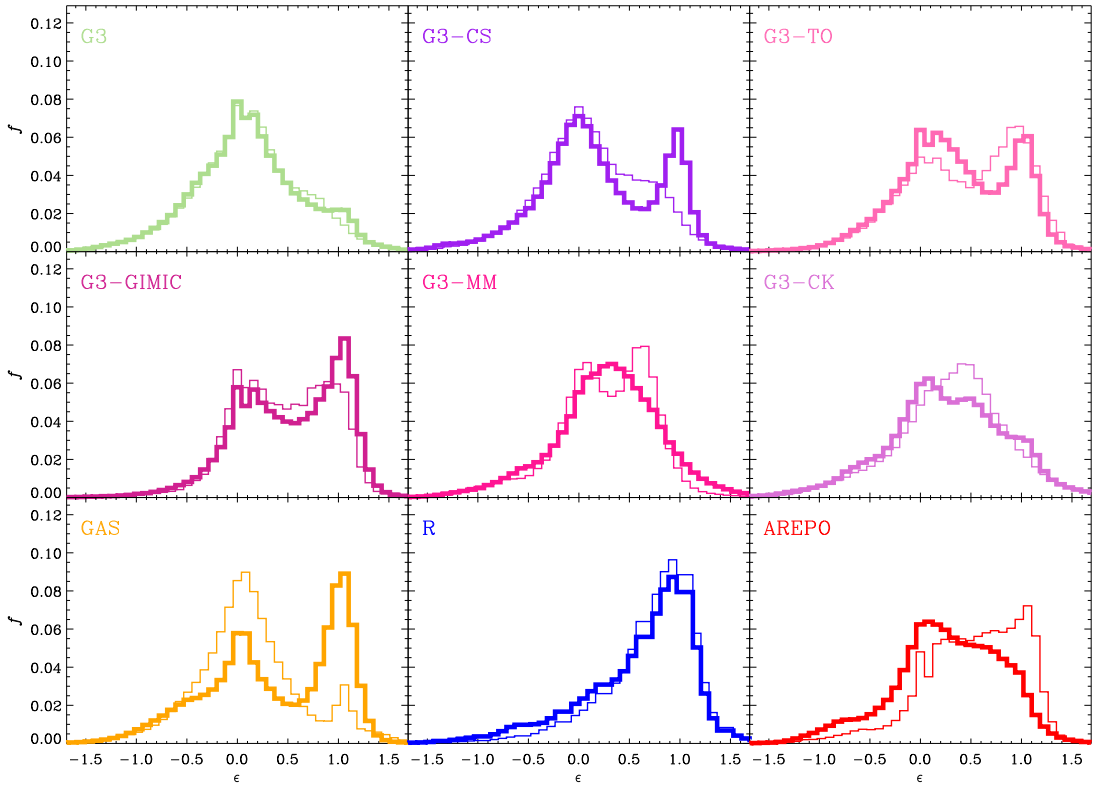

Figure 3.22 The distribution of circularities $\epsilon = J_z/J_c$ for stars within r_{gal} in the nine fiducial Aquila models, normalised to the total stellar mass in each case. The level five and level six simulations are represented by thick and thin lines respectively.

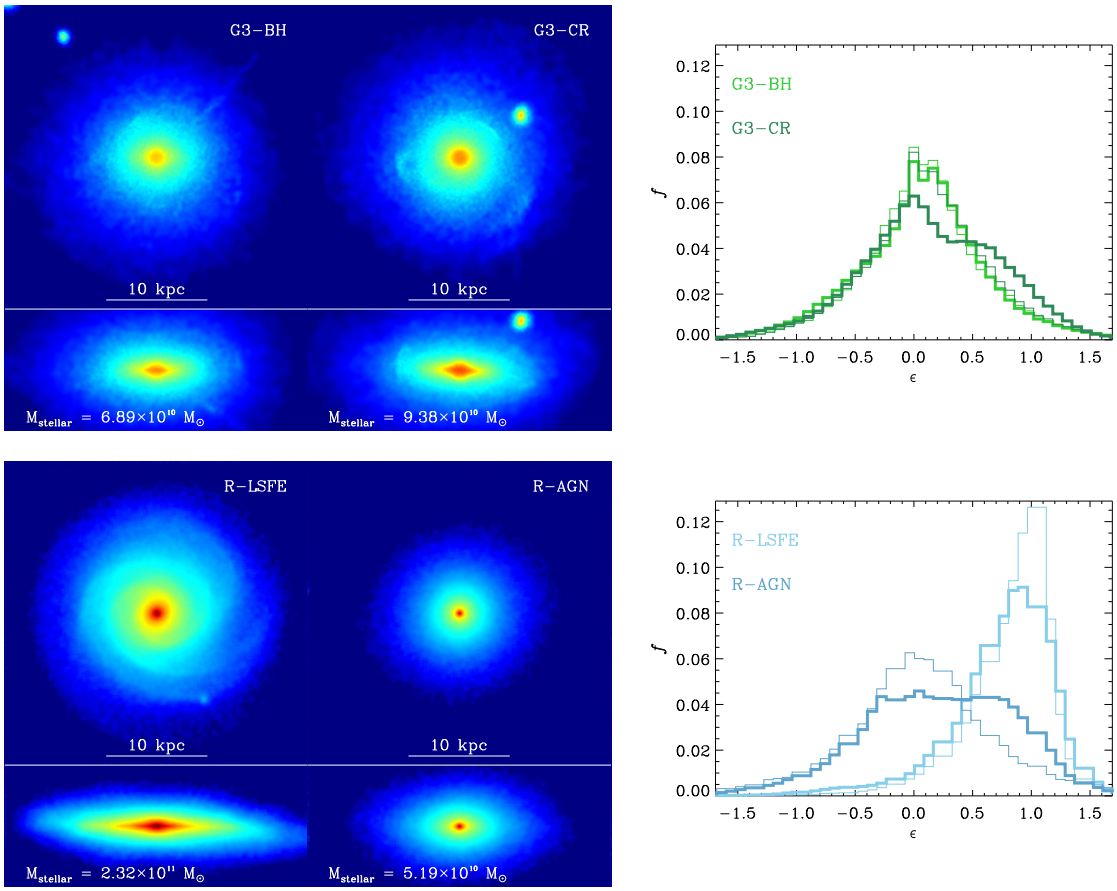

Figure 3.23 *Left Panel*: Face-on and edge-on maps of the projected stellar mass density for the four additional Aquila models. See Fig. 3.21 for details of the physical scale, orientation and colour scheme. *Right Panel*: The distribution of circularities ($\epsilon = J_z/J_c$) for stars within r_{gal} in the same set of models, normalised by the total stellar mass. Thick and thin lines represent the level five and level six resolution simulations respectively.

which may reflect the presence of a thick or misalligned disk, or a spheroidal component with non-zero rotation. A strong resolution dependence is apparent in G3-CS, AREPO and GAS, with the latter changing from strongly bulge-dominated to strongly disk-dominated between levels six and five. We discuss the resolution dependence of the codes in subsection 3.7.9.

We will show in subsection 3.7.7 that these differences are largely generated by aspects of the models that affect star formation efficiency at high redshift. Models that are able to delay star formation either by driving large scale outflows (G3-CS, G3-TO, G3-GIMIC, G3-CK, GAS) or simply by specifying a low efficiency (R, R-LSFE) tend to be those with the most significant disk components at $z = 0$.

3.7.4 Galaxy Formation Efficiency

In this subsection we investigate the efficiency with which each model turns the available baryons into stars. This is a function of how rapidly gas is able to cool and the extent to which star formation is regulated by feedback processes. In Fig. 3.24 we show how the stellar mass within $r_{\rm gal}$ evolves with the total halo mass for all thirteen models at level five resolution. Curves follow the evolution between $z = 2$ and $z = 0$ (indicated by symbols). The dotted line shows the relation obtained by Guo et al. (2010), who populated dark matter haloes from a ΛCDM N-body simulation with galaxies from the SDSS survey, assuming a monotonic increase in stellar mass with halo mass, a technique known as abundance matching. The dashed line indicates the stellar mass that would result from converting all available baryons into stars, if the halo had the cosmic baryon fraction ($M_{200} \times \Omega_{\rm b}/\Omega_{\rm m}$). We note that most models predict a stellar mass much higher than the abundance matching estimate, except those in which the most significant outflows are generated (G3-TO, R-AGN). The same codes also have a much lower total halo mass, by an amount exceeding the total baryonic mass, suggesting that less dark matter is accreted as a result of the shallower potential. Also shown in Fig. 3.24 is the prediction of the GALFORM semi-analytical model, which is tuned to reproduce the luminosity function of the MW satellites. It predicts a similar stellar fraction to many of the hydrodynamic codes, which is fairly close to the abundance matching estimate; the higher halo mass may be the result of the model output including gas re-heated by feedback energy in the total halo mass. While the top three simulations by stellar mass

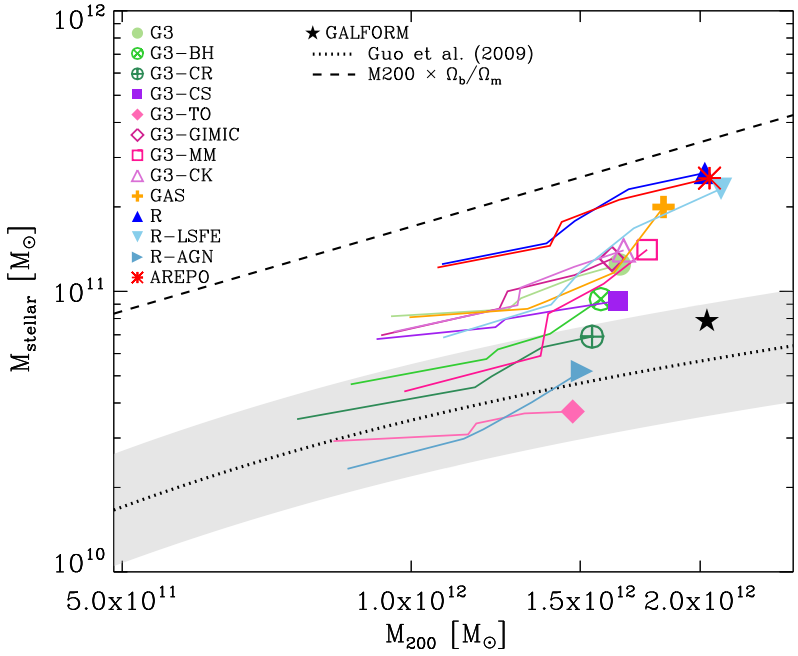

Figure 3.24 The stellar mass of the central galaxy as a function of the virial mass of the surrounding halo. Curves of different colour track the evolution of the galaxy in each simulation between $z = 2$ and $z = 0$. The dotted line indicates the stellar mass expected at $z = 0$ from the abundance-matching analysis of Guo et al. (2010). The dashed line shows the value of the stellar mass expected if all of the available baryons are turned into stars - the halo mass multiplied by the cosmic baryon fraction (Ω_b/Ω_m). The solid star symbol indicates the prediction of the semi-analytical model GALFORM (Cooper et al., 2010) for the Aquila halo.

are all non-SPH codes, we note that another AMR model employing a strong feedback prescription (R-AGN) in fact has the second lowest stellar mass. Hence while it could be the case, for instance, that SPH underestimates the amount of cold gas relative to mesh-based methods, such an effect would be dwarfed by the impact of different feedback implementations.

With the exception of R-AGN, the models with the highest final stellar mass tend to form proportionally more of their mass after $z = 2$. We examine the cumulative buildup of stellar mass in more detail in subsection 3.7.7.

3.7.5 Galaxy Sizes

The sizes of the cold gas and stellar components of the galaxies reflect the complex interplay of many processes. The size of the gas disk depends, among other factors, on how much of the gas is turned into stars, the efficiency of heating and cooling processes and the mechanism by which it is accreted. As we have seen in earlier results, an extended stellar disk is more likely if star formation can be delayed until after the peak in the merger activity. This is another manifestation of the angular momentum problem discussed in Section 3.6.7.

In Fig. 3.25 we plot the ($z = 0$) half-mass radii of the stellar disk and cold gas disk, as a function of total stellar mass in each of the Aquila models. Red and blue points in the left panel indicate stellar sizes derived for nearby ($z < 0.1$) SDSS galaxies, split into "red sequence" and "blue cloud" as described in the figure caption. In the right-hand panel we include gas sizes derived from HI observations by Swaters et al. (1999), Verheijen (2001) with stellar masses from Bell et al. (2003). Also shown in both panels are estimates for the size and mass of the Milky Way. The prediction of the GALFORM semi-analytical model for the stellar size is shown in the left panel, though not in the right panel, since the model predicts a negligible gas mass at $z = 0$. The size of the stellar disk is computed by assuming that gas retains the specific angular momentum of the halo and that the disk adopts an exponential surface density profile. Although, hydrodynamic simulations have found in the past that the former assumption is a poor approximation (e.g van den Bosch et al., 2002), we note that there is good agreement with most of the Aquila models shown here.

A factor of four separates the most compact (G3-TO) and most extended (G3-BH) stellar objects. In a few cases, the models have a size and mass similar to the MW, but in general, the galaxies are more massive and/or more concentrated. We note that those galaxies with a larger fraction of stars on high ϵ orbits (see Fig. 3.22 and Fig. 3.23) are not necessarily those with the most extended stellar distributions, for instance the disk-dominated GAS galaxy has a much smaller size than the bulge-dominated G3-CR galaxy. Two models with especially compact disks are G3-TO and G3-GIMIC. Both use kinetic feedback, which only mildly heats the existing disk as it outflows. In G3-TO, although type Ia SNe is distributed thermally, the type II SNe feedback does no heating locally, since gas is hydrodynamically decoupled at first. The remaining gas can cool efficiently

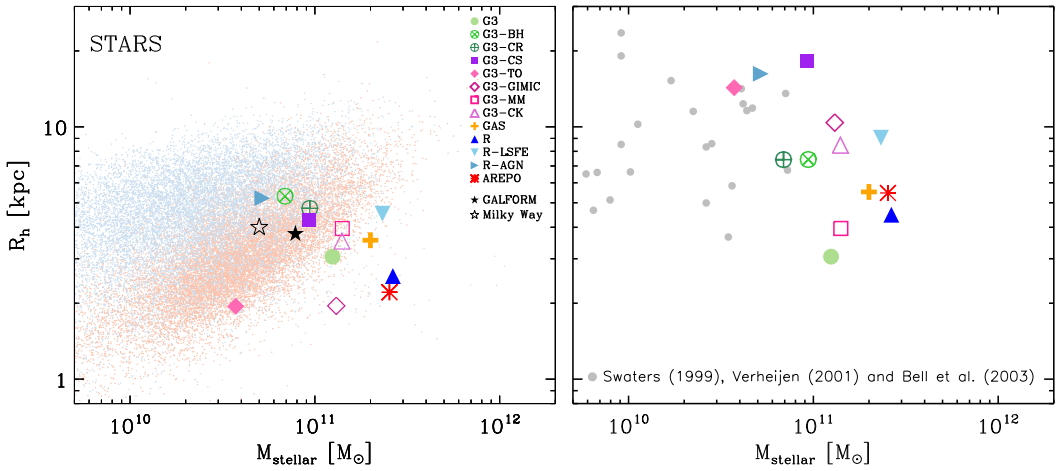

Figure 3.25 *Left Panel*: The projected half-mass radii of stars for the Aquila models as a function of their stellar mass within $r_{\rm gal}$=($0.1r_{\rm vir}$). Blue and red points indicate the Petrosian half-light radii of a sample of nearby ($z < 0.1$) SDSS galaxies from the MPA-JHU DR7 release. They are split into "blue cloud" or "red sequence" galaxies depending on whether their g-r colour is greater than or less than the quantity $0.59 + 0.052\log_{10}(M_{\rm stellar}/{\rm M}_\odot) - 10.0$. Also shown are an estimate for the Milky Way's stellar half-mass radius (open star symbol) and the prediction of the GALFORM semi-analytical model of Cooper et al. (2010) for this halo (filled star symbol).

Right Panel: The projected half-mass radius of cold ($T < 10^5$ K) gas in the Aquila models, as a function of their stellar mass. Grey circles indicate the half-mass radii of HI disks taken from Swaters et al. (1999), Verheijen (2001) with stellar masses from Bell et al. (2003). Note that the GALFORM semi-analytical model predicts a negligible gas mass at $z = 0$.

and form a compact (but fairly low mass) disk. In addition the G3-GIMIC feedback becomes extremely inefficient at late times when the high pressure ISM causes more drag on the outflows and the halo grows too massive for wind particles to escape.

The sizes of the cold gas disks also vary widely between models from 3 kpc (G3) to 18 kpc (G3-CS). While much of the observational data is for galaxies of lower stellar mass, in the regime where simulations and observations overlap, the sizes are comparable. The fact that the gas disks of the simulated galaxies are larger than the stellar disks is also consistent with observations of the MW. Both the cold gas and stellar half-mass radii tend to decrease with stellar mass, with a clearer correlation for the cold gas sizes. This may be related to the amount of heating by feedback expected in each case. Models such as G3-BH, G3-CR and R-AGN all inject a substantial amount of thermal energy into the gas at late times, while G3, AREPO and R all employ much weaker prescriptions.

3.7.6 Circular Velocities

In Fig. 3.26 we plot circular velocity profiles ($V_{\rm c} = \sqrt{GM(<r)/r}$) for each of the simulated galaxies. Also included are the profile obtained for the dark-matter-only Aquarius run of this halo at level four resolution (black line) and a selection of observational results for the Milky Way (grey points) compiled by Sofue et al. (2009)[2].

The galaxies with the highest stellar masses (R, R-LSFE and Arepo) tend to overpredict the peak circular velocity of Milky Way-Mass disk galaxies by a large factor. Most codes also produce a strongly peaked curve, such that V_c falls by a factor 1.5-3 from the maximum to the virial radius (not shown in Fig. 3.26) The only galaxies with rotation curves similar to those observed in the Milky Way and other spirals are those with the strongest feedback prescriptions G3-CR, G3-BH, G3-CS, G3-TO and R-AGN which also tend to have the lowest stellar masses. Their profiles have peak values between 200 and $280{\rm kms}^{-1}$ and are relatively flat out to large radii.

3.7.7 Stellar Mass Assembly and Disk Formation

Recalling that the initial conditions and hence the cosmological environment are identical for each of these models, they produce a remarkable range of star formation histories.

[2]Note that Sofue et al. (2009) rescale some of the observations to use consistent values for the Galactocentric radius (8 kpc) and velocity (200 ${\rm kms}^{-1}$) of the sun.

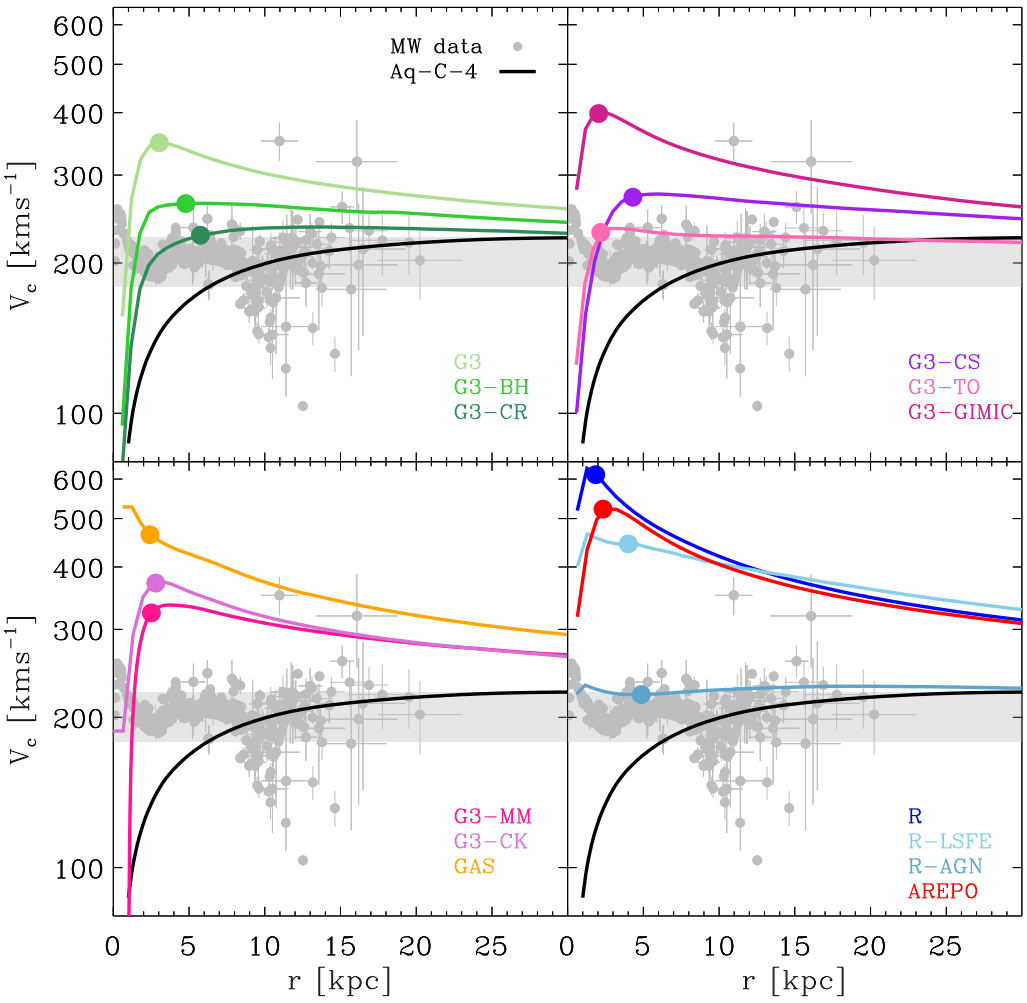

Figure 3.26 Circular velocity curves ($V_c = (GM(< r)/r)^{1/2}$) of the galaxies for all Aquila models at level five resolution. Different panels show several of the simulation codes as indicated by the labels. The solid circles indicate the position of the stellar half-mass radius in each case. The thick black line shows the rotation curve for the dark-matter-only (Aquarius) simulation of the same halo at level four resolution. For reference, the region shaded in light grey is bounded by the peak and virial velocities of the Aquarius halo. Observations of the Milky Way's rotation curve, as compiled by Sofue et al. (2009) are indicated by dark grey points with error bars.

In Fig. 3.27, we plot the cumulative stellar mass formed as a function of time and expansion factor for each of the models, including all stars that end up within $r_{\rm gal}$ at $z = 0$. The epoch at which half (ten percent) of the final stellar mass is formed is indicated by solid circles (squares) in each case and ranges between 0.17 and 0.46 (0.11 and 0.21). At $a = 0.125$, $z = 7$, for example, there is almost an order of magnitude difference between the most massive, G3-CS and least massive, R-LSFE, and yet by the final time R-LSFE has a mass ~ 2.5 times larger than G3-CS.

The differences between the models seen in Fig. 3.27 is driven primarily by the evolution in the efficiency of feedback. For example, the G3-GIMIC and G3-TO models both form ten percent of their final mass by $a = 0.18$ ($z \sim 5.5$), but their late time evolution is very different. The kinetic feedback in G3-GIMIC, where a constant wind speed is used, becomes ineffective after the main halo reaches a certain mass, allowing star formation to accelerate at low redshift. Feedback remains effective in G3-TO however, due to the scaling of the wind speed with the halo circular velocity and the hydrodynamical decoupling of wind particles. The G3-CS model builds in a time-delay in the SNe feedback prescription (such that a reservoir of energy is built up sufficient to heat gas beyond the peak in the cooling function). This results in a SFR that is relatively high at early times, but strongly suppressed later on. The behaviour of R-LSFE in this plot is governed, not by feedback, but by its defining characteristic of a very low star formation efficiency. A huge amount of gas remains at late times, resulting in a very high SFR, despite the low efficiency.

In Fig. 3.28 we compare the $z = 0$ star formation rates in each model to those of nearby ($z < 0.1$) galaxies from the MPA-JHU SDSS DR7 catalogue. The simulated galaxies with lower final stellar mass ($M_{\rm stellar} \lesssim 10^{11}$ M$_\odot$) have star formation rates of 0.3-0.5 M$_\odot$yr^{-1}, placing them in the intermediate region between red and blue galaxies in the observational data. Some of the more massive galaxies are forming stars at much higher rates, however, such that they fall in the extreme high SFR tail of the observational distribution at that stellar mass. This result continues the trend for the strong feedback, low final stellar mass models to provide a better match to the observational data.

Previous results have suggested that later forming galaxies tend to produce "diskier" stellar distributions. We test this directly in Fig. 3.29 by comparing metrics for the stellar formation time and "diskiness" of the morphology. We define the quantities a_{50}, the

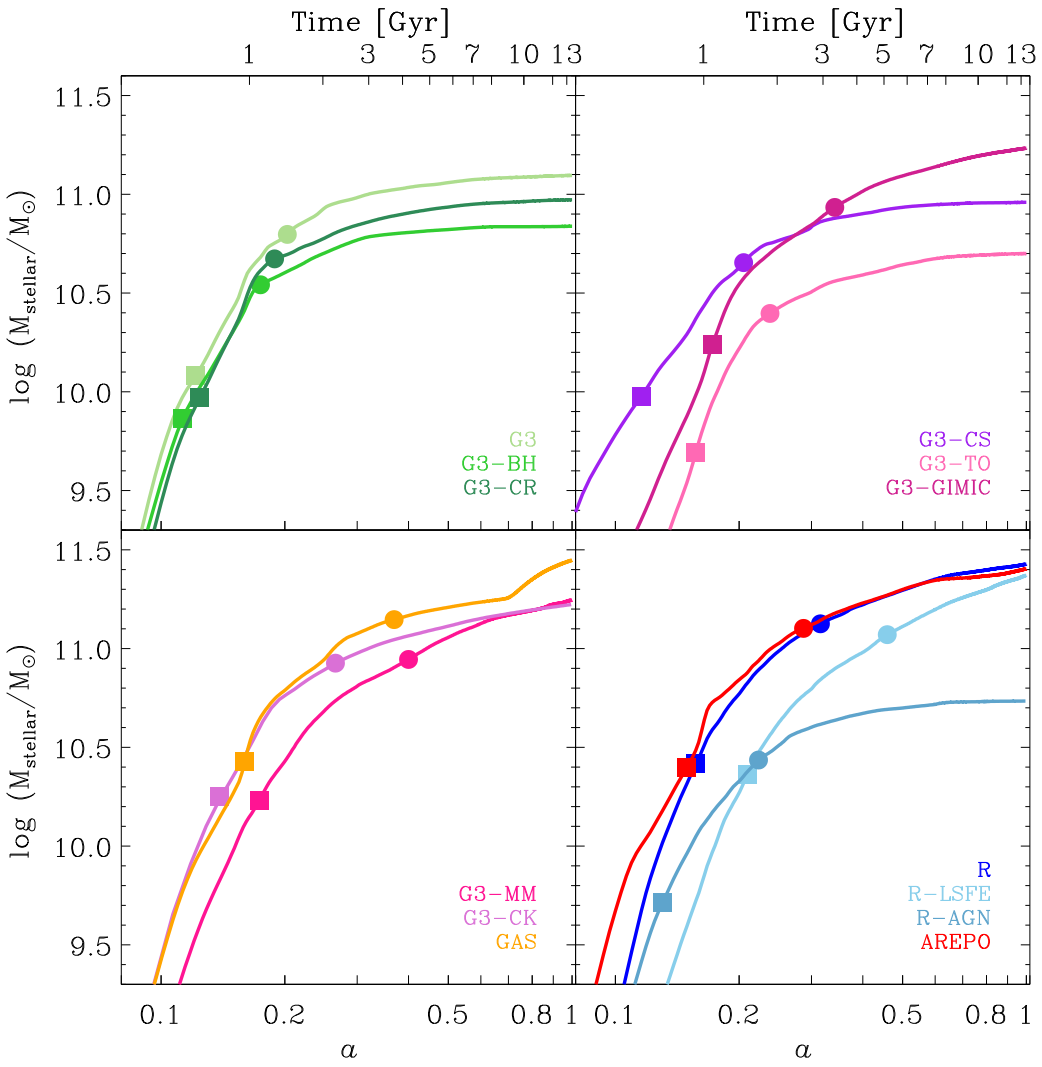

Figure 3.27 Cumulative distributions of the formation times of stars in each of the level five Aquila galaxies. Different panels show several of the simulation codes as indicated by the labels. The epoch at which half (ten percent) of the final stellar mass is formed is indicated by solid circles (squares) in each case.

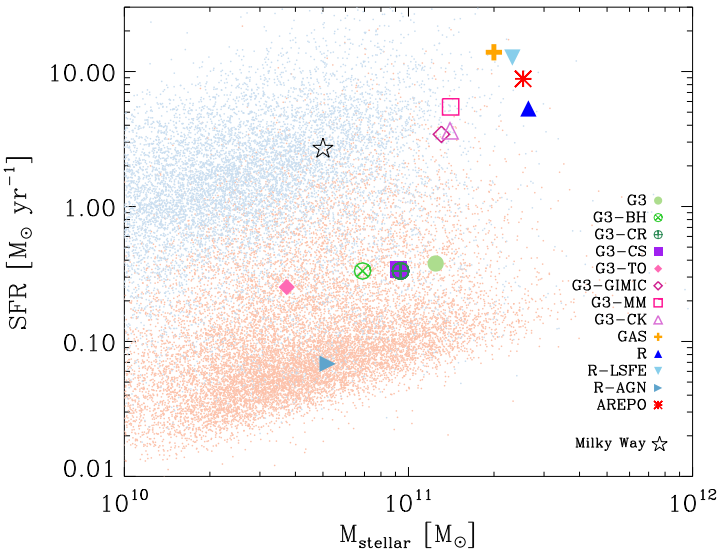

Figure 3.28 The present day star formation rates in each of the Aquila models as a function of stellar mass. Blue and red points correspond to a sample of nearby ($z < 0.1$) SDSS galaxies, split into "red sequence" and "blue cloud" as described in the caption of Fig. 3.25 Note that the GALFORM semi-analytical model has a negligible star formation rate at $z = 0$.

expansion factor at which half the stars were formed and $\epsilon_{0.8}$, the fraction of stars with circularity > 0.8 and plot them for each of the thirteen models. A clear positive correlation between a_{50} and $\epsilon_{0.8}$ is apparent, reflecting the fact that late forming stars are much less likely to be scattered out of circular orbits by mergers, interactions or instabilities. Suppressing gas condensation in the high redshift progenitors also increases the angular momentum of the final object. There is clearly a large scatter in this relation, however; models with very efficient early star formation are still able to form reasonable disks (e.g. G3-CS) and models with high late-time SFRs can produce disk-dominated (R) or bulge-dominated galaxies (Arepo).

3.7.8 The Tully-Fisher Relation

An important observed property of spiral galaxies is the correlation between stellar mass or luminosity and circular velocity - the Tully-Fisher relation. Hydrodynamical simulations have historically struggled to match the relation as a consequence of producing

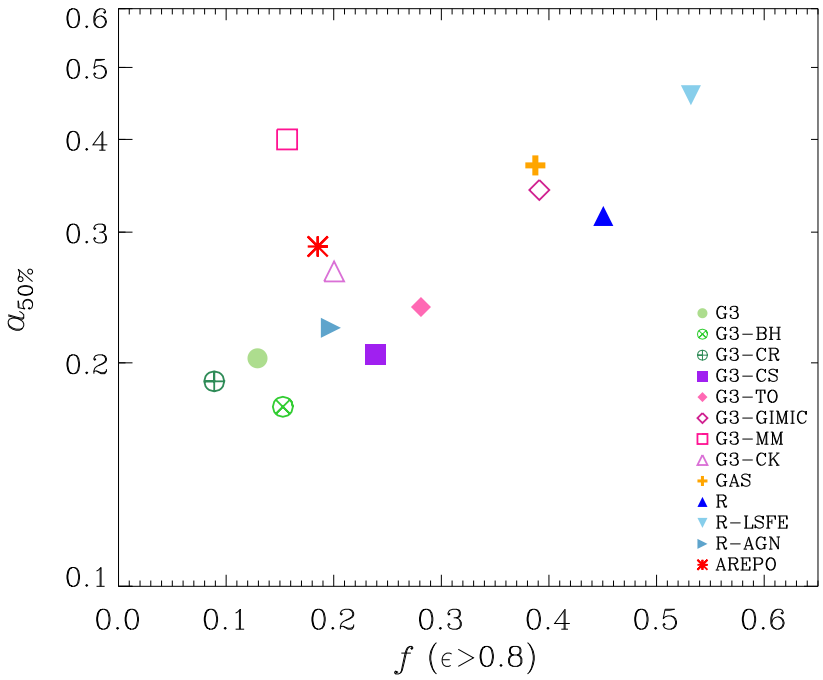

Figure 3.29 The expansion factor at which half of the final stellar mass is formed, as a function of the fraction of stars with circularities larger than 0.8, plotted for each of the Aquila models.

overly concentrated disks with too much stellar mass. Fig. 3.30 demonstrates that this remains an issue for most, if not all, of the models. We plot the circular velocity at the half-stellar-mass radius against total stellar mass for each of the simulated galaxies (symbols) and compare to observational data from Pizagno et al. (2007), Verheijen (2001) and Courteau et al. (2007) (black points). Models that predict a stellar mass greater than 10^{11} $M_\odot$ have circular velocities at the half-stellar-mass radius between 1.5 and 2.5 times larger than observed galaxies at the same stellar mass. The simulated galaxies less massive than 10^{11} $M_\odot$ are closer to the observed relation, but nonetheless fall in the high-velocity tail of the distribution at that stellar mass.

If only the contribution from the dark matter in each simulated galaxy is considered, we obtain the velocities (at the same radii) indicated by the symbols connected with a solid line. Symbols connected by the dotted line indicate the velocity in the Aquarius *dark-matter-only* simulation, with $M(< r)$ scaled by a factor (1-Ω_b/Ω_m), once again at the same half-stellar-mass radii obtained for each model. The difference between these

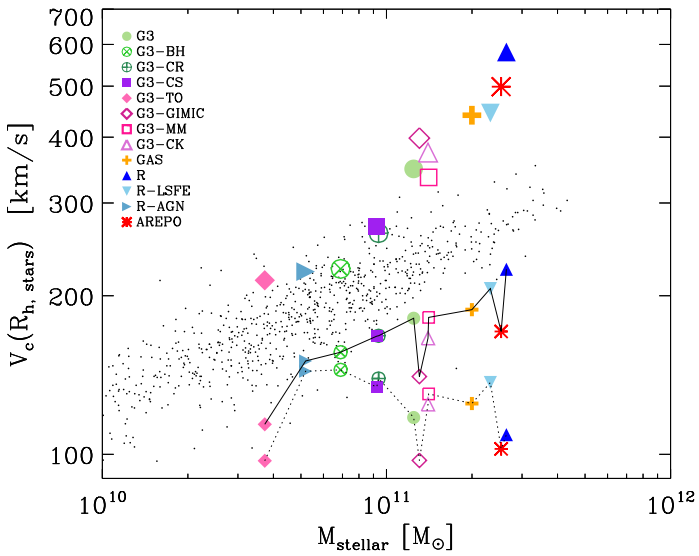

Figure 3.30 The Tully-Fisher relation for each of the Aquila models at level five resolution. The circular velocity at the stellar half-mass radius is plotted as a function of stellar mass. Observational data taken from Pizagno et al. (2007), Verheijen (2001) and Courteau et al. (2007) are plotted as black points. The symbols connected by a solid line show the contribution of the dark matter to the circular velocity at $R_{\rm h,stars}$. Those connected by the dotted line show the circular velocity of the dark matter-only Aquarius simulation (Aq-C-4) at the corresponding radii.

two lines allows us to estimate the effect that the baryons have had on the dark matter in each case. Where the symbols connected by the solid line indicate a higher velocity, the baryons have caused a net contraction of the dark matter halo. Models with the highest final stellar mass, typically those with the least efficient feedback, show the most contraction. In the simulations with very strong feedback (G3-TO,G3-AGN), the effect is greatly reduced.

3.7.9 Resolution Effects

An idea of how the behaviour of the models varies with resolution can be obtained by comparing the properties of the level five and level six realisations in each case. We define a measure of convergence for each quantity of interest (Q) as the fractional difference

between the level five and six simulations:

$$\Delta Q/Q = [Q(6) - Q(5)]/Q(5), \tag{3.16}$$

where $Q(5)$ and $Q(6)$ are the values of the quantity in the level five and six simulations. We caution however that, resolution dependent behaviour is expected to some degree, since the Jeans length and Jeans mass of star forming gas are not well resolved in either the level six or level five simulations. For instance, in several of the codes, stars are allowed to form at a density of $0.1\ \mathrm{Hcm}^{-3}$ and temperature of $10^4\ \mathrm{K}$, equating to a Jeans length of $\sim 1.5\,\mathrm{kpc}$ which is not much larger than the value of the gravitational softening parameter at level five.

In the top left panel of Fig. 3.31, we show that total stellar mass agrees to better than fifty percent in all but one model (R-AGN) and typically to better than twenty percent. The stellar half-mass radius is similarly stable in most cases, although three models show deviations greater than fifty percent. We note that in the level six G3-TO simulation, the size of the stellar object is close to the gravitational softening and may be overestimated as a result. This effect could also play a part in models that have a small stellar disk at level five (Arepo,R,G3-GIMIC).

The mass and size of the gaseous component of the galaxies is much less stable with resolution (top right panel), with only a few models converged to within fifty percent in both quantities. In the cases where differences are larger than a hundred percent, the position of the model in the plane is indicated by an arrow. There is a general trend for the half-mass radius to be *larger* in the level five simulations, which runs counter to any effect expected due to changes in the spatial resolution. However the change in size with resolution is likely driven by a change in the cold gas mass, as suggested by the rough correlation seen in the upper right panel. The explanation for the discrepancy in the final gas mass appears to vary from model to model and is a fairly complex function of the different cooling, star formation and feedback prescriptions. In at least one case though the root cause is easily identified; the final gas mass in R-AGN at level six resolution is zero ($\Delta Q/Q = -1$), owing to an apparent increase in the AGN feedback efficiency as energy is injected over a larger volume.

In the lower left panel we show $\Delta Q/Q$ for $V_{\rm max}$ and $R_{\rm max}$ (the radius at which $V_{\rm max}$ occurs). Perhaps unsurprisingly, the value of $V_{\rm max}$ is far better converged than $R_{\rm max}$, which is very sensitive to small variations in the profile where $V_{\rm c}(r)$ turns over. In three

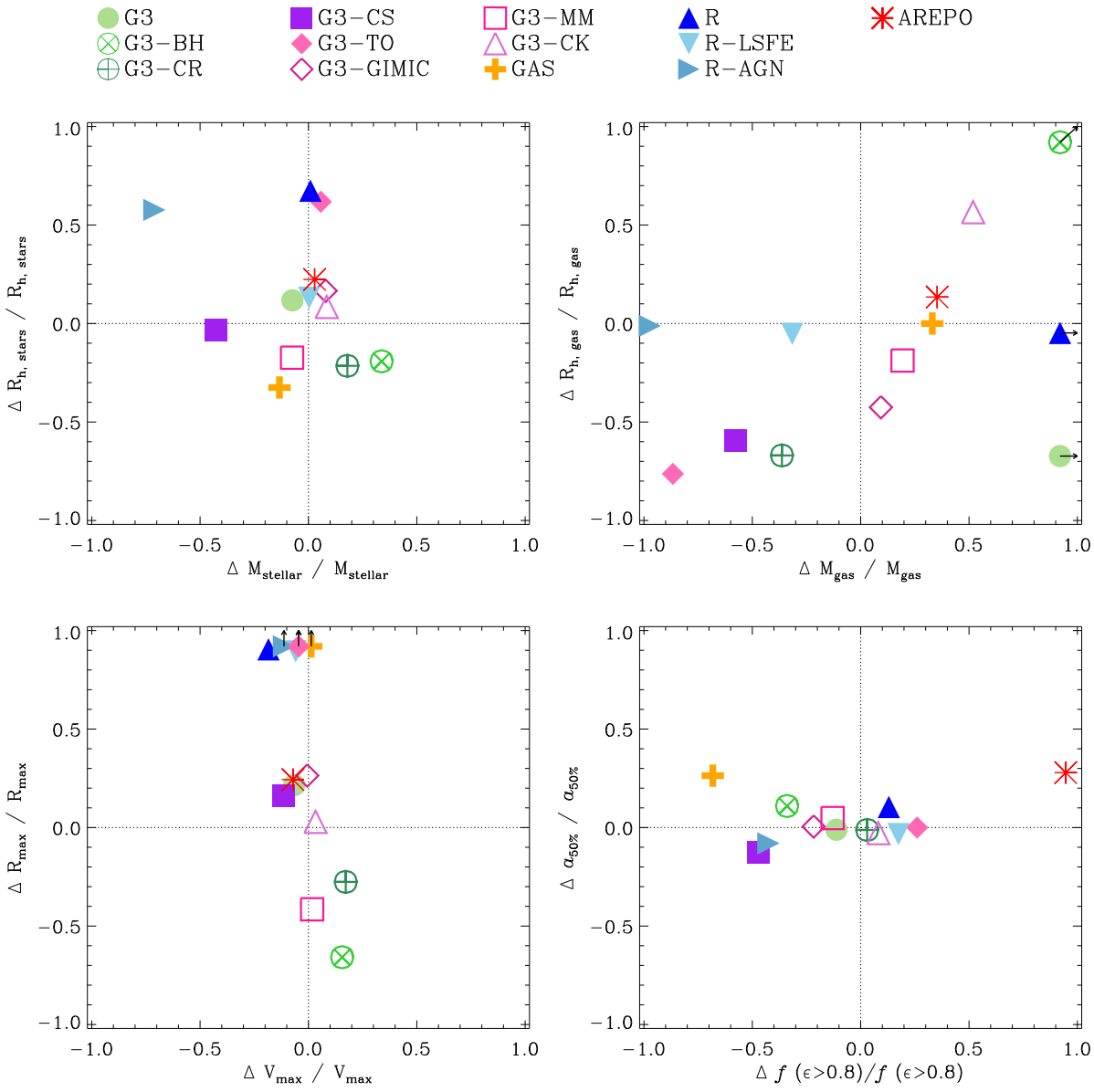

Figure 3.31 Convergence of various quantities (Q) between the level five and level six realisations of each model, measured as $\Delta Q/Q = [Q(6) - Q(5)]/Q(5)$. $\Delta Q/Q$ is plotted for stellar mass vs. stellar half-mass radius (top left), cold gas mass vs. cold gas half-mass radius (top right), peak circular velocity vs. corresponding radius (bottom left) and expansion factor of stellar formation vs. fraction of high circularity stars (bottom right). Models for which $\Delta Q/Q$ falls outside the plotted range are indicated as arrows.

cases $R_{\rm max}$ is more than a factor of two larger in the level six simulation (as indicated by the arrows), whereas $V_{\rm max}$ doesn't change by more than twenty percent for any model. The large changes in $R_{\rm max}$ are unlikely to be affected by the difference in gravitational softening in the two sets of simulations, though presumably the adiabatic contraction of the halo is suppressed to some extent in the level six simulations.

Finally, the bottom right panel we examine the convergence of $f(\epsilon > 0.8)$, the fraction of stars with circularity greater than 0.8 and a_{50}, the expansion factor at which the galaxy has formed half of its final stellar mass. The latter is converged to within thirty percent for all models and typically to within ten percent, although of course large values of $\Delta Q/Q$ are unlikely in this case, since $0 < a_{50} < 1$. We note that in the model for which the convergence is worst in this quantity, Arepo, the difference in a_{50} equates to a delay in formation time in the level six simulation of ~ 1 Gyr with respect to level five. Larger differences are observed in the disk fraction, though in all but two cases (Arepo and GAS) they correspond to differences of less than ten percent in the value of $f(\epsilon > 0.8)$ itself. We would argue then that in most cases (as can be seen in Figs. 3.22 and 3.23, the morphologies of the galaxies are relatively well converged.

3.8 Summary

In this chapter we have presented a model for galaxy formation based on the N-body-SPH code GADGET-3. We described our modelling of various key baryonic processes, including radiative cooling, reionisation, the multiphase ISM, star formation, stellar evolution, chemical enrichment and SNe feedback. The first results obtained with this model demonstrated a worrying resolution dependence in terms of many key baryonic properties, including the star formation history, morphology and baryon fraction. This behaviour was caused, at least in part by outflowing gas being able to escape to much larger distances at higher resolution, preventing it from re-accreting later.

We also found that the Aq-C-$4_{\rm i}$ simulation (and to some extent the Aq-C-$5_{\rm i}$ simulation) resolved the formation of numerous cold clouds of gas. The clouds appeared shortly after the first significant star formation ($z = 10 - 8$) and were found to be abundant in the halo by $z = 5$. They are found to form through the fragmentation of gravitationally unstable structures in the gas ejected by SNe feedback which appears to be

suppressed by the gravitational softening at lower resolution. The low filling factor and high mass fraction of the clouds makes for a more porous distribution of halo gas, which presumably allows wind particles to escape more easily.

Four modifications were made to the code in order to improve convergence. These were i) allowing non-equation-of-state gas particles to be added to the wind, ii) moving gas neighbours of wind particles to shorter timesteps to ensure they interact properly, iii) adding an artifical conductivity prescription to improve the modelling of contact instabilities and iv) scaling the star formation threshold with resolution to suppress star formation in low density environments. With these changes in place, the star formation histories, baryon fractions and morphologies were found to agree well between Aq-C-4 , Aq-C-5 and Aq-C-6 . The formation of clouds was also suppressed, with a much smoother distribution of gas in the halo. We note, however, that a set of runs employing only changes i) and iv) showed similarly good convergence (Takashi Okamoto, Private Communication) suggesting ii) and iii) may be unrelated to the improvement.

We presented an in-depth study of the Aq-C-4 simulation, finding that it produces a galaxy with an extended gas disk, a stellar component with a barred spiral structure and a total stellar mass about two thirds that of the Milky Way. Its rotation curve peaks at $\sim 250\ \mathrm{kms}^{-1}$ and declines fairly gradually out to the edge of the disk. A particularly interesting aspect of the galaxy's evolution is that it undergoes at least one and possibly several episodes of disk collapse, due to misallignment between the existing disk and the angle of gas accretion. The initial tilt appears to be induced by the merger of a large satellite which drags the disk into the orbital plane. As gas continues to accrete with the angular momentum of the halo, it forms an unstable configuration that causes the existing (inner) disk to buckle.

In the final section, we presented results from the *Aquila* code comparison project. Nine different hydrodynamical codes were invited to simulate the Aq-C halo at level five and level six resolution, beginning from identical initial conditions to those described in Section 3.3. A few of the codes were run with variations on their fiducial models, including extra physics or different parameters; this amounted to thirteen models in total. The main aims of the project were to establish how the properties of the main galaxy vary depending on the modelling technique and the physical mechanisms included. In particular we examined which aspects of the models promoted the formation of a realistic

galaxy disk.

Properties of individual codes agree relatively well between different resolutions, other than the detailed structure of the gas and stellar disks, which may be affected by the gravitational softening. Despite a common halo merger history we found large differences in the morphologies, star formation histories, mass profiles and sizes. The main driver behind this variation was found to be the implementation of feedback processes, dwarfing any differences relating to the choice of hydrodynamical technique. A general theme is that most of the models predict a significantly larger stellar fraction and a much more strongly peaked rotation curve than the observational data support. The exception to this are the codes employing the strongest feedback prescriptions, though they also tend to have less extended disks as a result of removing such a large fraction of gas from the halo. We speculate that this apparent contradiction may be a consequence of distributing the feedback over too large a volume of the ISM.

The Aq-C-4 , Aq-C-5 and Aq-C-6 simulations presented in this chapter were intended primarily to study the central galaxy, but as we have seen, its local cosmological environment must also be resolved in order to model its formation accurately. As a consequence, the same simulations can be used to investigate the evolution of its satellite galaxies, which are expected to be analogues of the dSphs and dIrrs seen in the Local Group. In the next chapter, we examine the satellite population in Aq-C-4 , focussing in particular on how their structures can be used to test ΛCDM .

Chapter 4

Dynamical Masses of the Milky Way Satellites

4.1 Introduction

Substantial progress has been made over the last few years in modelling the formation of galactic dark matter haloes using high resolution N-body simulations (Springel et al., 2008b; Diemand et al., 2008; Stadel et al., 2009). Hydrodynamical simulations of such systems inevitably lag behind in terms of resolution, but are now reaching a point where they can be used to investigate the detailed evolution of the baryonic component of satellite galaxies, as demonstrated by several recent studies. Okamoto et al. (2010) studied the effects of different feedback models on the chemical properties and luminosities of the satellite populations around three Milky Way (MW)-mass haloes. Okamoto & Frenk (2009) showed that a combination of the early reionisation of pregalactic gas at high redshift and the injection of supernovae (SNe) energy is sufficient to suppress star formation in the myriad of low mass subhaloes that form in the ΛCDM cosmology, confirming results from earlier semi-analytical modelling (Benson et al., 2002; Somerville, 2002). Wadepuhl & Springel (2010) further argued that cosmic rays generated by SNe may play an important role in suppressing star formation in satellites.

From an observational point of view, the release of data from the Sloan Digital Sky Survey (SDSS) (York et al., 2000) over the last decade has transformed the study of the Local Group satellites. The ~ 30 faint dwarf galaxies discovered using those data (e.g., Zucker et al., 2004; Martin et al., 2006; Belokurov et al., 2007a; McConnachie et al., 2008) have prompted a new phase of detailed testing of current galaxy formation theories on smaller scales and in more detail than ever before. The SDSS data also reduced the discrepancy that existed between the number of low mass dark matter haloes predicted

by the ΛCDM cosmological model and the number of faint satellites identified around the MW: the 'missing satellite problem' (Klypin et al., 1999; Moore et al., 1999). Over the same period, numerous theoretical models (e.g., Li et al., 2010; Macciò et al., 2010; Font et al., 2011b) have confirmed early conclusions that a combination of a photoionising background and feedback processes from SNe are capable of bringing the two into good agreement.

However, it is important to recognise that the satellite problem is not simply a statement that star formation must be suppressed in low mass haloes. A more subtle, but equally important test of any cosmological model is whether the potential wells in which satellite galaxies form are capable of supporting stellar systems with realistic kinematics. Strigari et al. (2010) demonstrated that all of the classical MW satellites for which high quality kinematic data are available are consistent with having formed in dark matter subhaloes selected from the high resolution ΛCDM N-body simulations of the Aquarius project (Springel et al., 2008b). However, successful models must satisfy both constraints, producing realistic luminosity functions *and* forming stars in potentials like those inferred from observations.

Boylan-Kolchin et al. (2011) have recently argued that the most massive subhaloes in high resolution simulations of cold dark matter haloes are too concentrated to be able to host the brightest observed satellites of the Milky Way. Lovell et al. (2011a) have shown that subhaloes formed from warm, rather than cold, dark matter have suitably low concentrations, but both they and Boylan-Kolchin et al. emphasise that other solutions to the discrepancy are possible. One promising possibility is the mechanism originally proposed by Navarro, Eke & Frenk (1996a), whereby the rapid expulsion of dense central gas in a starburst can unbind the inner parts of the halo, significantly reducing its concentration. We find an example of this process in one of the subhaloes formed in the simulations analysed in this chapter.

From a theoretical perspective, *ab initio* hydrodynamic simulations are uniquely well-suited to investigating the effects of galaxy formation on the dark matter haloes of satellite galaxies. It has been known for some time that baryons may significantly alter the behaviour of dark matter on some scales. Dissipative processes such as gas cooling, star formation and feedback decouple the dynamical evolution of the baryons from that of the dark matter. The resulting change in the shape of the overall potential in turn affects

the phase space structure of the dark matter halo.

Central concentrations of cold baryonic matter can induce an adiabatic, radial contraction of the central regions (Blumenthal et al., 1986; Gnedin et al., 2004), while the opposite effect can be achieved if dense clumps of baryonic material heat the central distribution of dark matter (El-Zant et al., 2001, 2004; Mo & Mao, 2004; Mashchenko et al., 2006, 2008; Goerdt et al., 2010) , or if the blowout mechanism of Navarro, Eke and Frenk is effective (see also Gelato & Sommer-Larsen, 1999; Gnedin & Zhao, 2002; Mo & Mao, 2004; Read & Gilmore, 2005; Governato et al., 2010; Pontzen & Governato, 2011). This latter mechanism was originally proposed as a means to erase the central dark matter cusps in dwarf galaxies, though whether or not such 'cored' profiles are required by the observations remains a matter of ongoing debate (Goerdt et al., 2006; Sánchez-Salcedo et al., 2006; Strigari et al., 2006; Gilmore et al., 2007; Walker et al., 2009). If baryons really do modify the dark matter in satellites on sub-kpc scales significantly, then the value of studying dwarf galaxies with post-processed N-body simulations may be very limited.

In this chapter, we make use of the simulations described in Chapter 3 to study the formation of satellite galaxies, focussing in particular on determining whether their structures are compatible with those of the MW satellites, as inferred from stellar kinematical data. Our model has already been shown to reproduce the shape and approximate normalisation of the MW's satellite luminosity function, as well as the metallicity-luminosity relation observed in the Local Group (Okamoto et al., 2010). In Section 4.2, we expand on the theoretical predictions of the model by examining what effect baryons have had on the dark matter profiles of satellites. We perform tests in Section 4.3 to ensure that key properties of our satellite population do not depend on the numerical resolution. In Section 4.4, several observable and derived properties of the simulated satellites are compared Local Group data. Finally, in Section 4.5 we discuss the evolution of one particularly interesting satellite in the simulation, which is dominated by its stellar component at $z = 0$. Our main results are summarised in Section 4.6.

4.1.1 Satellite Identification

Galaxies are identified using a version of the SUBFIND algorithm (Springel et al., 2001a) adapted by Dolag et al. (2009), which identifies self-bound structures and includes the internal energy of gas when computing particle binding energies. From the ~ 5 Mpc

high resolution region, we select all galaxies within 280 kpc of the centre of the most massive (central) galaxy. This distance was chosen to match the limiting magnitude of the completeness-corrected satellite luminosity function constructed by Koposov et al. (2008). The largest satellite in our Aq-C-4 run is resolved with about 1.5×10^5 particles in total, $\sim 3 \times 10^4$ of which are star particles. In the following, we consider all galaxies with more than ten star particles, which, taking into account the typical mass fraction lost through stellar evolution for our choice of IMF, implies a stellar mass limit of $\sim 1.2 \times 10^5\ \mathrm{M}_\odot$ for Aq-C-4.

4.2 The Effect of Baryons on Satellite Dark Matter Haloes

Using a dark matter only (DMO) counterpart of our Aq-C-4 run, simulated as part of the Aquarius project (Springel et al., 2008b), we have examined the extent to which the dynamics of the baryons alter the structure of dark matter (sub)haloes of satellite galaxies over the course of their formation. The DMO run had identical initial conditions to our Aq-C-4, but for the absence of baryons and a correspondingly higher dark matter particle mass by a factor $\sim 1/(1 - \Omega_\mathrm{b}/\Omega_\mathrm{m})$.

Naively, one might simply compare each subhalo with its DMO equivalent at $z = 0$, but this turns out to be problematic. As has been noted in previous N-body simulations at different resolutions, small phase deviations in subhalo orbits get amplified over time, such that subhaloes can be in quite different positions at $z = 0$ (e.g., Frenk et al., 1999; Springel et al., 2008b). We see similar differences between Aq-C-4 and the DMO run. Subhalo orbits are also affected by other factors such as subhalo-subhalo scattering and variations in the potential due to small differences in the growth history of the main halo.

Since the strength of tidal shocking is strongly dependent on pericentric distance (Gnedin et al., 1999; Mayer et al., 2001c), small orbital deviations can cause large differences in subhalo structure, which are entirely unrelated to the presence or absence of baryons. This complication can be avoided, either by choosing subhaloes with no close pericentre, or by making the comparison at the epoch when the satellite is first accreted into the halo of the main galaxy, before the orbits have had a chance to diverge. We choose the latter option, since the former restricts us to a very small number of cases, although we note that one massive halo in a low eccentricity (~ 0.2) orbit with a distant

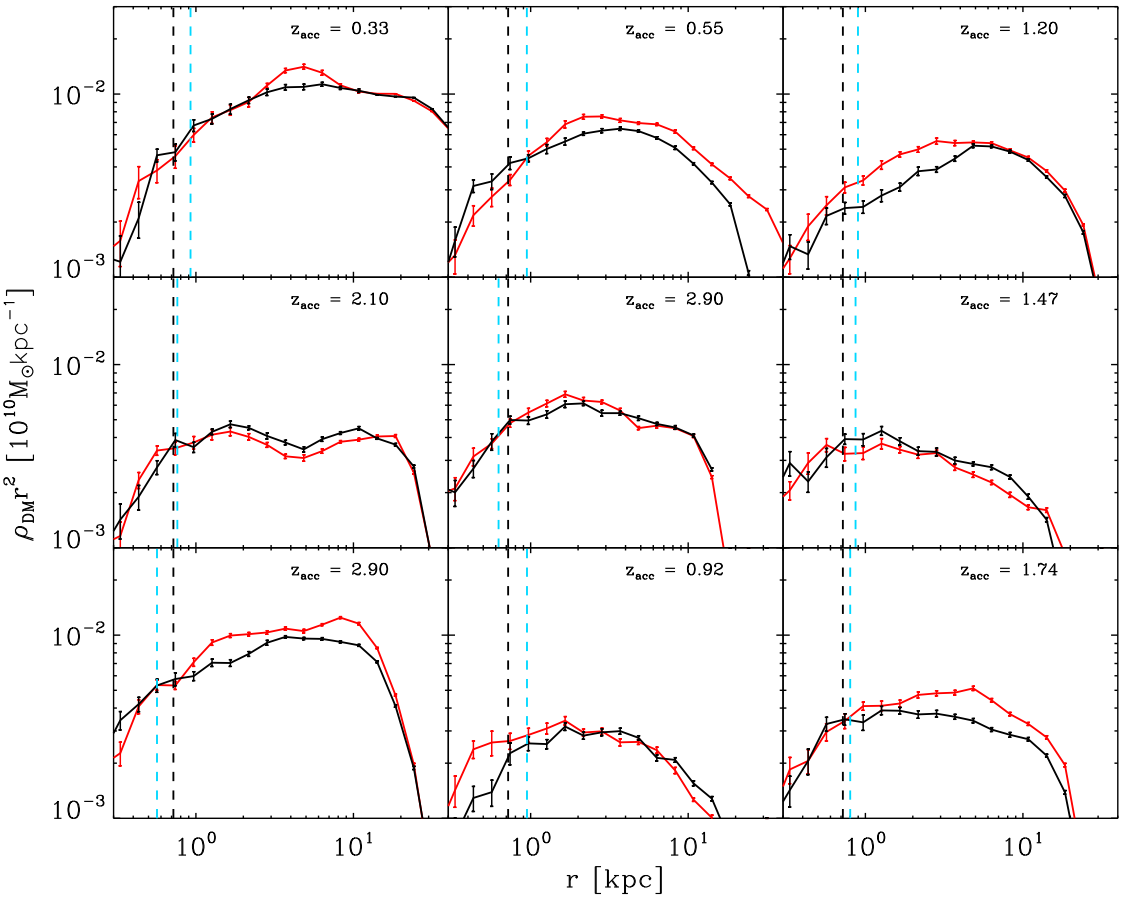

Figure 4.1 The spherically averaged dark matter density profiles of the nine most massive satellite galaxies in our high resolution hydrodynamic (red) and dark matter only (black) runs. Error bars are obtained by bootstrap resampling. The comparisons are made at the redshift where the galaxy is first accreted as a satellite, which is shown as a label at the top of each panel. Black dashed vertical lines indicate the scale on which softened gravitational forces become fully Newtonian. Blue dashed vertical lines indicate the convergence radius of Power et al. (2003).

pericentre (~ 200 kpc) shows comparatively small differences in its dark matter density profile at $z = 0$ relative to the DMO case. In the few instances where the accretion times of the subhalo differ slightly between the hydrodynamical and DMO runs, we choose the earlier of the two epochs.

In Fig. 4.1 we show spherically averaged profiles for the dark matter density (plotted as ρr^2 to emphasise small differences) of our most massive satellites, for Aq-C-4 and the DMO run at the output time when each satellite first joins the main friend-of-friends

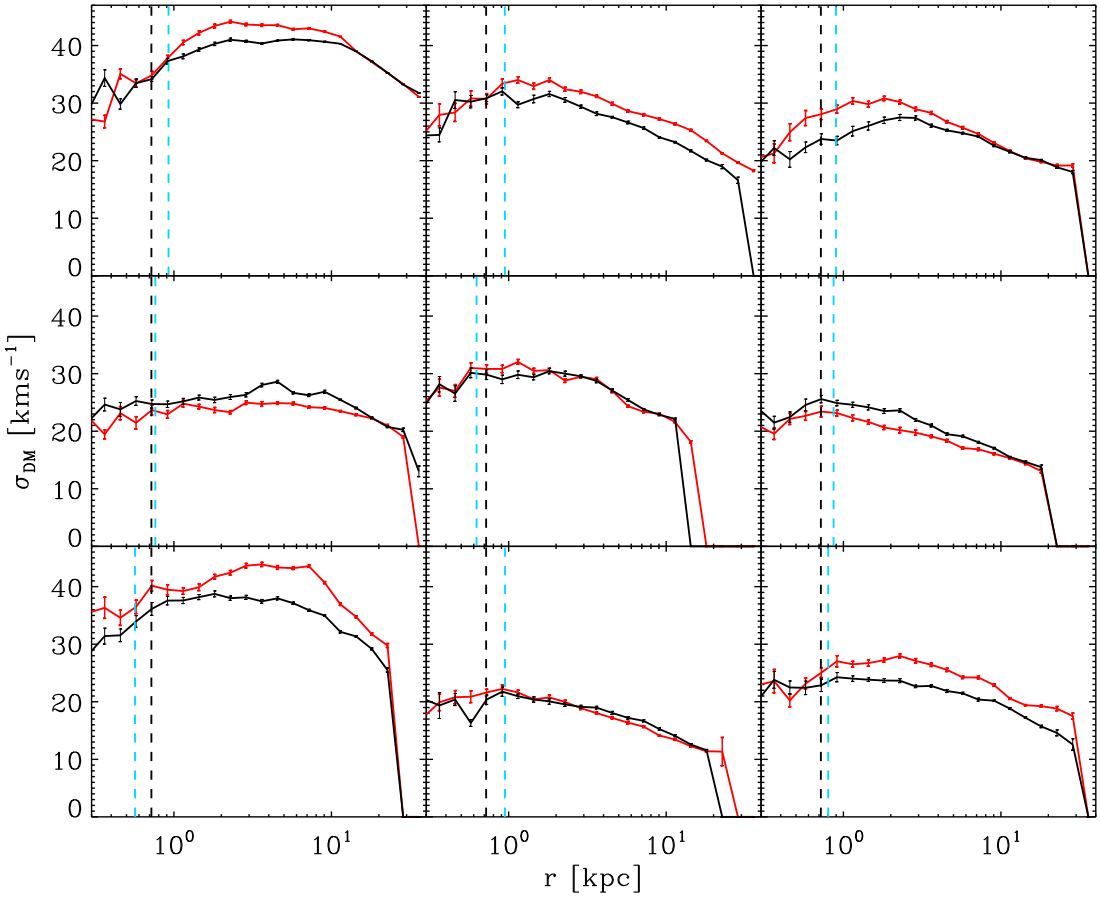

Figure 4.2 The spherically averaged 1D velocity dispersion profiles of the most massive satellite galaxies in our high resolution hydrodynamic (red) and dark matter only (black) runs. Error bars are obtained by bootstrap resampling. The comparisons are made at the redshift when the galaxy is first accreted as a satellite, which is indicated on the corresponding panels in Fig. 4.1. Black dashed vertical lines indicate the scale on which softened gravitational forces become fully Newtonian. Blue dashed vertical lines indicate the convergence radius of Power et al. (2003).

(FOF; Davis et al., 1985) group. [1] The differences in the subhalo density profiles with and without baryons clearly exceed the uncertainties associated with finite sampling, indicated by the error bars. They are also greater than, for example, the differences expected between dark matter realisations of the same subhalo at different resolutions (Springel et al., 2008b). Some subhaloes (e.g. top left and centre right panels) appear to have been largely unaffected, whilst others (e.g. top and bottom right panels) show more substantial changes of up to thirty percent in some radial bins. In Section 4.5, we describe an extreme example of a subhalo which suffered much more extensive damage as a result of baryonic processes. In general, however, there does not seem to be any consistent trend for baryons to increase or decrease the central density of the dark matter.

In Fig. 4.2, we show spherically averaged dark matter velocity dispersion profiles for the same selection of satellites in Aq-C-4 and the DMO run. The largest differences are seen in those subhaloes that show the most change in their density profiles in Fig. 4.1. Once again, the differences are typically less than ten percent in any given radial bin, but as much as thirty percent in some instances, with no apparent trend for baryons to raise or lower the dark matter velocity dispersion.

From these results, we conclude that the baryons have had a relatively small impact on the dark matter phase-space structure of the subhaloes, with the important caveat that it is unclear whether such effects are limited by the resolution of our simulations. Another important factor contributing to this conclusion is the strength of our feedback, since it dictates how easily baryons are able to condense in the centre of low mass haloes and affect the dynamics of the dark matter. Models with much weaker feedback might achieve more pronounced differences than we see here, but as we will show in Section 4.4.1, such models typically overpredict the luminosities of satellite galaxies.

Although some satellites are accreted at fairly high redshift (see the labels on each panel in Fig. 4.1), it is unlikely that the baryons would have an increased effect in the remaining time to $z = 0$. In all but the largest satellites, gas is lost fairly rapidly following accretion, as we will show in Section 4.3.2.

[1] In practice, we require the subhalo to be counted in the main FOF group for two consecutive snapshots to avoid instances where subhaloes are spuriously joined to the main group for a short time.

4.3 Convergence of Satellite Properties

In this section we investigate the convergence of various key properties of our simulated satellite galaxies. We make the comparison on an object-to-object basis, matching up satellites between runs. As explained in Section 4.2, this cannot be accomplished simply by choosing subhaloes that are spatially closest at the final time. Instead, we trace particles back to the initial conditions and match them spatially there. In the following analysis we consider the most massive satellites in Aq-C-4 for which resolved counterparts exist in Aq-C-5 and often also in Aq-C-6.

4.3.1 Stellar Mass

We begin by considering the total stellar mass in each satellite at $z = 0$. This is a function of the rate at which gas can cool onto the galaxy and the efficiency of star formation, dictated by the gas physics and feedback. As well as checking that our results do not depend on resolution, we compare with an independent modelling technique, presented by Cooper et al. (2010), hereafter C10. They used the Aquarius simulations to track the formation of dark matter substructures in six different haloes and a version of the semi-analytical galaxy formation code GALFORM to compute the baryonic properties of satellite galaxies.[2] At each output time, the stellar mass formed since the last simulation snapshot is assigned to some fraction of the most tightly gravitationally bound dark matter particles in the subhalo, providing spatial and kinematic information for the stars. The 'tagged' fraction was chosen to match the distribution of sizes (half-light radii) for Local Group satellites and also to produce results robust to changes in resolution.

Fig. 4.3 demonstrates that the stellar mass in each subhalo agrees relatively well between the three resolutions, particularly for the most massive examples, although the difference is as large as a factor of six in one case. Some of this scatter (between different resolutions and between the semi-analytical and hydrodynamical realisations) is likely related to the deviations in subhalo orbits between simulation runs described in Section 4.2. Small differences in pericentric distance and eccentricity can strongly affect the tidal field and hence the extent to which stars can be stripped from subhaloes. Examples

[2]Their semi-analytical model is essentially that presented by Bower et al. (2006), but with a lower circular velocity threshold ($30\ \mathrm{kms}^{-1}$) to identify haloes in which cooling is suppressed by reionisation. This value is motivated by recent hydrodynamical simulations (Hoeft et al., 2006; Okamoto et al., 2008a).

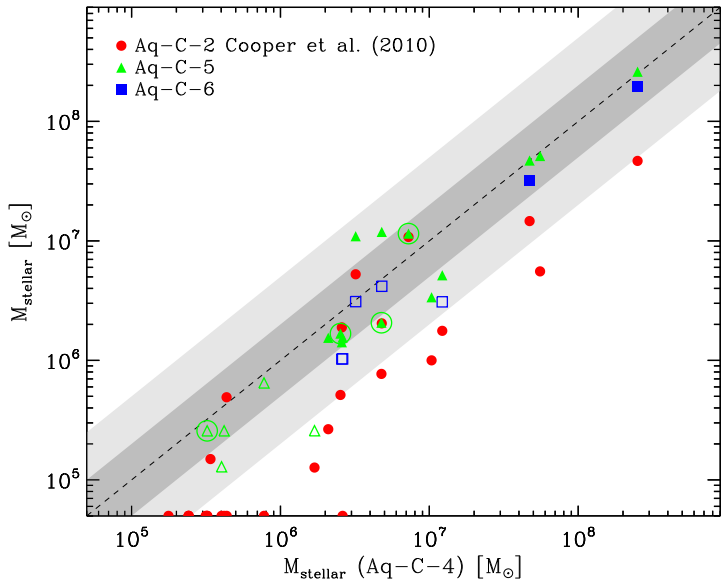

Figure 4.3 A comparison of the stellar mass that forms in each satellite at the three different resolutions of our hydrodynamical runs, as well as in the independent semi-analytical model presented by Cooper et al. (2010). Note that not all satellites in the high resolution run have resolved counterparts at intermediate and low resolution. Points that lie on the abscissa correspond to subhaloes with $M_{\rm stellar} < 5 \times 10^4\ {\rm M}_\odot$. Data points are plotted for all satellites in the high resolution run with more than ten star particles. If the satellite also has ten star particles in the lower resolution run, it is plotted as a filled, rather than open symbol. Satellites that have lost more than 50 percent of their maximum stellar mass through tidal stripping are indicated by circled points. The dark and light gray shaded regions represent factors of two and five respectively away from the line of equality.

of subhaloes that have lost more than 50 percent of their peak stellar mass (excluding the effects of stellar evolution) in one or more of the runs are indicated in Fig. 4.3 by circled points.

The C10 prescription typically predicts a lower stellar mass in each subhalo, although the correlation indicates that the ranking of subhaloes by stellar mass is similar to that in our simulations. This offset between the two techniques is not obviously attributable to a single aspect of either model, but one mechanism that may be important is ram pressure stripping. In the semi-analytical model, any hot gas is instantaneously stripped from satellites upon infall. In combination with strong SNe feedback, this quenches star formation in satellites very rapidly following accretion. As we will show in the next subsection, ram pressure and feedback act to produce a similar effect in our simulations, but star formation is able to continue for an appreciable time after accretion and right up to $z = 0$ for the most massive satellites.

4.3.2 Mass Evolution

We now examine how satellites in the three runs acquire their dark and baryonic mass and form stars. Fig. 4.4 shows the gravitationally bound mass of dark matter, stars and gas for the nine most massive satellites as a function of redshift. For reference, we also include Table 4.1, which lists the masses at $z = 0$. Reionisation ($z = 9$) is marked with a vertical dashed line and arrows indicate the accretion time, that is, the time when the galaxy first becomes a satellite in the high resolution run. Where the accretion times differ slightly between runs, the value for the high resolution case is shown.

Apart from numerical convergence, which we will discuss next, there are a number of interesting features to note in Fig. 4.4, many of which were also observed in the simulations of Okamoto et al. (2010), Wadepuhl & Springel (2010) and Sawala et al. (2011). There are instances of satellites being periodically stripped of mass as they pass through pericentre, most obviously the satellite tracked in the bottom right panel, which loses dark matter and gas from its outer parts in two close approaches. None of these massive satellites appear to be on orbits with sufficiently high eccentricity and/or a close pericentre to strip the more tightly bound stellar component, although there are several examples of satellites in the simulation that were heavily stripped or disrupted entirely and hence are not among the most massive at $z = 0$.

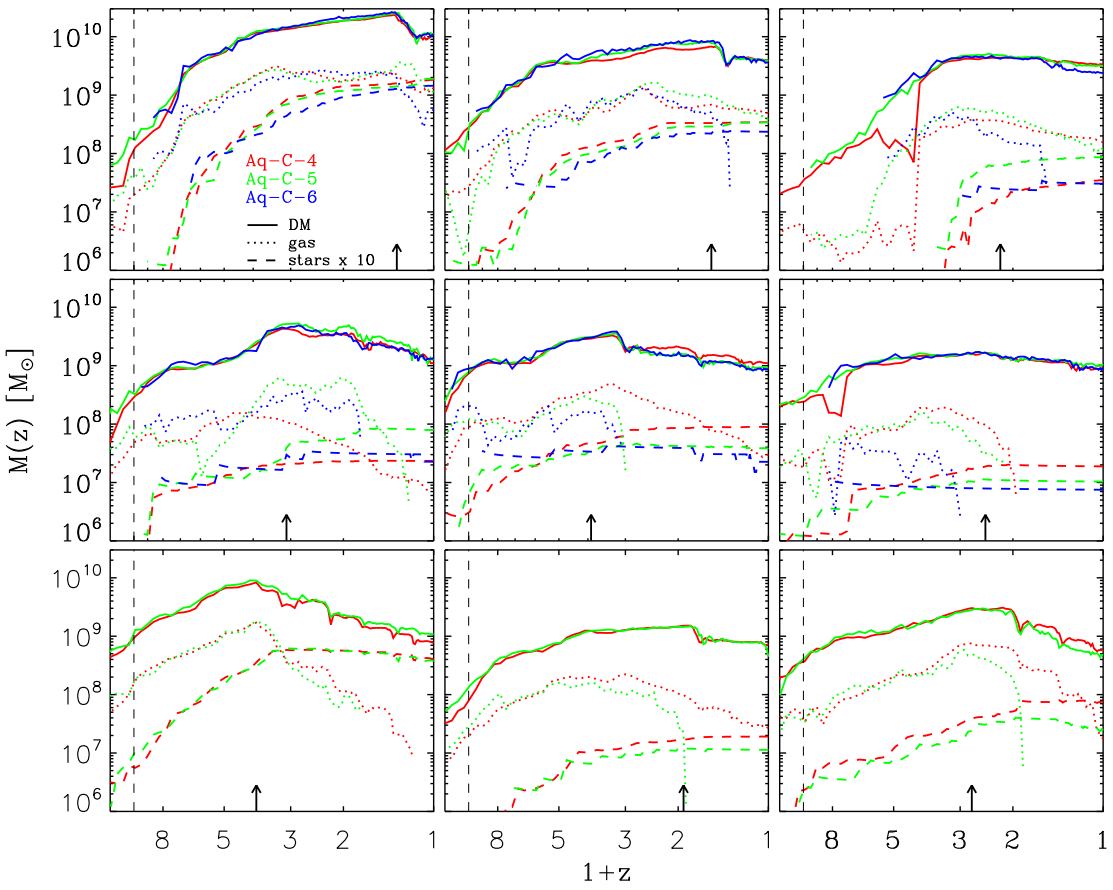

Figure 4.4 The mass evolution in dark matter (solid lines), stars (dashed lines) and gas (dotted lines) for the nine most massive satellite galaxies in our Aq-C-4 (red), Aq-C-5 (green) and Aq-C-6 (blue) simulations. Note that no resolved counterpart was identified in the Aq-C-6 simulation for the satellites tracked in the bottom row of panels. Stellar masses are scaled up by a factor of ten to reduce the range of the ordinate axis. The vertical dashed line indicates the redshift of reionisation and arrows the epoch at which the galaxy was first accreted as a satellite in Aq-C-4. The panels are ordered by total mass, from left to right along each row, beginning at the top.

$M_{\rm DM}$ $[10^6 {\rm M}_\odot]$	$M_{\rm gas}$ $[10^6 {\rm M}_\odot]$	M_* $[10^6 {\rm M}_\odot]$
14822.3	1734.8	250.5
14236.2	584.1	27.7
5436.6	678.1	47.2
4634.8	215.2	4.8
1548.1	0.0	3.2
1496.5	40.6	12.2
1229.1	0.0	2.6
1049.7	0.0	55.4
1001.8	37.6	2.6

Table 4.1 The mass in dark matter, gas and stars gravitationally bound to the nine most massive satellites at $z = 0$

The loss of gas following accretion in most cases is fairly rapid and is brought about through a combination of ram pressure stripping and stellar feedback. As noted by both Okamoto & Frenk (2009) and Wadepuhl & Springel (2010), reionisation appears to have virtually no impact on satellites this large (the lowest mass example in Fig. 4.4 has final total mass of 5×10^8 ${\rm M}_\odot$); the gas mass rises steadily through $z = 9$, and star formation continues unabated. We note that the three largest satellites retain a substantial amount of gas and are still increasing their stellar mass at the present day, analogously to the ongoing star formation in the MW dIrrs.

In terms of numerical convergence, in most respects, there is good agreement between the three resolutions. The exceptions to this are the rate at which gas is lost from some satellites following accretion and the resulting effect on the late-time star formation rates. In most cases, there is a clear tendency for more efficient ram pressure stripping with decreasing resolution. This effect appears to be related to the force resolution, which results in gas particles in lower resolution runs being less tightly bound and hence more susceptible to ram pressure stripping. The slightly different timescales over which satellites are able to retain their gas and continue to form stars account, at least in part, for the often lower final stellar masses in Aq-C-5 and Aq-C-6 noted in the previous subsection.

4.4 Observed Properties

In the previous section, we demonstrated that our model produces satellite galaxies with properties that show reasonable convergence with resolution and stellar masses that scale with subhalo mass in a fashion expected from an alternative modelling technique. We now proceed to examine how well their observable properties match those of the Local Group satellites. Where photometric quantities are required, we use the stellar population synthesis model PEGAS$\acute{E}$ (Fioc & Rocca-Volmerange, 1997), summing the luminosities of all star particles gravitationally bound to the subhalo at $z = 0$.

4.4.1 Satellite Luminosity Function

One of the most fundamental properties of any galaxy population is its luminosity function. Encoded in its shape and normalisation are a range of physical processes that are key to understanding the formation and evolution of the population.

In Fig. 4.5 we plot the luminosity function of simulated satellites at each resolution. Also plotted is the (completeness-corrected) average luminosity function for MW and M31 satellites from Koposov et al. (2008) that includes the SDSS ultra-faint objects. We find good agreement between resolutions at all resolved luminosities, consistent with the convergence of stellar masses and star formation histories demonstrated in Section 4.3. The simulated populations provide good matches to the Local Group average at the faint end, consistent with the findings of Okamoto et al. (2010) in another of the Aquarius haloes, but have no galaxy as bright as the Large Magellanic Cloud (LMC). The brightest galaxy (in Aq-C-4) has a similar V-band magnitude to that of the Small Magellanic Cloud (SMC).

Note that there is still a significant observational uncertainty in the total mass of the MW. Current estimates put it between 0.8 and 3×10^{12} $\mathrm{M}_{\odot}$ (Dehnen et al., 2006; Li & White, 2008; Xue et al., 2008; Watkins et al., 2010). Our halo has a mass slightly closer to the lower end of this range of $M_{crit,200} = 1.42 \times 10^{12} M_{\odot}$. Clearly, if we are simulating a halo twice or half as massive as the MW, we should not expect to reproduce the luminosity function of its satellites exactly. A further consideration is whether the MW has a typical satellite population for its halo mass or total luminosity. To this end, we have also plotted a black solid line and two shaded regions indicating the mean and

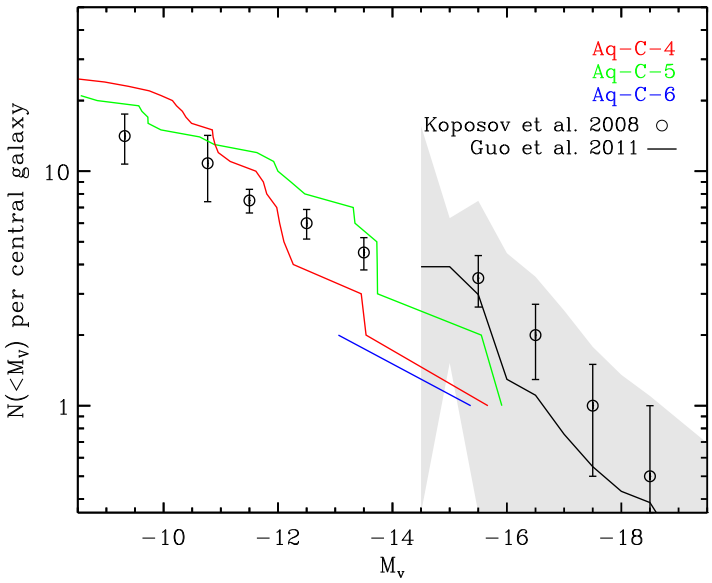

Figure 4.5 The rest frame, V-band luminosity function of satellite galaxies in our high (red), intermediate (green) and low (blue) resolution simulations. Circles with error bars indicate the average MW+M31 satellite luminosity function, corrected for completeness, by Koposov et al. (2008). For consistency with their data, only simulated satellites within 280 kpc of the central galaxy are included. The solid black line and shaded regions indicate the mean and spread in the satellite luminosity functions of Milky Way mass galaxies in an analysis of SDSS data by Guo et al. (2011). The light grey region shows the RMS scatter about the mean in each bin.

spread of the luminosity function (see figure caption for details) for satellite systems in the SDSS around central galaxies with r-band luminosity close to that of the MW (Guo et al., 2011). These data suggest that the Local Group is fairly typical, although satellites like the Magellanic Clouds are found in fewer than half of the systems in the sample. In another study, Liu et al. (2010) found that > 80 percent of MW-like galaxies have no satellite as bright as the SMC within 150 kpc. In this statistical context, perhaps the lack of very bright satellites in our simulations should not be a major cause for concern.

4.4.2 Sizes

An important and readily observable property of the most massive Local Group satellites is the distribution of their sizes, usually measured as the radius containing half the luminosity in projection. Unfortunately, a combination of the spatial resolution and the limitations of our subgrid model for star formation mean that we cannot hope to reproduce the observed sizes in our simulations. As explained in Section 3.2.2, a minimum pressure is maintained in star forming gas to ensure that the Jeans length on the equation of state, $\lambda_{\rm J,EoS}$, is always resolved. Our subgrid model assumes that stars form on much smaller (unresolved) scales, inside molecular clouds, but the star particles that are created must nonetheless inherit the dynamical properties of the SPH particle from which they formed. As a result, the minimum size of star-forming regions will be dictated by the warm/hot phase density and temperature, through $\lambda_{\rm J,EoS}$, or by the gravitational softening, if this is larger.

These limits are apparent in Fig. 4.6, where we plot the absolute V-band magnitude of simulated satellites as a function of their half-light radius. The observed half-light radii are de-projected by multiplying by a factor of $4/3$, an approximation that is accurate to 2% for the exponential, Gaussian, King, Plummer and Sersic profiles commonly used to fit the MW satellites (Wolf et al., 2010). The stars in both the Aq-C-4 and Aq-C-5 runs typically have much less concentrated distributions than the observed satellites. An exception to this is the third brightest satellite in Aq-C-4, which has a V-band magnitude of -12.2 and a half-light radius of ~ 480 pc. It has a very high mass fraction in stars and an unusual history, forming in a series of violent major mergers at $z \sim 4$ before being subjected to strong tidal disruption between $z = 2$ and $z = 0$. We discuss this satellite in detail in Section 4.5.

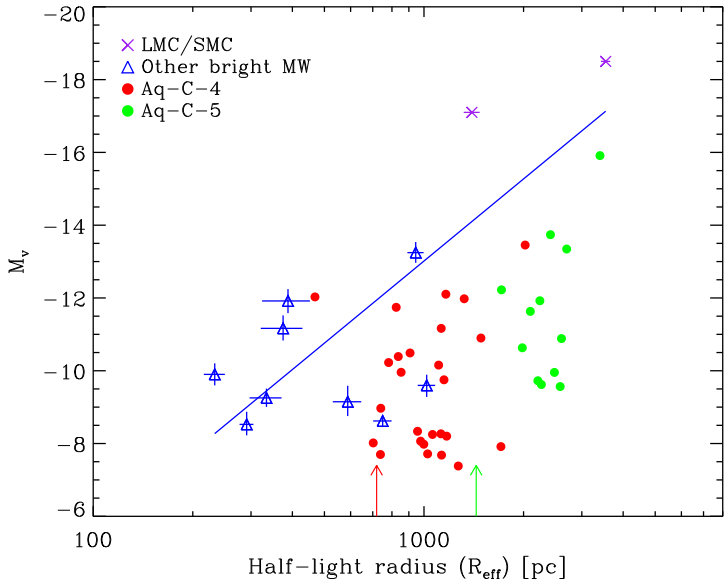

Figure 4.6 Absolute V-band magnitude as a function of de-projected half-light radius for satellite galaxies in our Aq-C-4 (red filled circles) and Aq-C-5 (green filled circles) runs. The Magellanic Clouds are represented by purple crosses. Their projected half-light radii were derived from angular values taken from Bothun & Thompson (1988) and distance estimates from Hilditch et al. (2005) and Pietrzyński et al. (2009). 3D half-light radii were calculated by multiplying these values by 4/3, as suggested by Wolf et al. (2010). All other MW satellites brighter than -7.5 (except Saggitarius) are shown as blue triangles with luminosity and de-projected half-light radii taken from Wolf et al. (2010). The solid blue line is a least-squares fit to all the observational data points. Arrows indicate the scales on which softened gravitational forces become fully Newtonian for each resolution.

In the highest resolution run, Aq-C-4, we expect the gravitational softening to be the main factor limiting the minimum sizes of star forming regions, since it is always larger than $\lambda_{\mathrm{J,EoS}}$. In Aq-C-5 and Aq-C-6 (not shown here), which have lower threshold densities for star formation by factors of four and sixteen respectively, $\lambda_{\mathrm{J,EoS}}$ at the threshold is comparable to the softening, so should also be important in setting the sizes of the stellar component. For both Aq-C-4 and Aq-C-5, the half-light radius of the most massive galaxy should not be limited by either effect and is consistent with the observations, given the large scatter.

4.4.3 Dynamical Masses

The stellar kinematical properties of Local Group dwarf galaxies provide an important test of the ΛCDM cosmology. Subhaloes that form in N-body simulations of MW-mass systems appear to have potentials compatible with the stellar kinematics of the brightest MW satellites (Stoehr et al., 2002; Strigari et al., 2010). Nonetheless, the analytic calculations required to reach such conclusions necessarily include simplifying assumptions. Hydrodynamic simulations attempting to model star formation self consistently in a cosmological setting are inevitably some way behind the best N-body simulations in terms of resolution and must also model uncertain baryonic physics on sub-kiloparsec scales. As such, our simulations are not suitable for studying the detailed kinematics of the stars directly; instead, we resort to a somewhat cruder comparison and ask whether our satellites form in realistic potential wells, by comparing simulated and observationally determined masses.

Historically there has been significant uncertainty associated with determining satellite masses from observations. Typically, estimates are derived from the line-of-sight stellar velocity dispersion with three key assumptions: i) the system is spherically symmetric, ii) stellar orbits are isotropic and iii) the system is in equilibrium. Two recent studies have attempted a more general approach, with the aim of reducing the systematic uncertainties. Using an approach based on the spherical Jeans equation, Walker et al. (2009) showed that for the brightest MW dSphs, the mass within the projected half-light radius is robust to changes in the anisotropy and underlying density profile. This relation was explained analytically by Wolf et al. (2010) who demonstrated that, if the stellar velocity dispersion profile remains relatively flat in the centre, as observations

suggest (e.g., Walker et al., 2007), then the uncertainty introduced by assuming a particular anisotropy is minimised at the (3D) radius where the logarithmic slope of the stellar number density profile, $-\mathrm{dln}n_*/\mathrm{dln}r = 3$. They also showed that, for a range of realistic light profiles that have been used to model the MW dSphs, this minimum lies close to the (de-projected) half-light radius. It is this radius, therefore, at which we choose to compare the enclosed masses of satellites in the simulations and observations.

In the previous subsection we described how aspects of our simulations, particularly the limitations of the subgrid treatment of the ISM and the gravitational softening scale, can set an artificial lower limit to the sizes of the stellar components of the satellites. However, we also demonstrated that the luminosity function of the simulated satellites is close to that observed, the stellar mass in each satellite is relatively well converged and stellar mass is found to scale with subhalo mass similarly using an alternative modelling technique.

With these checks in mind, we proceed with the assumption that the cooling, star formation and feedback prescriptions in our model result in a realistic stellar mass in each satellite, but that stars form in a configuration that is too diffuse. We then ask what the projected half-light radius of each simulated satellite *should be* at a fixed luminosity, based on the observed sizes of the brightest MW satellites. We take a simple least-squares fit to the data points in Fig. 4.6 (minimising the sum of the squared differences in the magnitude coordinate) and compute the scatter in the (log) radius coordinate about this line. For each simulated satellite, we assume a Gaussian distribution of possible sizes, with a mean equal to the fit evaluated at the satellite's luminosity and dispersion defined by the observed scatter.

Following this procedure we find that, for magnitudes $M_\mathrm{V} > -12$, our fit to the observed data implies sizes below the scale at which softened gravitational forces become non-Newtonian in the Aq-C-4 simulation, which leads to an underestimation of the enclosed mass. We choose instead to measure the mass of each satellite in a much higher resolution dark matter only realisation of the simulation, Aquarius-C-2, which has a smaller softening scale by a factor of ~ 4, such that the fitted half-light radii of satellites down to $M_\mathrm{V} \sim -7.5$ are larger than the force resolution. The central masses measured in the higher resolution simulation are typically forty to eighty percent higher for the ten brightest satellites, but the difference can be a factor of three for satellites with $M_\mathrm{V} \sim -8$.

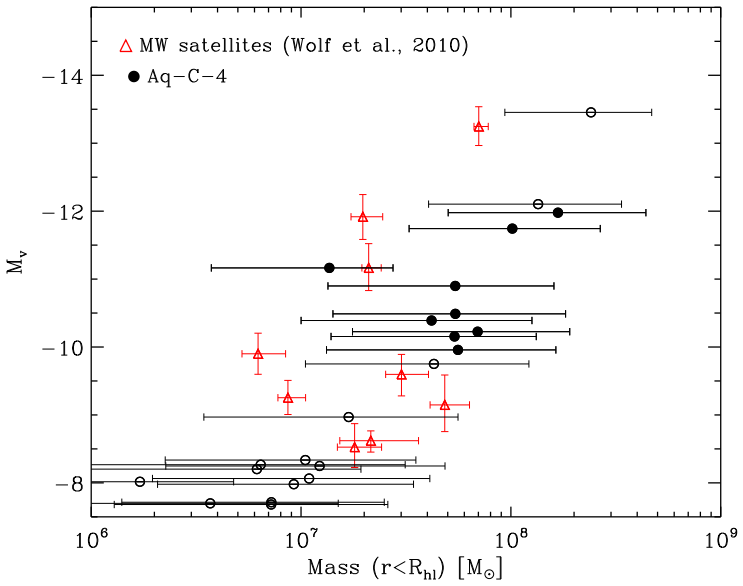

Figure 4.7 The total mass contained within the projected half-light radius ($R_{\rm hl}$) of simulated satellites, measured in the high resolution, dark matter only, Aquarius-C-2 simulation (open and filled black circles). The radii are inferred from the observed luminosity-size relation (see text for details). The filled circles indicate those satellites that are used in the statistical comparison with the observed data, illustrated in Fig. 4.8. The error bars on the simulated data points show the masses obtained by assuming half-light radii 1σ above and below the mean fitted values, where σ is determined by the scatter about the fit to the observed data. Red crosses with error bars are estimates from Wolf et al. (2010) for a selection of MW satellites.

Given the results presented in Section 4.2, we do not expect the omission of baryons from Aquarius-C-2 to have had a large impact on the central densities and hence the measured masses of these satellites.

Fig. 4.7 shows the mass enclosed within the mean half-light radius chosen for each satellite, with error bars indicating the masses corresponding to $\pm 1\sigma$ sizes. Although the range of plausible values is large, the brightest simulated satellites have mean masses three to five times higher than the MW satellites of the same luminosity. While there is less of a discrepancy at fainter magnitudes, our model seems to show a more gradual increase in luminosity with mass than is suggested by the observational data. We note that, starting from identical initial conditions to our Aq-C-4 simulation, Wadepuhl &

Springel (2010) found that the mass-to-light ratios of their satellites were typically higher than those quoted observationally by a very similar factor and were also more discrepant in the most massive satellites (see their Fig. 15). In a hydrodynamic simulation of the Local Group, again with resolution similar to our Aq-C-4, Knebe et al. (2010) found a similar result for satellites bound to their MW and M31 analogues, with mass-to-light ratios a factor ~ 7 too high. We note, however, that they measured half-light radii for their satellites using the star particles forming in their simulation, which, as we have shown, can be too large when the scales associated with star formation are not resolved.

To quantify the discrepancy in Fig. 4.7 statistically, we construct multiple realisations of the half-light masses of the simulated satellites by drawing sizes from the distributions described above and computing the mass enclosed in the corresponding high resolution Aquarius-C-2 satellites. We then combine the samples to define a model distribution for the cumulative fraction of satellites with mass larger than a given value and calculate the probability that the observed masses could have been drawn from it, using a one-tailed Kolmogorov-Smirnov (KS) test.

In order to make a like-for-like comparison with the masses quoted by Wolf et al. (2010), we consider only the $4^{th} - 12^{th}$ brightest simulated satellites in our Aq-C-4 simulation that are within 280 kpc, corresponding to all of the classical MW satellites except the Magellanic Clouds and Sagittarius, and including Canes Venatici (which is approximately the same luminosity as Draco). The sample is indicated in Fig. 4.7 by filled circles. Note that the third brightest satellite in Aq-C-4 is in the midst of tidal disruption (see Section 4.5), a process that, as a result of small differences in the orbits of the subhaloes, is already complete in Aquarius-C-2, hence no counterpart is found. Although Wolf et al. (2010) derived masses for fainter satellites, these correspond to simulated galaxies with fewer than ten star particles, whose luminosities are uncertain in our simulations and which we therefore choose to exclude. In Fig. 4.8 we plot cumulative model distributions, drawing masses for the sample of nine satellites multiple times to define each distribution, as indicated by the labels in the top left of the plot. The probabilities that the observationally derived masses are consistent with those distributions are found to be around six percent.

As both Fig. 4.7 and Fig. 4.8 demonstrate, the masses of the brightest simulated satellites are too high compared to those derived for the MW satellites. This is another man-

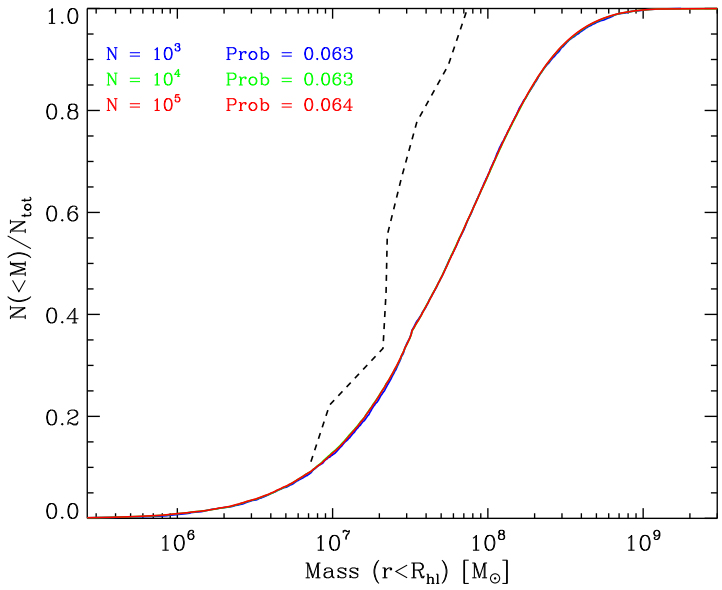

Figure 4.8 The cumulative fraction of the $4th - 12th$ brightest satellites as a function of the mass contained within the half-light radius in three model distributions (solid blue, green and red lines) and those derived for MW satellites by Wolf et al. (2010) (dashed line). Labels in the top left indicate the number of times we repeat the process of drawing masses for our sample of nine satellites in order to define the model distribution, along with the probability that each model is consistent with the observed masses.

ifestation of the problem recently highlighted by Boylan-Kolchin et al. (2011) who compared the measured masses within the half-light radii of the same satellites considered here with results from high-resolution simulations of cold dark matter haloes, including the Aquarius suite. Assuming an NFW density profile (Navarro et al., 1996b, 1997), they showed that the most massive subhaloes in the simulations are too concentrated to be able to host the brightest observed satellites.

The mismatch seen in Fig. 4.7 and in the results of Boylan-Kolchin et al. (2011) could, in principle, be due to an underestimate of the central masses of the observed satellites. However, for the errors quoted by Wolf et al. (2010) to be substantially underestimated would require rather extreme variations in the anisotropy profile, which would be poorly fit by their fairly general parameterised form. This seems unlikely to be the sole source of the disagreement between model and data.

While the discrepancy could be simply due to statistics, it might also reflect a seri-

ous shortcoming either of the standard CDM cosmogony or of current models of galaxy formation, such as those assumed in our simulations. A possible explanation of the discrepancy between the mass-to-light ratios measured for the real and simulated satellites is that the central dark matter densities predicted in the CDM model are reduced by baryonic physics. One mechanism for achieving this, proposed by Navarro et al. (1996a), is the condensation of a dense baryonic component followed by the rapid expulsion of gas by stellar feedback. The dark matter adjusts to this change in the potential by developing a central "core", shifting the rotation curve maximum to a larger radius and reducing the mass-to-light ratio in the central parts. This process does indeed appear to play an important role in the evolution of one satellite in Aq-C-4 (see Section 4.5), which forms in the subhalo that has the largest mass prior to accretion. If this process is common, it is possible that it is not seen here in less massive subhaloes due to lack of resolution.

A more radical explanation of the discrepancy is that the dark matter consists of warm, rather than cold, particles. In this case, subhaloes of a given mass form later and have lower concentrations than in the CDM model (see Navarro et al., 1997; Hogan & Dalcanton, 2000). Lovell et al. (2011a) have recently shown explicitly that the masses and concentrations of subhaloes in a warm dark matter model agree well with the data.

4.5 A Star-Dominated Satellite

The formation history of one of the satellite galaxies in our high resolution hydrodynamical simulation is particularly interesting. By $z = 0$, we find that it has become dominated by its stellar component, with a mass-to-light ratio of ~ 2.4 and its dark matter has become much less concentrated than otherwise similar subhaloes. It appears as an outlier in Fig. 4.6, as it has a very small half-light radius for its luminosity. In this section, we briefly describe its formation history and explain why it develops into such an unusual object.

At $z = 0$ the satellite is, in fact, in the process of being tidally disrupted and has a substantial stellar stream associated with it. Fig. 4.9 illustrates the structure of the stream in two orthogonal projections centred on the main galaxy. The dense stellar nucleus of the satellite that remains identifiable as a bound structure is also visible. We track all star particles associated with the satellite at the epoch when it is accreted and plot their

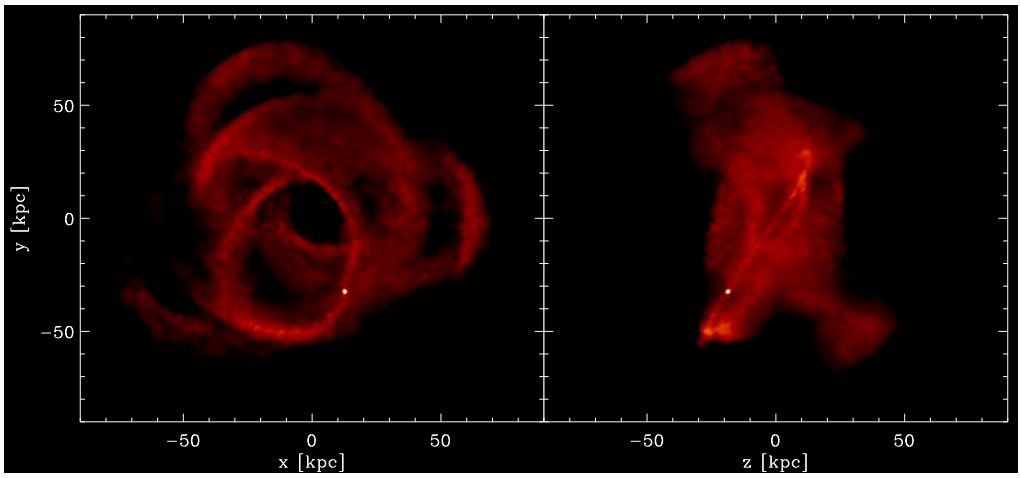

Figure 4.9 Two orthogonal projections, centred on the potential mininimum of the main halo, showing the stellar stream associated with the satellite. Projected stellar mass density is plotted on a white-to-red scale as indicated by the colour bar. The stream is defined by selecting all stars associated with the satellite at the time of accretion and locating them at $z = 0$. The surviving satellite is clearly seen as the bright concentrated object lying along the stream.

projected mass density at $z = 0$. The stripped stars account for a large fraction of the mass of the stellar halo of Aq-C-4, as we will demonstrate in Chapter 5.

The stream is a result of a fairly eccentric orbit with several close pericentres, illustrated in the bottom panel of Fig. 4.10, which shows the distance of the satellite from the centre of the main galaxy as a function of redshift. The dashed line indicates the virial radius of the main halo. The accretion time is the point where the two lines intersect. The top panel tracks the mass in gas, dark matter and stars bound to the satellite over the same redshift interval, as well as the total mass fraction in stars. At accretion, it is the brightest satellite of the central galaxy, but only the third brightest at $z = 0$, as a result of the reduction in stellar mass through tidal stripping. The stellar fraction at accretion (~ 0.02) is fairly typical of the surviving satellites. Note that it is very common for the stellar fraction of a satellite to increase with time after it is accreted, since the outer parts of the dark matter halo are less tightly bound than the stars and hence more susceptible to tidal stripping (e.g. Peñarrubia et al., 2008; Sawala et al., 2011). The middle panel of Fig. 4.10 shows the evolution of the central ($r < 1$ kpc) density of the subhalo in gas

and dark matter, both of which drop sharply when the satellite is close to pericentre. A decline is also evident after $z \sim 3$, well before the satellite is accreted, the origin of which we discuss in more detail below.

During the first few orbits, the stellar component remains unaffected while the dark matter lying beyond the radial extent of the stellar component is stripped. In fact, some of the dark matter particles with pericentres *within* the stellar component are also stripped, as a result of the dark matter having a higher radial velocity dispersion than the stars. The final masses of the stellar and dark matter components are factors of ~ 50 and 2×10^4 lower than their peak values respectively.

The extent to which the two components are stripped is strongly affected by their radial density profiles, which are shown in Fig. 4.11 at the time of accretion. The overplotted regions indicate the range of densities ($\pm 1\sigma$) in each bin for the nine most massive surviving satellites. Clearly, the stellar component of this galaxy is unsually concentrated relative to those other galaxies, whilst the dark matter and gas have shallower than average central density profiles. It is unclear how much effect the gravitational softening has in this respect, since forces begin to become sub-Newtonian on scales less than $\lesssim 720\ \mathrm{pc}$, but we note that the profiles also differ outside that radius. The highly 'cusped' stellar profile allows the central stellar nucleus to resist the strong tidal forces that unbind the majority of the dark matter. It also accounts for the unusually small half-light radius shown in Fig. 4.6.

The origin of these density profiles is related to the satellite's violent formation history. In a series of major mergers at $z \sim 3$, gas is funnelled to the centre of the main progenitor, initiating an intense burst of star formation that gives rise to a highly concentrated stellar distribution. The subsequent burst of feedback energy rapidly removes a large fraction of the gas and leads to a fall in the mean binding energy of the central dark matter. This episode is clearly visible in the middle panel of Fig. 4.10, which shows the central gas density drop as it is expelled by feedback and turned into stars, followed by a decline in the dark matter density in response to the change in the potential. This sequence of events is effectively the process originally proposed by Navarro et al. (1996a). The reduced binding energy of its central dark matter, along with an extreme orbit, combine to produce the unusual properties of this satellite at $z = 0$.

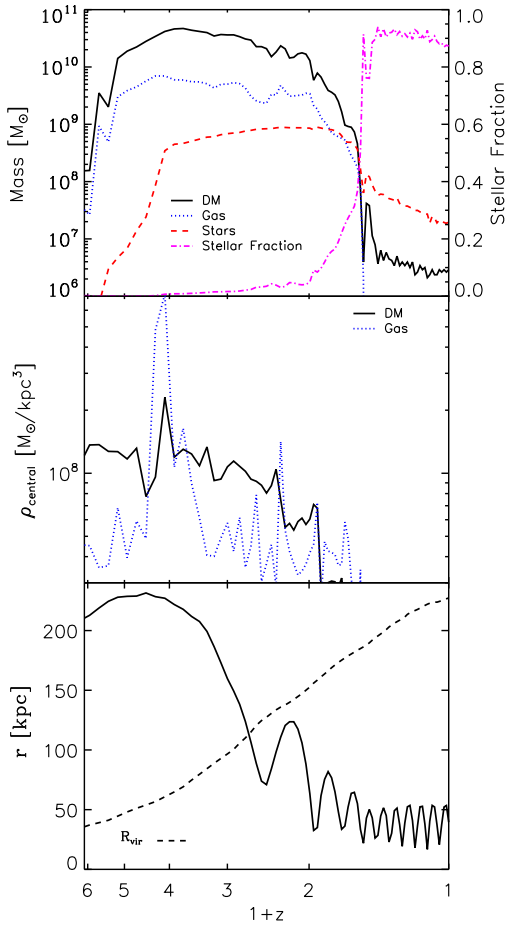

Figure 4.10 Top panel: the mass in gas (blue, dotted), dark matter (black, solid) and stars (red, dashed) gravitationally bound to the satellite's main progenitor, and the stellar fraction (magenta, dashed; measured on the right vertical axis) as a function of redshift. Some of the small variations in the masses (and hence also the stellar fraction) at $z < 1$ are due to the difficulty in identifying the subhalo's particles against the high background density at the centre of the main halo. Centre panel: the density of dark matter (black, solid) and gas (blue, dotted) within the central 1 kpc. Bottom panel: the distance to the satellite from the centre of the main halo. The dashed line indicates the virial radius of the main halo.

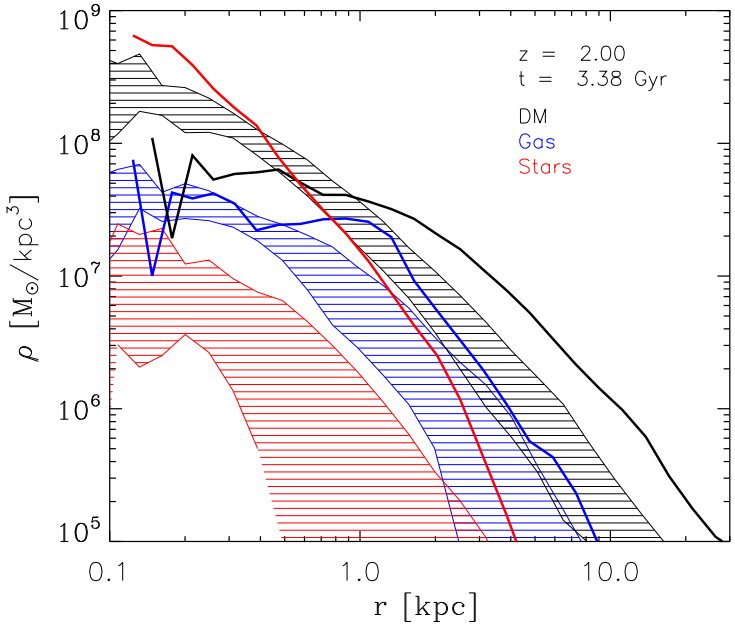

Figure 4.11 The dark matter (black), stellar (red) and gas (blue) density profiles of the galaxy at z $\sim$ 2, when it is first accreted as a satellite. Regions of the same colour indicate the spread of values ($\pm 1\sigma$) in each radial bin for the nine most massive surviving satellites at $z = 0$.

4.6 Summary

We have investigated the formation and evolution of a Milky Way-like satellite system in the set of simulations described in Chapter 3. The properties of our simulated satellites show relatively good numerical convergence, with the final stellar masses typically agreeing to within a factor of two, and always to within a factor of six. We also compared to an independent estimate of the stellar mass expected to form in each subhalo, using the semi-analytical model of Cooper et al. (2010). The two theoretical techniques produce a similar ranking of the subhaloes by stellar mass, although our simulations typically form a higher mass of stars by a factor of between two and six. This discrepancy may be partly explained by the assumption in the semi-analytical model that gas is stripped instantaneously when a galaxy becomes a satellite. The mass evolution in gas, stars and dark matter of each satellite agrees well between resolutions, except that gas is stripped more rapidly at lower resolution following accretion onto the main halo. Poorer force resolution causes gas particles to be more loosely bound to the subhalo and hence

more susceptible to ram pressure stripping. This phenomenon may account for many of the differences in the final stellar masses between resolutions.

By comparing the dark matter haloes of our satellite galaxies to those that form in a dissipationless version of the same simulation, we were able to quantify the expected impact of baryons on the phase-space structure of the dark matter. Due to small deviations in satellite orbits between different realisations of the same halo, it is necessary to make this comparison when the satellite first falls in rather than at $z = 0$. Although in some radial bins, in a few subhaloes, the density and velocity dispersion profiles are found to change by ~ 30 percent, the differences were typically less than 10 percent. With the caveat that the resolution of our simulation may limit the magnitude of such effects, we conclude that baryons have a relatively small impact on the structure of the dark matter haloes of satellite galaxies around MW-like hosts.

Our model provides a reasonable match to the faint end of the Local Group satellite luminosity function averaged between the Milky Way and M31, although there is a slight deficit at the bright end, with no LMC analogue. However, SDSS data (Liu et al., 2010; Guo et al., 2011) suggest that it is quite common for galaxies with luminosities like the MW to have no satellites as bright as the LMC and SMC.

Due to the limitations of the spatial resolution and the implementation of baryonic physics in our simulations, particularly the modelling of the multiphase ISM, stars do not form in sufficiently concentrated distributions to match the half-light radii of Local Group satellites. However, the reasonable agreement between the stellar masses in simulations with different resolution and different modelling techniques, combined with the match to the observed satellite luminosity function, suggest that the baryonic mass that is able to cool in each (sub)halo and form stars is realistic.

In order to test whether satellites of a given luminosity form in haloes with masses consistent with those observed, we compare their 'half-light masses' with values derived for a selection of the brightest MW satellites by Wolf et al. (2010). For this comparison, each satellite is assigned a distribution of half-light radii from the best fit to the observed luminosity-size relation and its variance. In the hydrodynamical simulation, the gravitational softening is comparable to these fitted half-light radii, so we instead measure the masses in a much higher resolution, dark matter only realisation of the simulation. We hence explicitly ignore any effects baryons may have had on the central density profiles,

which, in any case, the results in Section 4.2 suggest are small. The large scatter about the observed relation translates into a broad range of possible masses for each simulated satellite, but nonetheless, the mean masses for the brightest examples ($Mv < -11$) are about three to five times higher than their observed counterparts. The observed mass-luminosity relation seems to be somewhat steeper than that produced by our model, although due to the small sample sizes, the slope of the relation and the scatter about it are relatively poorly defined in both cases. A KS test, taking into account the uncertainties in the half-light radii assigned to the simulated satellites, returns a six percent probability that the observed masses could have been drawn from the distribution defined by the simulation data.

Although the apparent disagreement between the simulations and the data could be simply due to statistics, there are also a number of plausible physical explanations. It could be that baryonic processes significantly reduce the central dark matter densities of satellite galaxies. Possible mechanisms to achieve this include, for instance, a sudden change in the local potential, induced by the rapid expulsion of baryonic mass through stellar feedback (e.g. Navarro et al., 1996a) or heating due to bulk motions of dense clumps of gas (e.g. Mashchenko et al., 2006). The results in Section 4.2 imply that, if such processes are important, they are either not resolved in the Aq-C-4 simulation, or are not properly captured by our feedback prescription, except in one case, which happens to be the most massive subhalo at accretion. Less concentrated dark matter profiles would also result if the dark matter consists of warm, rather than cold particles (e.g. Lovell et al., 2011a).

The broad range of possible explanations of the discrepancy highlighted by our results illustrates how uncertain our understanding of galaxy formation still is on the scale of dwarf galaxies. Determining which, if any, is correct will be of critical importance in assessing the viability of the CDM cosmology and the success of galaxy formation models.

Chapter 5

Formation of the Stellar and Gaseous Haloes

5.1 Introduction

In this chapter, we further dissect the Aq-C-4 simulation discussed in the previous two chapters, identifying two additional components of the main galaxy that have not been discussed so far. In section 5.3, we investigate the formation of the stellar halo. As discussed in chapter 1, the dynamical and chemical properties of the stellar halo are potentially extremely valuable as observational probes of the formation histories of galaxies, particularly in the case of the MW and M31, where individual stars can be resolved. Stellar haloes and streams have also been observed in many nearby galaxies, suggesting that they are an inevitable consequence of the galaxy formation process (Sackett et al., 1994; Shang et al., 1998; Martínez-Delgado et al., 2009).

Several previous theoretical studies of stellar halo formation are discussed throughout section 5.3; those of Zolotov et al. (2009), Cooper et al. (2010) and Font et al. (2011a), which we will refer to as Z09, C10 and F11 respectively. Z09 employed a hydrodynamical simulation with resolution comparable to Aq-C-4 to highlight the distinction between halo stars formed *in-situ* and those *accreted* through mergers. The C10 study is of particular interest, since Aq-C was one of the six haloes they modelled, using the semi-analytical star-tagging technique described in chapter 4. Although the N-body simulations on which their models were based had a somewhat higher mass resolution (by about a factor of 30), they found that their haloes were predominantly built by the highest mass satellites, which should be well-resolved in our simulations, making it possible to directly compare the two methods. F11 took a different approach, using the GIMIC hydrodynamical simulations (Crain et al., 2009) to study stellar halo formation around

$\sim 400\ L_*$ galaxies at around 200 times lower mass resolution. Their statistical analysis is a useful reference with which to compare our single, high resolution case.

In section 5.4, we consider the properties of the hot diffuse gas that surrounds the main galaxy. The existence of hot gas around galaxies, groups and clusters is a fundamental prediction of ΛCDM galaxy formation models (White & Rees, 1978; White & Frenk, 1991). Milky Way-mass systems are expected to have virial temperatures high enough to place them in the 'quasi-hydrostatic' regime, such that gas pressure will restrict the rate of accretion from the IGM. As the models of White & Frenk (1991) (hereafter WF91) showed, thermal Bremsstrahlung and line-cooling in these hot haloes should lead to significant emission in the soft X-ray bands. X-ray coronae are commonly observed around elliptical galaxies (e.g. Jeltema et al., 2008), but it is very challenging to distinguish gas that may be accreting from the IGM in the manner described by WF91 from gas associated with supernovae and AGB stars (e.g. Read & Ponman, 1998) or with the group environments where such galaxies are typically found (e.g. Trinchieri et al., 1997). Isolated disk galaxies, particularly those with an edge-on orientation, offer a much cleaner test of the paradigm. Observations of such galaxies have, however, often resulted in either non-detections or measured X-ray luminosities one to two orders of magnitude below those predicted by the analytic WF91 model (e.g. Strickland et al., 2004; Wang, 2005; Owen & Warwick, 2009). When X-ray emission is observed, it is typically identified with supernovae outflows, rather than accretion, a conclusion motivated by a correlation between X-ray luminosity and star formation rate as well as the bi-conical form of the X-ray emission in a few cases.

A convincing explanation of the discrepancy between the X-ray observations and theoretical expectations was provided by Crain et al. (2010a). They used hydrodynamical simulations with the GIMIC code to demonstrate that, although the basic WF91 picture of the formation of quasi-static hot haloes appears to hold, the model overpredicts X-ray surface brightnesses for two reasons. Firstly, it includes a contribution from gas that should, in fact, be used up in star formation or expelled by stellar feedback. Secondly, it assumes that the hot gas traces the dark matter distribution. In reality, entropy injection by supernovae and the removal of low entropy gas through star formation results in a much more diffuse distribution and a much reduced surface brightness.

Further support for quasi-static hot halo formation comes from a recent analysis of

X-ray data by Crain et al. (2010b). They found that K-band luminosity and X-ray temperature scale with X-ray luminosity in a similar way regardless of the (optical) morphology of the galaxy. This may suggest that most of the hot gas around these galaxies comes from the same process, namely the shock-heating and compression associated with direct accretion from the IGM.

In section 5.4 we examine the properties of the hot gas around the main galaxy in the Aq-C-4 simulation and investigate its origin. To our knowledge, this represents the highest resolution ab-initio hydrodynamical study of hot halo formation yet carried out. In order to study both the hot gas and stellar haloes, it is first necessary to identify which of the baryonic particles belong to each component; the procedure we use is outlined next.

5.2 Identifying Halo Particles

Our analyses of the hot gas and stellar haloes include all baryonic mass within the virial radius ($r_{\rm crit,200}$) that is not gravitationally bound to a resolved satellite, with the exception of the disk. Satellites are identified using the SUBFIND algorithm, as described in Section 4.1.1. The disk is identified and subtracted using the following procedure, which is similar to that described by Scannapieco et al. (2009). We define the orbital circularity ϵ of each baryonic particle as in Eqn. 3.14, where the 'z' direction is defined by the net angular momentum of all baryons within $0.1r_{\rm vir}$. Fig. 5.1 illustrates the distribution of gas particles (left panel) and star particles (right panel) in the $radius - \epsilon$ plane for the Aq-C-4 simulation.

Two 'disk' structures are evident in the distributions of both gas and stars at $\epsilon \sim 0.65$ and $\epsilon \sim 1.0$. The first of these is the dominant stellar disk, extending to around 30 kpc with a substantial amount of associated gas that extends to much larger radii. The other disk contains less stellar mass, is gas dominated and is well alligned with the net baryonic angular momentum. The distribution of gas in this second disk joins up smoothly to gas being accreted from the halo. This is the same structure alluded to in Section 3.6.8, which forms as a result of the tilting of the existing baryonic disk by torques from the massive satellites with close pericentres. The second disk hence represents the result of newly accreted gas. As expected, its stars are much younger than those in the

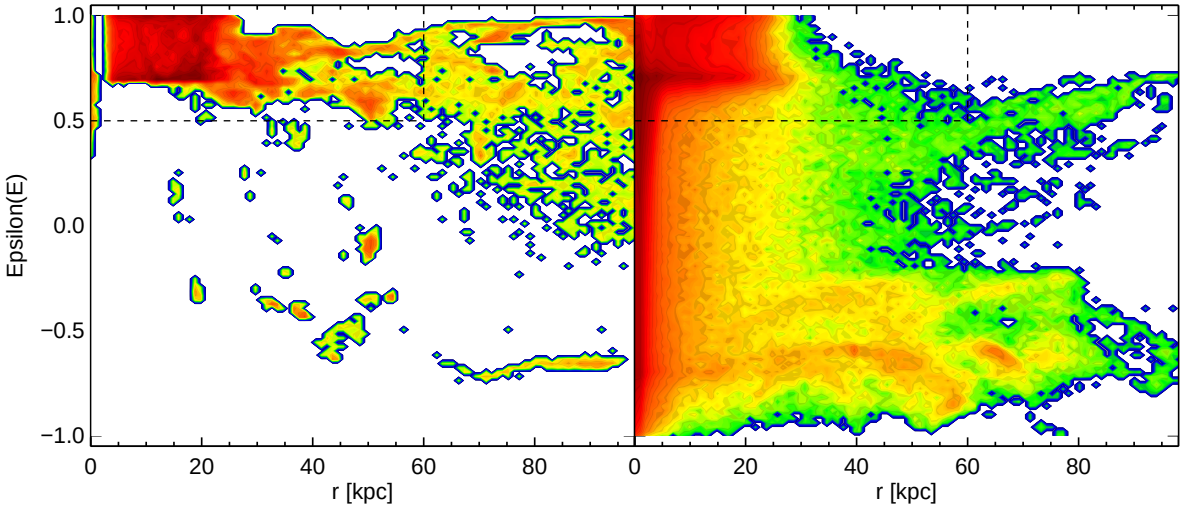

Figure 5.1 The distribution of gas particles (left panel) and star particles (right panel) in the $radius - \epsilon$ plane, with coloured contours indicating the density of points from high (red) to low (blue). Dashed lines indicate the region of the plane chosen to identify the disk component.

main stellar disk and it accounts for most of the galaxy's ongoing star formation.

A dispersion dominated component is visible in the inner few kpc, with orbits that are effectively randomly orientated, which would conventionally be identified as a bulge. It is unclear whether drawing a distinction between the bulge and the halo components is useful, given that their formation mechanisms undoubtedly overlap and there is no clean divide between them spatially or kinematically. However, we will assume $r_{\rm bulge} = 3$ kpc, in order to compare directly to the results of C10, which is in fact close to the value suggested by a photometric decomposition of the two components, as we will show in subsection 5.4. At least two prominent stellar streams are identifiable at $\epsilon \sim -0.4$ and $\epsilon \sim -0.7$. The latter example is associated with the satellite discussed in detail in Section 4.5 being disrupted, with stars only recently unbound from the core visible as a clump at $r = 40$ kpc. This satellite contributes significantly to the stellar halo and is referred to several times in this chapter; for convenience we will label it "sub1".

Any attempt to dynamically decompose simulated galaxies into spheroid and disk components tends to involve an unavoidably arbitrary choice of parameters. We find that the criteria $\epsilon > 0.5$ and $r < 60$ kpc describe the stellar disk(s) and most of the

extended gas disk. With these high angular momentum particles subtracted from the inner regions, we are left with a spheroidal distribution of gas and stars, which is a superposition of i) the galaxy bulge, ii) the stellar halo, iii) the hot gas halo and iv) a small amount of cool gas, most of which is in the process of accreting onto the disk. We will discuss the properties of both iii) and iv) in Section 5.4, but first we investigate the formation of the stellar component.

5.3 The Stellar Halo

We begin our discussion of the stellar halo in Aq-C-4 with a summary of its bulk properties, which are listed in table 5.1. The second column lists the properties for the outer spheroid, excluding the 'bulge' in the inner $3\ \mathrm{kpc}$. The outer halo accounts for ~ 16 percent of all stellar mass within $r_{\rm vir}$, significantly larger than the range $0.1 - 1\%$ typically quoted for the MW, though it is not obvious what fraction of these stars might be identified with the bulge observationally. As has been shown by several past theoretical studies, the outer stellar halo is much more concentrated than its dark matter host, with a half mass radius of $12\ \mathrm{kpc}$, compared to $78\ \mathrm{kpc}$ for the dark matter. The outer halo has a slightly higher mean $[\mathrm{Fe/H}]$ than the value of -1.5 typically quoted for the MW (e.g. Sesar et al., 2011), although we note that most observational studies tend to include very few stars inside 10kpc, in order to avoid disk contamination. Considering only stars outside 10kpc, we find $\langle[\mathrm{Fe/H}]\rangle$ of -1.5. The mean value of $[\mathrm{O/Fe}]$, an often-used proxy for $[\alpha/\mathrm{Fe}]$, is roughly consistent with the range found for halo stars in the MW (Nissen & Schuster, 2010). The radial variation of both $[\mathrm{Fe/H}]$ and $[\mathrm{O/Fe}]$ are investigated in more detail in subsection 5.3.4.

In much of the following discussion, we will distinguish between halo stars that form *in-situ*, within the main progenitor and those that are brought in by mergers, the *accreted* component. In practice, this is achieved by tracing back all stars belonging to the halo at $z = 0$ and assigning them to the accreted component if they were ever gravitationally bound to a (sub)halo other than the main progenitor. We confirm the findings of several previous studies that the outer halo is predominantly accreted, with $f_{\rm acc} = 0.52$, increasing to ~ 0.7 if the central $10\ \mathrm{kpc}$ are excluded. The inner halo (bulge) forms almost exclusively in-situ, though we note that the merger history of Aq-C is fairly quiet rela-

Table 5.1 Bulk properties of the stellar spheroid in Aq-C-4 . Values are listed for the total (r $<r_{\rm vir}=$ 227 kpc) and outer (3 kpc $<$ r $<r_{\rm vir}$) halo. The value of 3 kpc was chosen in order to directly compare to the stellar halo model for Aq-C presented by Cooper et al. (2010). $M_{\rm tot}$ is the total stellar mass, $L_{\rm V}$ the total V-band luminosity, $r_{\rm half-mass}$ the radius containing half the stellar mass and $r_{\rm half-light}$ the radius containing half the V-band light. $\langle$[Fe/H]$\rangle$and $\langle$[O/Fe]$\rangle$are the logarithms of the respective mean abundance ratios, normalised to the solar values. $f_{\rm acc}$ is the fraction of the halo that was accreted from satellites and $f_{\rm sur}$ the fraction from satellite that survive to $z = 0$.

	Total	Outer
$M_{\rm tot}[10^9$ M$_\odot]$	25.8	6.7
$L_{\rm v}[10^8 L_\odot]$	62.3	21.9
$r_{\rm half-mass}$[kpc]	2.3	12.1
$r_{\rm half-light}$[kpc]	2.3	14.3
$\langle$[Fe/H]$\rangle$	-0.5	-1.3
$\langle$[O/Fe]$\rangle$	0.35	0.39
$f_{\rm acc}$	0.13	0.52
$f_{\rm sur}$	0.04	0.10

tive to the other Aquarius haloes, which are themselves quieter than the average for all $\sim 10^{12}$ M$_\odot$ haloes in the Millennium II cosmological simulation (Boylan-Kolchin et al., 2010). Stars stripped from satellites that survive to $z = 0$ account for only 4% of the halo in total, and 10% of the outer halo.

The two component nature of stellar haloes has been emphasised by several recent hydrodynamical studies (Zolotov et al., 2009; Font et al., 2011a; Scannapieco et al., 2011) and is also evident in our simulations. It has even been claimed that the MW halo can be separated into two kinematically and chemically distinct parts (Carollo et al., 2010), which could be a signature of the different modes of star formation seen in the theoretical models (Zolotov et al., 2010). In the following subsections we examine the origins of in-situ and accreted halo stars.

5.3.1 The Accreted Component

In the MW halo there is an abundance of substructure, with many prominent stellar streams and overdensities. Qualitatively, such features are straightforward to explain in hierarchical models; dwarf galaxies form stars early, fall into the deeper potential wells associated with more massive galaxies and are tidally stripped or disrupted entirely. In Aq-C-4, these processes generate a significant amount of structure with morphology similar to features in the MW halo. This is illustrated by Fig. 5.2, in which we show a 160 kpc x 160 kpc map of the V-band surface brightness. Only the accreted component is shown, in order to highlight some of the structure in the central regions, which is obscured if the smoother in-situ contribution is also included. Several well-defined streams are visible, including that belonging to the main contributor (sub1), its most recent orbit arcing from the 1 o'clock to 5 o'clock positions and the previous one from 6 o'clock to 12 o'clock, passing just to the left of centre in this projection. Note that existing satellites are not included here; the clump embedded in the stream consists of stars only recently unbound from the surviving core. At least two fainter streams generated in recent accretion events are visible towards the bottom left, as well as significant structure in the region between 20 and 60 kpc from the centre.

Much of the more diffuse background in the image can be attributed to stars added to the halo at high redshift, which have had sufficient time to phase-mix by exchanging energy. Comparing with the C10 model of Aq-C, we find that many of the same features are identifiable, most obviously the dominant stellar stream. The central regions of our accreted halo tend to look more spherical (also in other projections) than in C10, which may reflect the influence of baryons on the central potential found by Kazantzidis et al. (2010) and suggested by results in Chapter 3 (see discussion of Fig. 3.20). Much of this light would conventionally be attributed to the galaxy bulge, which we have so far defined arbitrarily to be the central 3kpc of the spheroid. In subsection 5.3.3 we consider the distribution of mass and light in a quantitative fashion and investigate whether a two component bulge+halo model provides a good description of the radial profile.

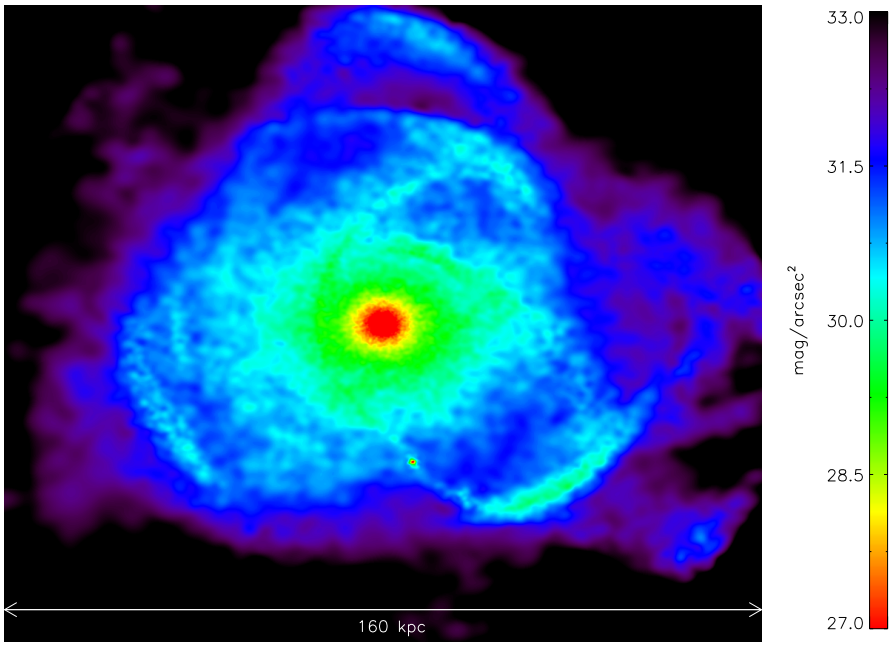

Figure 5.2 A map of the V-band surface brightness, as indicated by the colour bar, for the accreted component of the Aq-C-4 stellar halo, projected through a cube 160 kpc on a side.

5.3.2 The In-Situ Component

While accreted stellar haloes are understood to be a natural consequence of hierarchical structure formation, the existence of in-situ halo stars is much less easily explained in the context of the standard (idealised) picture of star formation in dark matter haloes. The complex nature of gas accretion onto galaxies, highlighted by recent ab-initio hydrodynamical simulations, suggests several plausible formation mechanisms for in-situ stars. Cold and potentially star forming gas can exist outside of the central galaxy i) as a result of thermal instability in the hot halo, ii) having been stripped from an orbiting satellite or iii) as part of a large scale inflow. The last of these is often termed *cold accretion* and occurs when the cooling time of gas is shorter than the time taken to free fall to the centre of the dark matter halo (Rees & Ostriker, 1977; White & Frenk, 1991). In this regime, the gas achieves much higher densities before thermalising its infall energy and a shock forms closer to the central galaxy, rather than around the virial radius (Birnboim & Dekel, 2003). Cold accretion is mostly seen in low mass haloes, which have lower virial temperatures, and at high redshift, when accreting gas has higher density. It is

also seen in more massive haloes if gas is fed in along collapsed filaments, which can in fact co-exist with a "classical" hot halo (van de Voort et al., 2011). Gas entering the halo at such densities could potentially be eligible to form stars and hence contribute to the in-situ halo. A fourth, more conventional, explanation is that in-situ stars formed within the main galaxy disk and were subsequently scattered to larger radii by, for instance, the nuclei of satellite galaxies in the final stages of mergers. Scattering in this way could also redistribute stars formed in the inner portions of cold flows, which was the mechanism found to be dominant by Z09.

To understand the distribution of in-situ stars at $z = 0$, it is instructive to consider the galacto-centric radii at which they formed, relative to the virial radius at that time. We plot the cumulative distribution of this quantity in the left panel of Fig. 5.3. The vast majority of halo stars are found to have formed centrally, with only one in ten forming outside six percent of the virial radius and one in a hundred outside 35%. The main gaseous object (disk) typically has a radius between five and fifteen percent of the virial radius, but is highly flattened, even at high redshift. In-situ stars may then form in the disk, but could equally form in cool gas outside the disk plane. In either case, some fraction must be scattered to larger radii to explain the in-situ population there. This is shown explicitly in the right panel of Fig. 5.3 which compares the radius at which stars form relative to their radius at $z = 0$. [1]

Inner halo (< 3 kpc) stars typically formed in place, but many also formed at larger radii. At least some of this apparent inward "migration" is the result of stars forming initially in disks that gravitationally collapse after becoming misalligned with the direction of gas accretion (see Section 3.6.8). However, these disks never grow to a size larger than 5 kpc before buckling, so cannot be the sole cause of this behaviour. Many of the outer halo stars formed within the central few kpc, with only a tiny fraction actually forming close to their $z = 0$ radius. These results are quite different from those of F11, who found that stars tend not to move significantly from the sites where they formed. They claim that their result implicates direct cooling out of the hot gas halo as the main mechanism for in-situ star formation. Fig. 5.3 is qualitatively consistent with Z09, however, who

[1] We note that some care should be taken in interpreting these radii; some of the variation will be due to the eccentricity of the stellar orbits. We do not, however, expect any systematic change between formation and the final radius as a result.

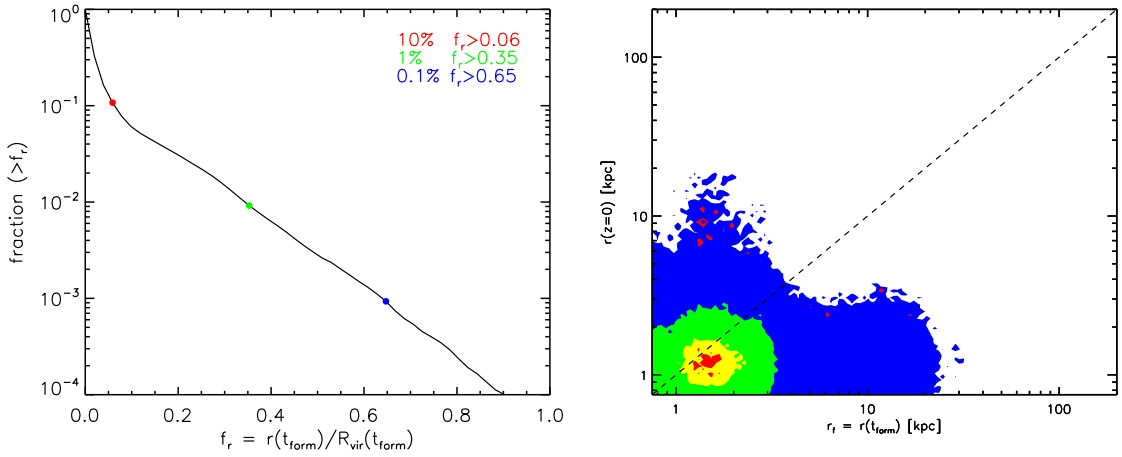

Figure 5.3 Left Panel: The formation radii of in-situ stars as a fraction of the virial radius of the main halo at their formation time. Red, green and blue points and their corresponding labels indicate the fraction of the virial radius outside which 10%, 1% and 0.1% of stars formed. Right panel: The initial and final radii of in-situ stars. Contours coloured red, yellow, green, blue and grey contain 10,20,50,90 and 99 percent of the datapoints respectively.

found that in-situ stars formed mostly within the central few kpc, in cold, inflowing gas.

To summarise the last two subsections, the stellar halo is made up of stars that were either stripped from infalling satellites or that formed in or around the central gas disk. Some of those centrally formed stars are today found at much larger radii. A smaller fraction of the in-situ population formed initially in disks which became unstable, contributing to the formation of the bulge or inner halo. In the following subsections we examine some of the properties of the in-situ and accreted components and consider in further detail the epochs at which they formed and were added to the halo.

5.3.3 Surface Brightness and Mass Density Profiles

In Fig. 5.4 we show the surface brightness profile of the halo, averaged over circular annuli and projected parallel to the minor axis of the galaxy disk. We also indicate a possible decomposition which assumes the bulge follows a Sersic profile and the halo a (single) power-law. That is, the surface brightness at a radius r is:

$$\Sigma(r) = S_0 \exp\left[-\left(\frac{r}{r_s}\right)^{\frac{1}{n}}\right] + P_0 r^{\alpha} \tag{5.1}$$

The fit is carried out over the range indicated by the thick black line, which ignores the region expected to be affected by the gravitational softening, as well as the halo beyond ~ 80 kpc, where the slope steepens substantially. We will demonstrate below that the halo density profile out to the virial radius is better fit by a broken power law, but since we are only concerned with separating the bulge and inner halo here, the outer halo is excluded in order to simplify the fitting process. The Sersic index of the 'bulge' component is found to be ~ 1.1, close to a pure exponential. We note that such profiles are often associated with "pseudo-bulges" formed by secular processes. Pseudo-bulges are normally assumed to be associated with gas inflows due to bars or bar instabilities (e.g Kormendy & Kennicutt, 2004b), but presumably the collapse of the whole disk at high redshift, as seen in Section 3.6.8 could produce the same effect. The radius containing ninety percent of the bulge light, marked by an arrow, is (coincidentally) close to 3 kpc, the bulge radius chosen for consistency with C10.

In Fig. 5.5 we plot the spherically averaged mass density profiles of the stellar halo. Red and blue curves indicate the contributions of the accreted and in-situ components. The green dashed line is the best-fit broken power law, the parameters of which are indicated by the labels. In the accreted component, there is a clear change in slope around 60 kpc, which is also evident in the total profile. This is qualitatively similar to the break observed in the density profile of the Milky Way's stellar halo (Deason et al., 2011; Sesar et al., 2011), albeit at about twice the radius. The slopes of both the inner and outer components of the halo are also steeper than the values found by Deason et al. (2011) (-2.3/-4.6) and Sesar et al. (2011) (-2.6/-3.8). Interestingly the C10 model of the accreted stellar halo in Aq-C has a slightly shallower inner slope and larger break radius of $\sim 90kpc$. Since the cosmological environments are identical, we speculate that this is related to the exact orbits of substructure within the halo and/or the star formation histories of satellites; these differences are examined further in subsection 5.3.5. The total mass in their stellar halo is less than ours, as expected from the fact that satellites typically form fewer stars in their model (see Fig. 4.3).

We find that the in-situ component (including the bulge) dominates the mass density within ~ 19 kpc. This value is strikingly similar to that found by F11, (20 kpc) for the stacked profiles of ~ 400 L_* disk galaxies in their simulations, though the fact that the profiles of the accreted and in-situ components have different slopes suggest this

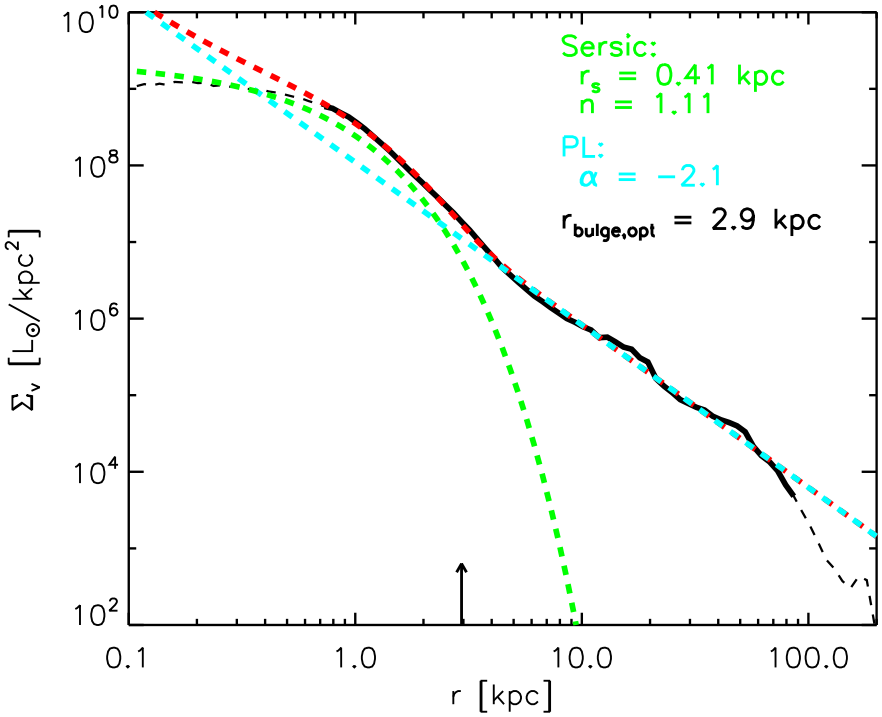

Figure 5.4 The V-band surface brightness profile of the bulge and halo of Aq-C-4 (black dashed line) and the best-fit Sersic+power law profile (red dashed line). The fit is computed using only the portion of the profile plot as a thicker black line, which excludes radii within 2.8 times the softening parameter and beyond 80 kpc, where the halo profile changes slope (see text for the motivation behind this choice). The Sersic and power law components are plotted separately as green and cyan dashed lines, with the corresponding parameters indicated by the labels. An upward arrow marks the radius containing 90% of the bulge (Sersic profile) light.

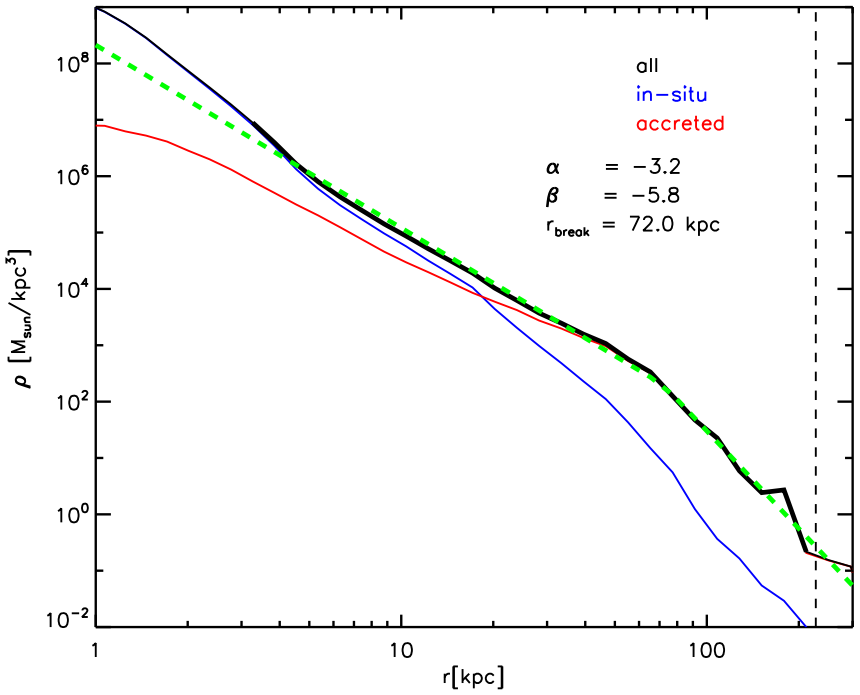

Figure 5.5 The spherically averaged density profiles of the accreted (red) and in-situ (blue) components of the stellar halo in Aq-C-4. The parameters of the best-fit broken power law (dashed green line) are indicated by the labels, where α is the inner slope, β the outer slope and $r_{\rm break}$ the transition radius. The part of the profile used to define the fit is indicated as a thicker black line.

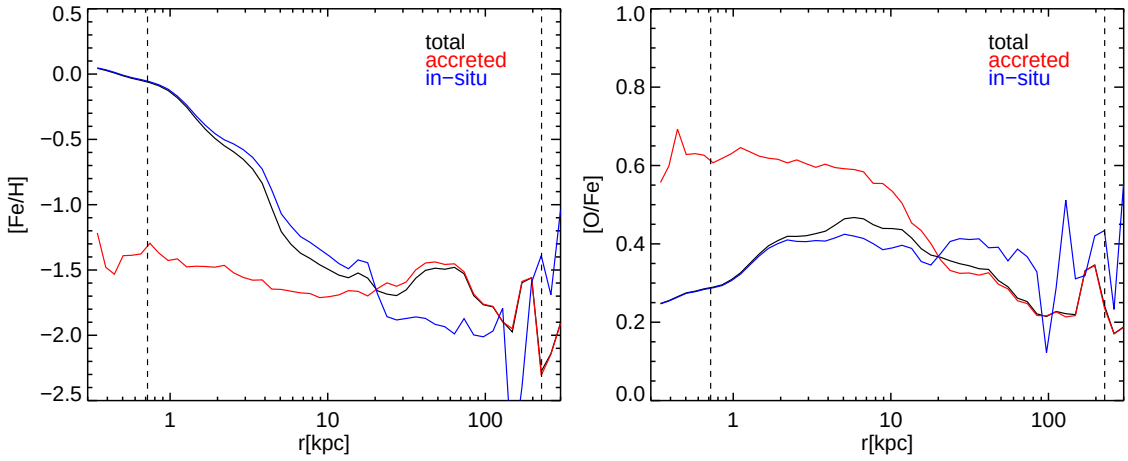

Figure 5.6 Spherically averaged $[\mathrm{Fe/H}]$ and $[\mathrm{O/Fe}]$ profiles for the Aq-C-4 stellar halo. Red and blue curves indicate the values for the accreted and in-situ components separately, black the total. The inner and outer dashed vertical lines indicate the Plummer equivalent gravitational softening and r_{vir} respectively.

agreement may be coincidental.

5.3.4 Chemical Composition

Several authors have found that both the MW and M31 stellar haloes are more metal-rich in the inner regions (Carollo et al., 2007, 2010; de Jong et al., 2010). Models of the stellar halo which only consider the accreted component typically fail to find such a gradient, which may indicate that it reflects a transition between dominant in-situ and accreted populations (Zolotov et al., 2010; Font et al., 2011a). In this subsection, we consider the radial variation of the abundance ratios $[\mathrm{Fe/H}]$ and $[\mathrm{O/Fe}]$ and how the two modes of star formation affect them. We define $[\mathrm{Fe/H}]$ and $[\mathrm{O/Fe}]$ for each star particle in the conventional way, taking the logarithm of the particle's abundance ratio normalised to the solar value. We assume solar mass fractions in H, O and Fe of 0.7065, 0.00549 and 0.0011 respectively, for consistency with the CLOUDY tables used in our cooling prescription. Spherically averaged profiles for $[\mathrm{Fe/H}]$ and $[\mathrm{O/Fe}]$ are plotted in Fig. 5.6.

A clear difference is apparent between in the in-situ and accreted components in both $[\mathrm{Fe/H}]$ and $[\mathrm{O/Fe}]$, reflecting the different environments in which they form. For in-situ stars, $[\mathrm{Fe/H}]$ declines steeply with radius inside the central $20\ \mathrm{kpc}$, where successive generations of supernovae have enriched the ISM. In the accreted component, $[\mathrm{Fe/H}]$ de-

clines only gradually from around -1.5 in the bulge, to -1.8 in the outskirts of the halo, though there is also a notable excess between 30 and 80 kpc caused by the stream associated with sub1. Recalling that sub1 was the most massive satellite at infall, these high levels of enrichment are expected. If the stars stripped from sub1 are excluded, there is a clear negative gradient in the total [Fe/H] outside 10 kpc. Over the same range in radius, there is a corresponding dip in [O/Fe], reflecting the more extended nature of the star formation in sub1 and possibly the other larger satellites that contribute to the outer halo. In contrast, in-situ stars show relatively little variation in [O/Fe] with radius, except in the inner few kpc where the bulge dominates.

5.3.5 Halo Formation and Assembly History

The halo of the MW is populated predominantly by old, metal-poor stars, with some age estimates consistent with formation just a few hundred million years after the Big Bang. In this subsection we investigate whether such early formation epochs are reproduced in the simulation and also consider the assembly history of the halo, identifying the satellites that dominate the formation of the accreted component. In Fig. 5.7 we show the formation redshifts (or ages on the top axis) of all halo stars (black), the accreted component (red) and the in-situ component (blue). The left panel includes all stars in the spheroid, the right panel only those found outside the central 3 kpc at $z = 0$.

We find that more than 85% (90%) of all (outer) halo stars are older than 10 Gyr. The formation epochs of in-situ and accreted stars are similar except in two ways. Firstly, virtually all stars in the accreted component are older than 6 Gyr, whereas an appreciable fraction (5-10%) of in-situ stars formed more recently. Secondly, there are a large subset of accreted stars that form in a narrow interval between $z = 7$ and $z = 6$. This star formation appears to be related to bursts in two large progenitor satellites, induced as they spiralled into the main galaxy; we discuss them further later in this subsection. We also note that in-situ star formation in the outer halo lags behind that in the halo as a whole. Again, this may reflect the contribution to the bulge from high redshift disk instabilities. The stellar halo forms half its mass slightly earlier than the galaxy itself (defined by all stars within $0.1r_{\rm vir}$, as shown in Fig. 3.27). This behaviour is expected from the relative ages of halo and disk stars; the dominant in-situ halo forms mostly before $z = 3$, well in advance of most of the disk.

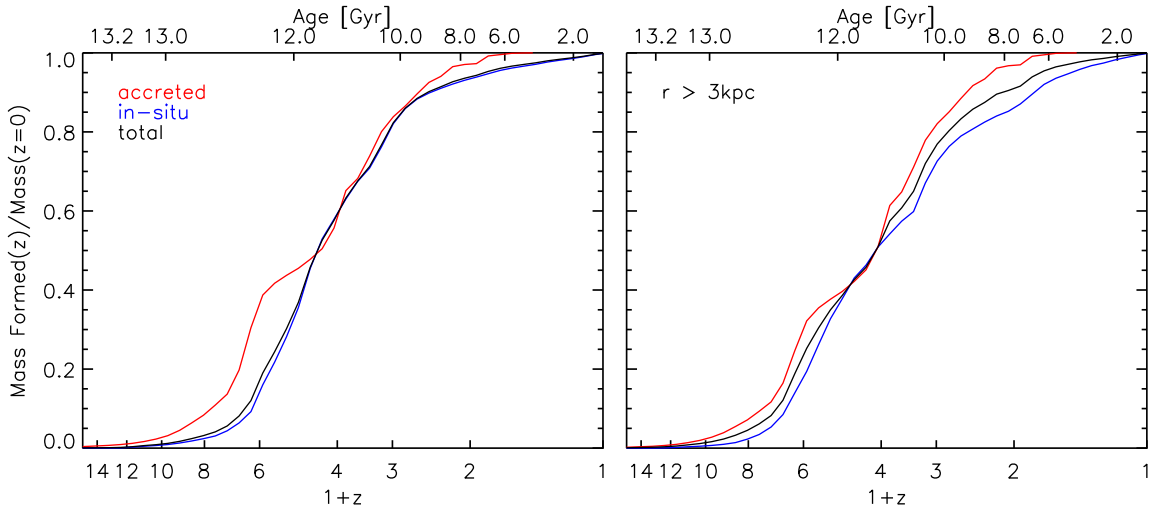

Figure 5.7 The formation history of the stellar spheroid of Aq-C-4. The left panel includes all stars in the spheroid ($r < r_{\rm vir}$), while the right excludes stars within 3 kpc. The three curves show the cumulative fraction of the $z = 0$ mass formed in the accreted component (red), the in-situ component (blue) and the whole spheroid (black).

In Fig. 5.8 we show how the stellar halo assembles with redshift, with the same panels and colour scheme used in Fig. 5.7. In-situ stars are, by definition, part of the halo when they form and hence the blue curves in Figs. 5.7 and 5.8 are identical. Accreted stars are considered to be part of the halo in the snapshot after they were last bound to a subhalo. The main events that build the accreted halo are easily identified as sharp increases in the red curves at $z = 6.5, 3.5$ and 2. The largest of these is from sub1, which crosses $r_{\rm vir}$ around $z = 2$, but is only stripped significantly between $z = 1$ and 0.6. Comparing the left and right panels, one can also see that the earlier mergers contribute disproportionately to the inner halo ($r < 3$ kpc) and the later mergers to the outer halo. The main accretion events are neatly summarised in Fig. 5.9, which emulates a plot from C10 (their fig 10.). For consistency with C10, we exclude stars that fall within a radius of 3 kpc at $z = 0$.

Thirteen satellites provide the bulk (90 percent) of the accreted stellar spheroid, two of which remain identifiable as bound structures at $z = 0$. We note this is somewhat larger than the eight contributors identified by Cooper et al. (2010) in Aq-C. The dominant contributor, accounting for about a third of the mass, is sub1. The stellar core and

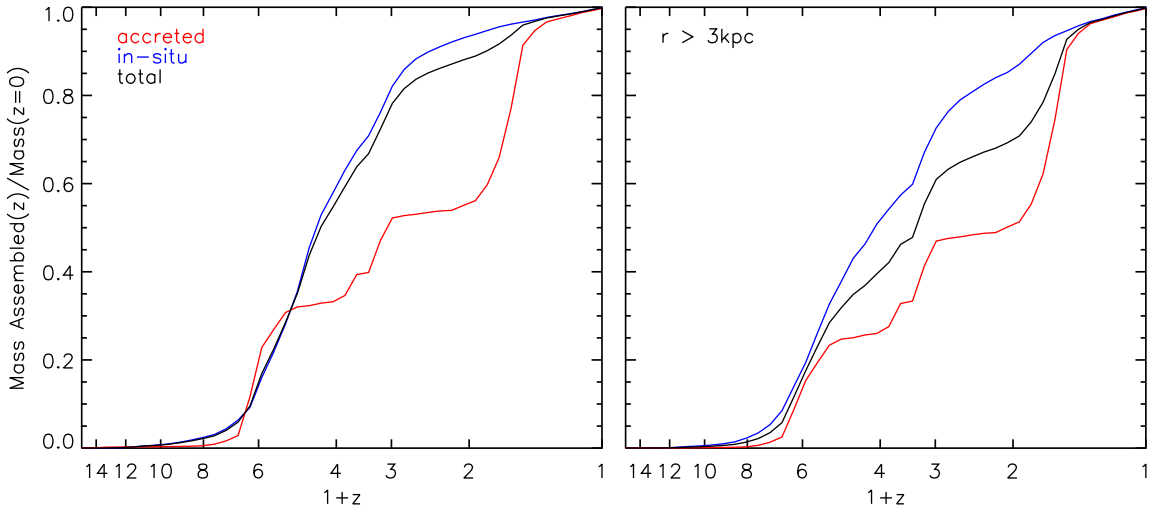

Figure 5.8 The assembly history of the stellar spheroid of Aq-C-4. The left panel includes all stars in the spheroid ($r < r_{\rm vir}$), while the right panel excludes stars within 3 kpc. The three curves show the cumulative fraction of the $z = 0$ mass that belongs to the accreted component (red), the in-situ component (blue) and the whole spheroid (black) at that epoch. Note that the assembly redshift of in-situ stars is identical to their formation redshift by definition.

clear associated stream make it tempting to identify this satellite with Saggitarius (it is also at roughly the same Galacto-centric radius), however the total stellar mass in the simulated stream exceeds that estimated for the Saggitarius stream by roughly an order of magnitude (Niederste-Ostholt et al., 2010). Two particularly interesting contributors are the pair of satellites that each add $\sim 3 \times 10^8$ M$_\odot$ to the halo and fall in around $z = 6.5$. At this epoch, the stellar mass of the main galaxy is only $\sim 2 \times 10^9$ M$_\odot$, so these are major mergers, distributing stars all around the central parts of the main progenitor halo before the remnants sink to the centre. Together they account for about 20 percent of the accreted halo mass, with most of their stars found in the central few kpc. The star formation rate in both galaxies is magnified by tidally driven inflows in the period before they are disrupted, generating the spike in the stellar age distribution of the accreted component seen in Fig. 5.7. By $z = 0$, little evidence of this violent sequence of events remains, the stellar streams having been well mixed and dispersed. We note that C10 do not rank these two satellites among the top contributors to the Aq-C halo, despite the fact that

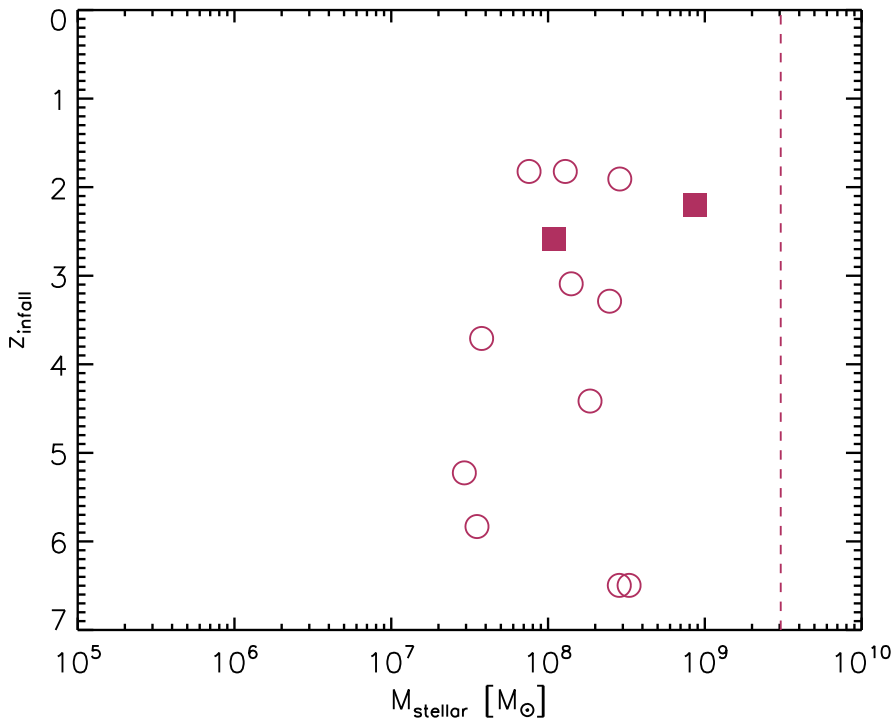

Figure 5.9 Our version of fig. 10 in Cooper et al. (2010), showing the infall redshift and masses of satellites contributing to the stellar spheroid of Aq-C-4. For consistency with their model, we also exclude stars that are within a $3\,\mathrm{kpc}$ radius at $z = 0$, which they label as the bulge. We rank satellites by the mass that they add to the halo and then select a sufficient number of the top contributors to account for 90 percent of the total. Filled squares correspond to satellites that remain as bound, resolved objects at $z = 0$ while empty circles signify satellites that were completely disrupted. The vertical dashed line indicates the total mass of the accreted stellar halo.

they account for about 20% of our accreted outer halo. This presumably implies that the semi-analytical prescription corresponds to a much lower star formation efficiency in such objects, at least at high redshift.

While the stellar haloes of galaxies have been the subject of several recent hydrodynamical simulations and numerous semi-analytical models, the hot gas halo has received significantly less attention, particularly at the level of resolution available here. In the next section, we conclude our study of Aq-C-4 by examining the observable properties and origin of this final component.

5.4 The Hot Gas Halo

In this section we investigate some of the properties of the gaseous halo around Aq-C-4 . Although we mostly discuss the *hot* gas ($T > 10^5$ K), our analysis includes all particles assigned to the halo component by the procedure described in section 5.2, which in principle can have any temperature. This allows us to also track gas that may be condensing out of the hot halo, either in a smooth cooling flow or through thermal instability. However, as one might expect, the vast majority ($\sim 95\%$) of this gas is hot, with a mean temperature of 8×10^5 K. The total mass of the gas halo within the virial radius is $\sim 5.4 \times 10^{10}$ $\mathrm{M}_\odot$, although gas well beyond that maintains a temperature above 10^5 K. Gas cooling radiatively at these temperatures emits primarily at X-ray wavelengths, making observations using modern X-ray telescopes with high spatial and energy resolution the only way to detect it directly. For that reason the following analysis focuses predominantly on the X-ray properties of the hot gas. We note, in particular, the biases that can be introduced by assuming that the X-ray-bright gas is representative and investigate whether the classical picture of cooling in a quasi-static halo, as introduced by White & Frenk (1991), provides an accurate description of Aq-C-4 .

5.4.1 X-ray Surface Brightness

We compute the X-ray luminosities of all gas particles assigned to the halo component using software written by Rob Crain and described in Crain et al. (2010a). In brief, the soft X-ray luminosity is a function of the electron and ion densities, which depend on chemical composition, and the integral of the cooling function over the $0.5 - 2$ keV

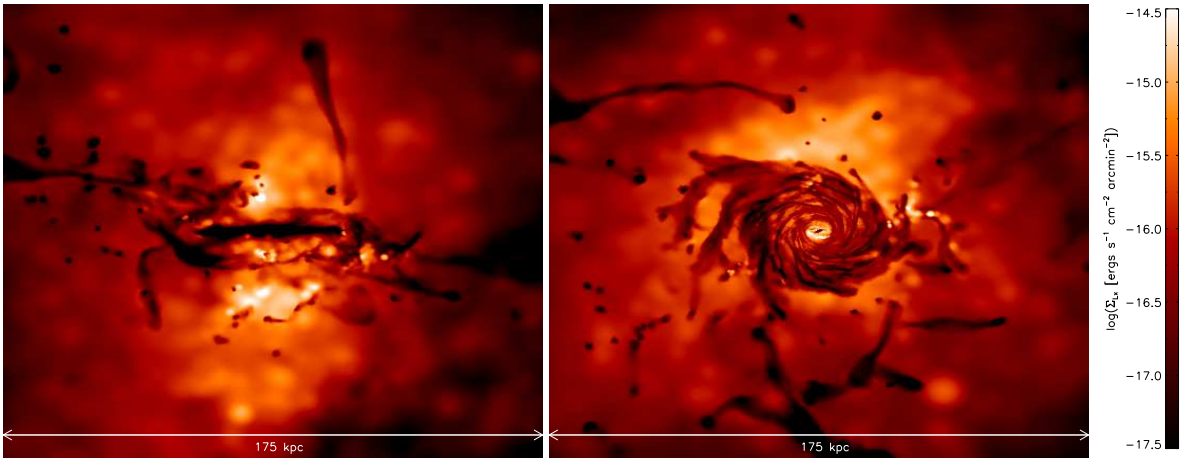

Figure 5.10 Maps of the soft X-ray ($0.5 - 2.0$ keV) surface brightness of the gas in Aq-C-4, projected through a cube of side 175 kpc, oriented edge-on and face-on to the main galaxy disk.

passband, which depends on composition, density and temperature. Summing the contributions of all gas within $r_{\rm vir}$ yields a total soft X-ray luminosity for the halo of $\sim 2.2 \times 10^{39}$ ergs s^{-1}. However, the spatial distribution of this emission is key to its potential observability. In Fig. 5.10 we show two 160 kpc x 160 kpc maps of the soft X-ray (0.5-2keV) surface brightness of *all* gas, projected edge-on and face-on to the disk. The disk itself has near-zero X-ray luminosity, such that it is silhouetted against the (relatively) X-ray-bright hot halo. Several bright 'spots' are visible, which correspond to regions of particularly high metallicity. At least some of this variation is a numerical artefact, since metals cannot diffuse once assigned to a particle; mixing is instead modelled approximately by smoothing particle abundances over the SPH kernel when computing the luminosities. Some of the central emission appears to have a bi-conical morphology, suggesting that it is being heated by SNe feedback directed perpendicular to the disk plane. The denser and more enriched central regions have a higher surface brightness, except for several large tracts of gas cooling onto the disk. The centrally concentrated nature of the emission has important implications for the distribution of the hot gas that would be inferred from observations (given a sufficiently sensitive X-ray telescope), which we examine next.

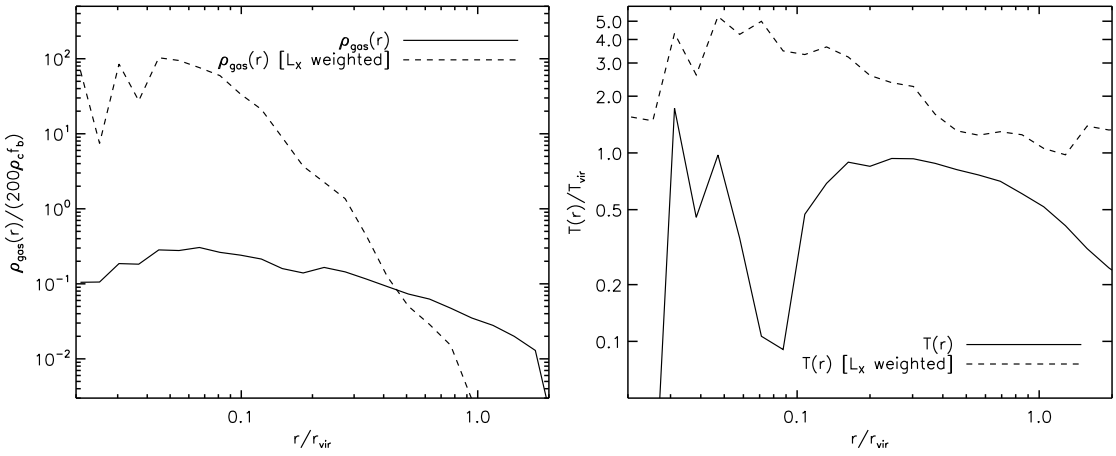

Figure 5.11 Spherically averaged density (left panel) and temperature (right panel) profiles weighted by mass (solid lines) and soft X-ray ($0.5 - 2.0$ keV) luminosity (dashed lines). The density is normalised to the mean value expected in the halo if the cosmic baryon fraction $f_b = \Omega_{\rm b}/\Omega_{\rm m}$ were retained. The temperature is normalised to the virial temperature, as given by Eqn. 5.2

5.4.2 Distribution and Temperature of Hot Gas

In Fig. 5.11 we plot spherically averaged profiles of the density (left panel)) and temperature (right panel) of the hot gas around Aq-C-4 , indicating the effects of weighting by mass (solid lines) and by soft X-ray luminosity (dashed lines). Galacto-centric radius is plotted as a fraction of $r_{\rm vir}$ in each case. The density is normalised to the mean value expected if the halo had the cosmic baryon fraction and the temperature to the virial temperature, $T_{\rm vir}$, which we compute as:

$$T_{\rm vir} = \frac{1}{3}\frac{\mu m_p}{k_B} V_{\rm vir}^2 \tag{5.2}$$

where μ is the mean molecular weight, m_p is the mass of a proton, k_B is the Boltzmann constant and $V_{\rm vir} = \sqrt{GM_{\rm vir}/r_{\rm vir}}$ is the circular velocity at the virial radius. This equates to a value of $\sim 1.2 \times 10^6$K for Aq-C-4 at $z = 0$. The most obvious feature of these plots is the large difference between the mass-weighted profiles and those that might be inferred from X-ray observations. The X-ray luminosity depends on the chemical composition of the gas and the detailed form of the cooling function, but to first order can be approximated as $L_{\rm X} \propto \rho^2$. This scaling results in an apparent steepening of the density profile from approximately $\rho(r) \propto r^{-1}$ to $\rho(r) \propto r^{-4}$. The mass-weighted temperature profile

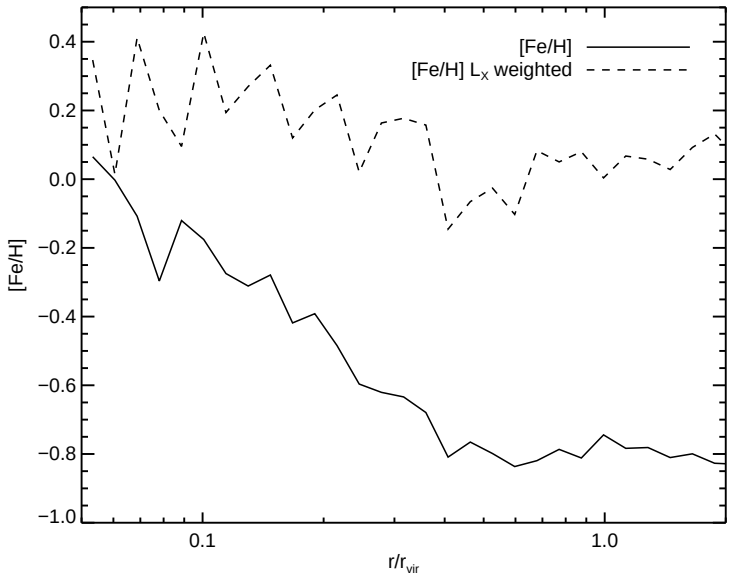

Figure 5.12 X-ray luminosity-weighted (dashed line) and mass-weighted (sold line) $[\mathrm{Fe/H}]$ as a function of radius for the hot ($T > 10^5 K$) gas halo of Aq-C-4.

shows that the hot gas adopts an r^{-1} distribution in the outer halo, flattening to approximately isothermal in the region around the disk and dropping sharply in the inner regions where the cooling time is short. There is some suggestion of a high temperature component within $0.1r_{\rm vir}$, which could be due to wind-generated shocks above and below the galactic plane; however the hot gas mass in that region is very low, making the profile extremely noisy. There is clearly also some temperature dependence in L_X since the X-ray luminosity-weighted temperature has a much higher normalisation than in the mass-weighted case. It has a shallow slope of $r^{-0.5}$ outside the central regions and becomes almost isothermal within $0.1r_{\rm vir}$. This plot also demonstrates that much of the X-ray-bright gas achieves super-virial temperatures, particularly towards the centre of the halo. This agrees well with the findings of Crain et al. (2010a) who analysed stacked profiles of simulated disk galaxies at lower resolution. They suggested that the steepening of the inner potential due to adiabatic contraction could also contribute to this effect. In Aq-C-4 , however, the adiabatic contraction is minimal (see Section 3.7.8) and so most of the X-ray-bright gas is presumably generated by shocked outflows.

5.4.3 Metal Content

An argument commonly advanced against the quasi-static halo scenario is that the chemical properties of hot gas around galaxies are found to be inconsistent with a primordial origin. The two counter-arguments are that i) the hot halo could have been polluted by a small mass fraction of SNe ejecta, well mixed with the primordial accreted gas and ii) the X-ray observations from which this conclusion is derived are inherently biased towards enriched gas, leading to a systematic overestimate of the metallicity. The importance of the latter point is highlighted by Fig. 5.12, where we plot the spherically averaged metallicity of hot gas weighted by mass (solid lines) and by soft X-ray luminosity (dashed lines). In the outer parts of the halo, the luminosity-weighted estimate leads to higher metal fractions by 0.8 dex, with the discrepancy reducing to 0.5 dex in the vicinity of the disk ($0.1r_{\rm vir}$). However, the mass-weighted distribution clearly demonstrates that the hot gas has an appreciable fraction of metals. There is also a notable negative gradient out to $0.4r_{\rm vir}$ (~ 90) kpc and an approximately constant metallicity of -0.8 in the outer halo. The gradient likely reflects the abundance of recently enriched wind particles around the main galaxy, but it is unclear why there should be such a clear transition radius well beyond the edge of the disk.

5.4.4 Inflows, Outflows and the Quasi-Static Halo

In the past, X-ray emission around disk galaxies has almost exclusively been identified with outflows generated by SNe. In the GIMIC suite of simulations, Crain et al. (2010a) found that, in fact, less than half of the X-ray emission from gas around L_* disk galaxies came from outflowing gas, with the majority due to a static hot halo formed by the shock heating and gravitational compression of accreting gas. We can investigate this directly in Aq-C-4 by considering the radial velocities of gas particles assigned to the halo, which are shown as a function of radius in Fig. 5.13. Blue and red points correspond to gas above and below a temperature of 10^5 K and thick lines indicate the mean velocity of gas at that radius. Much of the hot gas is distributed in an extended halo from ~ 100 kpc out to beyond the virial radius. Its mean velocity is approximately zero, although the mean velocity for all hot gas (thick red line) is skewed slightly to positive values by a small number of outflowing wind particles. A flow of gas cooling out of the hot halo

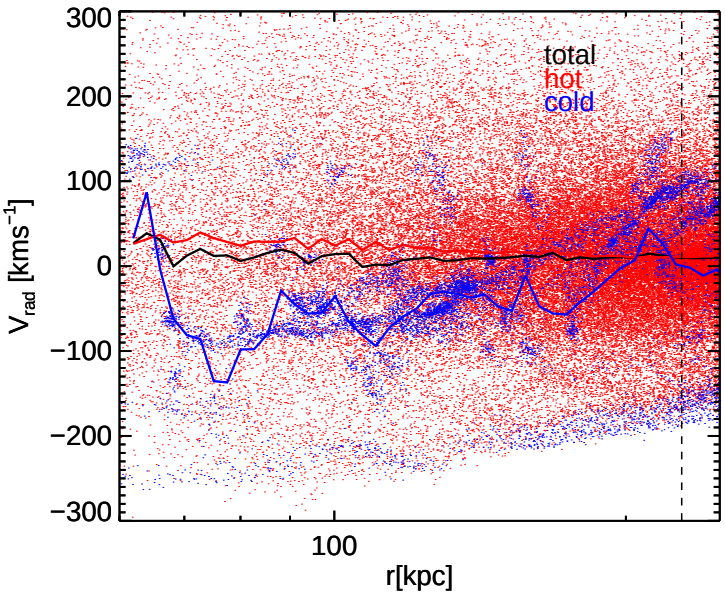

Figure 5.13 The radial velocities for ten percent of halo gas particles as a function of their radius. Red and blue colours indicate temperatures above and below 10^5 K. Red, blue and black lines indicate the mean radial velocity for hot cold and all halo gas. The virial radius is indicated by a vertical dashed line. The inner 60 kpc, where most of the gas is assigned to the disk, are excluded from this plot.

is clearly visible inside 150 kpc, accelerating as it loses pressure support and falls in. A much smaller fraction of the gas is found to be rapidly inflowing at -150 to -250 kms^{-1}, remaining below 10^5 K as it does so. This gas forms a dense filament extending from the virial radius down to the main gas disk at ~ 20 kpc.

We quantify the fraction of halo gas that is inflowing, outflowing and approximately static in Fig. 5.14. The left panel shows the contribution to the total soft X-ray luminosity from gas as a function of its radial velocity; the right panel shows the contribution to the total mass. In both cases, we show a possible fit to the distributions using a superposition of three Gaussians. The mean of one of the Gaussians is fixed at zero but all other parameters are free to vary. The three components are intended to model the contributions from inflowing (green), outflowing (red) and quasi-static (blue) gas. While there is no reason to expect a Gaussian distribution of velocities for inflowing or outflowing gas, this simple model provides a relatively good fit to each distribution. The labels at the top of each panel indicate the fraction of the luminosity or mass contributed by each com-

ponent. In both cases, the "static" contribution is dominant, accounting for 75 percent of the halo by mass. Only around five percent appears to be outflowing, though a much larger fraction might be inferred from the contributions to the X-ray luminosity. The X-ray bright, rapidly infalling component at $\sim v_{\rm rad} = -200\ {\rm kms}^{-1}$ is the gas identified in Fig. 5.13 as a dense, warm ($10^4 - 10^5$ K) filament flowing onto the disk from beyond the virial radius. As can be seen from the right hand panel of Fig. 5.14, gas at that radial velocity contributes a much smaller fraction by mass.

Although Fig. 5.14 establishes the existence of a static hot halo around Aq-C-4 , it does not reveal where the gas originated. Our simulation code does not store any history for gas particles that would indicate whether they had previously accreted onto the disk and then taken part in an outflow, but since no diffusion of chemical elements takes place between particles, gas accreting for the first time should have a primordial composition. We make an estimate of the primordial fraction of the static component by randomly sampling each radial velocity bin so as to obtain the mass fraction in each bin given by the blue curve in the right panel of Fig. 5.14. The fraction of particles selected in such a fashion that retain the chemical composition assigned to them at the beginning of the simulation is ~ 22 percent. Hence the majority of the static halo appears to have been enriched by SNe feedback at some time in the past. The same procedure carried out for the "outflowing" component, returns a primordial fraction of less than two percent. While it is possible that some star formation could have taken place in the outer part of the halo and enriched gas there, this result can only imply that the majority of the static component has either been ejected from the main galaxy and re-accreted, or been enriched inside a satellite galaxy and stripped after infall.

5.5 Summary

In this chapter, we have studied the properties of both the stellar and gaseous haloes in a hydrodynamical simulation of a MW-mass galaxy. The orbital circularities of baryonic particles were used to define and extract the central disk of the galaxy, with all remaining baryonic material not associated with a satellite assumed to belong to either the stellar or hot gas halo. This includes a central dispersion dominated stellar component which would typically be identified as a bulge.

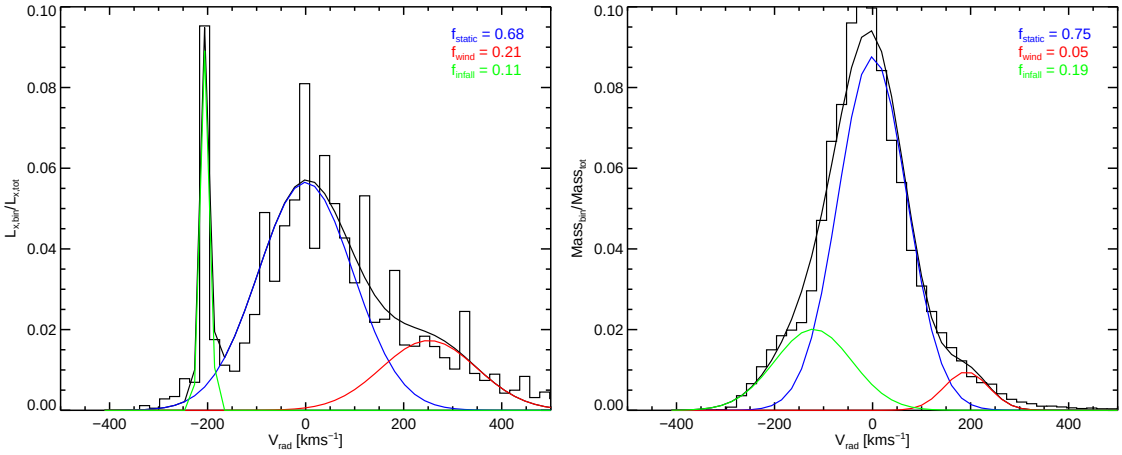

Figure 5.14 The fraction of the total soft X-ray ($0.5 - 2$ keV) luminosity (left panel) and mass (right panel) contributed by gas as a function of its radial velocity. The distributions (black histograms) are fit with three Gaussians; the amplitudes and dispersions of all three are free to vary, while we fix the mean of one of them at zero. These three components are intended to approximate infalling (green), quasi-static (blue) and outflowing (red) components. The combination of the three components is the smooth black line.

In agreement with several previous theoretical studies (Zolotov et al., 2009; Font et al., 2011a; Scannapieco et al., 2011), we find that the outer halo is formed primarily through the accretion of stars from satellites, most of which do not survive to the present day as resolved substructures. The majority of the inner halo is formed in-situ in the main progenitor. These in-situ stars predominantly form close to the centre of the dark matter halo at high redshift and some are the result of the collapse of the gravitationally unstable stellar disks identified in Section 3.6.8. In-situ stars found in the outer halo at $z = 0$ also form centrally and are likely scattered to these radii as a result of mergers and interactions with satellite galaxies.

The surface brightness of the inner halo is relatively well fit by a Sersic profile with n=1.1 and scale length 0.4 kpc combined with a power-law with slope -2.1. Such exponential bulges are often claimed to be generated through secular processes (e.g. Kormendy & Kennicutt, 2004b) such as the buckling of bars, but which presumably could also be due to the disk collapse seen in Chapter 3. In common with the MW, the density profile of the outer halo can be approximated by a broken power law, although the slopes of -3.2 and -5.8 in our model are somewhat steeper than those observed and the break

radius, $\sim 70\ \mathrm{kpc}$, is much larger. There is a strong negative metallicity gradient driven by the in-situ component, whereas accreted stars have a metallicity that is almost constant with radius, in agreement with results from Cooper et al. (2010) in this halo. The vast majority of halo stars are older than 10 Gyr, though a small fraction of the in-situ component is much younger, with ages less than 6 Gyr. While the two components form at similar times, several of the satellites that contribute to the accreted halo fall in after $z = 2$, which means a substantial amount of structure in the form of streams and overdensities survives to $z = 0$ without phase-mixing. We find that the accreted component is dominated by a relatively small number of massive satellites, two of which survive to $z = 0$, though the number of substantial contributors is somewhat larger (thirteen rather than eight) than that found by Cooper et al. (2010) in Aq-C using an alternative modelling technique.

In the final section of the chapter we discussed the properties of the hot gas halo around Aq-C-4 . We computed luminosities for each gas particle in a soft X-ray band ($0.5 - 2\ \mathrm{keV}$) as a function of their density, temperature and chemical composition and demonstrated that the surface brightness of most of the gas would make the hot halo very difficult to detect observationally. The X-ray luminosity in Aq-C-4 is fairly centrally concentrated, with some fraction of the emission clearly due to gas heated by SNe feedback. As expected from the approximate scaling $L_X \propto \rho^2$ and from the concentrated nature of the emission, a much steeper density profile results when it is weighted by X-ray luminosity. Examining the radial velocities of the halo gas revealed the existence of a quasi-static component, with gas clearly condensing from it to accrete onto the disk, as well as a distinct, dense filament of cool gas rapidly inflowing from the virial radius. By fitting the distribution of radial velocities with three Gaussians intended to loosely correspond to inflowing, static and outflowing gas, we find that approximately 75 percent of the halo mass belongs to the quasi-static component. By statistically selecting particles expected to be in the quasi-static halo based on their velocity, we also showed that only ~ 20 percent of it has a primordial chemical composition. This suggests that most of the static component may be the result of gas re-accreting, having been ejected by SNe feedback at an earlier time.

Chapter 6

Conclusions and Future Work

6.1 Galaxy Morphology from Semi-Analytical Models

In Chapter 2, we used publicly available data from two semi-analytical models to investigate the origins of galaxy morphology, defined in terms of the bulge-to-total ratio of K-band light. Morphology was defined using each galaxy's bulge-total ratio (B/T) measured in the K-band, with a value of $B/T = 0.4$ separating spirals from S0s and $B/T = 0.6$ separating S0s from ellipticals. The fractions of the total galaxy population belonging to each morphology evolve very differently between the two models, with the Durham prescription predicting elliptical galaxies to be dominant at $z > 4$. At $z = 0$, however, the models predict a similar morphological mix. It is difficult to distinguish between them using observational data, which is subject to large systematics associated with fitting light profiles to galaxy images.

Spirals form half of their stellar mass later than either ellipticals or S0s and experience very few mergers of any kind, forming stars almost exclusively in-place. In agreement with previous studies (Kauffmann, 1996; De Lucia et al., 2006), elliptical galaxies tend to form most of their stars some time before theyare assembled in a single object. They also have earlier formation times than galaxies of other morphological types. The Durham model predicts a population of late-forming ellipticals not seen in the MPA model that correspond to spirals that collapse due to gravitational instability at low redshift and do not have time to re-grow a disk.

The most important conclusion from this study is that the relative contribution of major mergers to spheroid formation is small in all but the most massive elliptical galaxies ($M_* \gtrsim 2.5 \times 10^{11}\ h^{-1} M_\odot$). In the Durham model at least, this result is robust to the

definition of a major merger and to the modelling of the way gas is stripped from satellites after they are accreted. More than half of all elliptical galaxies identified at $z = 0$ and > 95 percent of spirals do not experience a major merger at any time during their formation history. This conclusion is common to both models, so does not appear to be sensitive to the details of the star formation and feedback prescriptions. Spheroids in low mass galaxies are built predominantly by minor mergers in the MPA model and disk instabilities in the Durham model. Since instabilities are likely to result in spheroids with an appreciable net angular momentum, it may in principle be possible to discriminate between the models observationally. However, detailed hydrodynamical simulations may be required to determine whether "disky" bulges formed through gas-rich mergers and those formed through instabilities can be distinguished.

6.2 Hydrodynamical Simulations of a Milky Way Sized Galaxy

In Chapter 3 we outlined some of the most important features of a smoothed particle hydrodynamics code suitable for modelling galaxy formation in a cosmological context. Initial simulations demonstrated a strong resolution dependence in terms of stellar mass, morphology and baryon fraction. The behaviour appears to have been a result of gas particles ejected by SNe energy being able to escape to larger radii at high resolution, suppressing late-time re-accretion and the formation of a disk. Higher resolution simulations also resolved the formation of cold clouds of gas in the halo, formed through the fragmentation of outflows, which was suppressed at lower resolution. The clouds themselves may have been responsible for the resolution dependent properties by creating a more porous halo and allowing wind particles to escape more easily. Modifications to the code, including allowing non-equation-of-state gas to be added to the wind and increasing the star formation threshold with resolution, significantly improved the convergence.

With a more stable numerical model established, we presented a more detailed study of the high resolution Aq-C-4 simulation. The main galaxy at $z = 0$ was found to have an extended gas disk, a stellar component with a barred spiral structure and a total stellar mass of around $4 \times 10^{10}\,\mathrm{M}_{\odot}$, about two thirds that of the Milky Way. It was also found to have a reasonably realistic rotation curve, peaking at $\sim 250\,\mathrm{kms}^{-1}$ and declining

fairly gradually out to the edge of the disk. A particularly interesting characteristic of its formation history is that it undergoes at least one and possibly several episodes of disk collapse, as a result of a misallignment between the disk and the angle of newly accreting gas. The original disk becomes tilted, apparently as a result of torques from a merging satellite and buckles after a new disk forms around it on a different allignment.

Finally we presented results from the Aquila code comparison project. Aquila involved nine different hydrodynamical codes simulating the Aq-C halo from identical initial conditions at two resolutions, equivalent to our Aq-C-5 and Aq-C-6 simulations. The main aims of the project were to study the consequences for the main galaxy properties of including particular physics and employing different numerical implementations, focussing on the capacity of each model to produce a realistic disk galaxy. Despite the common merger history, different models produce widely varying results in terms of final stellar mass, morphology and star formation history. The implementation of feedback was found to be key in this respect. Codes employing more effective feedback were able to produce less concentrated galaxies, form a lower fraction of their stars early and obtain more realistic stellar fractions. However, strong feedback was also linked to a less prominent disk component as a result of expelling the majority of baryons from the halo. The fine balance seemingly required to obtain a realistic disk may simply reflect the fact that these simulations have insufficient resolution to model feedback realistically, distributing the energy over much too large a volume.

6.3 Dynamical Masses of the Milky Way Satellites

In Chapter 4 we studied the properties of the satellite galaxies in the simulations introduced in Chapter 3, with the aim of shedding light on the observed properties of the MW's satellite population. We found that the structure of each satellite's dark matter halo changed very little relative to a dissipationless version of the simulation, suggesting that the dynamical presence of baryons is unimportant, with the caveat that the force resolution may limit any possible effect.

The luminosity function of simulated satellites in Aq-C-4 was found to match that of the MW fairly well at the faint end; there is no satellite as bright as the LMC, but observations suggest many MW-like galaxies may be similarly defficient (Liu et al., 2010;

Guo et al., 2011).

Estimating the masses of the MW satellites from stellar kinematical data is typically complicated by ignorance of the anisotropy of the stellar orbits (β). However, Wolf et al. (2010) showed that the mass within the half-light radius is insensitive to β, giving a robust measure of the depth of the potential well. A direct comparison to the same quantity is not possible even in our highest resolution hydrodynamical simulation, since both the half-light radii and the central masses are affected by numerical factors. We instead choose to measure the masses in the corresponding satellites in the dark-matter-only simulation and select half-light radii using the observed luminosity-size relation. The large scatter about the relation translates to a large range of possible sizes and hence masses for each satellite. Nonetheless, we find that the simulated satellites are more massive at a fixed luminosity than those observed by a factor of three to five. A KS test that takes into account the range of possible masses for each simulated satellite, based on the uncertainty in the size at fixed luminosity, returns a six percent probability that the simulated and observed masses are consistent.

There are a number of possible explanations for the discrepancy. It could be simply that there is significant halo-to-halo scatter in the mass-to-light ratios of satellites. Alternatively, some physical mechanism not properly captured by our simulations could have reduced the central densities of the observed satellites. Warm dark matter models, for instance, predict lower central densities. Baryonic processes can also have a similar effect, as demonstrated by the evolution of one particular satellite in the simulation. In this case, SNe feedback rapidly ejects gas from the centre of the halo, causing the central dark matter to expand in reponse. It is possible that this effect would be more significant in other satellites if resolution was sufficient to properly resolve the structure of the ISM and distribute feedback on smaller scales.

6.4 Formation of the Stellar and Gaseous Haloes

In Chapter 5, we further dissected the high resolution simulation from Chapter 3 by studying the hot gas and stellar haloes. Our definition of the stellar halo also includes the entire galactic "bulge". We do not attempt to separate the bulge and halo in any sophisticated fashion, instead choosing $3\ \mathrm{kpc}$ as the divide between the inner and outer

haloes. We note, however, that a "Sersic-plus-power-law fit to the surface brightness profile suggests a central component with roughly that radius. The light profile of the “bulge" is almost exponential ($n = 1.1$), much like the pseudo-bulges often associated with secular evolution processes (e.g. Kormendy & Kennicutt, 2004b). It may be that a formation history involving the collapse of an unstable disk configuration (see Chapter 3) naturally leads to this form of profile.

The stellar halo forms both through the disruption of accreted satellites and “in-situ” star formation within the most massive progenitor. In agreement with several recent studies (Zolotov et al., 2009; Font et al., 2011a; Scannapieco et al., 2011), we find that the outer halo is mostly accreted, while the inner halo is dominated by in-situ star formation, with a transition region between the two regimes around $20\ \mathrm{kpc}$. The in-situ component forms close to the centre of the main dark matter halo at $z >$. At least some of these stars originate in early-forming disks that buckle and collapse as described above. Another subset of in-situ stars are scattered to larger radii by $z = 0$, perhaps due to interactions with the inspiralling nuclei of merging satellites.

The density profile of the stellar halo is well fit by a broken power, similar in form to a fit proposed for the MW’s halo, although with somewhat steeper slopes and a larger break radius. We find a negative gradient in the total mean metallicity that is driven by the in-situ component; the metallicity of the accreted component is relatively flat, as also seen by Cooper et al. (2010). Stars older than 10 Gyr dominate at all radii, though a small amount of recent ($z < 0.5$) in-situ star formation also contributes to the inner parts ($r < 3\ \mathrm{kpc}$).

The dominant structures in the accreted halo are associated with satellites falling in at $z \lesssim 2$, including the satellite found to be stellar-dominated at $z = 0$ in Chapter 4. A relatively small number of satellites are responsible for building the accreted component, though a larger number than predicted by the hybrid N-body-semi-analytical technique of (Cooper et al., 2010) in the same halo.

In the final section of Chapter 5, we considered the properties of the hot gas halo, focussing in particular on its potential observability through soft X-ray (0.5-2keV) emission. X-ray luminosities were computed for each gas particle as a function of their density, temperature and chemical composition, giving a total luminosity of $\sim 2.2 \times 10^{39}\ \mathrm{ergs\,s^{-1}}$. The X-ray luminosity was found to be fairly centrally concentrated, with

some of the most luminous gas generated by shocked wind particles ejected from the disk. As expected from the approximate scaling $L_X \propto \rho^2$, weighting by X-ray luminosity substantially steepens the density profile of the hot gas. Considering the radial velocities of all gas particles in the halo revealed several distinct components. i) a quasi-static component with a velocity dispersion of $\sim 80\ \mathrm{kms}^{-1}$, most of which exists at radii beyond $100\ \mathrm{kpc}$, ii) a cooling flow of gas condensing from the halo and iii) a rapidly inflowing cool ($10^4 - 10^5\ \mathrm{K}$), dense filament, extending from the disk to the virial radius.

The distribution of mass and X-ray luminosity as a function of radial velocity can be fit by a simple superposition of three Gaussians, intended to loosely approximate inflowing, static and outflowing gas. This suggests that the static component contributes around 75 percent of the hot halo by mass. In agreement with the results of Crain et al. (2010a), we found that outflowing gas contributes disproportionately to the total X-ray luminosity. The rapidly inflowing filament of cool gas contributes around ten percent of the total luminosity owing to its high density. An approximate method for identifying particles belonging to the static component reveals that ~ 20 percent of it has a primordial chemical composition and hence must be falling in for the first time. Though some of the gas could have been enriched in satellites, the majority appears to have been ejected from the central galaxy by SNe feedback and re-accreted later.

6.5 Future Work

The questions raised by some of the results in this study present some clear possible directions for future work. Our comparison between the morphological evolution predicted by the Durham and MPA semi-analytical models highlighted a sensitivity to the implementation of the disk instability mechanism. Undoubtedly, a more sophisticated theoretical modelling of this process will be necessary to allow semi-analytical models to comment on galaxy morphology more accurately. To our knowledge, no systematic investigations of disk instability in hydrodynamical simulations have been carried out. Such studies would be extremely useful to constrain and improve the semi-analytical prescriptions for bar and possibly bulge formation enabling deatiled predictions to be made for the barred fraction, distribution of bar sizes and the rotation speeds of bulges, with the necessary statistics to compare to observations in a wide range of environments.

The latter is of particular interest in the light of results using integral field spectroscopy that have been able to quantify spheroid rotation in the local Universe observationally (e.g. Emsellem et al., 2007).

An obvious outstanding question from the first part of Chapter 3 is the details of the process by which the spurious cold clouds form in the Aq-C-$4_{\rm i}$ and Aq-C-$5_{\rm i}$ simulations. While it is clear that an interaction between outflowing material and infowing or re-accreting material is responsible, previous attempts to track the hydrodynamic evolution of gas that ends up in the clouds have proved inconclusive. The two modifications to the code known to be reponsible for suppressing the formation of clouds, either in combination or individually, are the scaling of the star formation density threshold with resolution and the ability to add non-equation of state gas to the wind. The latter certainly changes the hydrodynamic properties of the outflows and as such may affect cloud formation. We propose using idealised simulations of pre-formed disk galaxies to study the behaviour of outflowing gas without the additional complications introduced by the cosmological environment in our ab-initio simulations.

Our study of the stellar and hot has gas haloes around Aq-C-4 raised several important questions worthy of further study. The precise mechanism by which in-situ stars form and move between the inner and outer halo remains unclear. We intend to examine the nature of their formation sites and their progression from initial to final radius in more detail in the future. A large fraction of bulge stars are known to be the result of disk instability. This could be easily quantified by measuring their circularities at formation, $\epsilon(t_{form})$, or even tracking the evolution of the mean value of $[\epsilon(t_{form}) - \epsilon(t)]/\epsilon(t_{form})$ to identify instability events. In terms of the hot halo, we plan to study the thermodynamic history of the gas that ends up in the quasi-static component at $z = 0$ in much more detail and determine when it was first accreted onto the main object. It would also be interesting to directly compare the X-ray properties of the hot gas in our high resolution simulation to those of the ~ 400 MW-mass haloes analysed at lower resolution by Crain et al. (2010a).

Perhaps the most obvious criticism of studies that focus on high resoution examples of single galaxies is that their conclusions may be limited to one particular merger history, ignoring any halo-to-halo scatter. To ensure that our main conclusion are generic predictions of the model rather than a product of one particular halo's cosmological en-

vironment, it is clearly desirable to simulate other examples of Milky Way sized galaxies and compare the buildup of the disk and bulge, the half-light masses of satellites and the properties of the stellar and hot gas haloes. The remaining Aquarius haloes are a logical place to start in this respect, since they bracket the range of mass estimates for the MW's halo and a great deal is known about their evolution from previous studies of the dark-matter-only realisations (e.g. Springel et al., 2008b; Navarro et al., 2010; Cooper et al., 2010; Wang et al., 2011). We note that Scannapieco et al. (2009), Okamoto et al. (2010) and Scannapieco et al. (2011) presented hydrodynamical simulations of various Aquarius haloes at lower (level five) resolution and found significant variations in the main galaxy morphology, satellite properties and details of the stellar halo assembly. While this work was being finished, we completed simulations of the Aq-D and Aq-E haloes at level four resolution which will enable us to check whether our main conclusions are robust to assumptions about the mass and environment of the MW.

Bibliography

Abadi, M. G., Moore, B., & Bower, R. G. 1999, MNRAS, 308, 947

Abadi, M. G., Navarro, J. F., & Steinmetz, M. 2006, MNRAS, 365, 747

Abadi, M. G., Navarro, J. F., Steinmetz, M., & Eke, V. R. 2003, ApJ, 591, 499

Abel, T., & Haehnelt, M. G. 1999, ApJ, 520, L13

Agertz, O., Teyssier, R., & Moore, B. 2011, MNRAS, 410, 1391

Agertz, O., et al. 2007, MNRAS, 380, 963

Aharonian, F., et al. 2004, A&A, 425, L13

Alpher, R. A., & Herman, R. C. 1948, Physical Review, 74, 1737

Babcock, H. W. 1939, Lick Observatory Bulletin, 19, 41

Balsara, D. S. 1995, Journal of Computational Physics, 121, 357

Bardeen, J. M., Steinhardt, P. J., & Turner, M. S. 1983, Phys. Rev. D, 28, 679

Barnes, J., & Hut, P. 1986, Nature, 324, 446

Barnes, J. E. 1992, ApJ, 393, 484

Barnes, J. E., & Hernquist, L. 1996, ApJ, 471, 115

Bate, M. R., & Burkert, A. 1997, MNRAS, 288, 1060

Bekki, K., & Shioya, Y. 1997, ApJ, 478, L17

Bell, E. F. 2008, ArXiv e-prints, astro-ph/0801.0599

Bell, E. F., & de Jong, R. S. 2001, ApJ, 550, 212

Bell, E. F., McIntosh, D. H., Katz, N., & Weinberg, M. D. 2003, ApJS, 149, 289

Belokurov, V., et al. 2007a, ApJ, 654, 897

—. 2007b, ApJ, 657, L89

—. 2010, ApJ, 712, L103

Bensby, T., Feltzing, S., & Lundström, I. 2003, A&A, 410, 527

Bensby, T., Zenn, A. R., Oey, M. S., & Feltzing, S. 2007, ApJ, 663, L13

Benson, A. J. 2005, MNRAS, 364, 1104

Benson, A. J., & Bower, R. 2010a, ArXiv e-prints

—. 2010b, MNRAS, 405, 1573

Benson, A. J., Bower, R. G., Frenk, C. S., Lacey, C. G., Baugh, C. M., & Cole, S. 2003, ApJ, 599, 38

Benson, A. J., Dzanovic, D., Frenk, C. S., & Sharples, R. 2007, MNRAS, 379, 841

Benson, A. J., Frenk, C. S., Lacey, C. G., Baugh, C. M., & Cole, S. 2002, MNRAS, 333, 177

Bertola, F., & Capaccioli, M. 1975, ApJ, 200, 439

Bett, P., Eke, V., Frenk, C. S., Jenkins, A., Helly, J., & Navarro, J. 2007, MNRAS, 376, 215

Binney, J. 1978, MNRAS, 183, 501

Birnboim, Y., & Dekel, A. 2003, MNRAS, 345, 349

Blake, C., et al. 2011, MNRAS, 415, 2876

Blanton, M. R., et al. 2001, AJ, 121, 2358

Blumenthal, G. R., Faber, S. M., Flores, R., & Primack, J. R. 1986, ApJ, 301, 27

Blumenthal, G. R., Faber, S. M., Primack, J. R., & Rees, M. J. 1984, Nature, 311, 517

Bothun, G. D., & Thompson, I. B. 1988, AJ, 96, 877

Bournaud, F., Elmegreen, B. G., & Martig, M. 2009, ApJ, 707, L1

Bournaud, F., Jog, C. J., & Combes, F. 2005, A&A, 437, 69

Bower, R. G., Benson, A. J., Lacey, C. G., Baugh, C. M., Cole, S., & Frenk, C. S. 2001, MNRAS, 325, 497

Bower, R. G., Benson, A. J., Malbon, R., Helly, J. C., Frenk, C. S., Baugh, C. M., Cole, S., & Lacey, C. G. 2006, MNRAS, 370, 645

Boylan-Kolchin, M., Bullock, J. S., & Kaplinghat, M. 2011, ArXiv e-prints

Boylan-Kolchin, M., Springel, V., White, S. D. M., & Jenkins, A. 2010, MNRAS, 406, 896

Brinchmann, J., & Ellis, R. S. 2000, ApJ, 536, L77

Brook, C. B., Kawata, D., Gibson, B. K., & Freeman, K. C. 2004, ApJ, 612, 894

Bruzual, G., & Charlot, S. 2003, MNRAS, 344, 1000

Bullock, J. S., Kravtsov, A. V., & Weinberg, D. H. 2001, ApJ, 548, 33

Bullock, J. S., Stewart, K. R., Kaplinghat, M., Tollerud, E. J., & Wolf, J. 2010, ApJ, 717, 1043

Buonanno, R., Corsi, C. E., Castellani, M., Marconi, G., Fusi Pecci, F., & Zinn, R. 1999, AJ, 118, 1671

Busha, M. T., Alvarez, M. A., Wechsler, R. H., Abel, T., & Strigari, L. E. 2010, ApJ, 710, 408

Cabezón, R. M., García-Senz, D., & Relaño, A. 2008, Journal of Computational Physics, 227, 8523

Caldwell, R. R., Dave, R., & Steinhardt, P. J. 1998, Physical Review Letters, 80, 1582

Carollo, D., et al. 2007, Nature, 450, 1020

—. 2010, ApJ, 712, 692

Carroll, S. M., Press, W. H., & Turner, E. L. 1992, ARA&A, 30, 499

Cen, R., Miralda-Escudé, J., Ostriker, J. P., & Rauch, M. 1994, ApJ, 437, L9

Ceverino, D., Dekel, A., & Bournaud, F. 2010, MNRAS, 404, 2151

Ceverino, D., & Klypin, A. 2009, ApJ, 695, 292

Chabrier, G. 2003, PASP, 115, 763

Chandrasekhar, S. 1943, ApJ, 97, 255

Chen, B., et al. 2001, ApJ, 553, 184

Chiba, M., & Beers, T. C. 2000, AJ, 119, 2843

Christlieb, N., et al. 2002, Nature, 419, 904

Cole, S., Lacey, C. G., Baugh, C. M., & Frenk, C. S. 2000, MNRAS, 319, 168

Cole, S., et al. 2001, MNRAS, 326, 255

Colín, P., Avila-Reese, V., & Valenzuela, O. 2000, ApJ, 542, 622

Colless, M., et al. 2001, MNRAS, 328, 1039

Combes, F., Debbasch, F., Friedli, D., & Pfenniger, D. 1990, A&A, 233, 82

Cooley, J., & Tukey, J. 1965, Mathematics of Computation, 19, 297

Cooper, A. P., et al. 2010, MNRAS, 406, 744

Courteau, S., Dutton, A. A., van den Bosch, F. C., MacArthur, L. A., Dekel, A., McIntosh, D. H., & Dale, D. A. 2007, ApJ, 671, 203

Cowie, L. L., & McKee, C. F. 1977, ApJ, 211, 135

Cowsik, R., & McClelland, J. 1973, ApJ, 180, 7

Cox, T. J., Dutta, S. N., Di Matteo, T., Hernquist, L., Hopkins, P. F., Robertson, B., & Springel, V. 2006, ApJ, 650, 791

Crain, R. A., McCarthy, I. G., Frenk, C. S., Theuns, T., & Schaye, J. 2010a, MNRAS, 407, 1403

Crain, R. A., McCarthy, I. G., Schaye, J., Frenk, C. S., & Theuns, T. 2010b, ArXiv e-prints

Crain, R. A., et al. 2009, MNRAS, 399, 1773

Croft, R. A. C., Di Matteo, T., Springel, V., & Hernquist, L. 2008, ArXiv e-prints, astro-ph/0803.4003

Croton, D. J., et al. 2006, MNRAS, 365, 11

Daddi, E. 2004, ApJ, 600, L127

Dalla Vecchia, C., & Schaye, J. 2008, MNRAS, 387, 1431

Davies, R. L., Efstathiou, G., Fall, S. M., Illingworth, G., & Schechter, P. L. 1983, ApJ, 266, 41

Davis, M., Efstathiou, G., Frenk, C. S., & White, S. D. M. 1985, ApJ, 292, 371

Davis, M., & Geller, M. J. 1976, ApJ, 208, 13

de Jong, J. T. A., Yanny, B., Rix, H.-W., Dolphin, A. E., Martin, N. F., & Beers, T. C. 2010, ApJ, 714, 663

De Lucia, G., & Blaizot, J. 2007, MNRAS, 375, 2

De Lucia, G., Springel, V., White, S. D. M., Croton, D., & Kauffmann, G. 2006, MNRAS, 366, 499

de Vaucouleurs, G. 1959, Handbuch der Physik, 53, 275

Deason, A. J., Belokurov, V., & Evans, N. W. 2011, ArXiv e-prints

Dehnen, W., McLaughlin, D. E., & Sachania, J. 2006, MNRAS, 369, 1688

Dekel, A., & Silk, J. 1986, ApJ, 303, 39

Dicke, R. H. 1961, Nature, 192, 440

Dicke, R. H., Peebles, P. J. E., Roll, P. G., & Wilkinson, D. T. 1965, ApJ, 142, 414

Dickinson, M. 2000, in Royal Society of London Philosophical Transactions Series A, Vol. 358, Astronomy, physics and chemistry of H_3^+, 2001–+

Diemand, J., Kuhlen, M., Madau, P., Zemp, M., Moore, B., Potter, D., & Stadel, J. 2008, Nature, 454, 735

Dolag, K., Borgani, S., Murante, G., & Springel, V. 2009, MNRAS, 399, 497

Dressler, A. 1980, ApJ, 236, 351

Dressler, A., et al. 1997, ApJ, 490, 577

Driver, S. P., Popescu, C. C., Tuffs, R. J., Liske, J., Graham, A. W., Allen, P. D., & de Propris, R. 2007, MNRAS, 379, 1022

Dubois, Y., & Teyssier, R. 2008, A&A, 477, 79

Edsjö, J., & Gondolo, P. 1997, Phys. Rev. D, 56, 1879

Efstathiou, G. 1992, MNRAS, 256, 43P

Efstathiou, G., & Eastwood, J. W. 1981, MNRAS, 194, 503

Efstathiou, G., Lake, G., & Negroponte, J. 1982, MNRAS, 199, 1069

Efstathiou, G., Sutherland, W. J., & Maddox, S. J. 1990, Nature, 348, 705

Einasto, J., Saar, E., Kaasik, A., & Chernin, A. D. 1974, Nature, 252, 111

Einstein, A. 1916, Annalen der Physik, 354, 769

El-Zant, A., Shlosman, I., & Hoffman, Y. 2001, ApJ, 560, 636

El-Zant, A. A., Hoffman, Y., Primack, J., Combes, F., & Shlosman, I. 2004, ApJ, 607, L75

Elmegreen, B. G. 1989, ApJ, 338, 178

Emsellem, E., et al. 2007, MNRAS, 379, 401

Englmaier, P., & Gerhard, O. 1999, MNRAS, 304, 512

Eyre, A., & Binney, J. 2009, MNRAS, 399, L160

Feldmann, R., Carollo, C. M., & Mayer, L. 2011, ApJ, 736, 88

Ferland, G. J., Korista, K. T., Verner, D. A., Ferguson, J. W., Kingdon, J. B., & Verner, E. M. 1998, PASP, 110, 761

Ferramacho, L. D., Blanchard, A., & Zolnierowski, Y. 2009, A&A, 499, 21

Ferrarese, L., & Merritt, D. 2000, ApJ, 539, L9

Fioc, M., & Rocca-Volmerange, B. 1997, A&A, 326, 950

Font, A. S., McCarthy, I. G., Crain, R. A., Theuns, T., Schaye, J., Wiersma, R. P. C., & Dalla Vecchia, C. 2011a, ArXiv e-prints

Font, A. S., et al. 2008, MNRAS, 389, 1619

—. 2011b, ArXiv e-prints

Frebel, A., Christlieb, N., Norris, J. E., Thom, C., Beers, T. C., & Rhee, J. 2007, ApJ, 660, L117

Frebel, A., et al. 2005, in IAU Symposium, Vol. 228, From Lithium to Uranium: Elemental Tracers of Early Cosmic Evolution, ed. V. Hill, P. François, & F. Primas, 207–212

Frenk, C. S., Evrard, A. E., White, S. D. M., & Summers, F. J. 1996, ApJ, 472, 460

Frenk, C. S., White, S. D. M., Bode, P., Bond, J. R., Bryan, G. L., Cen, R., Couchman, H. M. P., & Evrard, A. E. 1999, ApJ, 525, 554

Frenk, C. S., White, S. D. M., Davis, M., & Efstathiou, G. 1988, ApJ, 327, 507

Frenk, C. S., White, S. D. M., Efstathiou, G., & Davis, M. 1985, Nature, 317, 595

Friedman, A. 1922, Zeitschrift fur Physik, 10, 377

Frogel, J. A. 1990, in European Southern Observatory Conference and Workshop Proceedings, Vol. 35, European Southern Observatory Conference and Workshop Proceedings, ed. B. J. Jarvis & D. M. Terndrup, 177–185

Frogel, J. A. 1999, in The Formation of Galactic Bulges, ed. C. M. Carollo, H. C. Ferguson, & R. F. G. Wyse, 38–+

Fukugita, M., Yamashita, K., Takahara, F., & Yoshii, Y. 1990, ApJ, 361, L1

Fukui, Y., Mizuno, N., Yamaguchi, R., Mizuno, A., & Onishi, T. 2001, PASJ, 53, L41

Fulk, D. A., & Quinn, D. W. 1996, J. Comput. Phys., 126, 165

Gadotti, D. A. 2008, ArXiv e-prints

Gamow, G. 1948a, Nature, 162, 680

—. 1948b, Physical Review, 74, 505

Gelato, S., & Sommer-Larsen, J. 1999, MNRAS, 303, 321

Genzel, R., Hollenbach, D., & Townes, C. H. 1994, Reports on Progress in Physics, 57, 417

Gerhard, O. 2002, in Astronomical Society of the Pacific Conference Series, Vol. 273, The Dynamics, Structure & History of Galaxies: A Workshop in Honour of Professor Ken Freeman, ed. G. S. Da Costa & H. Jerjen, 73–+

Giavalisco, M., Steidel, C. C., & Macchetto, F. D. 1996, ApJ, 470, 189

Gilmore, G., & Reid, N. 1983, MNRAS, 202, 1025

Gilmore, G., Wilkinson, M. I., Wyse, R. F. G., Kleyna, J. T., Koch, A., Evans, N. W., & Grebel, E. K. 2007, ApJ, 663, 948

Gilmore, G., & Wyse, R. F. G. 1998, AJ, 116, 748

Gilmore, G., Wyse, R. F. G., & Jones, J. B. 1995, AJ, 109, 1095

Gnedin, O. Y., Brown, W. R., Geller, M. J., & Kenyon, S. J. 2010, ApJ, 720, L108

Gnedin, O. Y., Hernquist, L., & Ostriker, J. P. 1999, ApJ, 514, 109

Gnedin, O. Y., Kravtsov, A. V., Klypin, A. A., & Nagai, D. 2004, ApJ, 616, 16

Gnedin, O. Y., & Zhao, H. 2002, MNRAS, 333, 299

Goerdt, T., Moore, B., Read, J. I., & Stadel, J. 2010, ApJ, 725, 1707

Goerdt, T., Moore, B., Read, J. I., Stadel, J., & Zemp, M. 2006, MNRAS, 368, 1073

Goldhaber, G., & Perlmutter, S. 1998, Phys. Rep., 307, 325

Goodman, M. W., & Witten, E. 1985, Phys. Rev. D, 31, 3059

Governato, F., Willman, B., Mayer, L., Brooks, A., Stinson, G., Valenzuela, O., Wadsley, J., & Quinn, T. 2007, MNRAS, 374, 1479

Governato, F., et al. 2009, MNRAS, 398, 312

—. 2010, Nature, 463, 203

Grillmair, C. J. 2009, ApJ, 693, 1118

Guedes, J., Callegari, S., Madau, P., & Mayer, L. 2011, ArXiv e-prints

Guiderdoni, B., Hivon, E., Bouchet, F. R., & Maffei, B. 1998, MNRAS, 295, 877

Gunn, J. E., & Gott, J. R. 1972, ApJ, 176, 1

Guo, Q., Cole, S., Eke, V., & Frenk, C. 2011, ArXiv e-prints

Guo, Q., White, S., Li, C., & Boylan-Kolchin, M. 2010, MNRAS, 404, 1111

Guth, A. H. 1981, Phys. Rev. D, 23, 347

Guth, A. H., & Weinberg, E. J. 1983, Nuclear Physics B, 212, 321

Haardt, F., & Madau, P. 1996, ApJ, 461, 20

Haardt, F., & Madau, P. 2001, in Clusters of Galaxies and the High Redshift Universe Observed in X-rays, ed. D. M. Neumann & J. T. V. Tran

Hahn, O., Teyssier, R., & Carollo, C. M. 2010, MNRAS, 405, 274

Harding, P., Morrison, H. L., Olszewski, E. W., Arabadjis, J., Mateo, M., Dohm-Palmer, R. C., Freeman, K. C., & Norris, J. E. 2001, AJ, 122, 1397

Häring-Neumayer, N., Cappellari, M., Rix, H. W., Hartung, M., Prieto, M. A., Meisenheimer, K., & Lenzen, R. 2006, ApJ, 643, 226

Harker, G., Cole, S., Helly, J., Frenk, C. S., & Jenkins, A. 2006, MNRAS, 367, 1039

Hawking, S. W. 1982, Physics Letters B, 115, 295

Haywood, M. 2008, MNRAS, 388, 1175

Helly, J. C., Cole, S., Frenk, C. S., Baugh, C. M., Benson, A., & Lacey, C. 2003, MNRAS, 338, 903

Helmi, A. 2004, ApJ, 610, L97

Helmi, A., & White, S. D. M. 1999, MNRAS, 307, 495

Helmi, A., White, S. D. M., & Springel, V. 2003, MNRAS, 339, 834

Hernquist, L. 1987, ApJS, 64, 715

Hernquist, L., Katz, N., Weinberg, D. H., & Miralda-Escudé, J. 1996, ApJ, 457, L51+

Hernquist, L., & Mihos, J. C. 1995, ApJ, 448, 41

Heyer, M. H., Carpenter, J. M., & Snell, R. L. 2001, ApJ, 551, 852

Hilditch, R. W., Howarth, I. D., & Harries, T. J. 2005, MNRAS, 357, 304

Hockney, R. W., & Eastwood, J. W. 1981, Computer Simulation Using Particles, ed. Hockney, R. W. & Eastwood, J. W.

Hoeft, M., Yepes, G., Gottlöber, S., & Springel, V. 2006, MNRAS, 371, 401

Hogan, C. J., & Dalcanton, J. J. 2000, Phys. Rev. D, 62, 063511

Hopkins, P. F., Cox, T. J., Kereš, D., & Hernquist, L. 2008a, ApJS, 175, 390

Hopkins, P. F., Cox, T. J., Younger, J. D., & Hernquist, L. 2008b, ArXiv e-prints

Hoyle, F. 1949, Ohio: Central Air Documents Office, 195

Hubble, E. 1929, Proceedings of the National Academy of Science, 15, 168

Hubble, E. P. 1926, ApJ, 64, 321

—. 1936, Yale University Press

Huchra, J., Davis, M., Latham, D., & Tonry, J. 1983, ApJS, 52, 89

Ibata, R., Irwin, M., Lewis, G. F., & Stolte, A. 2001, ApJ, 547, L133

Ibata, R. A., Gilmore, G., & Irwin, M. J. 1994, Nature, 370, 194

Ibata, R. A., & Gilmore, G. F. 1995, MNRAS, 275, 591

Illingworth, G. 1977, ApJ, 218, L43

Illingworth, G., & Schechter, P. L. 1982, ApJ, 256, 481

Jeltema, T. E., Binder, B., & Mulchaey, J. S. 2008, ApJ, 679, 1162

Johnston, K. V., Hernquist, L., & Bolte, M. 1996, ApJ, 465, 278

Johnston, K. V., Law, D. R., & Majewski, S. R. 2005, ApJ, 619, 800

Jungman, G., Kamionkowski, M., & Griest, K. 1996, Phys. Rep., 267, 195

Jurić, M., et al. 2008, ApJ, 673, 864

Kalberla, P. M. W., & Dedes, L. 2008, A&A, 487, 951

Kane, G., & Watson, S. 2008, Modern Physics Letters A, 23, 2103

Kang, X. 2005, Prog.Ast, 23, 135

Kang, X., van den Bosch, F. C., & Pasquali, A. 2007, MNRAS, 381, 389

Katz, N., Weinberg, D. H., & Hernquist, L. 1996a, ApJS, 105, 19

—. 1996b, ApJ, 105, 19

Kauffmann, G. 1996, MNRAS, 281, 487

Kauffmann, G., & Charlot, S. 1998, MNRAS, 297, L23

Kauffmann, G., White, S. D. M., & Guiderdoni, B. 1993, MNRAS, 264, 201

Kazantzidis, S., Abadi, M. G., & Navarro, J. F. 2010, ApJ, 720, L62

Kazantzidis, S., Bullock, J. S., Zentner, A. R., Kravtsov, A. V., & Moustakas, L. A. 2008, ApJ, 688, 254

Kennicutt, R. C. 1983, ApJ, 272, 54

Kennicutt, Jr., R. C. 1998, ApJ, 498, 541

Khochfar, S., & Silk, J. 2006, MNRAS, 370, 902

Kim, S., Staveley-Smith, L., Dopita, M. A., Freeman, K. C., Sault, R. J., Kesteven, M. J., & McConnell, D. 1998, ApJ, 503, 674

Kirby, E. N., Cohen, J. G., Smith, G. H., Majewski, S. R., Sohn, S. T., & Guhathakurta, P. 2011, ApJ, 727, 79

Klimentowski, J., Łokas, E. L., Kazantzidis, S., Mayer, L., & Mamon, G. A. 2009, MNRAS, 397, 2015

Klimentowski, J., Łokas, E. L., Kazantzidis, S., Prada, F., Mayer, L., & Mamon, G. A. 2007, MNRAS, 378, 353

Klypin, A., Kravtsov, A. V., Valenzuela, O., & Prada, F. 1999, ApJ, 522, 82

Klypin, A. A., & Shandarin, S. F. 1983, MNRAS, 204, 891

Knebe, A., Libeskind, N. I., Knollmann, S. R., Martinez-Vaquero, L. A., Yepes, G., Gottlöber, S., & Hoffman, Y. 2010, MNRAS, 1863

Knollmann, S. R., & Knebe, A. 2009, ApJS, 182, 608

Kobayashi, C., Springel, V., & White, S. D. M. 2007, MNRAS, 376, 1465

Komatsu, E., et al. 2011, ApJS, 192, 18

Koposov, S., Belokurov, V., Evans, N. W., Hewett, P. C., & Irwin, M. J. 2008, ApJ, 686, 279

Kormendy, J. 1993, in IAU Symposium, Vol. 153, Galactic Bulges, ed. H. Dejonghe & H. J. Habing, 209–+

Kormendy, J., & Fisher, D. B. 2008, ArXiv e-prints

Kormendy, J., & Gebhardt, K. 2001, in American Institute of Physics Conference Series, Vol. 586, 20th Texas Symposium on relativistic astrophysics, ed. J. C. Wheeler & H. Martel, 363–+

Kormendy, J., & Illingworth, G. 1982, ApJ, 256, 460

Kormendy, J., & Kennicutt, Jr, R. C. 2004a, ARA&A, 42, 603

Kormendy, J., & Kennicutt, Jr., R. C. 2004b, ARA&A, 42, 603

Lacey, C. G., Baugh, C. M., Frenk, C. S., Silva, L., Granato, G. L., & Bressan, A. 2008, MNRAS, 385, 1155

Lahav, O., Lilje, P. B., Primack, J. R., & Rees, M. J. 1991, MNRAS, 251, 128

Laird, J. B., Carney, B. W., Rupen, M. P., & Latham, D. W. 1988, AJ, 96, 1908

Larson, D., et al. 2011, ApJS, 192, 16

Larson, R. B. 1974, MNRAS, 169, 229

Larson, R. B., Tinsley, B. M., & Caldwell, C. N. 1980, ApJ, 237, 692

Law, D. R., Johnston, K. V., & Majewski, S. R. 2005, ApJ, 619, 807

Lecureur, A., Hill, V., Zoccali, M., Barbuy, B., Gómez, A., Minniti, D., Ortolani, S., & Renzini, A. 2007, A&A, 465, 799

Lee, M. G., Yuk, I.-S., Park, H. S., Harris, J., & Zaritsky, D. 2009, ApJ, 703, 692

Lemon, D. J., Wyse, R. F. G., Liske, J., Driver, S. P., & Horne, K. 2004, MNRAS, 347, 1043

Lemson, G., & Springel, V. 2006, in Astronomical Society of the Pacific Conference Series, Vol. 351, Astronomical Data Analysis Software and Systems XV, ed. C. Gabriel, C. Arviset, D. Ponz, & S. Enrique, 212–+

Lemson, G., & The Virgo Consortium. 2006, ArXiv e-prints, astro-ph/0608019

Li, Y., De Lucia, G., & Helmi, A. 2010, MNRAS, 401, 2036

Li, Y., & White, S. D. M. 2008, MNRAS, 384, 1459

Libeskind, N. I., Frenk, C. S., Cole, S., Helly, J. C., Jenkins, A., Navarro, J. F., & Power, C. 2005, MNRAS, 363, 146

Libeskind, N. I., Knebe, A., Hoffman, Y., Gottlöber, S., Yepes, G., & Steinmetz, M. 2011, MNRAS, 411, 1525

Liu, L., Gerke, B. F., Wechsler, R. H., Behroozi, P. S., & Busha, M. T. 2010, ArXiv e-prints

Łokas, E. L., Kazantzidis, S., Klimentowski, J., Mayer, L., & Callegari, S. 2010, ApJ, 708, 1032

Lovell, M., et al. 2011a, ArXiv e-prints

Lovell, M. R., Eke, V. R., Frenk, C. S., & Jenkins, A. 2011b, MNRAS, 413, 3013

Macciò, A. V., & Fontanot, F. 2010, MNRAS, 404, L16

Macciò, A. V., Kang, X., Fontanot, F., Somerville, R. S., Koposov, S., & Monaco, P. 2010, MNRAS, 402, 1995

Machacek, M. E., Bryan, G. L., & Abel, T. 2001, ApJ, 548, 509

Magorrian, J., et al. 1998, AJ, 115, 2285

Malbon, R. K., Baugh, C. M., Frenk, C. S., & Lacey, C. G. 2007, MNRAS, 382, 1394

Marconi, A., & Hunt, L. K. 2003, ApJ, 589, L21

Marigo, P. 2001, A&A, 370, 194

Marleau, F. R., & Simard, L. 1998, ApJ, 507, 585

Martin, C. L. 2005, ApJ, 621, 227

Martin, N. F., Ibata, R. A., Irwin, M. J., Chapman, S., Lewis, G. F., Ferguson, A. M. N., Tanvir, N., & McConnachie, A. W. 2006, MNRAS, 371, 1983

Martínez-Delgado, D., Pohlen, M., Gabany, R. J., Majewski, S. R., Peñarrubia, J., & Palma, C. 2009, ApJ, 692, 955

Mashchenko, S., Couchman, H. M. P., & Wadsley, J. 2006, Nature, 442, 539

Mashchenko, S., Wadsley, J., & Couchman, H. M. P. 2008, Science, 319, 174

Mateo, M. L. 1998, ARA&A, 36, 435

Mayer, L., Governato, F., Colpi, M., Moore, B., Quinn, T., Wadsley, J., Stadel, J., & Lake, G. 2001a, ApJ, 547, L123

—. 2001b, ApJ, 559, 754

—. 2001c, ApJ, 547, L123

McConnachie, A. W., et al. 2008, ApJ, 688, 1009

McMillan, P. J. 2011, MNRAS, 414, 2446

McWilliam, A., & Rich, R. M. 1994, ApJS, 91, 749

Meléndez, J., et al. 2008, A&A, 484, L21

Mighell, K. J. 1990, A&AS, 82, 1

Mihos, J. C., & Hernquist, L. 1994, ApJ, 437, 611

Minniti, D. 1996, ApJ, 459, 175

Minniti, D., White, S. D. M., Olszewski, E. W., & Hill, J. M. 1992, ApJ, 393, L47

Minniti, D., & Zoccali, M. 2008, in IAU Symposium, Vol. 245, IAU Symposium, ed. M. Bureau, E. Athanassoula, & B. Barbuy, 323–332

Mitchell, N. L., McCarthy, I. G., Bower, R. G., Theuns, T., & Crain, R. A. 2009, MNRAS, 395, 180

Mo, H. J., & Mao, S. 2004, MNRAS, 353, 829

Mo, H. J., Mao, S., & White, S. D. M. 1998, MNRAS, 295, 319

Monaghan, J. J., & Gingold, R. A. 1983, Journal of Computational Physics, 52, 374

Monaghan, J. J., & Lattanzio, J. C. 1985, A&A, 149, 135

Moore, B., Ghigna, S., Governato, F., Lake, G., Quinn, T., Stadel, J., & Tozzi, P. 1999, ApJ, 524, L19

Moore, B., Katz, N., Lake, G., Dressler, A., & Oemler Jr, A. 1996, Nature, 379, 613

Morrison, H. L. 1993, AJ, 106, 578

Murante, G., Monaco, P., Giovalli, M., Borgani, S., & Diaferio, A. 2010, MNRAS, 405, 1491

Naab, T., & Burkert, A. 2003, ApJ, 597, 893

Naab, T., Burkert, A., & Hernquist, L. 1999, ApJ, 523, L133

Naab, T., Jesseit, R., & Burkert, A. 2006, MNRAS, 372, 839

Nakamura, O., Fukugita, M., Yasuda, N., Loveday, J., Brinkmann, J., Schneider, D. P., Shimasaku, K., & SubbaRao, M. 2003, ApJ, 125, 1682

Navarro, J. F., & Benz, W. 1991, ApJ, 380, 320

Navarro, J. F., Eke, V. R., & Frenk, C. S. 1996a, MNRAS, 283, L72

Navarro, J. F., Frenk, C. S., & White, S. D. M. 1996b, ApJ, 462, 563

—. 1997, ApJ, 490, 493

Navarro, J. F., & White, S. D. M. 1993, MNRAS, 265, 271

Navarro, J. F., et al. 2010, MNRAS, 402, 21

Negroponte, J., & White, S. D. M. 1983, MNRAS, 205, 1009

Newberg, H. J., & Yanny, B. 2006, Journal of Physics Conference Series, 47, 195

Newberg, H. J., et al. 2002, ApJ, 569, 245

Niederste-Ostholt, M., Belokurov, V., Evans, N. W., & Peñarrubia, J. 2010, ApJ, 712, 516

Nissen, P. E., & Schuster, W. J. 2010, A&A, 511, L10+

Norris, J. E., Christlieb, N., Korn, A. J., Eriksson, K., Bessell, M. S., Beers, T. C., Wisotzki, L., & Reimers, D. 2007, ApJ, 670, 774

Okamoto, T., Eke, V. R., Frenk, C. S., & Jenkins, A. 2005, MNRAS, 363, 1299

Okamoto, T., & Frenk, C. S. 2009, MNRAS, 399, L174

Okamoto, T., Frenk, C. S., Jenkins, A., & Theuns, T. 2010, MNRAS, 406, 208

Okamoto, T., Gao, L., & Theuns, T. 2008a, MNRAS, 390, 920

Okamoto, T., Nemmen, R. S., & Bower, R. G. 2008b, MNRAS, 385, 161

Ortolani, S., Renzini, A., Gilmozzi, R., Marconi, G., Barbuy, B., Bica, E., & Rich, R. M. 1995, Nature, 377, 701

Ostriker, J. P., & Peebles, P. J. E. 1973, ApJ, 186, 467

Owen, R. A., & Warwick, R. S. 2009, MNRAS, 394, 1741

Papovich, C., Dickinson, M., Giavalisco, M., Conselice, C. J., & Ferguson, H. C. 2005, ApJ, 631, 101

Peñarrubia, J., Navarro, J. F., & McConnachie, A. W. 2008, ApJ, 673, 226

Peacock, J. A. 1999, Cosmological Physics

Peebles, P. J. E. 1969, ApJ, 155, 393

Peebles, P. J. E. 1982, ApJ, 263, L1

—. 1984a, ApJ, 277, 470

—. 1984b, ApJ, 284, 439

Penzias, A. A., & Wilson, R. W. 1965, ApJ, 142, 419

Percival, W. J., et al. 2007, ApJ, 657, 645

—. 2010, MNRAS, 401, 2148

Pietrzyński, G., et al. 2009, ApJ, 697, 862

Pizagno, J., et al. 2007, AJ, 134, 945

Polisensky, E., & Ricotti, M. 2011, Phys. Rev. D, 83, 043506

Pontzen, A., & Governato, F. 2011, ArXiv e-prints

Portinari, L., Chiosi, C., & Bressan, A. 1998, A&A, 334, 505

Postman, M., & Geller, M. J. 1984, ApJ, 281, 95

Postman, M., et al. 2005, ApJ, 623, 721

Power, C., Navarro, J. F., Jenkins, A., Frenk, C. S., White, S. D. M., Springel, V., Stadel, J., & Quinn, T. 2003, MNRAS, 338, 14

Price, D. J. 2008, Journal of Computational Physics, 2271, 10040

Purcell, C. W., Kazantzidis, S., & Bullock, J. S. 2009, ApJ, 694, L98

Rasera, Y., & Teyssier, R. 2006, A&A, 445, 1

Rattenbury, N. J., Mao, S., Sumi, T., & Smith, M. C. 2007, MNRAS, 378, 1064

Ravindranath, S., et al. 2004, ApJ, 604, L9

Read, A. M., & Ponman, T. J. 1998, MNRAS, 297, 143

Read, J. I., & Gilmore, G. 2005, MNRAS, 356, 107

Read, J. I., Hayfield, T., & Agertz, O. 2010, MNRAS, 405, 1513

Reddy, B. E., Lambert, D. L., & Allende Prieto, C. 2006, MNRAS, 367, 1329

Reddy, B. E., Tomkin, J., Lambert, D. L., & Allende Prieto, C. 2003, MNRAS, 340, 304

Rees, M. J., & Ostriker, J. P. 1977, MNRAS, 179, 541

Reid, B. A., et al. 2010, MNRAS, 404, 60

Rich, R. M., Reitzel, D. B., Howard, C. D., & Zhao, H. 2007, ApJ, 658, L29

Riess, A. G., et al. 1998, AJ, 116, 1009

—. 2009, ApJ, 699, 539

Robertson, B. E., & Kravtsov, A. V. 2008, ApJ, 680, 1083

Rubin, V. C., & Ford, Jr., W. K. 1970, ApJ, 159, 379

Sackett, P. D., Morrisoni, H. L., Harding, P., & Boroson, T. A. 1994, Nature, 370, 441

Saitoh, T. R., & Makino, J. 2010, PASJ, 62, 301

Sales, L. V., et al. 2009, MNRAS, 400, L61

Samland, M., & Gerhard, O. E. 2003, A&A, 399, 961

Sánchez, A. G., Crocce, M., Cabré, A., Baugh, C. M., & Gaztañaga, E. 2009, MNRAS, 400, 1643

Sánchez, E., & the Des collaboration. 2010, Journal of Physics Conference Series, 259, 012080

Sánchez-Salcedo, F. J., Reyes-Iturbide, J., & Hernandez, X. 2006, MNRAS, 370, 1829

Sandage, A. 1961, The Hubble atlas of galaxies (Washington: Carnegie Institution)

Saunders, W., Frenk, C., Rowan-Robinson, M., Lawrence, A., & Efstathiou, G. 1991, Nature, 349, 32

Sawala, T., Scannapieco, C., & White, S. 2011, ArXiv e-prints

Scannapieco, C., Tissera, P. B., White, S. D. M., & Springel, V. 2005, MNRAS, 364, 552

—. 2006, MNRAS, 371, 1125

Scannapieco, C., White, S. D. M., Springel, V., & Tissera, P. B. 2009, MNRAS, 396, 696

—. 2011, ArXiv e-prints

Schaye, J., & Dalla Vecchia, C. 2008, MNRAS, 383, 1210

Schaye, J., et al. 2010, MNRAS, 402, 1536

Schlegel, D., et al. 2011, ArXiv e-prints

Schmidt, M. 1959, ApJ, 129, 243

Schönrich, R., & Binney, J. 2009, MNRAS, 399, 1145

Sesar, B., Jurić, M., & Ivezić, Ž. 2011, ApJ, 731, 4

Sesar, B., et al. 2010, ApJ, 708, 717

Shang, Z., et al. 1998, ApJ, 504, L23+

Shen, S., Wadsley, J., & Stinson, G. 2010, MNRAS, 407, 1581

Shlosman, I., Frank, J., & Begelman, M. C. 1989, Nature, 338, 45

Simon, J. D., & Geha, M. 2007, ApJ, 670, 313

Skillman, E. D., Kennicutt, R. C., & Hodge, P. W. 1989, ApJ, 347, 875

Smith, A. J., Loveday, J., & Cross, N. J. G. 2008, ArXiv e-prints

Smoot, G. F., et al. 1992, ApJ, 396, L1

Sofue, Y., Honma, M., & Omodaka, T. 2009, PASJ, 61, 227

Solomon, P. M., & Rivolo, A. R. 1989, ApJ, 339, 919

Somerville, R. S. 2002, ApJ, 572, L23

Somerville, R. S., Hopkins, P. F., Cox, T. J., Robertson, B. E., & Hernquist, L. 2008, ArXiv e-prints

Soubiran, C., Bienaymé, O., & Siebert, A. 2003, A&A, 398, 141

Spergel, D. N., et al. 2003, ApJS, 148, 175

Spitzer, L. 1962, in Physics of Fully Ionized Gases, New York: Interscience (2nd edition), 1962, ed. Spitzer, L.

Springel, V. 2010, MNRAS, 401, 791

Springel, V., & Hernquist, L. 2002, MNRAS, 333, 649

—. 2003, MNRAS, 339, 289

—. 2005, ApJ, 622, L9

Springel, V., White, S. D. M., Tormen, G., & Kauffmann, G. 2001a, MNRAS, 328, 726

Springel, V., Yoshida, N., & White, S. D. M. 2001b, New. Astron, 6, 79

Springel, V., et al. 2005, Nature, 435, 629

—. 2008a, Nature, 456, 73

—. 2008b, MNRAS, 391, 1685

—. 2008c, MNRAS, 391, 1685

Stadel, J., Potter, D., Moore, B., Diemand, J., Madau, P., Zemp, M., Kuhlen, M., & Quilis, V. 2009, MNRAS, 398, L21

Starobinsky, A. A. 1982, Physics Letters B, 117, 175

Steinmetz, M. 1996, MNRAS, 278, 1005

Steinmetz, M., & Navarro, J. 2002, New.Astron., 7, 155

Stinson, G., Seth, A., Katz, N., Wadsley, J., Governato, F., & Quinn, T. 2006, MNRAS, 373, 1074

Stoehr, F., White, S. D. M., Tormen, G., & Springel, V. 2002, MNRAS, 335, L84

Strickland, D. K., Heckman, T. M., Colbert, E. J. M., Hoopes, C. G., & Weaver, K. A. 2004, ApJS, 151, 193

Strigari, L. E., Bullock, J. S., Kaplinghat, M., Kravtsov, A. V., Gnedin, O. Y., Abazajian, K., & Klypin, A. A. 2006, ApJ, 652, 306

Strigari, L. E., Bullock, J. S., Kaplinghat, M., Simon, J. D., Geha, M., Willman, B., & Walker, M. G. 2008, Nature, 454, 1096

Strigari, L. E., Frenk, C. S., & White, S. D. M. 2010, MNRAS, 1311

Sutherland, R. S., & Dopita, M. A. 1993, ApJS, 88, 253

Swaters, R. A., Schoenmakers, R. H. M., Sancisi, R., & van Albada, T. S. 1999, MNRAS, 304, 330

Tasca, L. A. M., & White, S. D. M. 2005, MNRAS, submitted (astro-ph/0507249)

Teyssier, R. 2002, A&A, 385, 337

Teyssier, R., Moore, B., Martizzi, D., Dubois, Y., & Mayer, L. 2011, MNRAS, 414, 195

Thacker, R. J., & Couchman, H. M. P. 2001, ApJ, 555, L17

Thomas, P. A., & Couchman, H. M. P. 1992, MNRAS, 257, 11

Toomre, A. 1977, in Evolution of Galaxies and Stellar Populations, 401–+

Tran, K. V., Simard, L., Zabludoff, A. I., & Mulchaey, J. S. 2001, ApJ, 549, 172

Trinchieri, G., Fabbiano, G., & Kim, D.-W. 1997, A&A, 318, 361

Truelove, J. K., Klein, R. I., McKee, C. F., Holliman, II, J. H., Howell, L. H., & Greenough, J. A. 1997, ApJ, 489, L179+

van de Hulst, H. C., Raimond, E., & van Woerden, H. 1957, Bull. Astron. Inst. Netherlands, 14, 1

van de Voort, F., Schaye, J., Booth, C. M., Haas, M. R., & Dalla Vecchia, C. 2011, MNRAS, 414, 2458

Van den Bergh, S. 1960, ApJ, 131, 215

—. 2002, PASP, 114, 797

van den Bosch, F. C., Abel, T., Croft, R. A. C., Hernquist, L., & White, S. D. M. 2002, ApJ, 576, 21

van Loon, J. T., et al. 2003, MNRAS, 338, 857

Van Waerbeke, L., Mellier, Y., & Hoekstra, H. 2005, A&A, 429, 75

Vera-Ciro, C. A., Sales, L. V., Helmi, A., Frenk, C. S., Navarro, J. F., Springel, V., Vogelsberger, M., & White, S. D. M. 2011, MNRAS, 1100

Verheijen, M. A. W. 2001, ApJ, 563, 694

Vikhlinin, A., et al. 2009, ApJ, 692, 1060

Villalobos, Á., & Helmi, A. 2009, MNRAS, 399, 166

Vivas, A. K., et al. 2001, ApJ, 554, L33

Wada, K., & Norman, C. A. 2007, ApJ, 660, 276

Wadepuhl, M., & Springel, V. 2010, ArXiv e-prints

Wadsley, J. W., Stadel, J., & Quinn, T. 2004, New. Astron, 9, 137

Wakker, B. P., & van Woerden, H. 1997, ARA&A, 35, 217

Walker, M. G., Mateo, M., Olszewski, E. W., Gnedin, O. Y., Wang, X., Sen, B., & Woodroofe, M. 2007, ApJ, 667, L53

Walker, M. G., Mateo, M., Olszewski, E. W., Peñarrubia, J., Wyn Evans, N., & Gilmore, G. 2009, ApJ, 704, 1274

Walsh, D., Carswell, R. F., & Weymann, R. J. 1979, Nature, 279, 381

Wang, J., et al. 2011, MNRAS, 413, 1373

Wang, Q. D. 2005, in Astronomical Society of the Pacific Conference Series, Vol. 331, Extra-Planar Gas, ed. R. Braun, 329–+

Watkins, L. L., Evans, N. W., & An, J. H. 2010, MNRAS, 406, 264

Watkins, L. L., et al. 2009, MNRAS, 398, 1757

Wheeler, J. C., Sneden, C., & Truran, Jr., J. W. 1989, ARA&A, 27, 279

White, S. D. M. 1978, MNRAS, 184, 183

—. 1984, ApJ, 286, 38

White, S. D. M. 1996, in Cosmology and Large Scale Structure, ed. R. Schaeffer, J. Silk, M. Spiro, & J. Zinn-Justin, 349

White, S. D. M., & Frenk, C. S. 1991, ApJ, 379, 52

White, S. D. M., Frenk, C. S., & Davis, M. 1983, ApJ, 274, L1

White, S. D. M., Navarro, J. F., Evrard, A. E., & Frenk, C. S. 1993, Nature, 366, 429

White, S. D. M., & Rees, M. J. 1978, MNRAS, 183, 341

Wiersma, R. P. C., Schaye, J., & Smith, B. D. 2009a, MNRAS, 393, 99

Wiersma, R. P. C., Schaye, J., Theuns, T., Dalla Vecchia, C., & Tornatore, L. 2009b, MNRAS, 399, 574

Wolf, J., Martinez, G. D., Bullock, J. S., Kaplinghat, M., Geha, M., Muñoz, R. R., Simon, J. D., & Avedo, F. F. 2010, MNRAS, 406, 1220

Xue, X. X., et al. 2008, ApJ, 684, 1143

Yanny, B., et al. 2003, ApJ, 588, 824

York, D. G., et al. 2000, AJ, 120, 1579

Zavala, J., Okamoto, T., & Frenk, C. S. 2008, MNRAS, 387, 364

Zeldovich, I. B., Einasto, J., & Shandarin, S. F. 1982, Nature, 300, 407

Zel'Dovich, Y. B. 1970, A&A, 5, 84

Zeldovich, Y. B., & Khlopov, M. Y. 1978, Physics Letters B, 79, 239

Zentner, A. R., Kravtsov, A. V., Gnedin, O. Y., & Klypin, A. A. 2005, ApJ, 629, 219

Zoccali, M., et al. 2003, A&A, 399, 931

Zoccali, M., et al. 2007, in IAU Symposium, Vol. 241, IAU Symposium, ed. A. Vazdekis & R. F. Peletier, 73–77

Zolotov, A., Willman, B., Brooks, A. M., Governato, F., Brook, C. B., Hogg, D. W., Quinn, T., & Stinson, G. 2009, ApJ, 702, 1058

Zolotov, A., Willman, B., Brooks, A. M., Governato, F., Hogg, D. W., Shen, S., & Wadsley, J. 2010, ApJ, 721, 738

Zucker, D. B., et al. 2004, ApJ, 612, L121

Zwicky, F. 1933, Helvetica Physica Acta, 6, 110